GEOPHYSICAL INVESTIGATION of the GEOTHERMAL SYSTEM within the CHROMO ANTICLINE

2015 GEOPHYSICS FIELD CAMP

Upper San Juan Basin
Archuleta County, CO

MINES

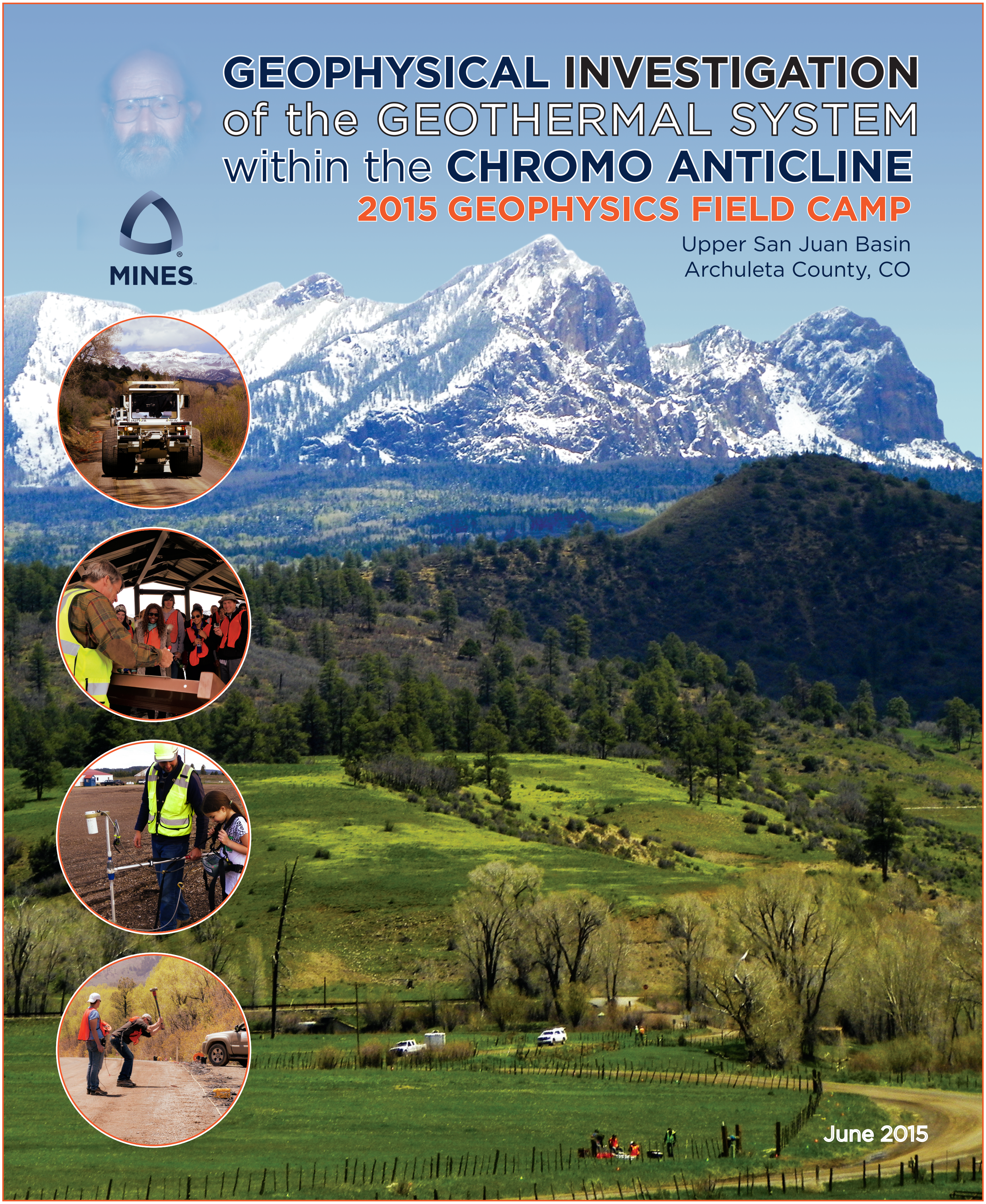

June 2015

Colroado School of Mines

Geophysics Field Camp 2015

Geophysical Investigation of Geothermal Systems in Chromo, CO

June 5th, 2015

In memory of Mike Batzle

Acknowledgments

The 2015 Colorado School of Mines Geophysics Field Camp would not have been possible without the generous financial contributions and support from a number of organizations and individuals. The students of this year's field camp are immensely appreciative of everyone involved in making this experience a reality.

We are incredibly grateful for the financial contributions provided by the following:

Colorado School of Mines
Colorado School of Mines, Department of Geophysics
Colorado School of Mines, Department of Enivronmental Health & Safety
Society of Exploration Geophysicists (SEG) Foundation
Anadarko Petroleum Corporation
ConocoPhillips
Marathon
QEP Resources
Shell

We want to thank the following for providing us with equipment, software, services, time and knowledge during out field session. The quality of our field time and seismic data would not have been possible without the help provide by:

Reservoir Characterization Project:
Tom Davis
Bob Benson

Dawson Geophysical:
Stuart Wright
Steve Kite
Mike Kite
Mike Lindholm

Sercel:
Tom Chatman

Landmark Services (Halliburton):
Bob Basker

United States Geologic Survey (USGS):
Seth Haines

Hugo Garcia

U.S. Army Corps of Engineers:
Ryan North

We would like to thank the following graduate research groups at the Colorado School of Mines for helping us process our field data:

Center for Gravity, Electrical & Magnetics Studies
Center for Hydrogeophysics & Porous Media

We would like to give special recognition to Marvin Johnson for his time and expertise during our acquisition. Marvin's contributions helped ensure smooth and efficient field procedures.

Additionally, thanks to Marvin and Pagosa Fire Protection Distric Station #7 Chromo for allowing use of firehouse for staging our field operations.

We are grateful for the support of:

CSU/Archuleta County Extension Office: Terry Schaaf
CSU/Archuleta County Extension Office, 4-H: Becky Jacobson
CSU/Archuleta County Extension Office: Roberta Tolan
Pagosa Baking Company: Kathy Keyes, Kirsten Skeehan
Pagosa High School: Laura Rand & staff
San Juan Motel: Laura Elguezbal & staff
The Springs Resort
Town of Pagosa Springs
The Water Runner: Chad & Christa Carnley

We cannot fully express our gratitude to the communities of Pagosa Springs and Chromo who allowed us to perform our surveys on their roads and private property. Special thanks to:

Archuleta County Road and Bridge Office
Colorado Department of Transportation
Darla Bramwell
Mark Houser/Joan Allmaras
Kevin Khung, US Department of Agriculture/US Forest Service
David Melass
Terry Schaaf

We would like to extend our utmost appreciation to the faculty and staff that helped to make this field camp possible. The donation of valuable knowledge, assistance, and time were a crucial part of making this experience a resounding success.

Joe Capriotti
Stephen Cuttler
Colton Kohnke
Rich Krahenbuhl
Andy McAliley
Liz Maag
Cici Martinez
Ed Nissen
Brian Passerella
Paul Sava
Thomas Rapstine
Bob Raynolds
Andre Revil
Andrei Swidinsky
Michelle Szobody
Dawn Umpleby
Matt Wisneiwski
Terry Young

In addition to the tremendous number of groups and people that helped make this field camp possible we would like to acknowledge the students who put in a tremendous amount of work into this project. These students, and their respective designations of this report are given in the tables below:

EM31 / EM34 / EM57	Deep Seismic		Hammer Seismic	MT
Denise Ruminski	**Daniel Rocha**	Victor Zhang	**Meghan West**	**Brandon Bolach**
Dana Gallegos	Abby Michel	Brett Yarborough	Austin Williams	Richmond Brininger
Kylee Brown	Alicia Johnson	Hongye Yuan	Stuart Farris	Ginevra Moore
Joseph Halloran	Renjie Wu	Andrew Cooper	Hui Wang	Andrew Markley
Rowdy Matthews	Dallas Hall	Steven Rennolet	Juliet George	
Yusef Ben-Masaud	Scott Harper	Varindra Pradhana		

Writing	DC/SP/IP	Gravity/Magnetics	Geology	GPS
Hank Cole	**Megan Gallagher**	**Sean Bader**	**Nicholas Fleegal**	**James Jordan**
Kira Dickey	Megan Fuhr	Jake Larson	Garrett Sickles	Samara Omar
Zach Simms	Ryan Meier	Qian Yin	Rowland Chen	Thomas Conklin
Upper Management	Nolan Leue	Samuel Smith	David Buswell	Aubrey Preble
Michael Sleevi	Flannery Dolan	Andrew Blaney		
Joni Sanborn				

Contents

List of Figures

List of Tables

SECTION 1

Abstract

This work describes the results of the Colorado School of Mines Department of Geophysics 2015 Field Camp which conducted investigative surveys in Chromo, Colorado from May 10th to May 21st. Several geophysical surveys have been done in this area during previous years' field camps to describe geological controls of the local hot springs. In order to understand geothermal activity on a regional scale it is important to identify the heat source driving the thermal gradient as well as the conduits providing pathways for fluid flow. Each of these topics can be investigated utilizing geophysical techniques to image various aspects of the subsurface. The Archuleta County area contains Pagosa Springs which has a variety of hot springs being fed by a 'mother spring'. Previous studies have helped to arrive at a reliable interpretation of the Pagosa geothermal system. This report has extended these interpretations to the Chromo anticline, approximately 30 miles south. The Chromo anticline is a subsection of the Archuleta anticlinorium, which has faults swarms which facilitate fluid flow on a regional scale. In an attempt to further characterize subsurface structure, areas of fluid presence, and potential gradients for fluid flow the surveys implemented seismic, gravity, electromagnetic, and electrical methods. Through the integration of these techniques we have constructed a framework for a conceptual model of regional geothermal systems.

SECTION 2

Introduction

1. Field Camp Background

The Department of Geophysics at the Colorado School of Mines has a successful summer field camp program in place. Each May, third year students along with several Teaching Assistants and a portion of the faculty travel to a previously scouted survey location. Over a period of two weeks, the students and faculty design and carry out practical surveys using several methods that students are introduced to in undergraduate coursework. From an educational perspective, field camp provides an opportunity for most students to conduct their first real geophysical investigations. The field camp survey scale is much larger than the demos performed on the CSM campus which challenges students to overcome logistical obstacles. Companies with connections to the department donate the time of their personnel and equipment to improve the learning experience and quality of data acquisition. Once the surveys have been executed, students and instructors return to Golden where the processing phase of field camp begins. During processing, students reduce collected field measurements into data products which are used to interpret local geology. The final product of the field camp and processing section is this document; a summary of the geophysical methods used with discussion and conclusions about the implications our surveys have on the understanding of the geology in the target area. It represents the combined knowledge and experience of participating students and intends to serve as a resource for community members in the survey area. The end result is a four week educational experience that prepares the participants to design geophysical surveys in their upcoming careers.

2. Brief History of Pagosa Springs

The town of Pagosa Springs in southwest Colorado is named after the local hot spring destination at the town's center. The native Utes named it "Pah-gosa" which means "boiling waters", or "healing waters," in recent literature [**1**]. Pagosa Springs sits near the base the large, volcanic San Juan mountain range. The hot spring at the center of town holds the Guinness World Record for the deepest geothermal spring which was measured in August of 2011 with a 1,002 foot plumbline [**1**]. The actual depth of the hot spring, as well as the location of the heat source, is still a mystery, provoking curiosity among geologists and geophysicists alike. During the gold rush of the late 19th century, the Pagosa area served as a military outpost. With the establishment of Fort Lewis on the banks of the San Juan river, roads were built as more settlers moved into the area. The town of Pagosa Springs was quickly settled after word spread about the medicinal qualities of the mineral rich springs. Although the exact origins of the geothermal activity have yet to be discovered, the tourism related to the hot springs continues to thrive. People travel from all over the world to experience the therapeutic waters of Pagosa Springs. Large interest in geothermal electricity has forged the need for further investigation in the area for the use of local renewable energy.

3. Results of Past Field Camps

Previous field camps have investigated the structural controls for geothermal activity in the Pagosa Springs area. The 2012 Field Camp conducted surveys within the municipality itself. They determined that the large Eightmile Mesa Fault propagates into basement material and is a potential conduit for the transportation of geothermally heated water. Geochemical analysis was also used to determine the meteoric origin of the hot springs water and that a significant portion of this water reaches the springs through the highly fractured Dakota sandstone. This field camp group also discovered a previously unknown fault which they named the Victoire Fault [**2**]. The 2013 Field Camp succeeded in characterizing the Eightmile Mesa Fault in greater detail. Their surveys revealed numerous other faults, several of which were previously undiscovered. Their results also agreed with the previous year's interpretation: that the Dakota Formation is the primary source and recharge zone for hot spring water [**3**]. The 2014 Field Camp located a large thrust fault in Chromo which cuts through the Dakota and isolates the fluid movement within the formation [**4**]. These previous surveys have been combined to characterize the large scale tectonic structures in the area and frame the investigation area of the 2015 Field Camp.

4. Brief Summary of Field Work Timeline

Field work for the 2015 Field Camp began on Monday, May 11th in Pagosa Springs. The first two days consisted of touring the area and learning about the geologic setting of Pagosa Springs and Chromo. This consisted of outcrop observation and the drafting of a local geologic cross section. The next eight days were spent gathering data with different geophysical methods along a main line in Chromo and at an isolated reconnaissance site in the San Juan National Forest. Preparation for the main line survey began on Wednesday, May 13th, and consisted of placing flags along County Road 391 for 11 kilometers and starting GPS point acquisition at each flag. By Thursday, the main line MT survey was initialized and several more GPS points were collected. Groups were also sent to begin EM surveys in the San Juan National Forest reconnaissance site. On Friday, the DC resistivity, TEM, and Gravity surveys along the main line were initialized as well. Due to inclement weather, no data was acquired on Saturday, May 16th. Seismic data acquisition of the entire line took place from May 17th to May 20th. This was also the time frame for completing DC, gravity, GPS, TEM, MT, and hammer seismic surveys. Thursday, May 21st consisted of cleaning up the main line and loading equipment for the trip back to Golden.

5. Objectives

The 2015 Field Camp survey attempts to further characterize the structural controls of geothermal activity in Archuleta County. The main line of the survey overlaps with that of the 2014 Field Camp, allowing for an expanded analysis of the Chromo anticline. This survey also includes characterization of fluid presence and flow at the previously targeted Stinking Springs. The presence of geothermal activity in Chromo hints at a possible geothermal conduit that connects to Pagosa Springs. Developing an understanding of the hot spring source could influence key decisions in the local economy of Pagosa Springs. If geothermal energy were to be exploited in this area without a thorough understanding of the source and conduits, the mother spring that serves as an integral component of the local economy could be negatively affected. The 2015 survey also includes a reconnaissance site situated between Chromo and Pagosa in the San Juan National Forest. Electrical surveys in this area cover an intersection between an exhumed dike and normal fault with the intention of identifying which structure acts as a better conduit for fluid flow. The surveys completed at the two locales, combined with the results and interpretation of the previous Pagosa field camps, will allow for development of a new model of the geothermal activity in Archuleta County. With the intention of providing a schematic of the hot spring system in Pagosa and guiding future surveys in the area, the logic behind the final model is supported in detail from the interpretation of a large scale geophysical investigation.

SECTION 3

Geologic Background

1. History

Covering the vast majority of Earth's history, the Pre-Cambrian era was the first geologic age. Remnants of this era can be seen as the peaks of many Colorado mountains. Sediments around the San Juan Basin have all been deposited on crystalline Pre-Cambrian terrane, which is made up of mostly granitic rocks, along with schist, gneiss, quartzite, phyllite, and greenstone [**5**]. Sedimentary rocks in Colorado were originally deposited in a marine environment during the Paleozoic era. The area experienced many fluctuations in ocean at this time with a consistent trend of deeper waters in the west. These fluctuations created a beach-like environment of deposition. An immature San Juan basin formed during this calm period [**6**].

An enormous uplift episode affected Colorado following this large-scale sedimentation, with the resulting terrain now known as the Ancestral Rockies. This Pennsylvanian and Permian aged event caused large mountains to form, the debris of which created sandstone layers around Colorado while shale formed in the oceans that existed between the uplifts [**7**]. These events are characterized by spasmodic deformations, and predated a vast Jurassic "healing". Regarding tectonic activity, this was a very widespread depositional period where mountains eroded and basins were filled. Although there was a geographically low relief, hundreds of meters of sediments accumulated, often containing fossils. Then the Sevier Orogeny, an early Cretaceous uplift in the west, was created by a fold-thrust belt that caused large-scale compression across North America and rapid seafloor spreading in the oceans. This lead to global sea level rise and the formation of The Cretaceous Interior Seaway. Many identifiable sandstone layers across Colorado originate from this seaway. Due to the movement of water and changing sea levels, many layers that were formed at this time are diachronous, tending to be younger to the east.

The event which disrupted the seaway is known as the Laramide Orogeny. This orogeny began during the late Cretaceous period 75 million years ago, and lasted roughly 40 million years [**8**]. This massive uplift filled the Colorado basins with sediments shed from surrounding mountains. During the Eocene, the Archuleta Anticlinorium formed, lying between the San Juan basin and the San Juan Sag. A sag basin is one that forms within continental masses as a result of isostatic equilibrium following termination of rifting [**9**]. The formation of the anticlinorium was likely due to a combination of two factors; loading and subsidence of sediments in the adjacent San Juan Basin, and a change in regional stresses associated with the end of the Laramide Orogeny [**10**]. This orogeny ended during the Eocene epoch, a phase of healing with little geologic activity. During this stasis, the interior of the Archuleta Anticline eroded, exposing older layers. After the Eocene ended, another period of regional uplift and rifting ensued as a result of large scale subsurface volcanic activity. The San Juan Mountains formed at this time by Oligocene and Miocene aged volcanism, along with many intrusive dikes. During this large scale uplift, the Archuleta Anticlinorium was exposed to small scale fracturing and folding events. The Chromo anticline is housed by this anticlinorium northeast of the San Juan Basin. This is a plunging anticline, with the fold axis dipping gently north by northeast. The Chromo anticline is comprised of multiple layers, from the Pre-Cambrian basement to the Upper Cretaceous Lewis shale. Over the ages, the center of the Chromo anticline experienced severe erosion, creating a breached anticline. The middle was subsequently filled with volcanic alluvium, gravels, and landslide debris. The Chromo anticline is the central focus of the 2015 Field Camp investigation.

2. Surface Geology

2.0.1. *Field Observations.* In order to become more familiar with the area, a day was devoted to local geology prior to geophysical data acquisition. Multiple outcrops were seen within and outside of the breached anticline. Important geologic features and units were identified, allowing us to create preliminary cross sections of the area. This cross section was later changed as more information about the subsurface was collected using previously gathered well logs and data acquired from geophysical surveys. The stops made on this trip can be seen in Figure 1 below.

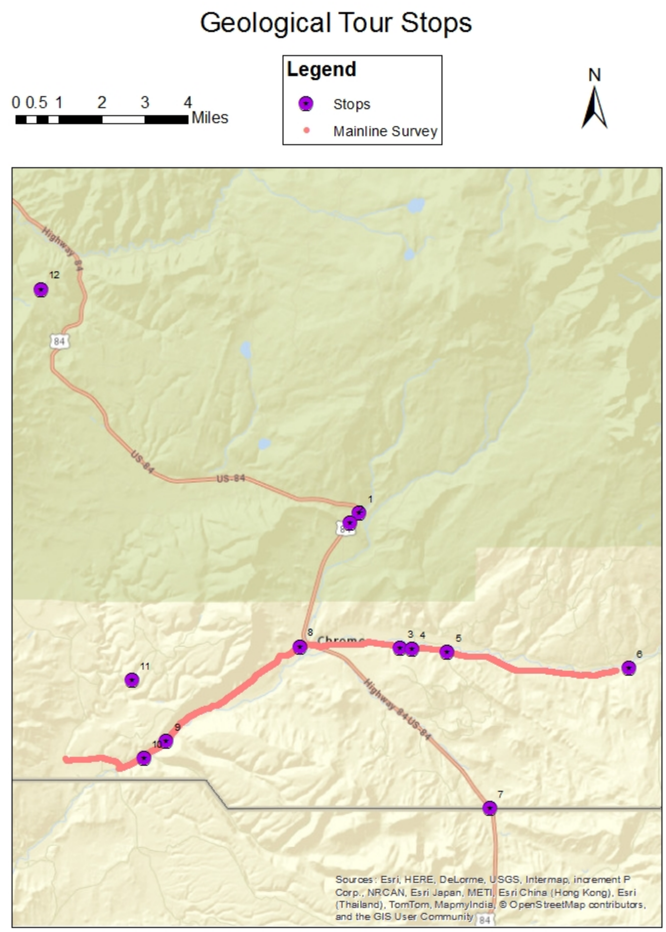

Figure 1. Map showing where the stops were along our geologic field trip centered around Chromo, CO.

Stop 1: Limestone outcrop within the Lewis shale located on the north end of the northwesterly plunging anticline. Many concretions are present in the limestone.

Stop 2: Mesaverde sandstone outcrop along the edge of the breached anticline. It was easy to see that the once shore-facing Mesaverde was steeply dipping at this location.

Stop 3: Fire station. This was our main meeting point in Chromo. From this point it was easy to see Quaternary alluvium deposits and terrace gravels.

Stop 4: Stinking Springs. This small geothermal feature comes through the Mancos shale, insinuating that there are many hydrological and geothermal questions that can be asked regarding this area.

Stop 5: Mesaverde sandstone outcrop (edge of anticline). Heading east, we quickly transitioned from Mancos shale to Mesaverde, and then the Lewis shale.

Stop 6: Oso Diversion Dam. This was the end of the geophysical surveying line from the 2014 field camp. 90

Stop 7: Colorado/New Mexico State line. This location was still inside the anticline, and therefore we were standing on Mancos shale. Greenhorn limestone was visible around us.

Stop 8: Within Mancos shale (middle of anticline). Excluding the line from last year and the overlap, this was the beginning of the main line. Faults were visible in the Mesaverde topped cliffs above.

Stop 9: Landslide. Erosion exposed Mancos shale and Mesaverde layers are seen in the hills. There were thin sandstone beds present that can be described as storm deposits created by a receding sea level.

Stop 10: Mesaverde sandstone outcrop, with faults present. Layers of Mancos, storm deposits, and Mesaverde could be seen with several faults cutting through them. The Mesaverde present at this location is much thicker than the outcrops on the east side of the anticline.

Stop 11: Mesaverde sandstone transitions into Lewis shale. This location was north of the fault we previously saw. There were larger rocks higher up, with more and more fractures present. The eroded shale left a shatter-zone wall along the fault. It can be assumed that there is no fluid flow along this fault because there is no discoloration or tufa. There were incised meanders present along the west side of the anticline, created when meanders from a geologic healing phase were uplifted.

Stop 12: Student reconnaissance site. Several methods performed surveys here in order to locate a fault and characterize a dike.

2.1. Geologic Map.

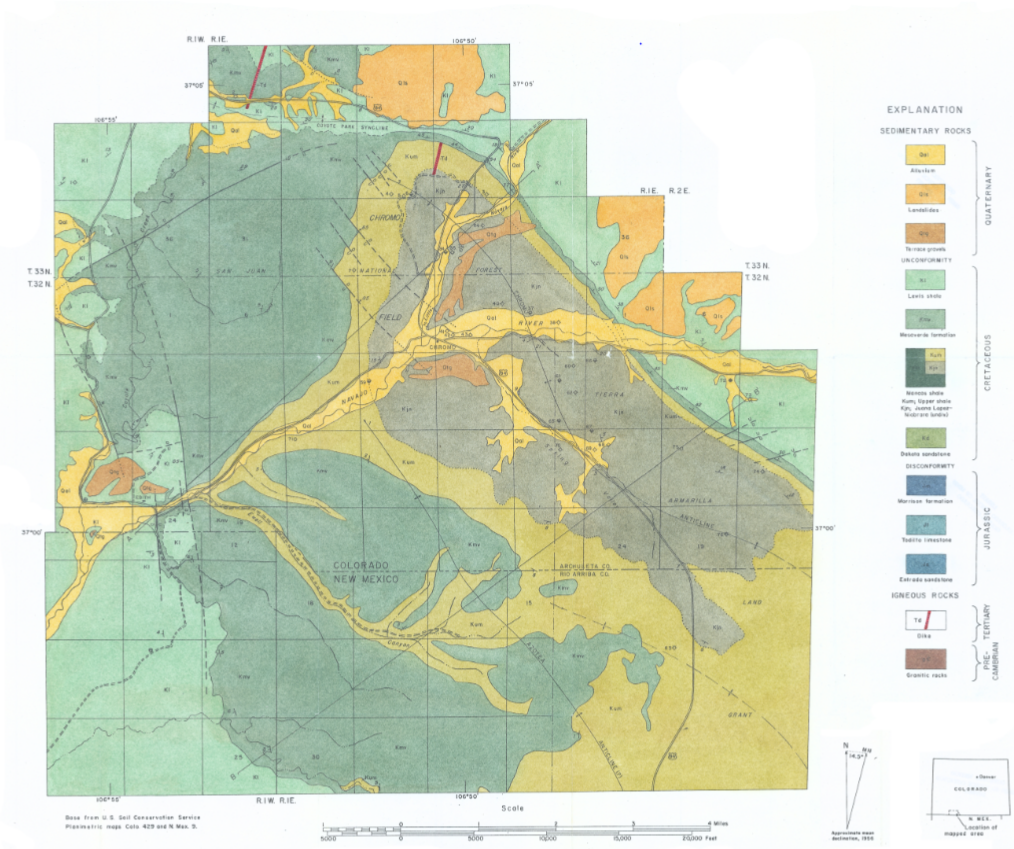

Figure 2. Map showing an interpretation of the surface geology based on outcrops near Chromo

3. Structural Geology

3.1. Basins/Anticlines/Dikes. Chromo nestled in between several mountain ranges and basins. Located in the very southwestern portion of the state, it is centered just North of the New Mexico border where a complicated system of folds and faults can be observed. A regional overview of structural features is necessary to understand these systems. The San Juan Basin lies to the southwest, and at nearly 12,000 km2 of area, the basin covers much of the four corners region and consists of mostly sedimentary rocks from the Mesozoic era. To the northeast, the San Juan Mountains dominate the skyline. These mountains are volcanic in origin and date to the Tertiary period (Oligocene). These mountains overlie the San Juan Sag, another sedimentary basin. Sediments in this basin correlate to deposition from the Cretaceous interior seaway, and later from the Laramide Orogeny. Chromo itself lies in the Archuleta anticlinorium, a 120 km long system of folds and faults that trend towards the northwest [**11**]. The uplift associated with the Laramide Orogeny was uneven, deforming the existing rocks and resulting in uneven rates of sedimentation. The creation of the anticlinorium was associated with these processes, although the northwestly orientation may be due to pre-existing faults in the Precambrian basement [**10**]. Uplift also caused extensional stress in the anticlinorium. This can be observed in several normal faults of near vertical incidence. Several volcanic dikes cut through the anticlinorium north of Chromo in the San Juan National Forest. They tend to run northeast-southwest and extend for several miles in each direction. These dikes are likely from the Miocene era, and are likely unrelated to the Laramide orogeny (which would have ended before the

Oligocene) [**12**]. A generalized regional map of structural features can be seen in Figure 3. The cross section labelled in this figure can be seen below as well, in Figure 4 [**11**].

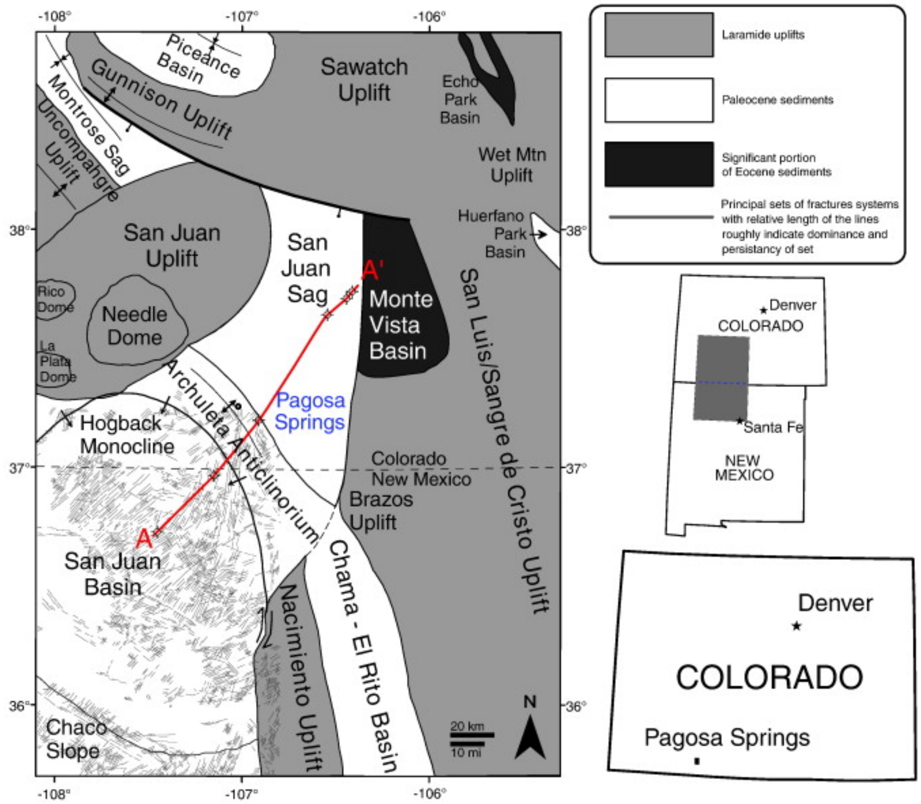

Figure 3. Aerial view of the geology surrouding the San Juan volcanic range

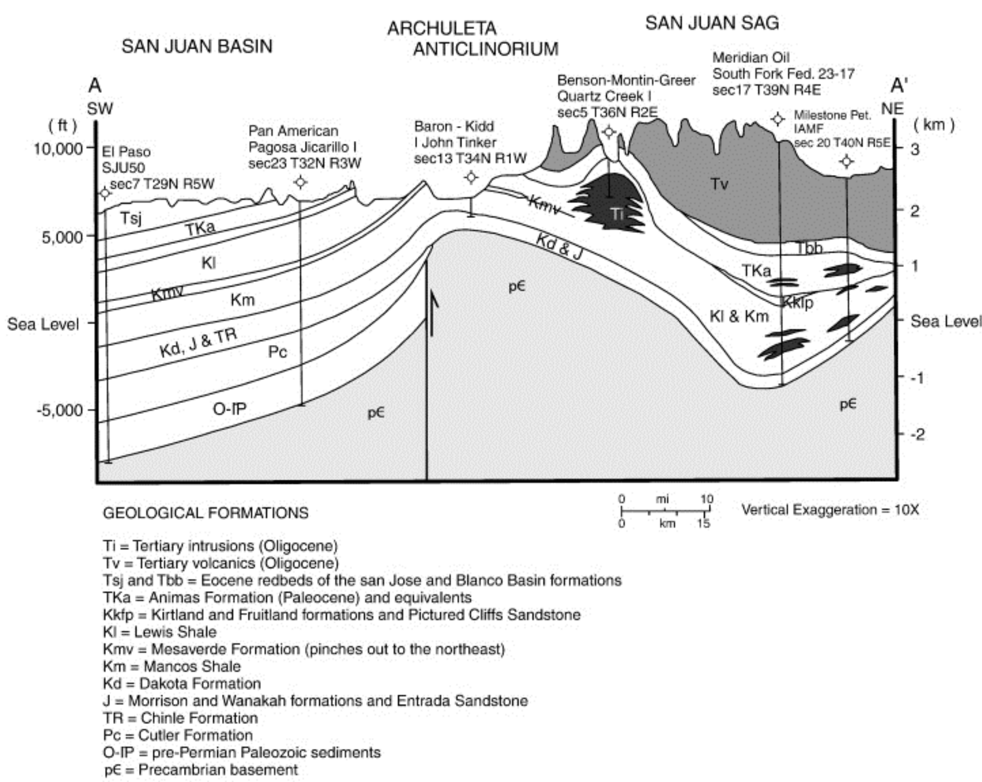

Figure 4. Map showing an interpretation of the surface structural geology based on outcrops near Chromo, along with a cross section of the area.

Our main survey line ran through Chromo. While regional structural features are important to understand, local features dominated the main survey line. Within the Archuleta Anticlinorium lies the Chromo anticline. This also trends northwest and has an asymmetrical shape. The northeast flank of the anticline maintains a roughly forty degree slope, while the southwest side has a much shallower dip of around five degrees. The extent of our current knowledge suggests that the rock formations have a relatively constant thickness throughout the anticline. As a result, we can conclude that the formation of the Chromo anticline was due to flexure folding [**13**]. The Mancos shale comprises much of the center of the anticline. Since shale erodes relatively fast and generally has poor surficial outcrops, it is hard to map the crest of the anticline. A geologic map of the Chromo anticline can be seen in Figure 4, with descriptions for the notations given in the chart below. As seen in the geologic map, there are several faults of interest along our survey line. Geophysical investigations conducted along the main line will be able to determine if there are more faults present in the area, along with their extent.

4. Statigraphy

This simple overview of the sedimentary layers local to the Chromo and Pagosa Springs area is meant to help readers understand the general processes and properties associated with historic deposition in the region. The oldest observed stratum in the chromo anticline is the upper Jurassic Entrada sandstone. This stratum lies on Precambrian basement rock, indicating a major nonconformity between Precambrian and Jurassic periods in the region [**14**]. The Entrada sandstone is composed of fine to medium grained quartz, commonly arranged in cross beds. This is a strong indicator of its eolian depositional environment. It was deposited in the upper Jurassic and is approximately 200-360 feet thick in this region [**15**]. The Entrada sandstone is one of the oldest regional sediments, although there could be small infills of pre-Jurassic sediment in areas of less significant erosion (the 2014 field camp main line serves as an example).

Overlying the Entrada sandstone is the Todilto limestone member of the Wanakah formation. This member is composed of a thin lacustrine basal limestone that was formed by the collection of organisms such as stromatolites and algae at the bottom of lakes. The Todilto limestone is commonly capped by a much thicker gypsum unit which is indicative of a marine depositional environment and oceanic transgression [**15**]. Limestone can also form in lakes where marine organisms are present. It is likely that this formation is not as thick as it is in northern New Mexico and eastern Utah, but is still approximately 100 feet thick in the region of the Chromo anticline. Moving up the local strata into younger Morrison sediments, it becomes clear that the Todilto limestone is a transitional formation; it splits the desert, eolian environment of the Entrada sandstone and the more humid, fluvial environment of the Morrison formation [**15**]. The continuous deposition of these three strata suggests significant changes in depositional environments and moisture to a more oceanic environment throughout Jurassic times in the San Juan basin.

As previously mentioned, the Morrison formation is a late Jurassic rock unit deposited in an alluvial plain environment. It consists of mudstone, sandstone, and claystone with almost 700 feet of sediment accumulation [**13**]. It overlies the Wanakah formation in the region of the Chromo anticline and contains the region's youngest Jurassic sediments. The Morrison formation is famous for its fossils, often indicating an anoxic environment of deposition.

The Dakota sandstone is above the Morrison formation and is separated by a 50 million year old disconformity [**16**]. The fluvial facies of the Morrison disappear and the well-known, recognizable Dakota sandstone emerges indicating a jump through geologic time to the beginning of the late Cretaceous. It is difficult to identify a specific disconformity between the Morrison formation and the Dakota sandstone because transitional zones exist in the upper Morrison formation [**17**]. In the region of the Chromo anticline, the Dakota sandstone is approximately 180 to 200 feet thick, and is composed of thick units of interbedded sandstone and shale [**13**]. It is possible to see outcrops of the Dakota sandstone further to the north and east of the Chromo anticline, as the San Juan basin transitions into the San Juan Mountains. This sandstone formation is indicative of the beginning transgression of the western interior seaway. The majority of Colorado was eventually submerged by this seaway as marine deposition of the Mancos shale began.

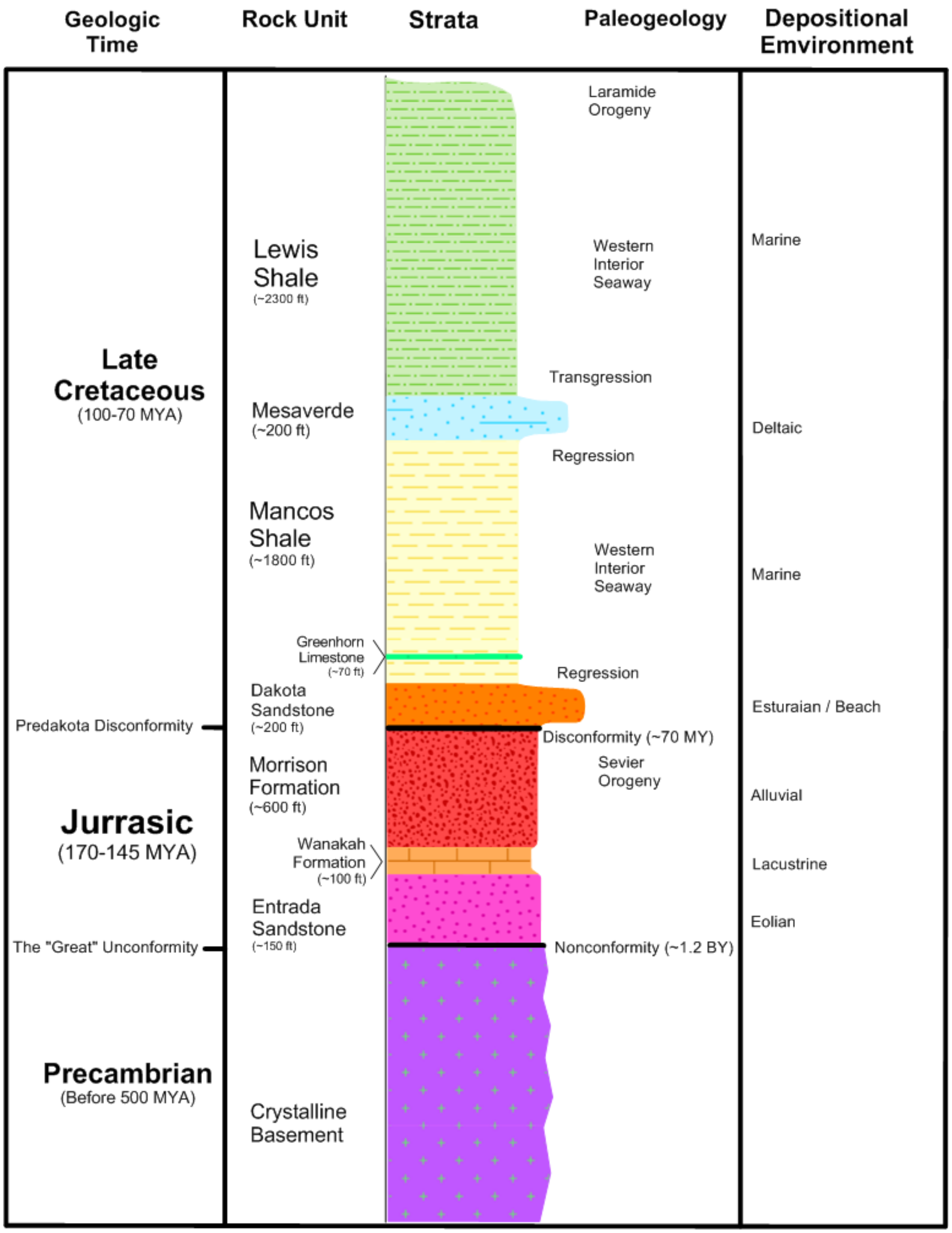

Figure 5. Stratigraphic section of the Chromo area. This shows the multiple layers within the Mancos shale. The nomenclature for these subunits is excessively varied among professionals.

As seen in Figure 5, the Mancos shale is a very large depositional layer. The Mancos shale is the oldest formation observed at the surface in the Chromo area. It consists of upper Cretaceous marine deposits, and it is approximately 1900 feet thick in the region of the Chromo anticline **[16]** **[13]**. Although this unit of rock is referred to as shale, it is interbedded with several sandstone and limestone units, including the niobrara sandstone and greenhorn limestone [18]. The Greenhorn limestone is important to the stratigraphy of the Mancos shale because it is a regional marker, roughly one meter thick in this area, and between 100 to 140 feet above the top of the Dakota sandstone **[19]**. The Carlile member and the Graneros member are shale layers within the Mancos, making up the top and bottom portions respectively.

The Mesaverde group succeeding the Mancos shale contains the resistive strata responsible for the mesas and hogbacks seen at the crest of the Chromo anticline. This unit of rock is up to 250 feet thick in the Chromo region, and is often much thinner at the surface [**13**]. It is composed of sandstone units deposited in a coastal plain environment during a regressive phase of the western interior seaway. This caused the layer to form unevenly, thinning out toward the east where there was less water present. The group's termination is coincident with a second significant transgression of the western interior seaway in the late Cretaceous [**19**]. This transgression is important because it correlates to the transition from the Mesaverde group into the Lewis shale. In places where the western interior seaway did not recede into a coastal plain depositional environment, the Mesaverde group does not exist, and the Lewis shale and Mancos Shale form a continuous unit, collectively referred to as Mancos shale.

The Lewis shale is above the Mesaverde group, outcrops of which can be seen at the surface along the outer flanks of the Chromo anticline. It is a marine shale that was deposited in the western interior seaway, much like the Mancos shale. The Lewis shale is also interbedded with thin sandstone and limestone layers. The Lewis shale is 2200 feet thick in most areas, however it is much thinner on the flanks of the Chromo anticline because it has been drastically eroded since the Cretaceous period [**13**]. Accumulation of the Lewis shale in the Chromo area is the thickest of anywhere in the San Juan basin. The previously listed layers are all present in the San Juan basin, and an image showing the behavior of these layers can be seen in Figure 6.

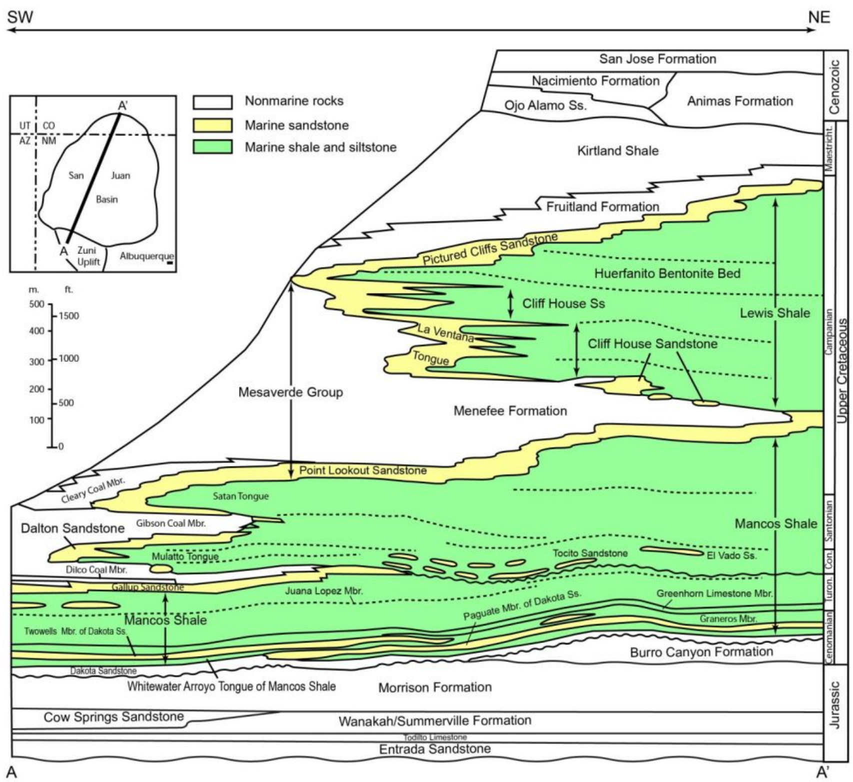

Figure 6. Image showing the relative thicknesses of each present layer across the San Juan basin. The cross sectional area goes across the basin, as seen in the top left on the section.

In the Chromo and Pagosa Springs region, there are multiple areas where igneous dikes are present. These intrusive bodies rose up during the Tertiary period, cutting through the existing upper Cretaceous layers [**13**]. One of the two main geologic features at the recon site is one of these Tertiary dikes which ruptured through the Lewis shale and transitions of Mesaverde, and can easily be seen at the surface. The other feature is a fault offsetting the dike.

Above all the previously listed layers in Chromo lay terrace gravels, volcanic alluvium, and landslide debris. The terrace gravels are typically 100 to 200 feet thick above where current river beds are. These gravels stand out because, while erosion occurred to the surrounding land, riverbeds containing larger rocks were more resistant to erosion. There is around 10 feet of volcanic gravel covering each of these terraces. Volcanic gravel flowed to Chromo's rivers from the San Juan Mountains, which are now a system of extinct volcanoes. The volcanic alluvium is found around rivers in the area and anticline, and consists largely of igneous fragments. Igneous rock fragments also make up a majority of the landslide debris in the area [4].

Further west toward the San Juan basin past the Archuleta anticlinorium, outcrops of many other layers can be seen; the Pictured Cliffs sandstones, Fruitland formation (coal-bearing), Kirtland formation, Ojo-Alamo formation, and Tertiary sediments. The Cretaceous-aged sediments are eventually overlain by the Sub Ojo-Alamo unconformity. The stratigraphic record in the San Juan Basin is well documented, but there are many interpretations of the local strata.

5. Preliminary Constructions

5.1. Preliminary Cross Section. From our research and field observations, we were able to make a preliminary cross section of the Chromo anticline along our main seismic line and the 2014 Field Camp main seismic line 7. This cross section includes all major faults, major geologic layers, and fold structure.

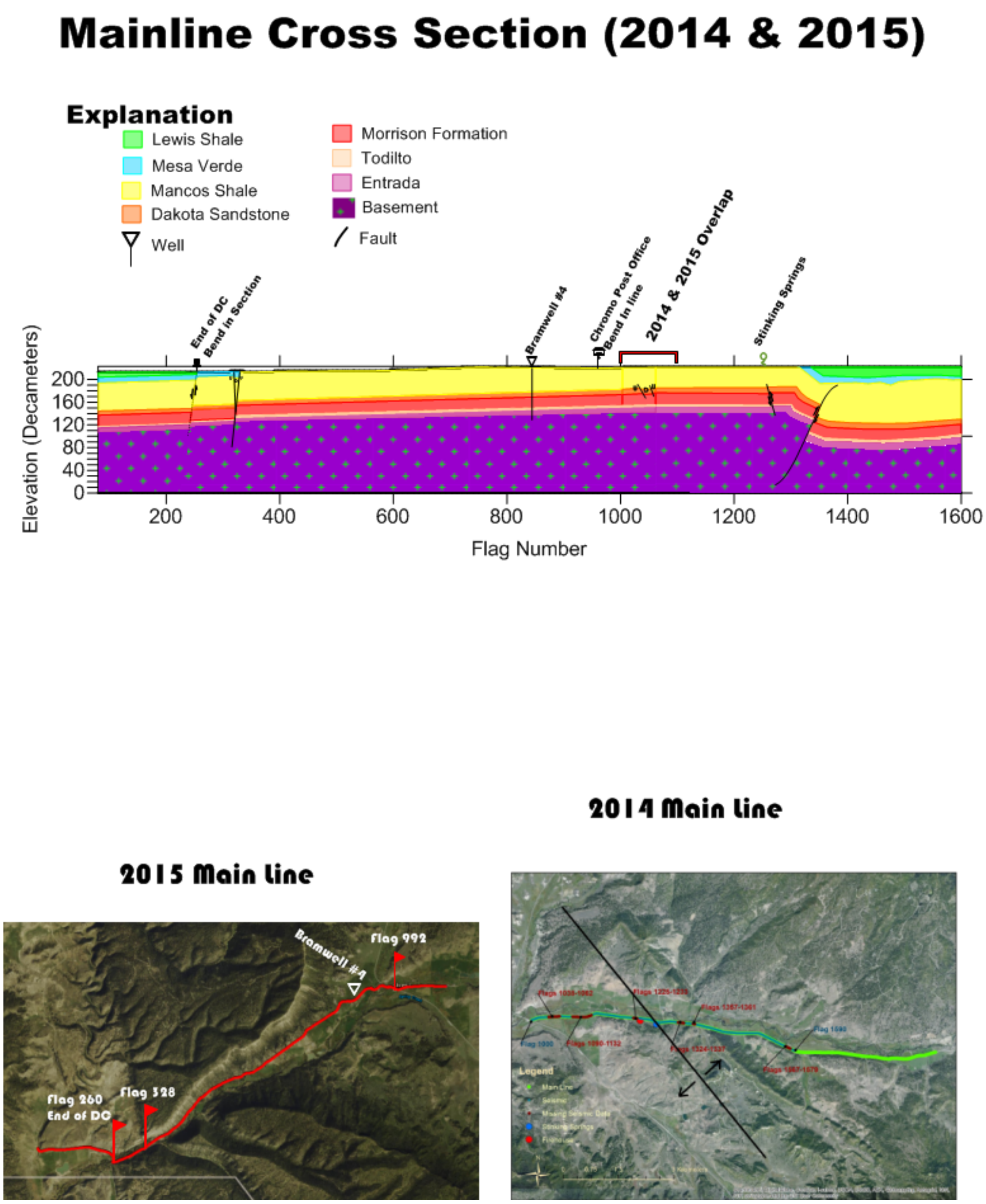

Figure 7. The preliminary cross section along the main seismic line. This cross section shows the known geologic layers and a plausible geologic structure. It was built to give a preliminary understanding of the subsurface to guide geophysical investigations.

In order to build an accurate cross section, we started with observed surface features.The major surface features include the Mesaverde outcrop observed at stop 5 and the faulted Mesaverde outcrop observed at stop 11. These gave us known strikes and dips of the Mesaverde, as well as a location on our main line. Stratigraphic columns in the area gave us information on what layers are in the subsurface, as well as thickness and depth information. We assumed that the thickness of the layers stayed relatively consistent, and that the structure of the fold stayed consistent with depth. This implies that there are no unexpected and dramatic changes in the stratigraphy. In addition to stratigraphic information of the area, we found a well in the area that had depth information for each of the major layers. This well is known as "Bramwell #4" and is marked on the cross section.

In addition to researching the geology, the 2014 seismic data was reinterpreted. This reinterpretation can be seen from flag 100 to flag 1600 on the cross section 7. The largest change to the 2014 interpretation is the expression of the large fault. The new interpretation of the fault is more simple and more consistent with regards to local geology. The cross section also includes a fault on the west end of the line around flag 260. We saw no surface expression of this fault along the main line, but research and satellite photos of the area suggest that it is there.

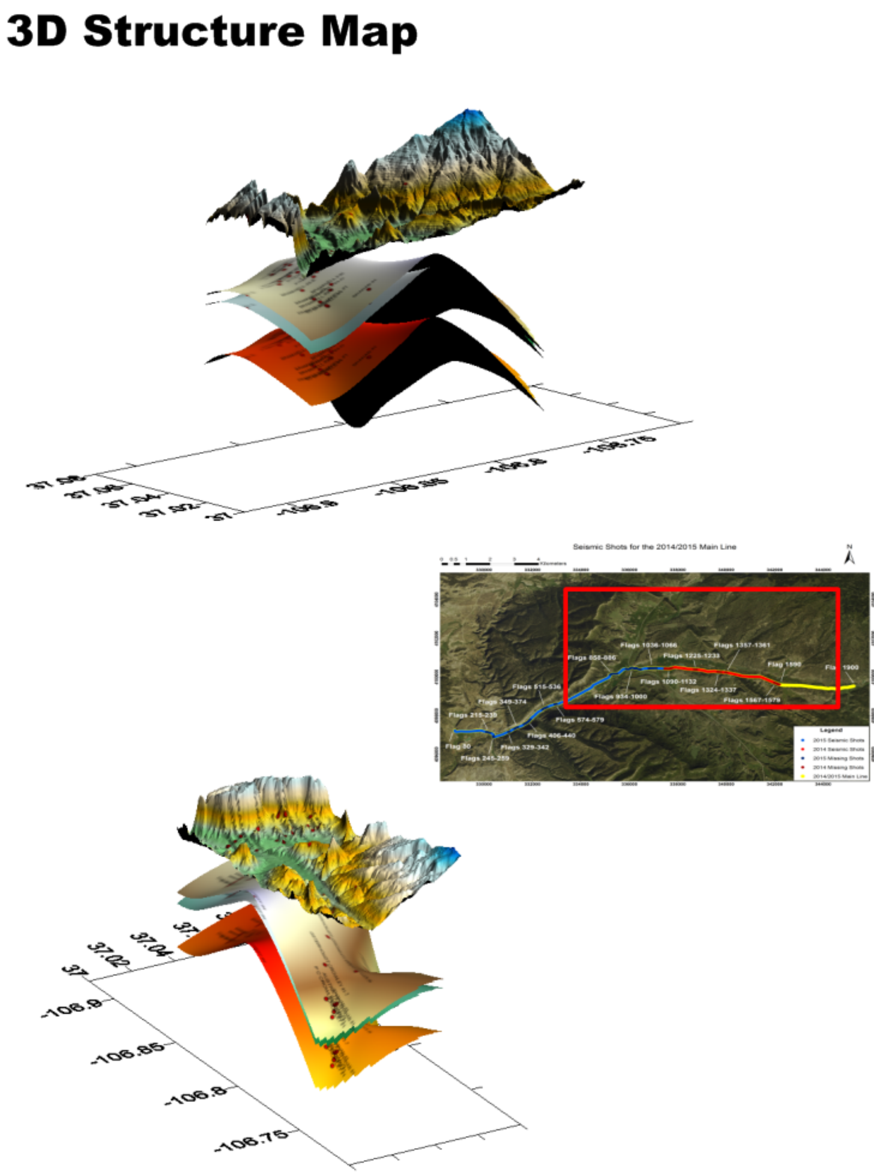

Figure 8. The 3D structural map of the Chromo anticline. This was constructed from dozens of wells in the area and shows the overall structure of the fault and the topography of the area. The model covers the area shown by the red box on the satellite photo of the main seismic line.

5.2. Introduction to the Model. In order to get a better understanding of the large scale geology of the Chromo anticline, a 3D structural model of the area was constructed using well log data gathered from the

Colorado Oil and Gas Conservation Commission well log database and our previously determined cross section. While this model is not perfect, it does provide a better understanding of the overall fold structure and how it changes in 3D.

The local faults are not included in this model as a consequence of them not being included in well log data. This doesn't affect the overall structure of the fold because the offset of the fault is relatively small compared to the scale of the model, but is noted nonetheless for other geophysical processing.

Another source of error is that the outer extremes of the model are not an accurate representation of the geologic structure. This is a result of little well data along the boundaries, the polynomials that were used to construct the contours between wells are continued to the edge of the model. This causes large high and low areas to occur, most notably in the north-central section where there is a large depression. This depression and other similar features along the extremes do not resemble the actual geologic structure.

6. Data Overview

The well data used for the model came from the Colorado Oil and Gas Conservation Commission. All the data sets have the same format that includes the latitude and longitude of the well, depths to tops of layers, well elevation. In order to make the 3D model, the elevation of the top of each layer was identified. This was accomplished by subtracting the depth to layer at a specific well from the elevation of that well.

7. Construction

Once the elevations of each layer were identified, the program "Surfer" was used to create a data file for each layer and associated elevations at the correct location. A grid file for each layer was created from this data with latitude longitude, and elevation as the X, Y, and Z axes respectively. A 3D layer was constructed from each grid file using the local polynomials method to link all the data points with a smooth, realistic contour.

In order to find which construction method would give the most realistic contour for each layer, a topographic model was created using the location and elevation of each well. Each of the construction methods in Surfer (Inverse Distance to a Power, Kriging, Minimum Curvature, Modified Shepard's Method, Natural Neighbor, Nearest Neighbor, Polynomial Regression, Radial Basis Function, Triangulation with Linear Interpolation, Moving Average, Data Metrics, and Local Polynomial) were then applied until a realistic topography was created. This process was consistent throughout all layers.

8. Problems and Corrections

The most prominent issue faced in model construction was the intersection between the Morrison Formation and Dakota sandstone. This intersection is not possible without a large and complex fault system, which is highly unlikely for this area. We concluded that this problem was coming from a lack of data regarding the layer contours. Not all of the wells have depths for every layer which causes each layer to have a unique profile. If the profiles differ enough, the layers intersect.

In order to fix this problem, "supplemental data" was added to the Morrison data file. The average thickness of the Morrison formation was then used to find the theoretical elevation where no data existed. This was done at points where there was an elevation for the Dakota but no elevation for the Morrison. Adding elevations for all layers at all wells is possible, but is avoided in order to minimize fictitious points in the model.

Another source of error is that the Mancos Shale is not consistently labeled in well log data. Some sources show labels for each sublayer in the Mancos while these sublayers are ignored in several others. This led to scattered depth and thickness data for the Mancos Shale and was corrected for by adding supplemental data as was done with the Morrison formation. The resulting model was determined not plausible as several intersections between the Mancos and other layers are shown. As a result, the Mancos Shale is not included in the model. The Mesaverde is also not included in the 3D model as it is above the surface for the majority of the main line.

The depth of the basement was also interpolated at several points using layer thicknesses and a depth recording in one of the well logs. This was included as an estimate as a consequence of minimal data.

8.1. Conclusions. The fold is expressed more significantly in the model than what was predicted in the preliminary cross section. The model also shows how the dip of the layers changes in 3D. This supports the preliminary assumption of little variation in layer thickness in the Chromo anticline and provides a broad understanding of the fold geometry.

9. Petrophysics

Petrophysical knowledge is necessary to further understand the rock units of the Chromo anticline. Since there was little petrophysical data available from Chromo, it has been assumed that petrophysical data regarding layers in Pagosa Springs is the same as for the layers in our area of interest. A majority of this information was gathered from previous geophysics field camps and well logs collected in Pagosa Springs. In these field camps, rock samples were taken in Pagosa Springs on which dry mass, porosity, and density tests were performed. These tests were completed at CSM as preliminary investigations. Gamma ray, resistivity, neutron porosity (NPHI) and density porosity logs were collected from several wells in the Pagosa area as well. The most reliable property that was gained by performing and comparing these tests performed at CSM and the well-log data were the porosity values derived from density. More thorough testing on the samples would have been necessary for highly accurate results. It was therefore assumed that the data gained from the well-logs was more reliable than the properties found by previous field camps. Unfortunately, the participants of the 2015 field camp did not collect any rock samples while in Chromo, so additional testing cannot be conducted. A chart showing several properties of the layers of interest can be seen below.

Layer	Density (g*cm^3)	Resistivity (ohm*m)	Density Contrast	Porosity (%)
Lewis	2.55	20	-0.25	3
Mesaverde	2.46	200	-0.34	8
Mancos	2.55	15-Oct	-0.25	3
Dakota	2.61	400	-0.19	9
Morrison	2.5	100 (top)	-0.3	4
		300 (bottom)		
Todilto			-2.8	
Entrada/Wanakah	2.565		-0.235	2
Basement	2.8	10000	0	0

10. Geothermal systems

Pagosa Springs has been extensively studied for its geothermal potential as numerous hot springs have been found in the surrounding area. The largest, Big Springs, has surface temperatures of 58° C and a flow rate of up to one cubic meter per minute [**20**] [**21**]. Wells drilled around Pagosa Springs show that the Dakota formation has the warmest water and resides between the Mancos Shale and Morrison Formation. Both of these layers have relatively low permeabilities that could act as boundaries for the water bearing Dakota Sandstone. Additionally, thermal profiles from wells indicate temperature spikes in the Dakota that decrease asymptotically at depth. Other wells drilled further away from Pagosa, however, have found no spike in temperature in the Dakota. This implies that the Dakota itself is not a geothermal reservoir but merely a local aquifer. Geochemical analysis of the water has shown that the water has a meteoric origin and likely flows through the precambrian basement [**20**] [**22**] [**23**]. No wells have been drilled down to the basement to test water temperature as the majority of the surrounding volcanic bodies are too old to provide a heat source. There is however a large batholith on the order 15000 square kilometers located under the San Juan mountains that could significantly alter the thermal gradient throughout southwestern Colorado. Gravity and transient electromagnetic surveys have shown that such a batholith is geologically plausible [**24**] [**25**]. The western portion of the batholith is twice as thick (20 km) could possibly explain the existence of the geothermal system in southwestern Colorado. Previous studies have shown that groundwater in the region tends to flow to the southeast [**26**].

Chromo is located approximately 25 miles south of Pagosa Springs, and it is assumed that the local geothermal system is disconnected from that in Pagosa. Research completed by Andre Revil suggests that Big Springs is fed by water upwelling through fractured rock near the intersections of faults [**11**]. Knowing that the geothermal water passes through basement rock at some point, a possible flow path could be the contact between the basement and Entrada. Any hot springs local to Chromo may be similar to the Pagosa Springs system such that hot water travels up from the basement to the to the surface via the Dakota sandstone and fracture systems. Another smaller laccolith may be located nearby which could provide a local heat source for stinking springs.

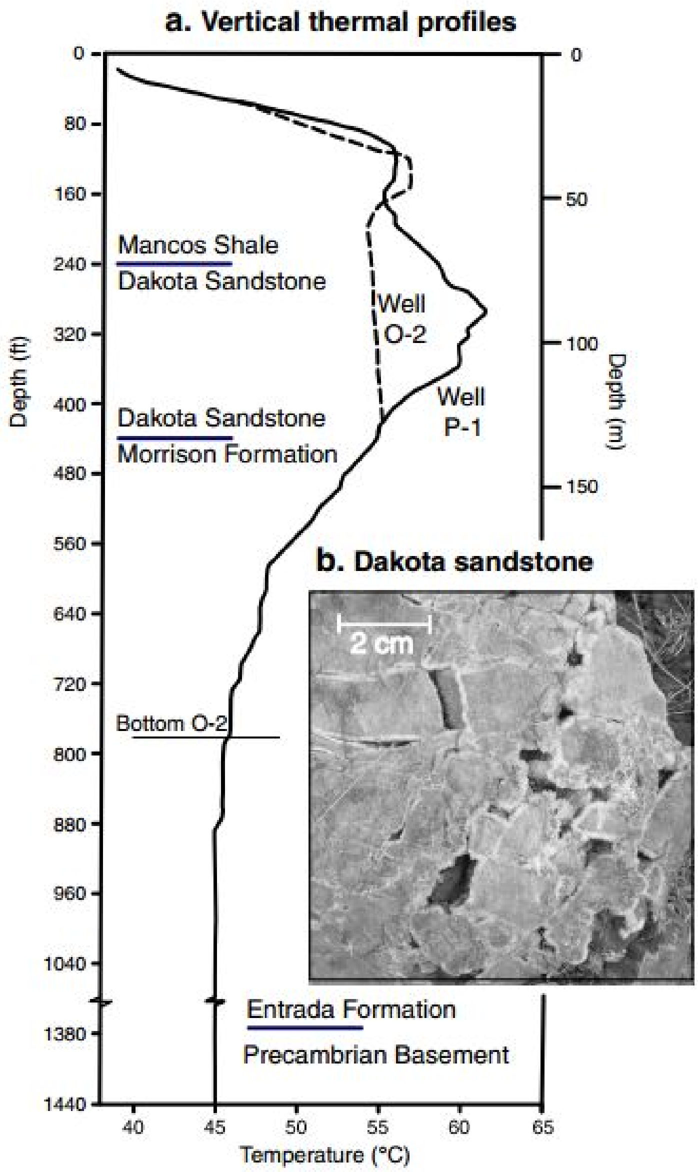

Figure 9. Thermal profile

SECTION 4

Geophysical Methods

1. GPS

1.1. GPS survey. GPS satellites transmit radio signals containing precise location and time information which are picked up by receivers on Earth's surface. The receivers calculate the travel time of each signal, after which the distance between the receiver and each satellite is calculated by multiplying the travel time by the speed of light. This distance is referred to as a pseudorange, since corrections for accuracy errors have not yet been made [**27**]. The position of the receiver is then determined by finding the intersection of the surfaces of spheres with radii equal to the pseudoranges with respect to the surface of the earth. This process is called trilateration.
DGPS was used to measure the location of every flag on the main line over which seismic, gravity, and DC resistivity surveys were conducted. The survey group was equipped with two rovers and a 'leap-frogging' technique was used. A clear line of site was required at all times between the base station and the rovers. The ideal location for the base station in the case of this survey was on a high, flat-topped cliff overlooking the flagged main line. The base station location was changed three times due to winding roads and hills interrupting line of sight (Figure 1). At location 1, the survey ran from flag 1100 to flag 640. At location 2, the survey ran from flag 640 to flag 340. Location 3, at the west end of the line, was used to cover the rest of the survey from flag 340 to flag 80.

Method	DGPS RTK	Handheld (Error: +/- 5m)	DEM Elevations
Deep Seismic (Mainline)	x		
Hammer Seismic (Mainline)	x		
Hammer Seismic (Recon)		x	
DC (Mainline)	x		
DC (Recon)		x	
SP (Mainline)		x	
Magnetics (Recon)		x	
Gravity (Mainline)	x	x	
EM-31, EM-34 (Recon)		x	
TEM (Mainline)		x	x
MT (Mainline)		x	x

Figure 1. DGPS base station locations.

1.1.1. *Motivation for Survey.* Differential GPS (dGPS) is an integral tool for methods supporting geophysical investigation (Figure 2). The consistent, highly accurate horizontal and vertical location measurements that dGPS acquires allow methods such as gravity and seismic to obtain useful results. The combination of a rover and a base station, which helps to eliminate error, provides millimeter accuracy. The resulting data can be used to produce high quality maps and other data products.
DGPS is the preferred form of geospatial data acquisition when a base station can be set up. DGPS was used on the main line where consistent, accurate data was required for data processing. The recon sites faced the

challenges of mobility, which made setting up a base station and rover combination cumbersome. As a result, the less accurate, handheld GPS receivers were used for recon site measurements.

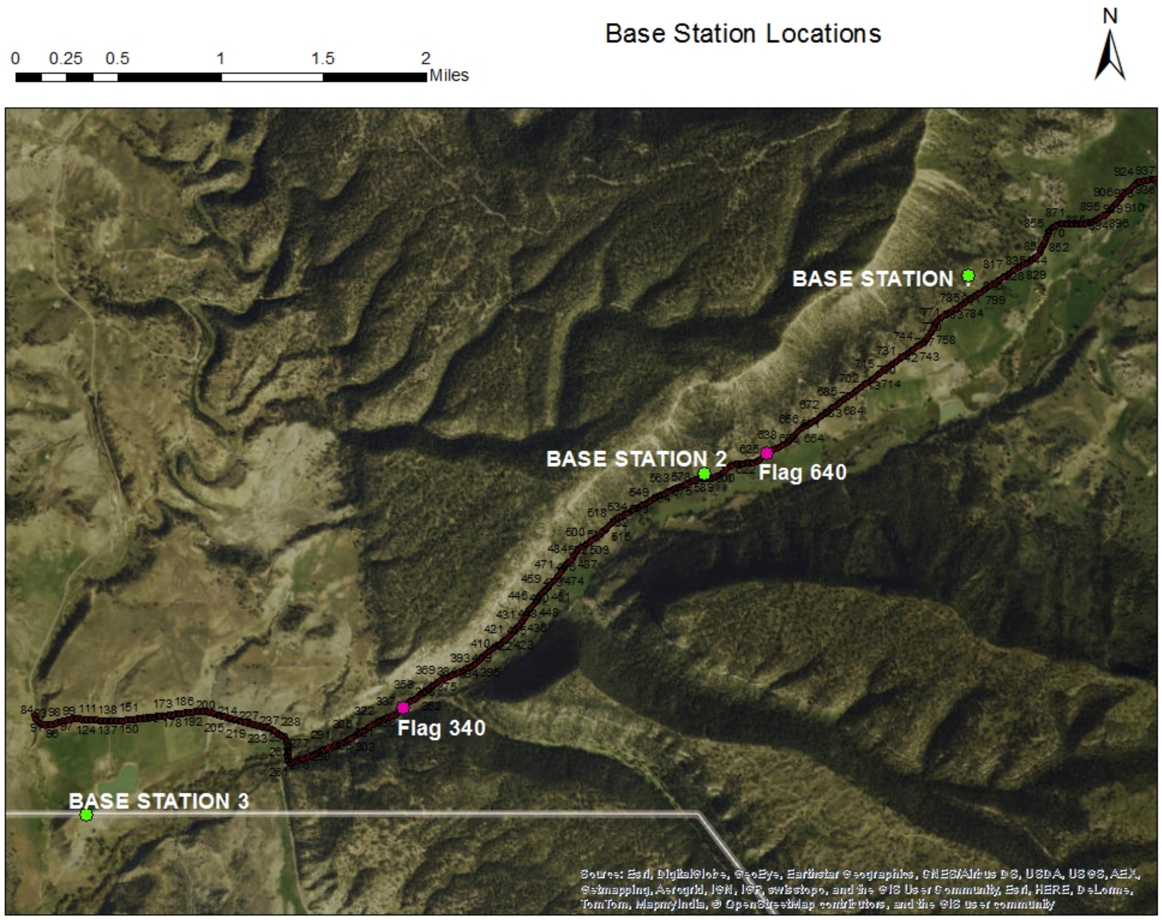

Figure 2. GPS/DEM types used for each method.

2. Gravity

2.1. Survey. The geophysical method of gravity can be used to measure changes in densities in the subsurface. Density is a physical property describing the amount of mass per unit volume of a given object, a measurement that is variable among different rock types. Changes in density between rock units lead to small changes in the Earth's gravitational field at the ground surface. Advanced devices can accurately measure these changes in gravitational pull, providing insight into geologic structure across a survey area. Prior geologic and petrophysical knowledge, along with advanced software packages, allow for detailed geologic models to be created based off of gravity data.

2.2. Motivation for Survey.

2.2.1. *Local Geology.* Before data was collected along the main line, we traveled around the Pagosa and Chromo area to get an idea of the local geology. One key geologic feature in the Pagosa area was the Archuleta anticlinorium. This feature is characterized by a high density basement rock that has been pushed up into lower density, overlying sediments. For more information about the Archuleta anticlinorium, see Geologic Background 3, which describes the observations from the geology field trip in greater detail. Because gravity accurately measures density contrasts, it is a useful method for imaging the contact between the dense basement rocks and overlying sedimentary packages. Being the largest local density contrast, the anticline feature dominates the gravity data in the survey area.

2.2.2. *Assisted Forward Modeling-Geology and Seismic.* While the largest density contrast near Chromo is between the basement and sedimentary units, smaller density contrasts also exist between each of the different overlaying sediment units, leading to higher order gravity responses that must be accounted for during modeling and interpretation. A major obstacle of modeling gravity data is that all solutions are non-unique, leading to an infinite number of possible models for a given set of data. By incorporating known surface geology, well logs, and petrophysical data, it is possible to invalidate models that seem to fit the gravity data. Other geophysical methods, seismic and DC resistivity in particular, can also be used to further constrain gravity models.

2.3. Survey Parameters. Our gravity survey was conducted along the entirety of the 2015 main line (flags 1100-80), including 1km of overlap with the 2014 gravity survey. Two separate Autograv CG-5 gravimeters were used to cut down the amount of time needed to carry out the survey. At the beginning of each survey session, both gravimeters took a base station reading, typically done at flag 1100. After the base station reading was taken, the gravimeters were leapfrogged every eight flags (80m) such that the total survey spacing was four flags (40m). For this survey, three 20 second readings were taken at each flag and data was not recorded if the standard deviation exceeded 0.1. After a section was completed, a final measurement was taken back at the base station to complete the loop.

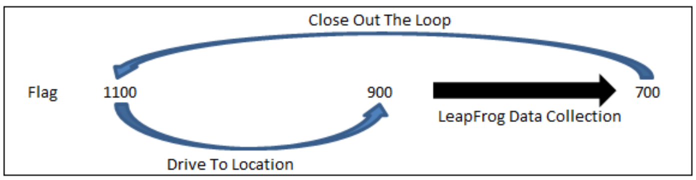

Figure 3. Example of a data collection loop

2.3.1. *Resolution vs. Practicality.* Gravity is a fairly low resolution method but is very useful in determining broad structural changes across an area. This imaging capability and time constraints lead to the decision of a 40 meter station spacing. Finer station spacing would have been redundant as the targets we were aiming to image were on the scale of kilometers. Three 20 second measurements were taken at each station to ensure precision and avoid gravitational noise from cars, pedestrians, wind, etc. These survey parameters proved to be practical as each measurement took approximately five minutes, allowing the survey to be completed in full within the time constraints.

2.4. Goals of Investigation. Gravity was carried out across the entire survey line to help understand the general geologic structure along the Chromo anticline. We felt that the first order information obtained through a gravity survey would help identify the depth of local basement rocks, data that is critical when developing a local geologic section. We also wanted to see if gravity could help constrain higher order anomalies such as faulting and fracture zones within the shallower sedimentary beds in the area.

3. Time Domain Electromagnetics

3.1. Survey. Transient electromagnetics (TEM) utilizes an oscillating electric current to induce electric and magnetic fields in the subsurface. Electric current is run through a transmitter and is rapidly turned off at specific times. The rapid shutoff of the current is followed by a decaying electric and magnetic field. TEM instrumentation measures this decay response in the form of voltages. Decay time and amplitude of the voltages are dependent vertical variations in conductivity in the survey area. From the decay response, it is possible to characterize the electrical conductivity and magnetic susceptibility of the subsurface. While TEM can be used to acquire information regarding both electrical conductivity and magnetic susceptibility, the electrical conductivity is most commonly sought after, as is the case in this investigation.

1D TEM soundings are used for mapping vertical conductivity changes in the subsurface. With multiple 1D soundings, it is possible to create a map of lateral conductivity change. For the purpose of characterizing the geothermal system, TEM is a useful method that allows us to map the electrical structure in the area. If there is groundwater within range of the TEM system, it might be possible to delineate the water from the surrounding rock units, assuming a considerable conductivity contrast. This information can lead to a well-supported stratigraphic section, which in turn can be used make a more informed general interpretation.

3.1.1. *Survey Parameters.* The TEM survey was conducted at four different sites around the Chromo area (Figure 4). Survey one consisted of seven transmitter loops on the northeast side of La Mesa del Media, and west of CR 391 (Figure 5). Nine more transmitter loops were deployed in survey two in the field to the west of La Mesa del Media, east of Archuleta Mesa, and south of Coyote Park Road (Figure 6). Survey three was completed using four additional loops located just north of site two on the other side of Coyote Park Road (Figure 7). Survey four consisted of five more transmitter-receiver loops within Kenney Flats, north of the other surveys, and south of the recon site.

TEM Survey Areas

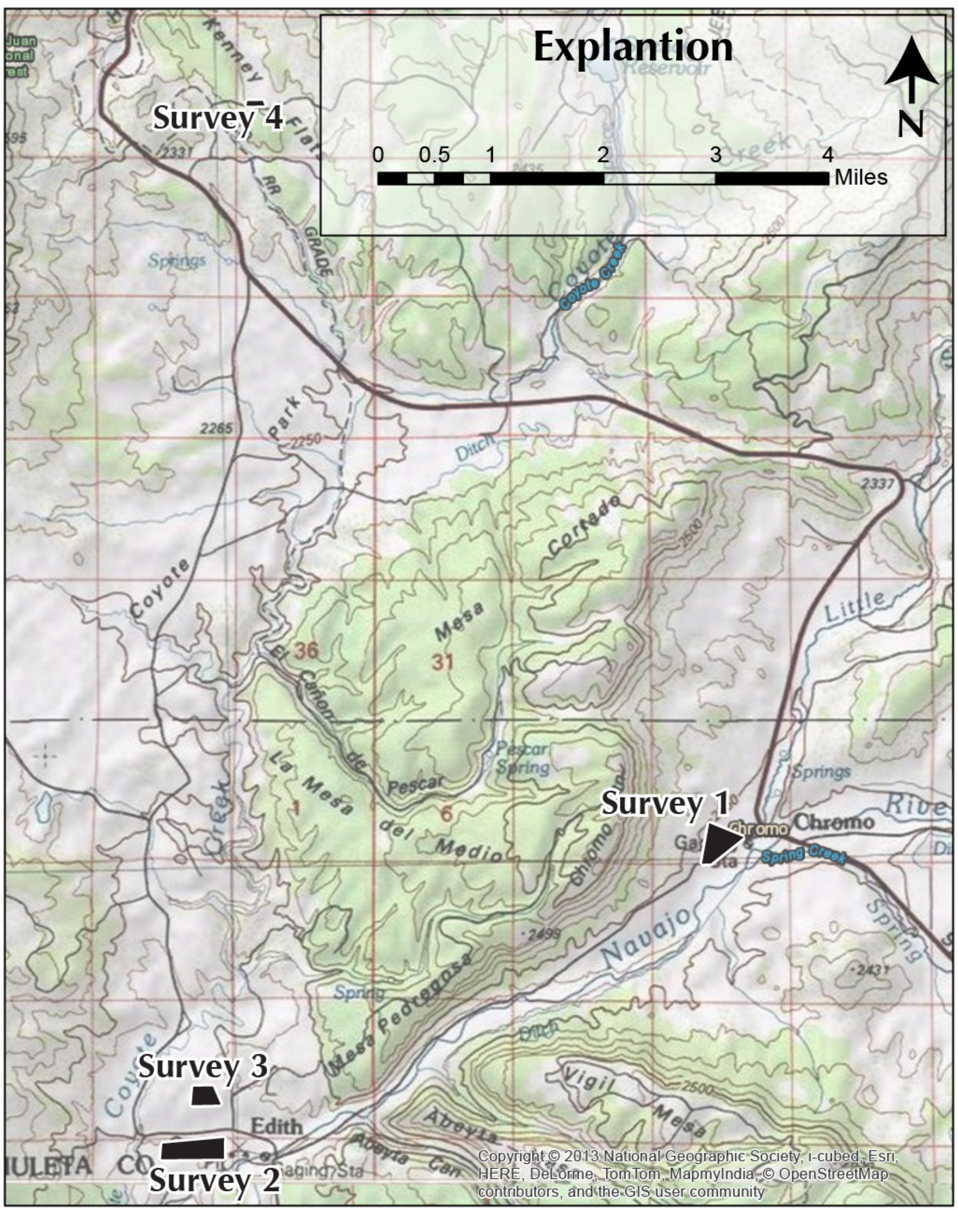

Figure 4. The TEM experiments survey the different geologic settings encountered during the field session.

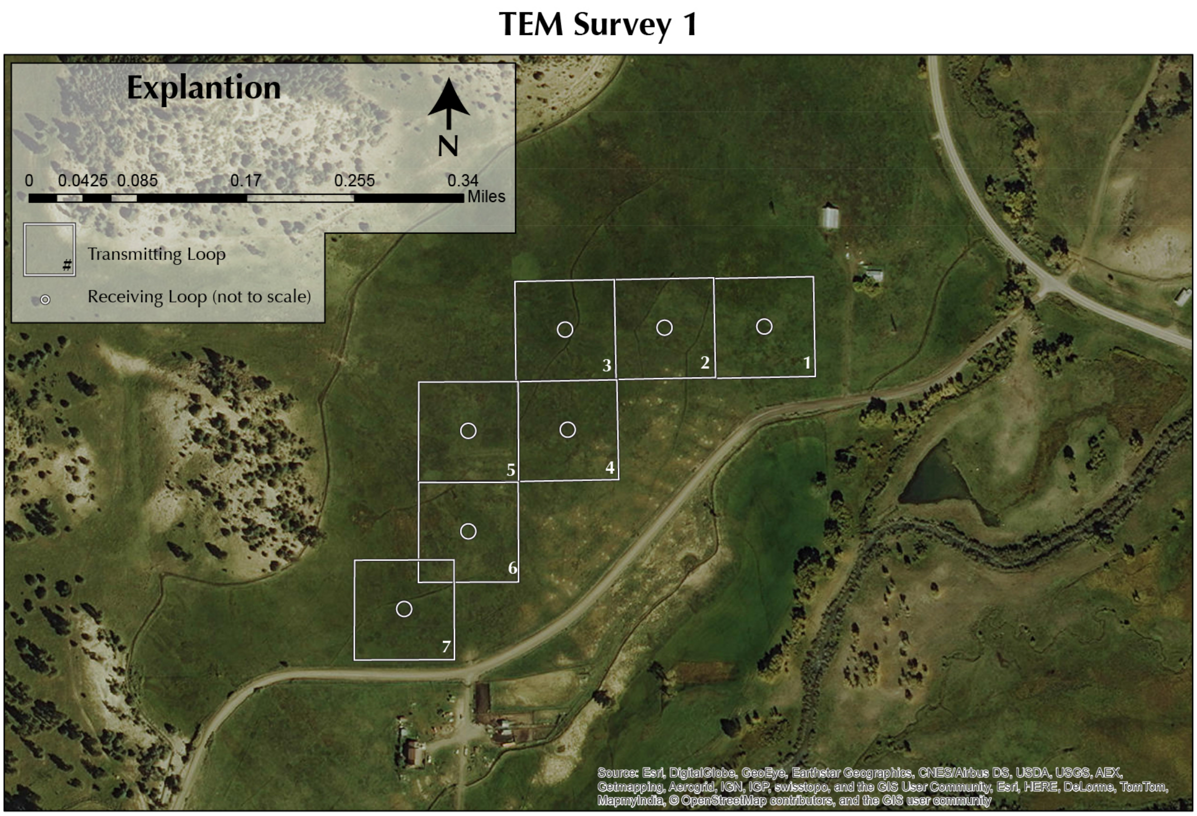

Figure 5. Survey 1 deployed 7 loop experiments towards the beginning of the main line.

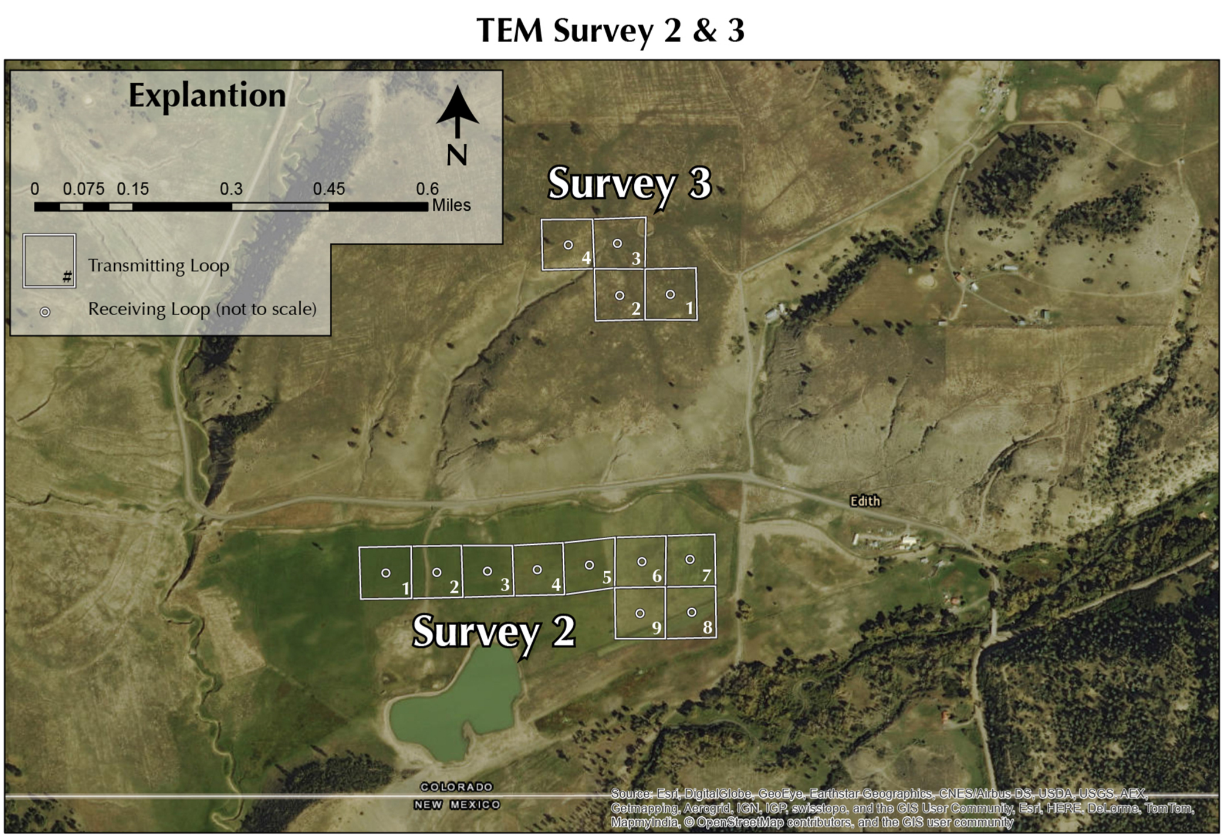

Figure 6. Survey 2 and 3 deployed 13 loop experiments towards the end of the main line.

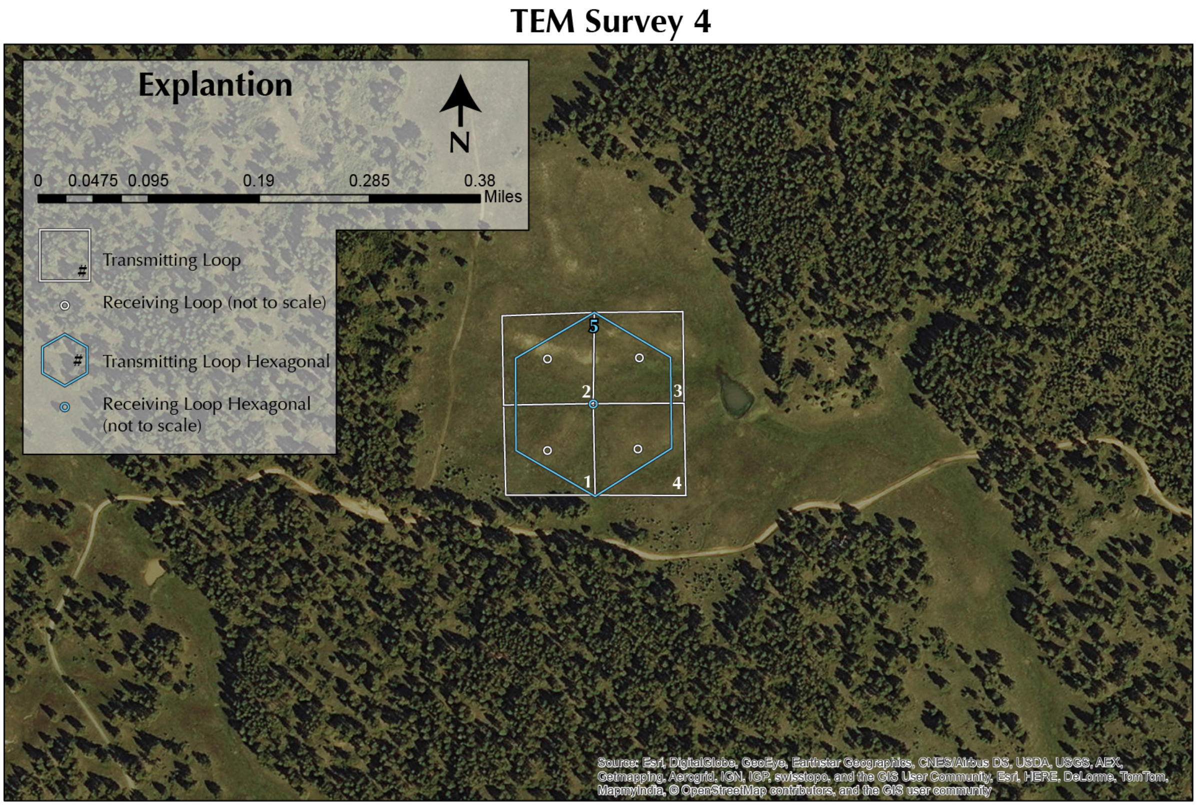

Figure 7. Survey 4 deployed 5 loop experiments near the reconnaissance site. The fifth loop was hexagonal.

.

In general, the survey parameters remained constant except for variations in transmitter current and turn off times (see Tables 1 and 3). The TEM survey used a 10000 m^2 transmitting loop and a 100 m^2 receiver loop. The receiver loop utilized 100 turns of cable within a 1 m loop, giving it an effective area of 100 m^2. There was also a deep sounding conducted at the 4th survey area using a hexagonal transmitter configuration. The transmitter had a current of 15 A and an area of 25,000 m^2, see Figure 7. Two measurement modes were used: high (30 Hz) and low (3 Hz) frequency. The receiver coil records voltages over 20 frequency specific time gates. The measured voltages for each gate are integrated over the length of the time gate and divided by that length to provide a single voltage measurement. High frequency measurements began and concluded at .088125 and 6.9785 milliseconds respectively while low frequency measurements began and concluded at .88125 and 69.785 milliseconds. Currents of 10-17 A were injected into the subsurface via the transmitting loop. Turn off times, also known as ramp times, varied from 55-100.5 microseconds for high frequency measurements and from 72-256 microseconds during low frequency measurements.

3.1.2. *Parameter Resolution vs Practicality.* Construction of an effective survey requires a uniform current. Given equipment limitations, the most practical loop configuration was a 100X100 square loop with a current of 15 A. The selected parameters allow us to see deeper than a survey with a smaller transmitter area or current strength. A square loop was chosen because a 100x100 m square can be recreated easily and consistently. Ideally, 1D soundings would have been gathered along the entire survey line. Due to topographic and spatial constraints, soundings could only be conducted in a few locations along the main line. A relatively large and flat area is needed for the survey, so data was only collected in the locations that had permitting and suitable terrain. Two sweeps, one 3 Hz and the other 30 Hz, were collected for each sounding. This allows for data collection over a larger range of depths rather than if just one sweep was conducted. The 30 Hz sweep provides better information on near surface features whereas the 3 Hz provides a better image of what is occurring at depth. Multiple soundings are taken at each site to ensure that quality data exists and to improve the results of later inversions.

3.2. Goals of Investigation. TEM can answer several questions that pertain to the overall goal of characterizing the geothermal system and structure beneath the Chromo anticline. TEM is specifically useful for mapping out vertical changes in conductivity. Knowing the approximate depths of various conductive units can support the creation of a stratigraphic column. TEM can also detect aquifers, given that there are conductivity contrasts between the water and surrounding rock units. The goal of using TEM in this investigation is to be able to map out the underlying structure and potentially locate ground water flow. In doing that, TEM can support the main investigation as well as the sub investigations being conducted by the other geophysical methods.

Site No.	Loop	Ramp Time (μs) 30 Hz	Ramp Time (μs) 3 Hz	Current (A)
1	1	68	117	10
1	2	90	90	10
1	3	88	104	10
1	4	91	107	10
1	5	100.5	100.5	15
1	6	60	101	15
1	7	60	101	15
2	1	60	256	15
2	2	57	80	15
2	3	57	77	15
2	4	56	72	15
2	5	56	72	15
2	6	56	72	15
2	7	56	72	15
2	8	56	72	15
2	9	56	72	15
3	1	55	72	15
3	2	55	72	15
3	3	55	72	15
3	4	55	72	15
4	1	55	72	15
4	2	55	72	15
4	3	55	72	15
4	4	55	72	15
4	5	75	100	15

Table 1. Current and ramp times for each survey loop.

Table 2. Time Gates (ms)

30 Hz	3 Hz
0.088125	0.88125
0.106875	1.06875
0.13125	1.3125
0.161875	1.61875
0.200625	2.00625
0.250625	2.50625
0.314375	3.14375
0.395625	3.95625
0.499375	4.99375
0.63125	6.3125
0.799375	7.99375
1.01375	10.1375
1.286875	12.86875
1.635625	16.35625
2.080625	20.80625
2.648125	26.48125
3.3725	33.725
4.296875	42.96875
5.4755	54.755
6.9785	69.785

Table 3. The time gates are geometrically spaced to collect more voltages for earlier times

4. Magnetotellurics

4.1. Survey. Two roaming MT stations were set up at the northeast end of the main line with three more located around the southwestern end. The survey positions were limited by the availability of flat, clear land that was distanced at least one kilometer from power lines. A UTM coordinate map of the roaming and reference stations is included in Figure 8. An additional remote reference site was set up approximately 6.5 kilometers northeast from Chromo. The remote reference and roaming sites recorded an equivalent magnetic field, but were differentiated by noise and illegitimate signal. By correlating the two data sets it is possible to distinguish between noise and plane waves at the survey sites to remove erroneous data points from the results.

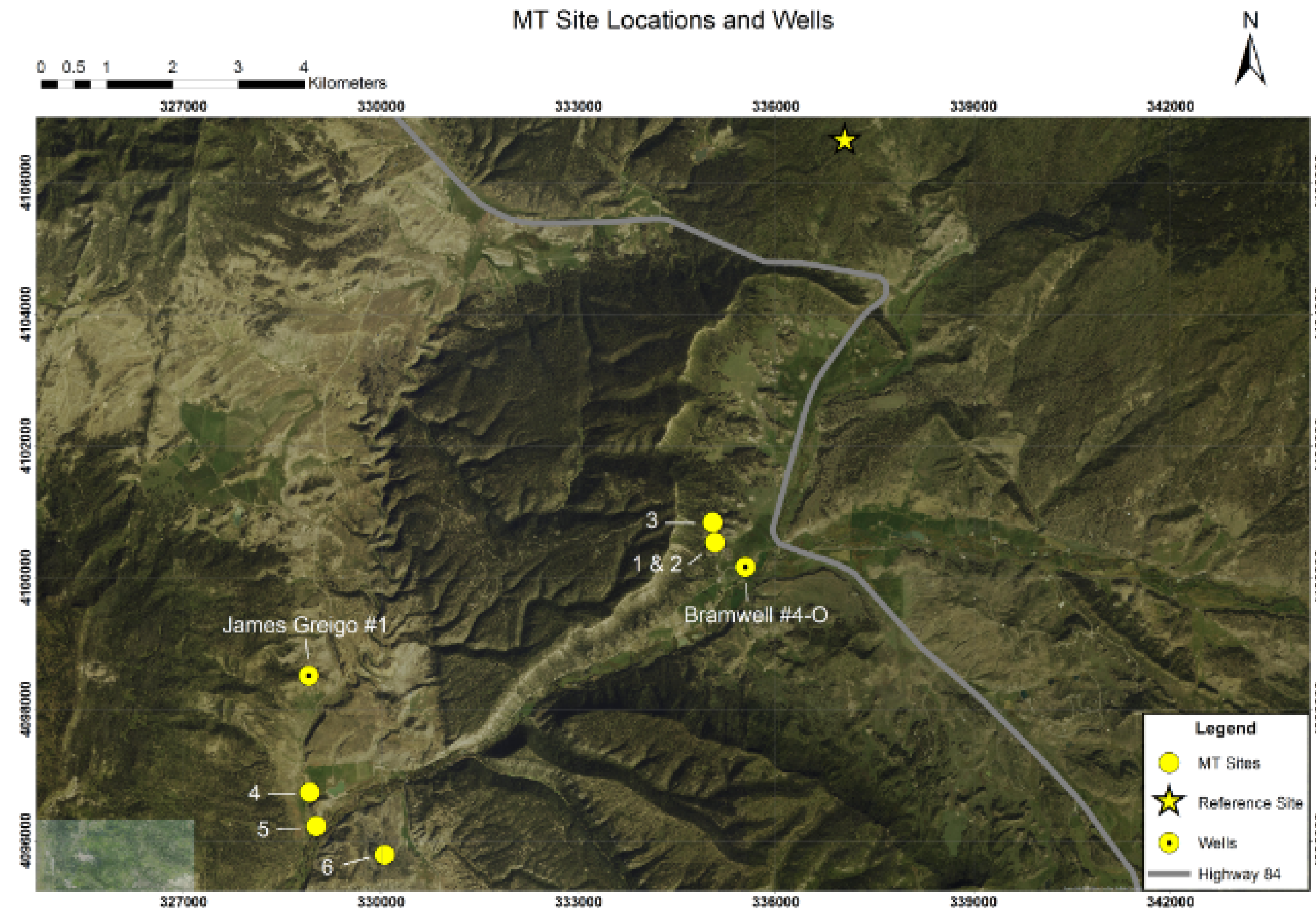

Figure 8. The UTM coordinates of the six MT survey sites are plotted in plan view west of Chromo, CO. The reference site and two well logs which were incorporated into the interpretation are also included.

The center point of the survey was chosen according to the availability of flat, clear space in the cardinal directions. Using a compass and measuring tape, four electrodes were placed 50 meters from the center in each of the four directions. Cables were then connected to the electrodes, run along the 50 meters to the center point, and connected to the appropriate port on the Analog-to-Digital Unit (ADU). Magnetometers were then placed one meter away from the northern and eastern cables, oriented in the respective directions, and connected to the ADU with 15 meter cables. The instrument set-up is depicted in Figure 9 with $\mathbf{E}_x$ and $\mathbf{H}_x$ oriented north/south and $\mathbf{E}_y$ and $\mathbf{H}_y$ oriented east/west. The horizontal positioning and orientation of the magnetometers is essential to collecting quality data, so the strike and dip were ensured using a compass. Additionally, the electrodes and magnetometers were all buried one foot beneath the surface to eliminate the influence of weather fluctuations on the data.

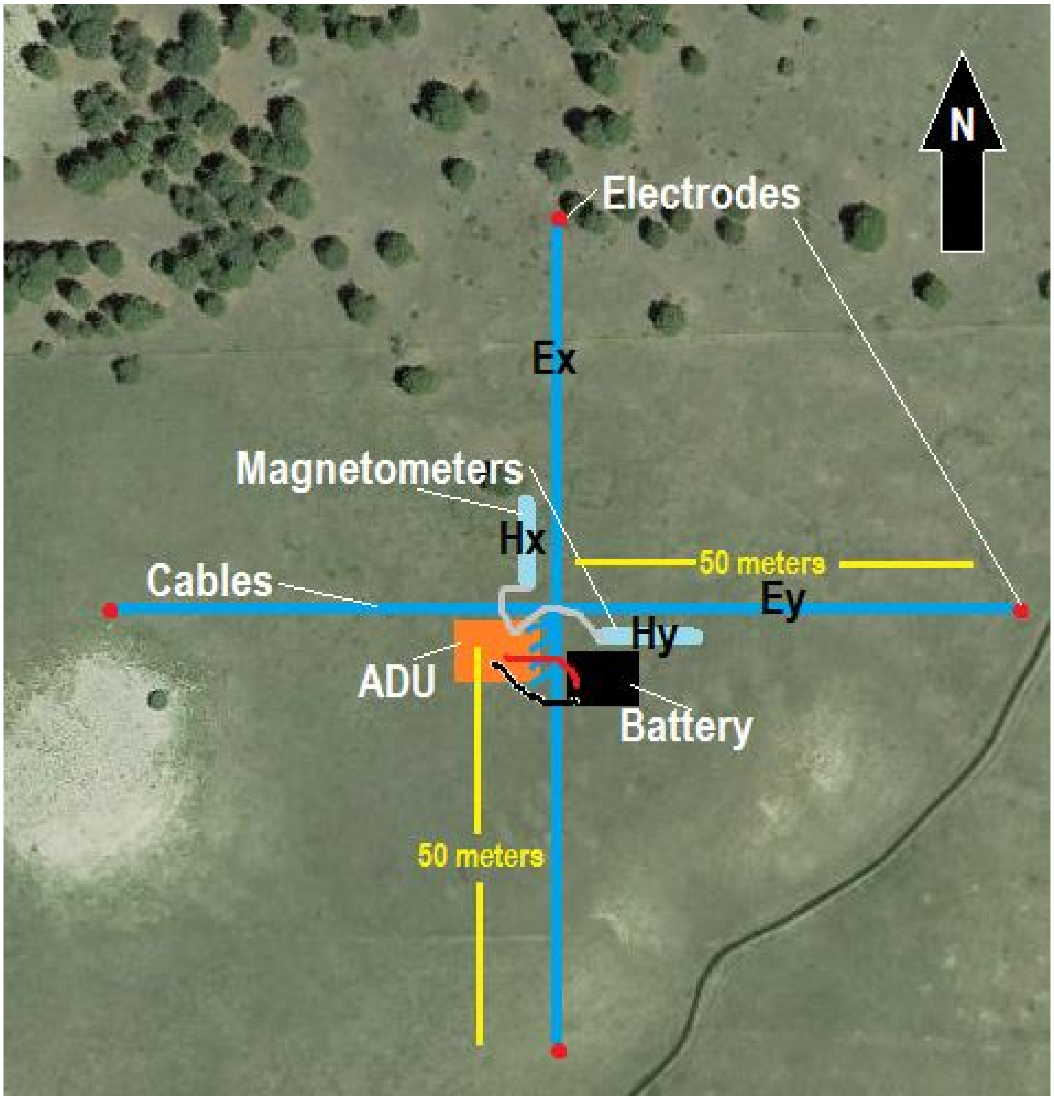

Figure 9. The general layout for an MT survey is depicted over site 1. $\mathbf{H}_x$ is the magnetometer oriented NS while $\mathbf{H}_y$ is oriented EW. The blue lines represent the cables connecting the electrodes at the ends to the ADU at the center.

The ADU was set up to collect data for a specified time using the wireless interface software ViewMT. Table 4 shows the start, stop, and total run time for each site, while Table 5 shows the four reference station runtimes. Prior to starting the run time for each survey, a test collection was performed to find the best gain and offset. The gain and offset were then set as the default parameters which were calibrated by the test result in ViewMT.

Site No.	**Start Time**	**Stop Time**	**Total Time**
1	20:50	6:00	9 hours
2	23:00	4:50	5.8 hours
3	23:00	7:00	8 hours
4	15:00	19:30	4.5 hours
5	21:00	9:00	12 hours

Table 4. ViewMT specifications

Reference No.	Start Time	Stop Time	Total Time
1	23:00	7:00	8 hours
2	23:00	7:00	8 hours
3	23:00	7:00	8 hours
4	16:00	9:00	17 hours

Table 5. ViewMT specifications

4.1.1. *Description of Physical Property.* MT surveys are designed to detect electric and magnetic fields at the surface that result from naturally occurring electromagnetic plane waves. The chosen orientation of electrodes and magnetometers allowed for differentiation between the orthogonal components of the electric **E**, and magnetic **B**, fields. According to Faraday's law, see Appendix 11.2 the ratio of the orthogonal components of **E** and **B** is mathematically related to the apparent resistivity of the subsurface. Collecting data for a significant amount of time allows for a wide range of frequencies of the EM wave to be recorded. A variety of frequencies is beneficial as it accounts accounts for a greater range of skin depths. High frequencies are representative of shallow depths and take a small amount of time to record, while low frequencies are representative of the deeper subsurface and take a long time to record. Thus, by recording the distinguished components of the electric and magnetic fields at a wide range of frequencies, we are capable of plotting a pseudo depth 1D profile of apparent resistivity as a function of frequency.

4.1.2. *Significance of Parameters to 2015 Field Camp.* The goals of investigation associated with MT method in Chromo are to support the interpretations of other geophysical methods along the main line. As described in section 2, the depth of investigation of MT measurements ranges from meters to kilometers. Consequently, these results are capable of supporting the interpretation of the deep seismic line at depths where other geophysical methods cannot. The size of the survey was the maximum possible in order to observe depths up to the Precambrian basement. Similarly, the collection times were maximized but were limited to 8-12 hours in order to collect data in a new location each day. Information gained using magnetotellurics is largely non-unique, and therefore a specific model cannot be determined without significant constraints. The results from this interpretation were constrained accordingly by those found by time domain EM and nearby well logs. The broad apparent resistivity curves generated in processing can be used to show the contrast in physical properties between the shale, sandstone, and crystalline basement formations local to Chromo and the associated hydrothermal system.

5. Direct Current Resistivity

5.1. Survey. DC Resistivity was used to observe the structure of the subsurface of the main line in Chromo, CO in addition to gaining information as to whether the water in the subsurface is connected to a larger geothermal system.

5.2. Physical Property. A DC resistivity survey consists of measuring the subsurface resistivity at the surface. A current is injected into the ground and interacts with the composition of the subsurface. The difference in the electric potential is measured between two electrodes, a value from which apparent resistivity can then be calculated. Resistivity is an intrinsic property of rock that measures how the material opposes the flow of electrical current. This opposition depends on several aspects of the composition including permeability, porosity, fluid content, and its dielectric constant.

5.3. Reasoning. The main line was located along a road which meant that it was easy to access with any type of geophysical equipment with little limitation from terrain. It can be used by other methods to aid in their interpretation including, but not limited to, seismic and gravity.

5.4. Survey. Main line:

- Array Type: Wenner-alpha
- Electrode Spacing: 20 m
- Number of Electrodes: 64

- Power Line Frequency: 60 Hz
- Midpoint:electrode 32
- Maximum Current: 200 mA
- Total Acquisition TIme:3.5 seconds
- Primary Acquisition Time: 2.0 seconds
- Initial Delay Time: 0.3 seconds
- Maximum Number of Stacks: 8
- Error Limit/ Standard Deviation: 5%

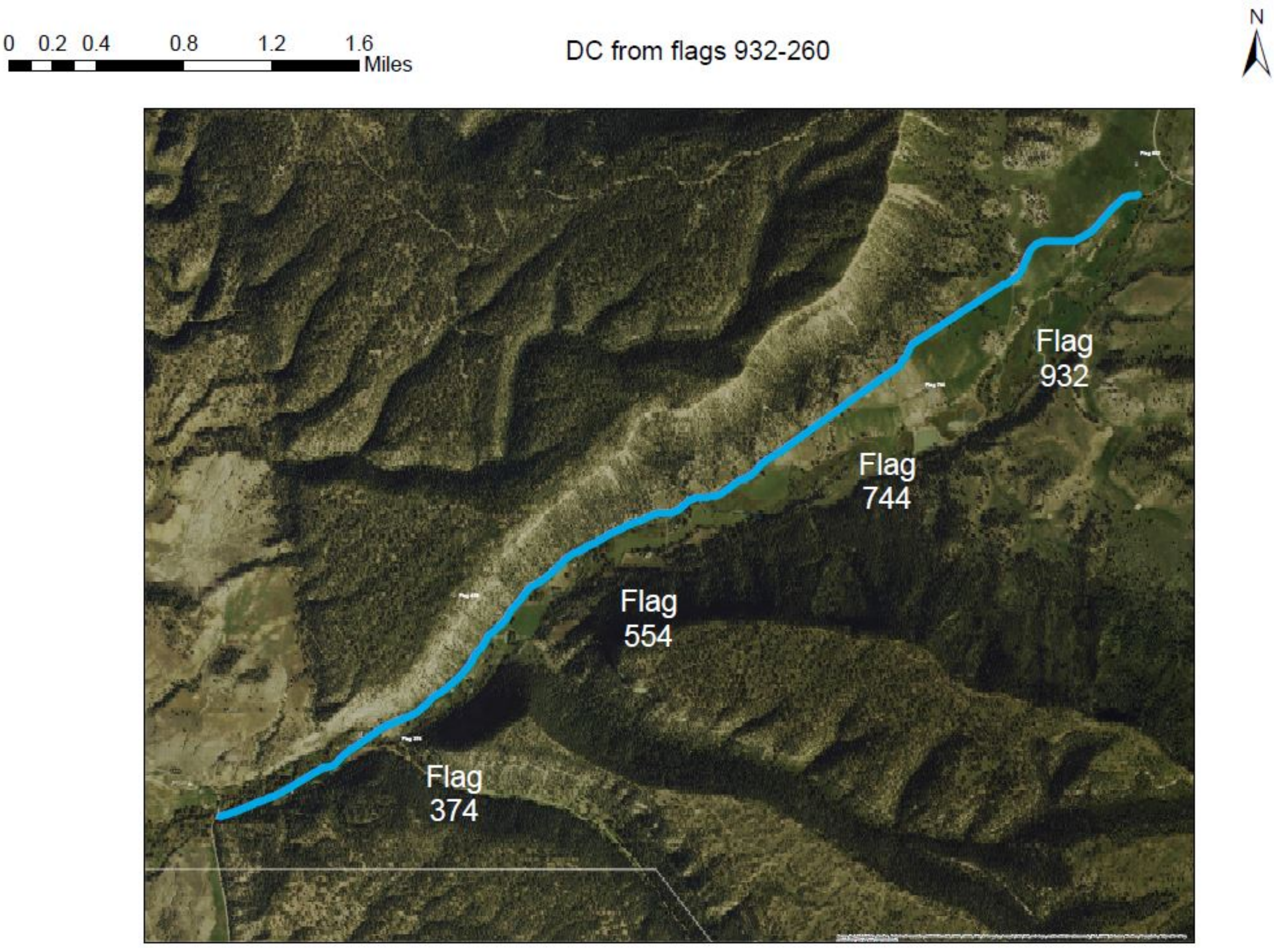

Figure 10. This shows the entire 2015 DC Resistivity survey along the main line located in Chromo, CO. Geological features that we expected to find in the survey include layers and potentially a fault.

5.5. Decision Process for Parameters. Choosing which array will be utilized proves to be the most significant parameter facing this survey, and has a notable impact on the resolution of the data. Geologic cross-sections of the area along the main line suggest horizontal layering. This Wenner Array was chosen as this setup has the best configuration to capture features with minimal lateral variability.

The number of electrodes was determined by the CVES cables and the desired length of the survey. Along the main line there were several kilometers across which data would be acquired, so it was determined that the longer CVES cables with 20 m takeout spacing and 8 takeouts per cable would be the most effective.

Another parameter that had to be chosen was the maximum current input. As an alternating current was applied, we wanted a relatively low current to prevent induction. Safety concerns were also a factor in this decision with regards to electrocution when current was actively running. We concluded that a maximum current of 200 mA would be ideal.

Time constraints led to the selection of 3.5 seconds of total acquisition, a measurement time of 2.0 seconds, and a 0.3 second start delay. The range of error associated with each measurement was also considered. A 5

5.5.1. *Goals for Investigation.* DC resistivity is used to image the subsurface in terms of the physical property resistivity. The primary objective on the main line was to clarify the gently dipping layers underlying the survey area. This led to the selection of a Wenner array and parameters that would yield a balance of both high resolution and practicality.
Data Processing

6. Self Potential

6.1. Survey. The self-potential (SP) method uses two electrodes to measure voltage variations within the subsurface. These voltage variations are produced by a multitude of sources, including groundwater flow, ore bodies, thermal gradients, or changes in vegetation. The largest voltage anomalies are produced by groundwater flow and redox reactions occurring in ore bodies and contaminant plumes. SP is therefore a very popular method in mineral exploration and environmental geophysics.

6.2. Acquisition/Map of Area.

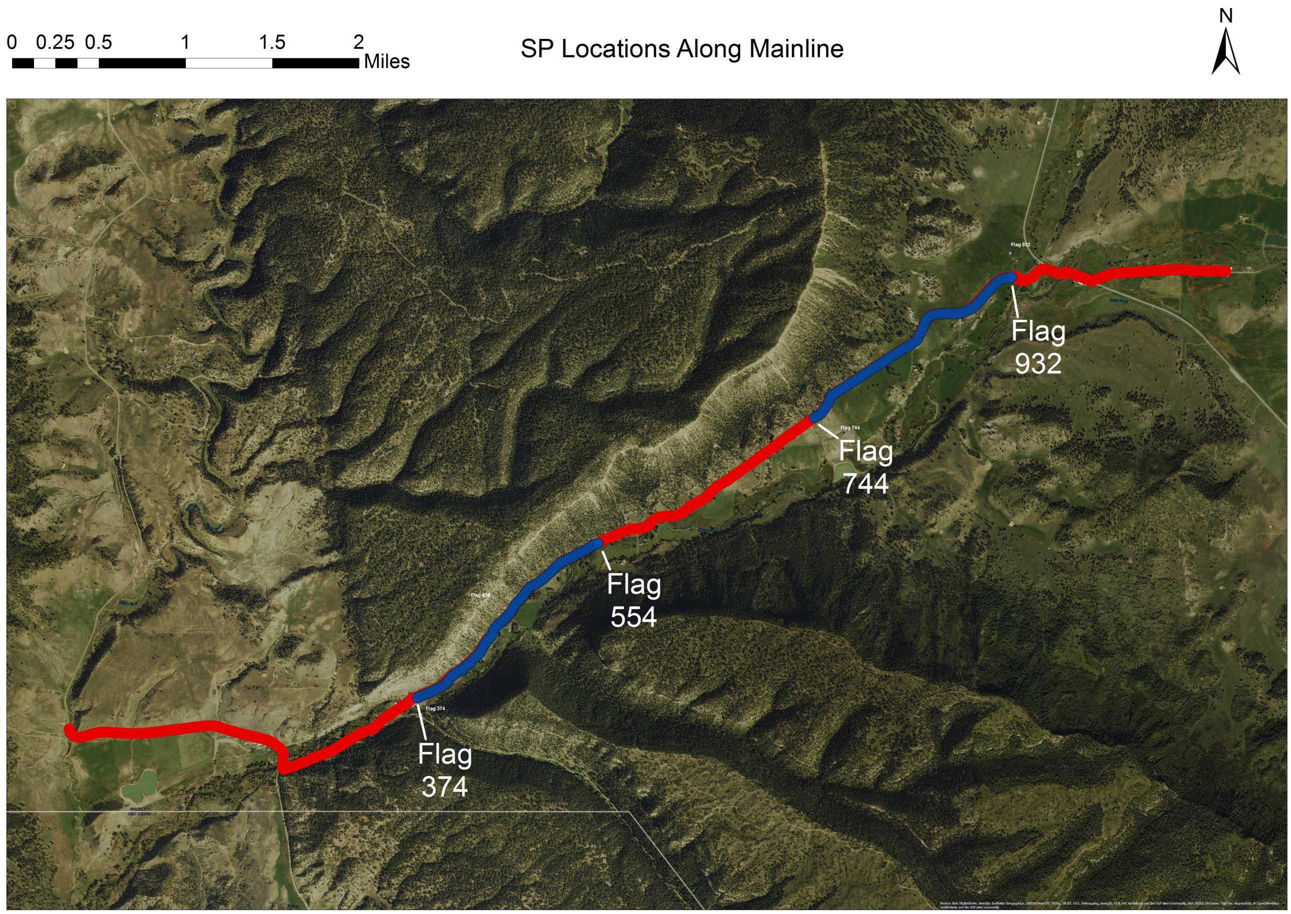

Figure 11. The location of the SP survey along the main line.

Four surveys were completed on the mainline with an additional survey near of the firehouse. There were two overlaps in these four lines, making two larger datasets on the mainline. The survey by the firehouse is pictured in Figure 12. A consistent 20 m spacing was applied to each survey. The length of the lines varied between each day.

Line	1	2	3	4	5-Firehouse
Flags	374-458	454-554	744-890	886-932	Electrodes 7-58

Table 6. Self Potential lines

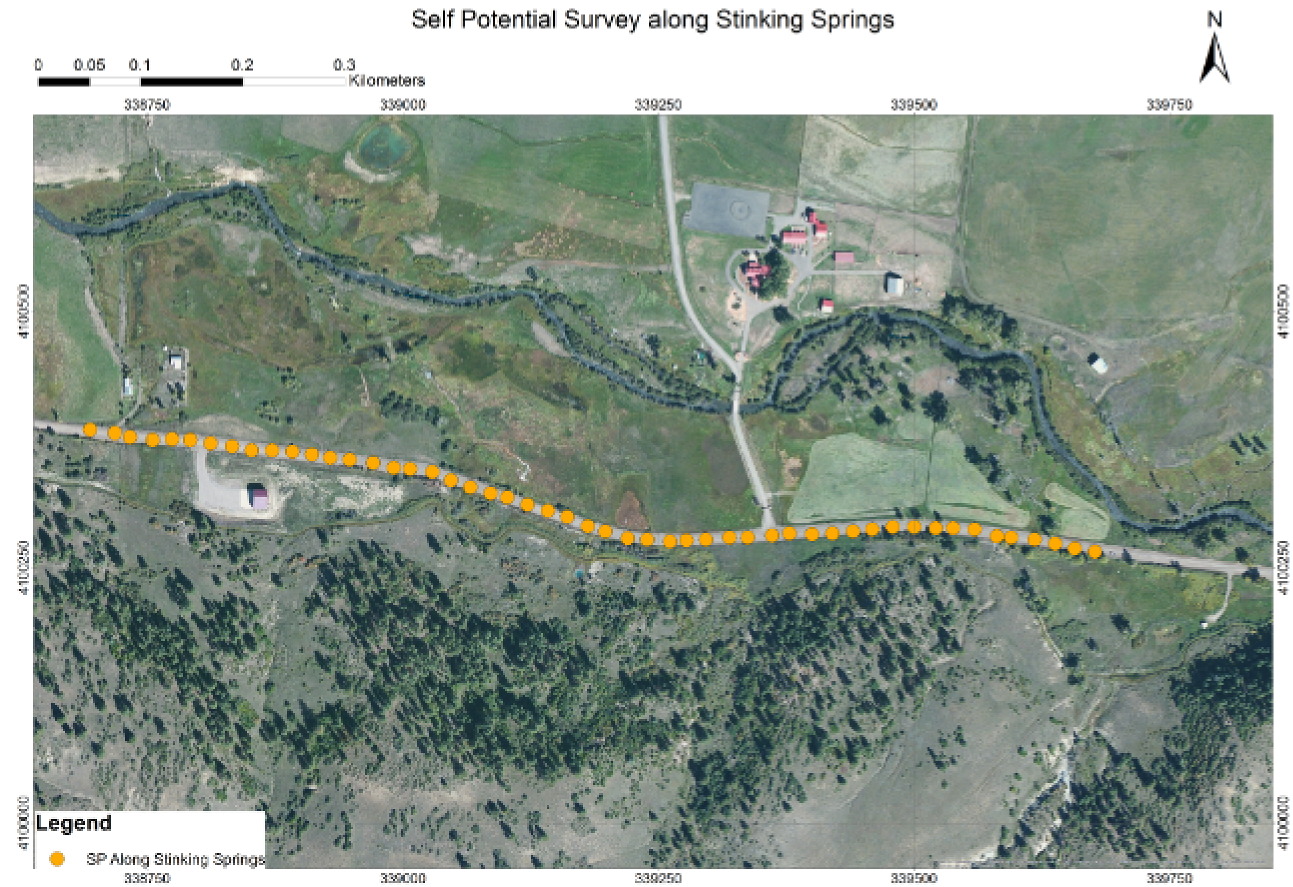

Figure 12. The location of the SP survey by Stinking Springs. Each point represents an electrode.

6.3. Reasoning and Goals. SP data was collected on four different days yielding 3.68 km of data along the main line and an additional 1.0 km line over Stinking Springs. These lines provide information that is applied to joint interpretation efforts with other methods along the main line. The surveys completed along the main line were spread out in order to gain preliminary data over as much area as possible. The Stinking Springs line was designed for groundwater flow characterization in a hydrologically interesting location east of Chromo. The goal is to find out information about groundwater flow, and any coincident geothermal activity in the area. Comparing the SP results to the geological cross section, topography, DC resistivity, and IP inversions will vaid in achieving these goals. Results that cannot be explained by this information are most likely relate to groundwater flow and thermal gradient information.

7. Induced Polarization

7.1. IP Survey. Induced polarization is a geophysical method which injects an electrical current into the subsurface to measure apparent chargeability and variation of electric permittivity. The method requires a carefully chosen alternating current, commonly referred to as a square wave. This creates a polarized accumulation of charge, or dielectric polarization. Dielectric polarization is the same physical behavior seen in capacitors. The polarization is caused by the interaction of an electrical double layer around the grains and the surrounding solution. This interaction causes polarization when the system is under the influence of an electric field. When the current is turned off, the polarization begins to decay. Chargeability is then determined by the measured time dependent decay curve of voltage.

Chargeability is a rock property measured in units of time (most commonly in milliseconds) and is described as "the polarisation voltage developed across a unit cube energised by a unit current" [**28**]. It is derived from the decay curve of the voltage when current is shut off. Once the inversion of the chargeability data is completed, a transformation of the inverted data can produce a measurement called normalized chargeability. Normalized chargeability is in units of siemens per meter and can differentiate between clays, sands, and shales with more success than the inverted chargeability.

7.2. Reasoning. The main goal in conducting our IP survey is to detect and locate the source of the hydrothermal resource in Chromo, Colorado. This particular line was taken over the Stinking Springs hydrothermal feature. There should be some chargeability contrast at or around the conduits and reservoirs for the hydrothermal system, if they exist in this area. These contrasts in chargeability would more than likely be due to the presence of water. We hope to image the conduits and fractures where fluid may be present. We should be able to see contrast in normalized chargeability between the Mancos shale and the Dakota sandstone. Normalized chargeability will give us extra information about sand, clay, and shale mixtures of which the Stinking Springs area consists of.

7.3. Survey Parameters. The Wenner-Alpha array type was chosen by Dr. Andre Revil as the best option for our survey area. The Wenner-Alpha array was chosen because it has a high SNR (signal to noise ratio) when compared to other types of arrays that could have been used. The Wenner-Alpha array is also more able to sense horizontal formations.

We used the 20 meter spacing for our electrodes because Dr. Andre Revil suggested it. We also had different DC cables that would allow for 20m, 10m, and 5m. The 20 meter takeout cable was chosen due to time constraints. A smaller spacing would yield more data and better resolution. The actual spacing used to collect data varied based on our array length. This was done to increase the amount of data collected and increase the depth of investigation after inversion. This variable, yet equal, spacing is a key determinate of the geometric factor.

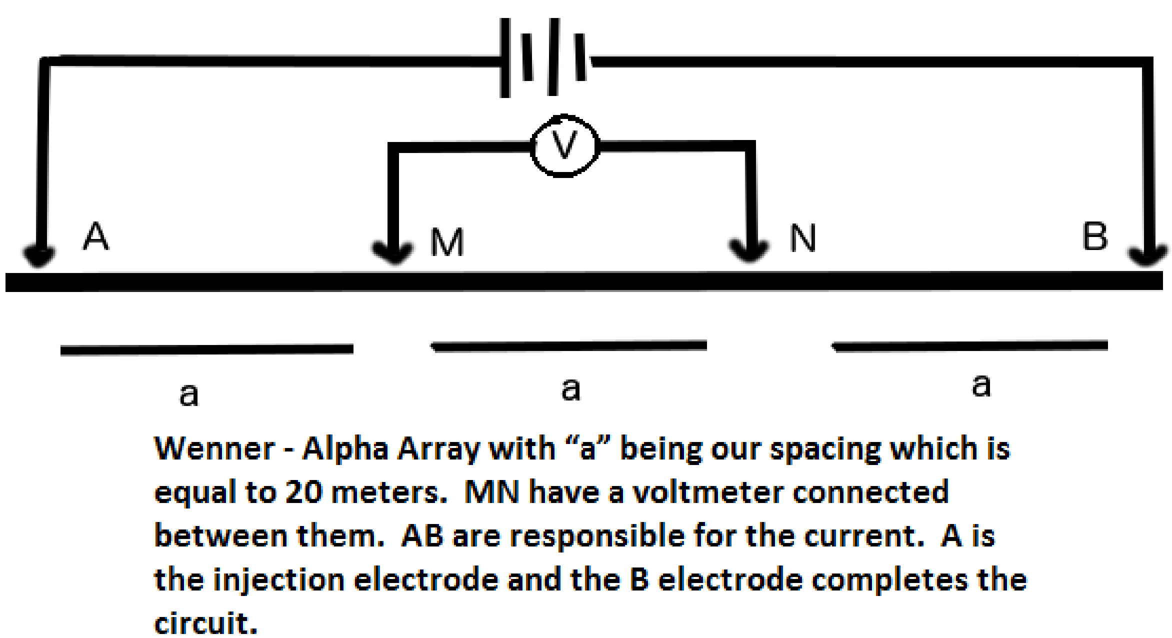

Figure 13. The above figure is a depiction of a Wenner - Alpha array. This array maintains an even spacing between each electrode. The value of "a" will change during the survey, however the spacing between each electrode will remain equal.

The total array length is 1270 meters and is an extremely important parameter. The array could be any length desired within reason. The most important information that the array length gives us is surface distance along our line. The surface distance between the electrodes is used to calculate depth of investigation during the inversion process. The larger the total array length, the larger the "a" spacing value can become, which leads to larger depths of investigation. Our current array length leads to a theoretical 171 meter depth of investigation.

The survey injected a 200 mA current. The current has to be at least some minimum value to overcome the natural telluric currents within the subsurface and achieve a good SNR. Also, the current chosen is lower than 1 amp to prevent deadly electrocution during operation of the equipment. Dr. Andre Revil chose this current based on his experience and knowledge of what works what does not when doing IP surveys.

The signal used for injecting the current consists of three stages. The first stage is the charging stage (primary voltage). The second stage is the dead time stage. The third stage is the positive discharging stage (secondary voltage). The fourth stage is negative charging (primary voltage). The fifth stage is the dead time stage again. The sixth stage is the negative discharging stage (secondary voltage). The dead time stage is necessary to allow coupling effects to dissipate.

We acquired 472 measurements during the survey. There have been many investigations into the nature of diminishing returns associated with collecting complete data sets. Collecting more than 472 measurements for a 64 electrode array of 1.27 kilometer length is not going to improve the data quality enough to warrant the extra time required. In previous studies, It has been discovered that after 472 measurements you have more than 90% of the information and acquiring the remaining 10% would cost too much time and would not return enough extra information. It would be more efficient to spend that time on extending the length of your array instead.

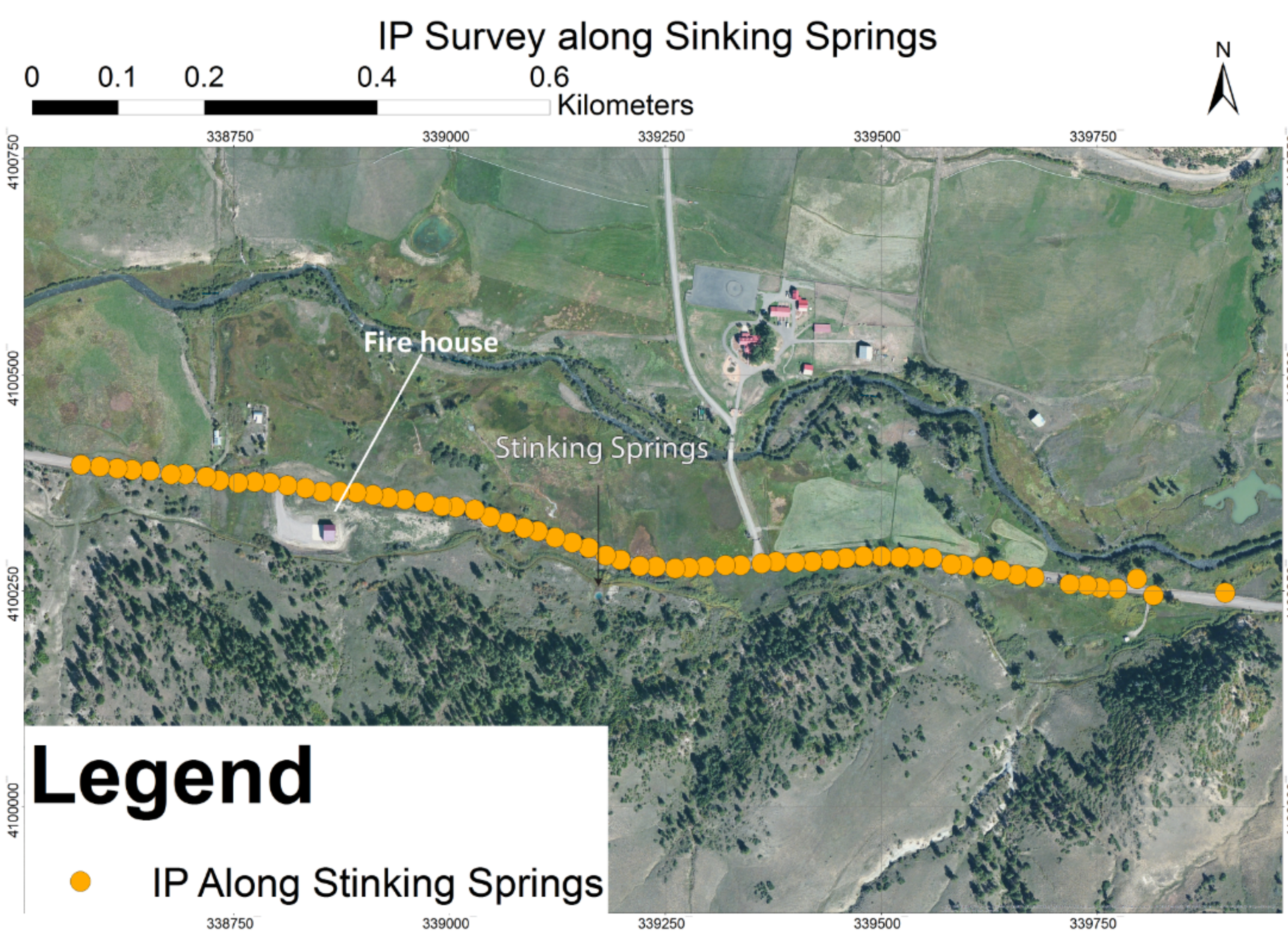

Figure 14. Map of the IP survey area: red dots are the GPS locations of electrodes. Electrode #1 is located on the east side of the line.

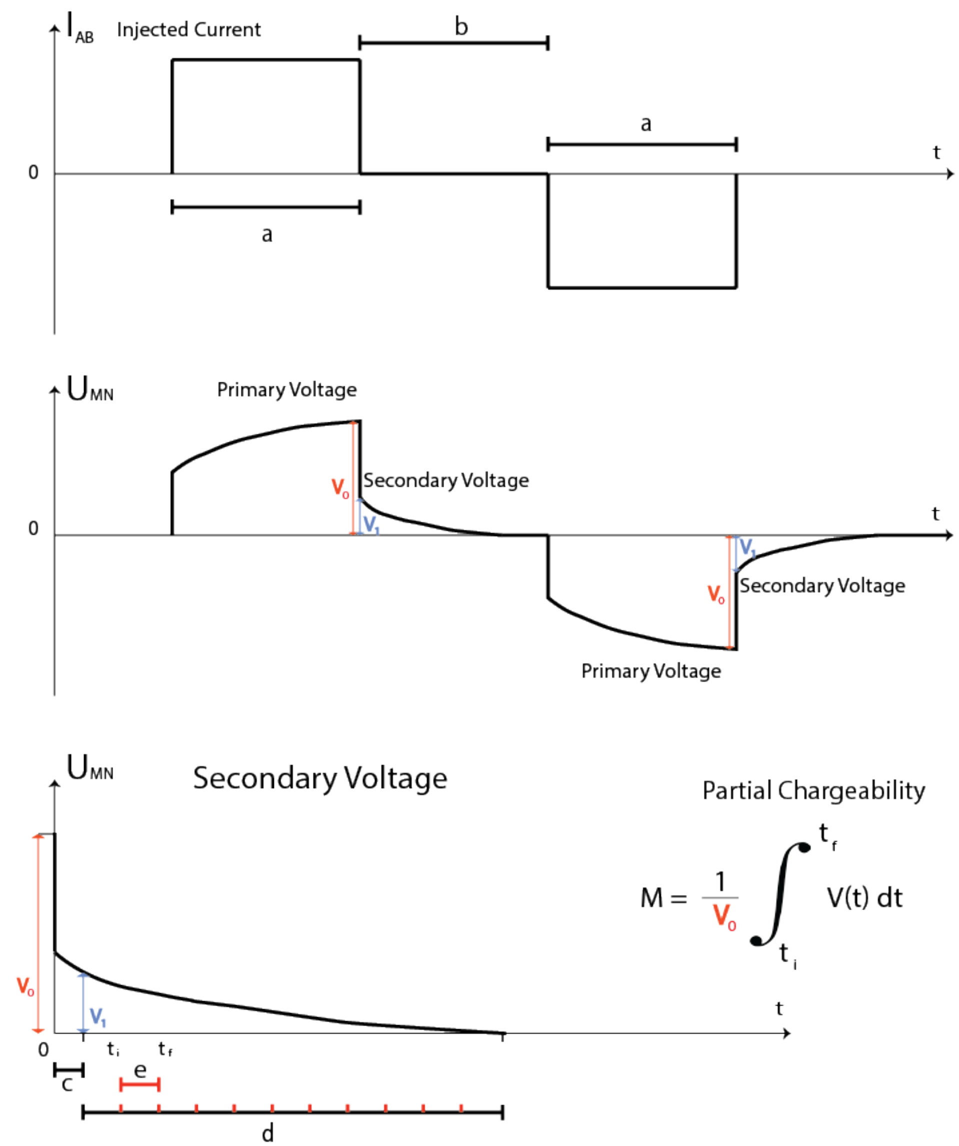

Figure 15. For the figure above, a = 3.5 s, b = 2 s, and c = 0.3 s (dead time), d = 3.1 s, e = .1 s. The top image is the square wave used when injecting current. The middle image is a plot of the voltage during charging (primary voltage) and discharging (secondary voltage). The bottom image is a portrayal of a standard voltage decay curve.

7.4. Goals of Investigation. The goals of this investigation are to determine the presence of highly saturated material and conduits or fractures that may have water in them. The presence of water would suggest we have located conduits, fractures, or a reservoir. The presence of water will produce a contrast in changeability within the survey area. We expect to see chargeability contrasts between the Dakota and Mancos formations and contrasts due to increased saturation around the spring. It would be ideal to locate the source of the Stinking Springs hydrothermal system in this area.

8. Deep Seismic

8.1. Survey. Seismic is one of the most common geophysical methods used today. Seismic surveys image the subsurface to distinguish geologic structure. Acquisition requires a source which is often generated by a vibroseis truck during industry surveys. The truck induces seismic waves which propagate through different mediums in the subsurface and reflect back to receivers on the surface. Reflections are utilized to image interfaces between rock layers, folds, faults, uplifts, and other geological structures. The goal of the 2015 Seismic Line is to locate boundaries between the Lewis Shale, Mesaverde Sandstone, Mancos Shale, Dakota Sandstone, Morrison Formation, Entrada Formation, and Precambrian basement, as well as image the anticline of the Mesa Verde

Sandstone and other potentially large faults in the subsurface. These observations may contribute to investigation of the geothermal system in Chromo.

8.1.1. *Motivation for Survey.* The objective of our seismic survey was to characterize the subsurface by obtaining information about geological layers along the survey line. We seek to model the subsurface acoustic velocity contrasts and create a geologic model with the assistance of other geophysical methods.

8.1.2. *Survey Parameters.* Along the main line, line acquisition unit land (LAUL) were placed with a spacing of 400m. Additionally, one line acquisition unit cross (LAUX) was located at the dog house. Flags representing receiver stations were placed every 10 meters along the line. Receiver spacing was chosen to be consistent with the 2014 acquisition parameters. Three Sercel SG-10 geophones were placed on both sides of each flag, resulting in a total of six geophones per station along with one FDU (Figure 16). The six geophones were used to produce a six-fold stack trace, allowing us to look at a response centered on the station that captures most of the vertical component of the wavefield. During acquisition, 240 live receiver stations recorded the seismic signal for each shot. Limited resources required that geophones from the beginning of the line were transferred to the end of the line when they were no longer within the live channel range. Dawson geophysical provided INOVA AHV-IV Commander vibroseis trucks, which initially shot every twenty meters, but began shooting every ten meters when geophone rollover constrained vibroseis progression. Shot locations along the line are shown in Figure 17. Gaps in the shot spacing are discussed in the Survey Errors section.

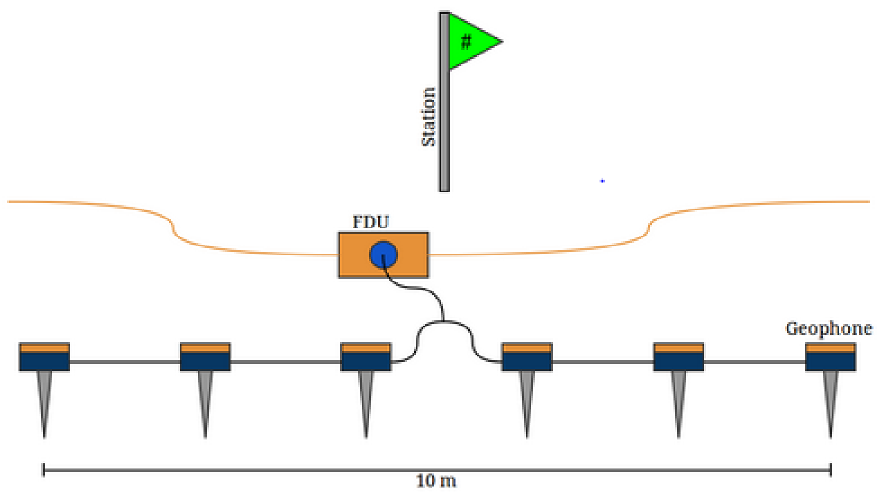

Figure 16. Geophone, FDU, and flag layout at each receiver and shot location.

8.1.3. *Sweep Parameters.* Frequency, length, and repetition of the vibroseis truck vibrations are defined as the sweep parameters. A frequency range of 4-128 Hz was chosen after analysis of test sweep results. Observation of the test data revealed that little useful signal appeared above 128 Hz. The lowest frequency was set to 4 Hz, low enough to propagate seismic energy beyond our depth of investigation while minimizing noise from low-frequency events. We chose to do four sweeps per shot location because limited time availability for field work. Each shot lasted ten seconds and receivers had a final record length of two seconds. An upsweep was chosen because it showed less noise during sweep tests. We chose a non-linear sweep because we wanted to acquire more information at high frequencies than at the low frequencies to obtain better resolution in the shallow subsurface. With a high frequency of 128 Hz and an assumed layer velocity of 3,000 m/s, the smallest vertical layer resolved in this survey is theoretically 6 meters. In a practical application, a 6m vertical resolution is not realistic, and the layers resolved by the seismic survey maintain a greater thickness.

8.1.4. *Map of Receiver and Shot Locations.*

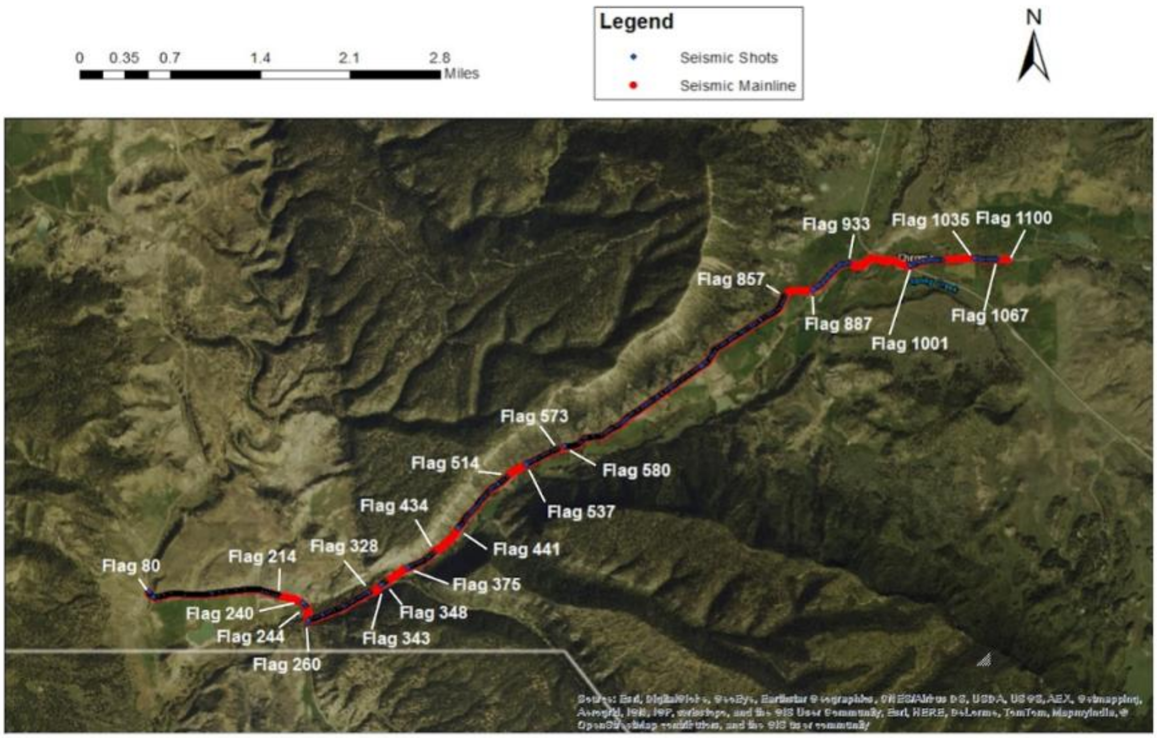

Figure 17. Receiver and shot locations along the 2014 and 2015 line.

9. Hammer Seismic

9.1. Survey. Hammer seismic is a geophysical method that transmits seismic energy into the subsurface with human generated sources which can be recorded, processed and interpreted. The hammer seismic method has been used for decades to investigate the thicknesses, depths, and seismic velocities of the subsurface. Hammer seismic surveys provide subsurface information on the order of tens of meters. The instruments used in hammer seismic surveys include sledgehammers, plates, geophones, cables, and seismographs [**29**]. Hammer seismic is sensitive to density, P-wave velocity, and S-wave velocity. The hammer seismic method is also used in areas where the equipment necessary for deep seismic surveys cannot be set up, or is not permitted due to the large disturbance. Because of its small depth of investigation, hammer seismic is very useful

9.2. Background. The hammer seismic method shown in 18 uses a sledgehammer to vibrate rock particles. The vibration generates elastic waves which propagate through the subsurface and are recorded by geophones. Geophones and plates require solid contact with the soil to improve data quality. The function of the geophone is to convert mechanical energy to electrical signals. The hammer seismic method is used for near surface seismic investigations, as it only has a shallow depth of investigation.

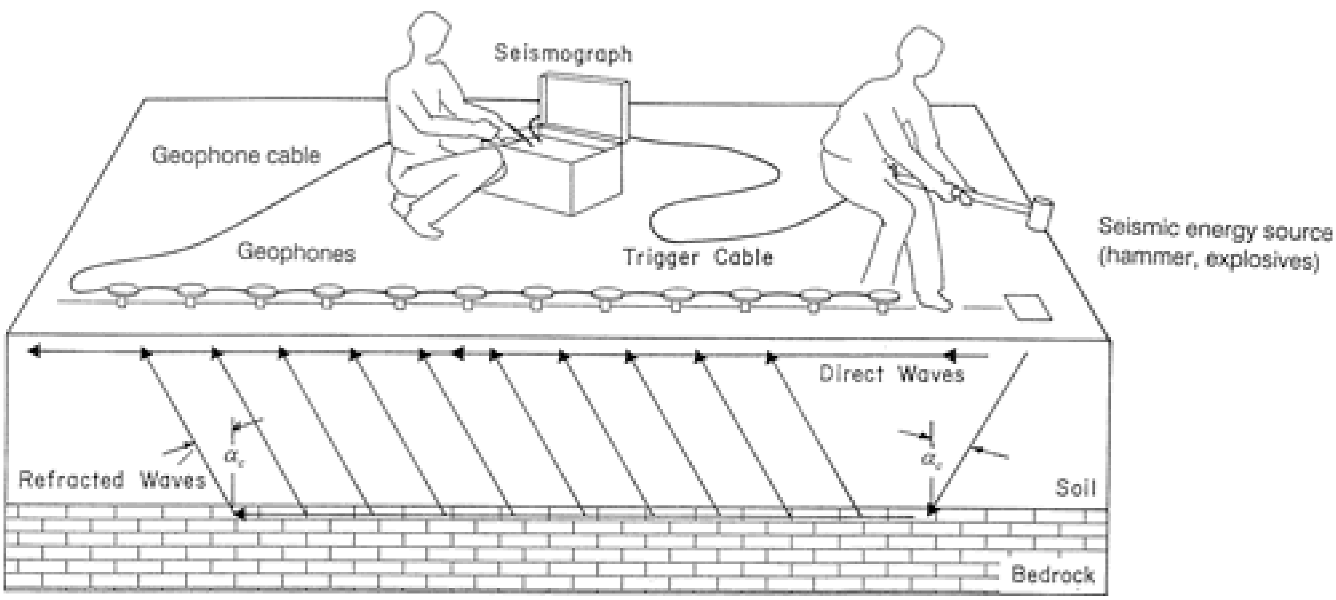

Figure 18. Field setup for a hammer seismic survey[**29**].

9.3. Motivation for Survey. The motivation for this survey was to image the large fault that has surface expression near the west end of the line. The deep seismic line in the same area will not be able to image the fault at shallow depths. Hammer seismic is a perfect way to complement deep seismic by imaging the shallow subsurface and potentially the fault. For this survey, seventy-two geophones were used: sixty 10Hz and twelve 40Hz. To see the potential fault and any reflectors dense geophone spacing was prefered. For this reason one meter spacing was used making the line 72 meters long. Shots were done every meter starting a half meter before the first geophone, then between every other geophone, and ending a half meter past the last phone. A shot is where the seismic source is created, in this case by hitting a hammer to a metal plate on the ground. Three stacks were made per shot: at each location the hammer was swung three times, these three shots were averaged, or stacked, for a more accurate image. For one second after each shot the geophones recorded the returning waves with a sampling interval of 0.25 milliseconds. After reaching the end of the line the first twenty-four geophones were moved to the end of the line, performing a roll-along. This was done twice making the line a total of 120 meters in length. Roll-alongs and dense receiver and shot spacing are time consuming in a survey, but the roadside conditions were very manageable and allowed for a very dense survey along the target area.

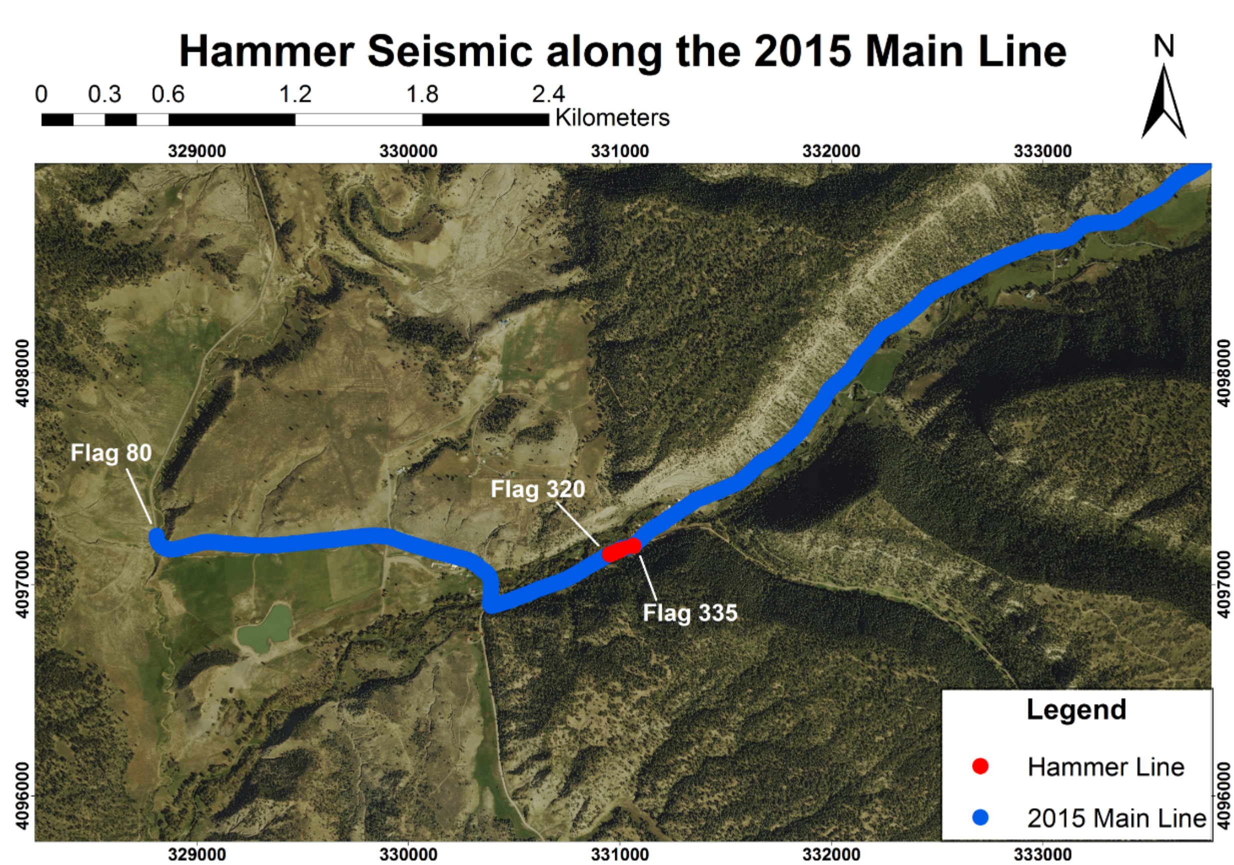

Figure 19. Field setup for a hammer seismic survey[29].

Line	Location	Length	Receiver Spacing	Shot Spacing
3000	Main Line	120 m	1 m	1 m

9.4. Goals of Investigation. The goal of the 3000 line was to image near surface characteristics of the fault that are overlooked by deep seismic data. The dense source and receiver spacing increased the resolution of our images to better locate the fault. By increasing the length of the line with the roll-along method, possible reflectors may appear. Near fault imaging could perfectly compliment the deep seismic in the same region to get a more complete image of the fault that can be seen at the surface.

SECTION 5

Data Processing

1. GPS

1.1. Location Corrections. There are two main types of location corrections required in differential GPS (dGPS) data processing. These include datum consolidation and a base station static drift correction. Several coordinate systems were used throughout the survey that had to be consolidated and corrected for. The first step in correcting a set of points is to upload them into ArcGIS and observe the mapped point in relation to where it should actually be located on the topography. Offsets of 200 m north-south and 50 m east-west typically indicate a datum shift between NAD27 and NAD83. After determining the datum of each data set, the GPS points are converted to the common datum of NAD83 using the program Surfer. Once a common datum across data sets is established, the next step is to apply a correction for the changing base stations. The base station location was changed six times throughout the survey and, because the rovers take GPS points relative to the base station, this resulted in lateral and elevation shifts in the data between different days. The lateral shifts varied between three and five meters for the different base station locations while the elevations were shifted up to 35 m. The corrections were made with a simple addition/subtraction function in Excel. After both corrections were made, accurate plots of all recon and main line surveys were plotted using ArcGIS.

1.2. Elevation Corrections. The elevation changes that were corrected were based on the differences between the GPS base station locations. The original GPS coordinates located on the west end of the survey lined up perfectly along the north side of the road, where the flags were actually located. Thus, this data was used as the reference elevation and every other data set was laterally shifted to match this elevation level using a function in Excel. A secondary quality control analysis (QC) of elevations was conducted using ArcGIS and Digital Elevation Models (DEM) downloaded from the USGS Map Viewer. The DEM files were plotted onto ArcGIS and the GPS points were overlaid. Using a sampling function, the DEM elevations were extracted based on our corrected GPS locations, and a comparison was made between these DEM elevations and our dGPS elevations. The difference between elevations (Flag 80 - Flag 1100) is seen in Figure 1.

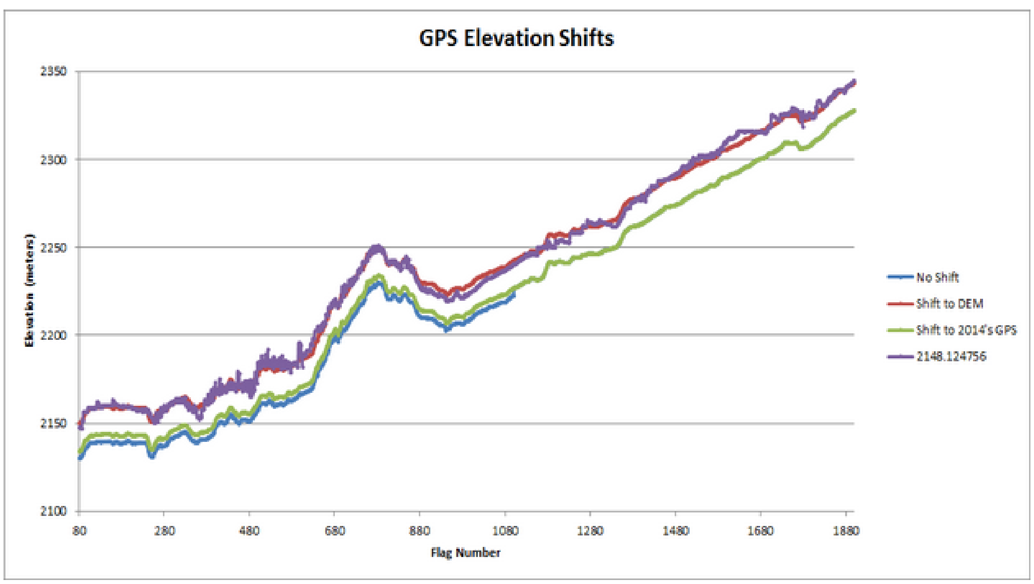

Figure 1. GPS elevation shifts

The QC revealed that the recorded dGPS elevations were approximately 20m below the DEM elevations. A further QC process involved comparing this year's dGPS elevations to last year's elevations. The elevations from

2014 field camp were higher by roughly 4m. The 2014 elevations were also corrected to a survey point that was located at the Stinking Springs near the fire station.

The geometry of our elevations matched the geometry of both the DEM files and that of last year's data. This included the dip in elevation where the stream was located (near flag 940). Because our geometry was similar to the true topography, most method teams were able to successfully complete their processing based on this corrected data. For the purposes of processing gravity data, a further elevation correction was done in which the 2015 data was corrected to the 2014 data and then an average was found relative to the DEM.

1.3. Sources of Error. In medium earth orbit, roughly 20,200km above sea level, there is an arrangement of at least 24 operational GPS satellites. They are arranged in six equally-spaced orbital planes called a constellation. The arrangement assures that there are at least four satellites available for any GPS receiver on any location of the earth with visibility to the sky. Each satellite connects to the receiver to triangulate its current location in accurate space and time. According to the GPS Standard Positioning Service (SPS) Performance Standard, GPS signals provided will always have, at worst, a pseudorange accuracy of 7.8 meters at 95% confidence level [**27**]. This is especially relevant to handheld GPS, which is more dependent on a good signal in order to provide any accuracy.

GPS broadcasts in two different frequencies, F1 and F2, but only F1 is available to civilians. When the government uses both F1 and F2, they are able to make ionospheric corrections, correcting the majority of location inaccuracies. These are at a peak during the day when the GPS receiver's side of the earth is being bombarded by the sun's radiation from sunspots and coronal mass ejections. As such, the solar cycle is also a factor in accuracy. The atomic clocks flown aboard GPS satellites are another source of error, as they tend to develop minute discrepancies over time. Multipathing, a phenomena in which the satellite signal bounces off of topography or buildings before reaching the receiver, can result in distance measurements that are longer than the actual distances between the satellites and receiver [**30**].

2. Results from Gravity Survey

2.1. Processing.

2.1.1. *Description of Raw Data.* The raw gravity data collected over the main line describes the relative acceleration in the vertical direction at each point along the survey. The initial raw data file contains three gravity measurements at every station along with respective standard deviations and the time of acquisition. It is important to note that we used a relative gravimeter, which measures the change in gravity from location to location rather than the absolute gravity.

Prior to modeling, the raw datasets from separate surveys must be combined into a single document. Before merging data sets, a correction for tidal forces and instrument drift must be applied, the details of which can be found in the Appendix Section. Using the average difference at overlapping survey locations between the 2014 and 2015 survey lines, a static shift was applied to merge the two drift corrected data sets into one line. The two data sets were seamless after the static shift, with the difference between overlapping points being well under the noise level.

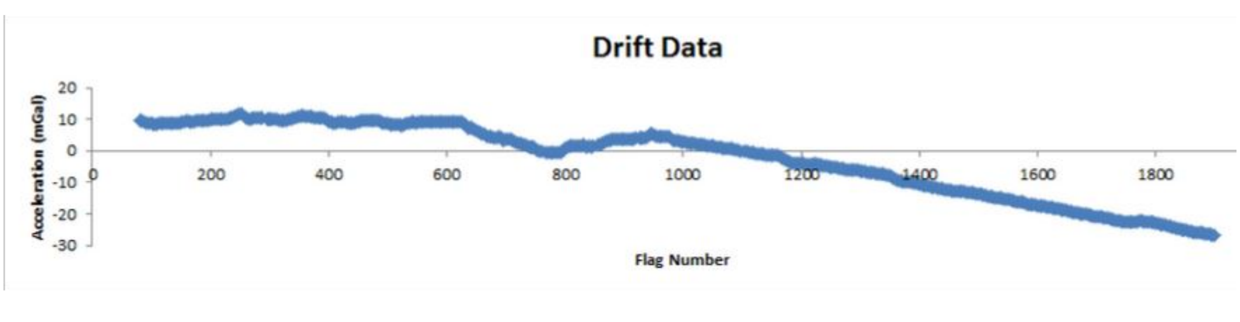

Figure 2. Resulting raw data, post drift correction, from 2014 and 2015 gravity acquisition along the main line.

2.1.2. *Assumptions.*

- All gravity data is collected in the same environment (weather, surrounding bodies, distance from ground surface)
- Topography information is accurate
- Flag coordinates are accurate
- Linear drift correction can be applied to all data
- No topography changes have occurs to alter the 2014 gravity data
- The main line is in the East/West direction, so the latitude correction is not needed
- Formation densities are constant throughout
- The Cutler Group pinches near the thrust fault
- The software used to forward model data accounts for the Bouguer correction
- The datum used for the terrain correction is accurate

2.1.3. *Software.* The GM-SYS package in Geosoft's Oasis Montaj was used to correct for terrain and forward model the gravity data. This software allows for the joint analysis of multiple data sources including seismic data and well logs. A detailed manual was created for this software that includes a processing/modeling workflow and troubleshooting notes. This manual was distributed to various professors and also exists on the CSM hard drives among the 2015 field camp files.

2.1.4. *Methods and Corrections.* To remove the effects of elevation changes (as Earth's gravity field decays with elevation), a free air correction was applied to the full data set. A terrain correction was also performed to remove gravity contributions from out of plane features such as mountains and valleys. The terrain correction was done in Geosoft's Oasis Montaj GM-SYS using a local digital elevation model. A Bouguer correction was initially applied to the data, the results of which can be seen in Figure 3. The Bouguer correction was ultimately not included when constructing our forward model. The slab typically removed during a Bouguer correction is signal for the purposes of our survey and had to be left in the data to properly model the local stratigraphy. Detailed descriptions of these corrections, including mathematical formulas, can be found in Appendix 2..

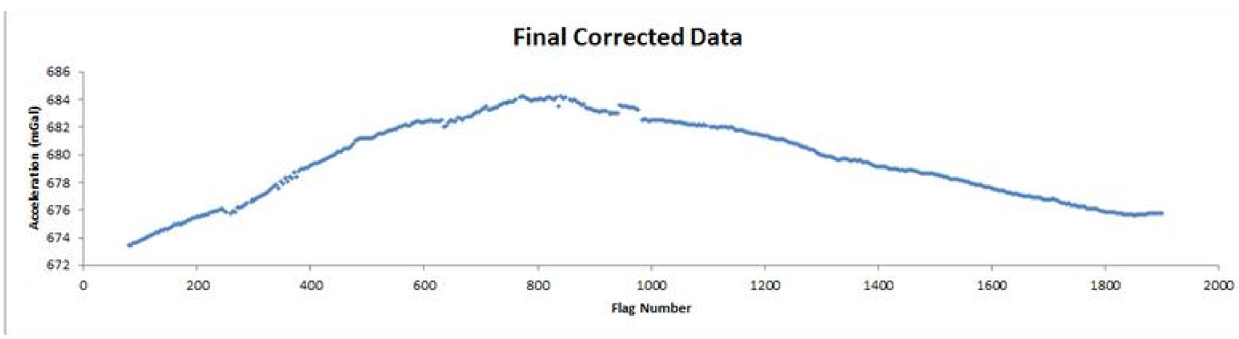

Figure 3. Plot of the final corrected gravity data over the entire 2014/2015 profile.

2.2. Results. The final, fully corrected data is consistent with the initial geologic interpretation along the main line. The first order trend is dominated by a steeply dipping anticlinal basement structure.

Interpretation of the gravity data was completed using the forward modelling software, GM-SYS. The goal of a forward model is to create a geologic section that matches the theoretical gravity response of the field recorded data. While general inversion softwares are available for gravity data, the forward modelling workflows we used were adequate as they allowed us to incorporate a large amount of previous information and cross sections provided by our surface geology and well log information.

To forward model the gravity data, we began with the geologic cross section illustrated in Figure 4. The geologic cross section provided a starting point for the forward model which incorporated the densities of each formation to create a theoretical gravity response. The densities used for each formation can be found in Table 1.

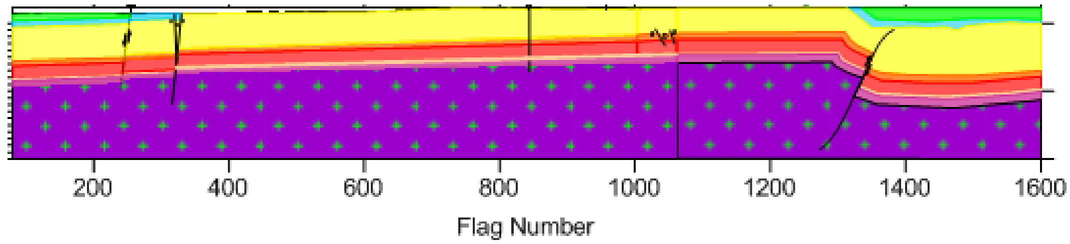

Figure 4. Geologic cross section of the main line generated from surface geology and well data

Formation	**Density (g/cc)**
Lewis Shale	2.4
Mesaverde	2.57
Mancos Shale	2.55
Dakota Sandstone	2.38
Morrison and Entrada	2.5
Cutler Group	2.55
Basement	2.8
Low Density Zone	2.6

Table 1. Density values from literature used to forward model the gravity anomaly (cite Geology)

The final interpretation of the gravity data, driven by the geological cross section and the respective forward modelled gravity response is shown in Figure 5 and Figure 6.

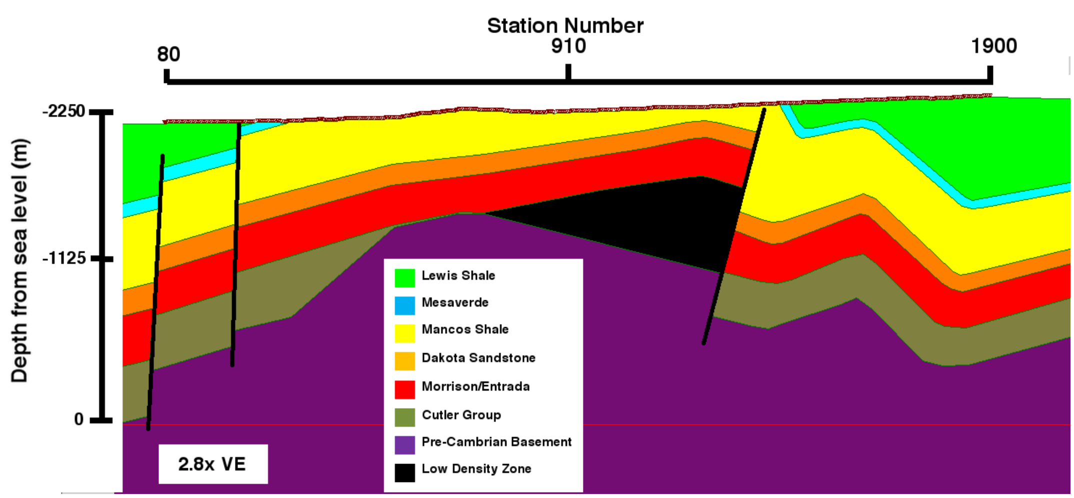

Figure 5. Final interpretation of gravity data, driven by geologic cross section

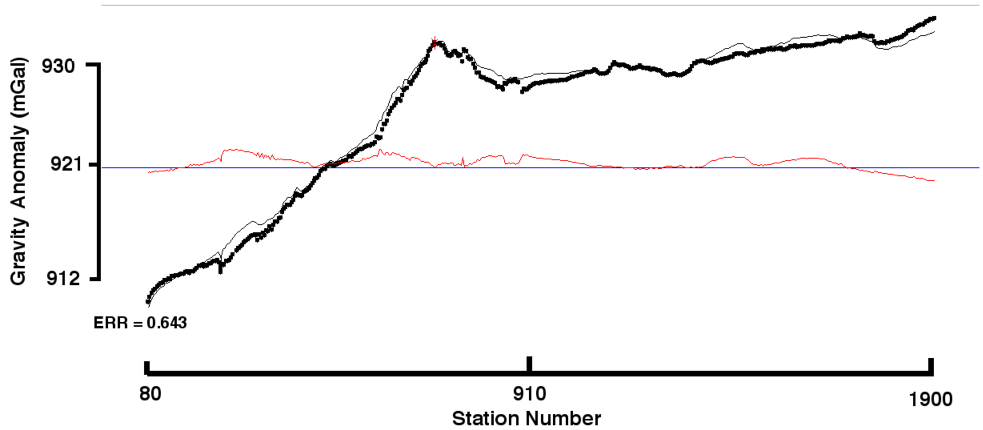

Figure 6. Plot of gravity anomaly response. Bold black line is field data, thin black line is forward modelled response from Figure 5, and red line is difference between field data and modelled response.

The modeled gravity data incorporates the major fault found by 2014 geophysical investigations around flag 1300 in addition to the fault around flag 300 which has a surface expression. To match the model response to the field data, a low density zone is introduced to the hanging wall of the thrust fault.

One potential solution is that the low density zone, needed to fit the gravity data, is a continuation of the nearby Cutler Group. Based on the geomorphology of the area, the Cutler Group is separated due to faulting and pinches out in areas as a result of erosion. Conversely, the low density zone may be fractured basement material. The fractured basement could have formed because of the continued reactivation of the nearby thrust fault. One assumption with this theory is that fractured basement has increased porosity, therefore decreased density, compared to the solid basement unit.

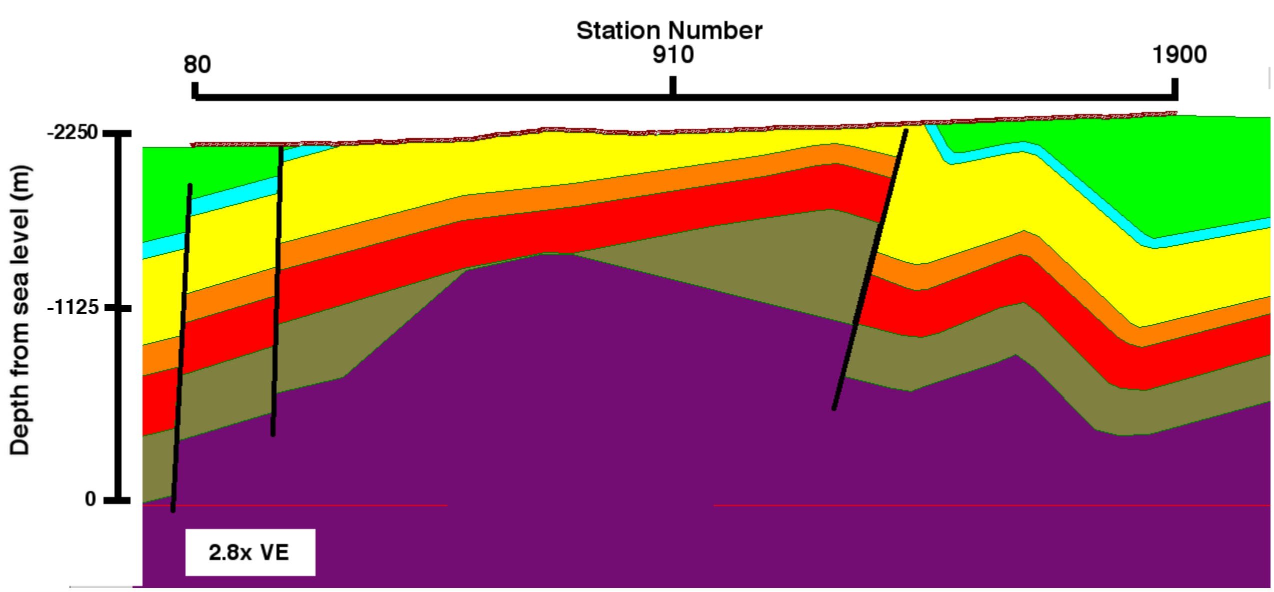

Figure 7. Final interpretation of gravity data, with a continuation of the Cutler formation as the low density zone mentioned in Figure 5.

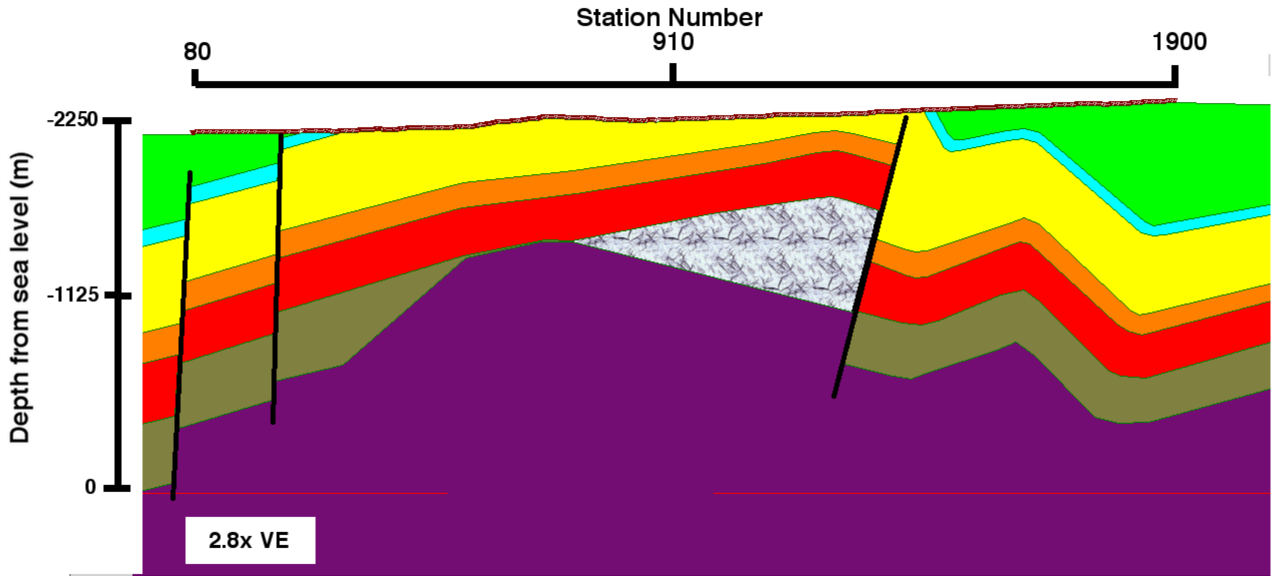

Figure 8. Final interpretation of gravity data, with a basement fracture zone as the low density zone mentioned in Figure 5.

2.2.1. *Error and Noise.* Noise during field data collection

- Failure to precisely level the gravimeter
- Failure to stomp base into the ground to ensure minimal movement of the gravimeter
- Wind, rain, or general weather that move the gravimeter
- People, cars, or animals standing or moving near the gravimeter
- Failure to close loop within five hours

Error during processing

- Improper drift correction – related to failure to close loop
- Failure to shift and match overlap points
- Incorrect elevation at each point
- Error in average crustal density

Infinite correct models exist that could fit the gravity data collected so information from other methods is required to determine the most accurate model.

2.3. Summary. The model described in Figure 5 incorporates gravity data, surface geology, well logs, and petrophysical data to describe subsurface structure. The model shows the general trend of the anticlinorium with some additional major features including a thrust fault around flag 1300, a normal fault around flag 300, and a previously unmapped low density zone. The low density zone is a perfect example of the non-uniqueness of gravity data interpretation. The potential hypotheses for the zone are either a continuation of the Cutler Group or a large bedrock fracture zone.

The continuation of the Cutler Group is a viable model because it was deposited as a complete layer before faulting and regional stress broke it into several pieces. The basement fracture zone could prove to be a source for the local geothermal system. The relatively high porosity of a fracture zone would allow for the storage and heating of fluids and the nearby thrust fault could act as a conduit for fluid movement to the surface.

The gravity method provides an additional model of the subsurface. Although gravity is a low resolution method, the results can be incorporated with methods such as seismic to ensure accuracy of time to depth models and horizon picks. Integration of gravity with other geophysical methods can constrain the model such that a unique solution is developed.

3. Transient Electromagnetics

3.1. Processing. Prior to any processing, the assumption is made that the EM-57 instrument is only measuring along a one dimensional profile of the subsurface beneath the center of the transmitter coil. Other TEM instruments are capable of measuring both the vertical and lateral components of the changing magnetic field. These components are neglected, however, in this investigation. A layered earth is presumed for the surveys conducted in the Chromo area. During processing, it is also assumed that the rate at which the current shuts off in the transmitter coil is linear. In the early time of the turn off, however, magnetic coupling within the transmitter causes nonlinear fluctuations in the current. The chaotic nature of the current can negatively affect the earliest time gates, leading to less reliable data for the 30 Hz survey.

The Geonics Protem receiver detects the induced voltage as an analog signal, and converts it to a digital signal. The signal is then stored in the internal memory of the Protem receiver. Data is transferred to a computer using a program called *ProtemW*, which exports the data as an ASCII file. SiTEM then imports the file and provides a user interface in which the data can be viewed. Next, the data for a particular survey is selected and saved from within the SiTEM program. Recorded voltage is then converted from milliVolts to Volts at predetermined time gates. The voltages at the respective time gates for each data set are then stacked together for a single survey and output into the **.tem* file. The file is then opened using Microsoft Excel and the voltages are converted manually to nanoVolts for each survey.

IX1D is used to invert the data and create models of the subsurface at the survey locations. The nanoVolt data is used as a primary input, along with the times representing the time of measurement acquisition at each gate. The inversion yields a one dimensional resistivity profile of the subsurface with respect to depth. For the low frequency data, there is a large amount of noise associated with the later time gates, so these data points are removed during the inversion process. In general, the last eight time gates are also removed from the low frequency data.

3.2. Results. The data for each site is inverted using IX1D, where prior geologic knowledge of the Chromo area is used to constrain the model. For each of the four survey sites, the high frequency (30 Hz) and low frequency (3 Hz) data sets corresponding to a specific survey loop are inverted together as one data set. Because transient electromagnetic data represents an average apparent resistivity of the subsurface, it is assumed that the results from analogous loops at the four sites should be correlated. Under this assumption, all data sets for a single survey location are inverted together, and only the data sets that closely follow the same trend are used for the final inversion of the respective site. The following results assume a five percent error in every data point, and act only as an approximate 1D resistivity profile of the subsurface. The nonuniqueness of geophysical inversion limits the accuracy and reliability of the models. This effect can be seen while using IX1D's equivalence analysis feature which provides alternative models that fit the data.

At the first survey site (shown in Figure 5) measurements were taken over seven loops. From the seven loops, five of the datasets were applied to the inversion. Geologic insight of the geometry of the Chromo anticline suggests the presence of an underlying layer of Mancos shale at this survey location. In Figure 9, a 1D inversion of the data shows a 100 m thick layer at the surface with a resistivity of approximately 200 Ωm, followed by a nearly 200 meter thick layer of more conductive material with a resistivity of 45 Ωm. Beneath that layer is an even more conductive layer that is 135 m thick and has a resistivity of 25 Ωm. At the very bottom of the model is the most resistive layer, located at a depth of approximately 435 m with a resistivity of 470 Ωm. The root mean square (RMS) error for this model was 15.15%. The geologic interpretation of this resistivity profile from the surface down can be described as: Mancos shale, saturated Dakota sandstone (conductive), followed by the upper Morrison formation.

At the second survey site displayed in Figure 6, measurements were taken over nine loops, two of which were used in the inversion. At this particular site, the surface geology was predominantly Lewis shale, with the Mesaverde cliffs to the east. These datasets were chosen because they trended in between an upper and lower bound of the other datasets, and thus were regarded as an appropriate averaged representation for the survey area. The inversion results shown in Figure 10 reveal an upper layer of more resistive material approximately 185 Ωm and 130 meters thick. The next layer is a thinner conductive layer of 40 Ωm at 30 m thick. Beneath this conductive layer is a relatively resistive layer that is 70 m thick with a resistivity of 320 Ωmeters. The fourth layer is a very resistive layer that is approximately 250 m thick, with a resistivity of 2,000 Ωm. The last layer of this model has a resistivity of 115 Ωm and extends beyond the depth of investigation. This model has an RMS error of 3.98%.

The basic geologic interpretation using this resistivity profile starting from the surface down consists of: Lewis shale, a potential conductive aquifer, Mesaverde sandstone, then a thick unknown resistive layer.

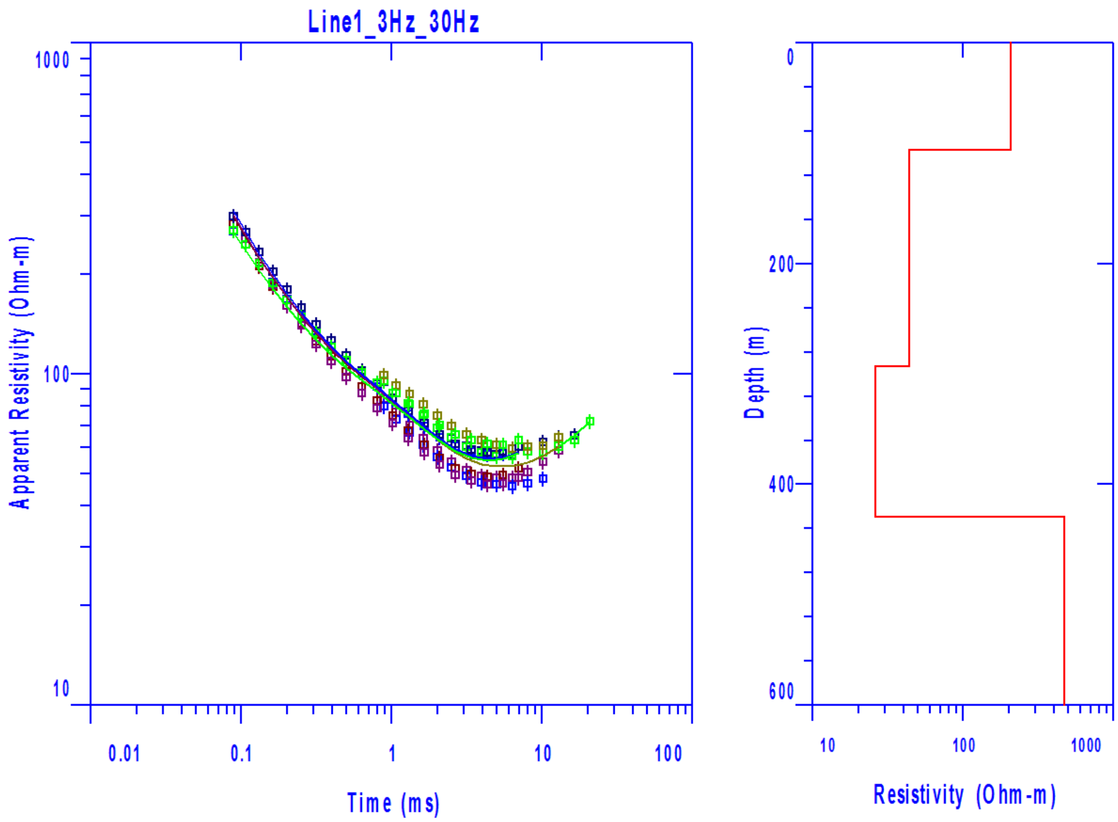

Figure 9. One dimensional resistivity profile at EM-57 survey site one

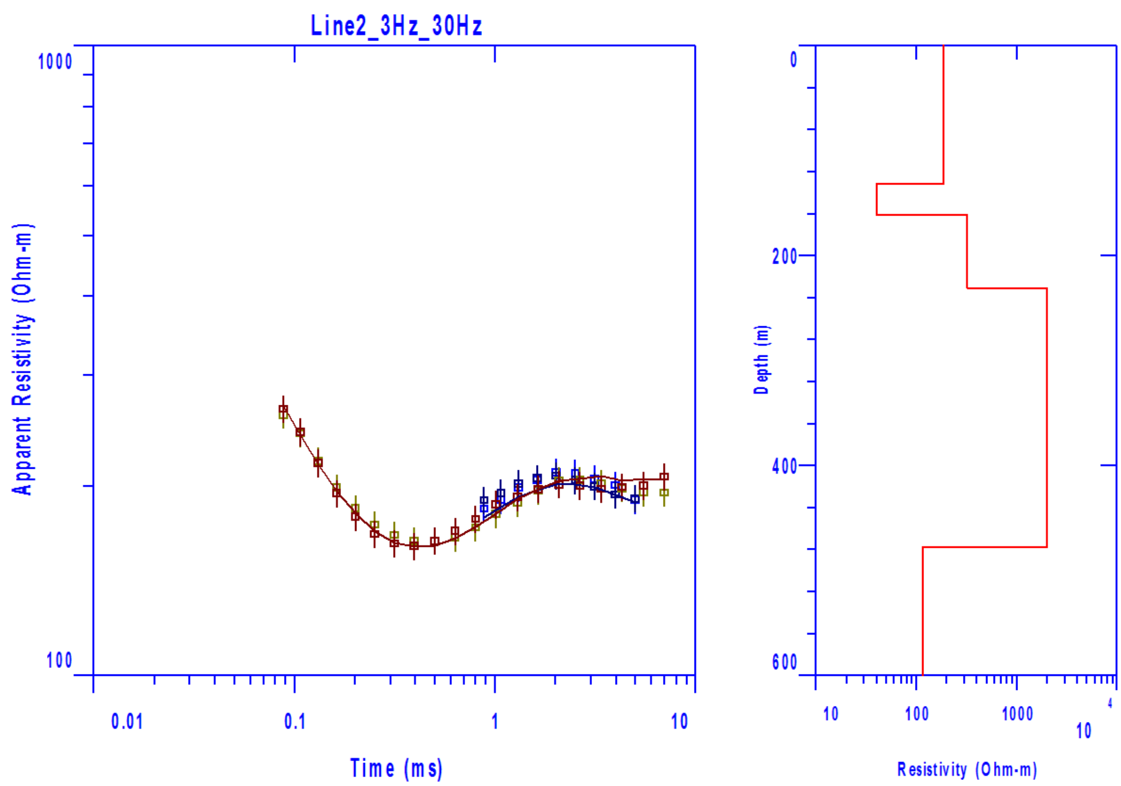

Figure 10. One dimensional resistivity profile at EM-57 survey site two

Site three can be found just north of Site 2, and is shown in Figure 7. There were four surveys conducted at this location, and three datasets were used in the inversion to construct the one dimensional resistivity model of the subsurface. The geology at this location was similar to the geology at Site two, with Lewis shale at the surface. Site 3 is approximately 30 meters higher in elevation than Site 2. Figure 11 shows the first layer in the model has a resistivity of 165 Ωmeters with a thickness of 150 m. Beneath the first layer, and much like the model in Site 2, there is a conductive layer with a resistivity of 50 Ωmeters that is approximately 25 m thick. The third layer at this site is identical to the third layer of the model for Site 2, with a thickness of 70 meters and a resistivity of 320 Ωmeters. This is underlain by a 200 meter thick layer of 2000 Ωmeters.The remainder of the model consists of a moderately resistive layer at a depth of 445 meters with a resistivity of 115 Ωmeters. The RMS error of this model is 4.48%. The geologic interpretation of this model from the surface down is interpreted as: Lewis shale, potential aquifer, Mesaverde, followed by an unknown resistive layer.

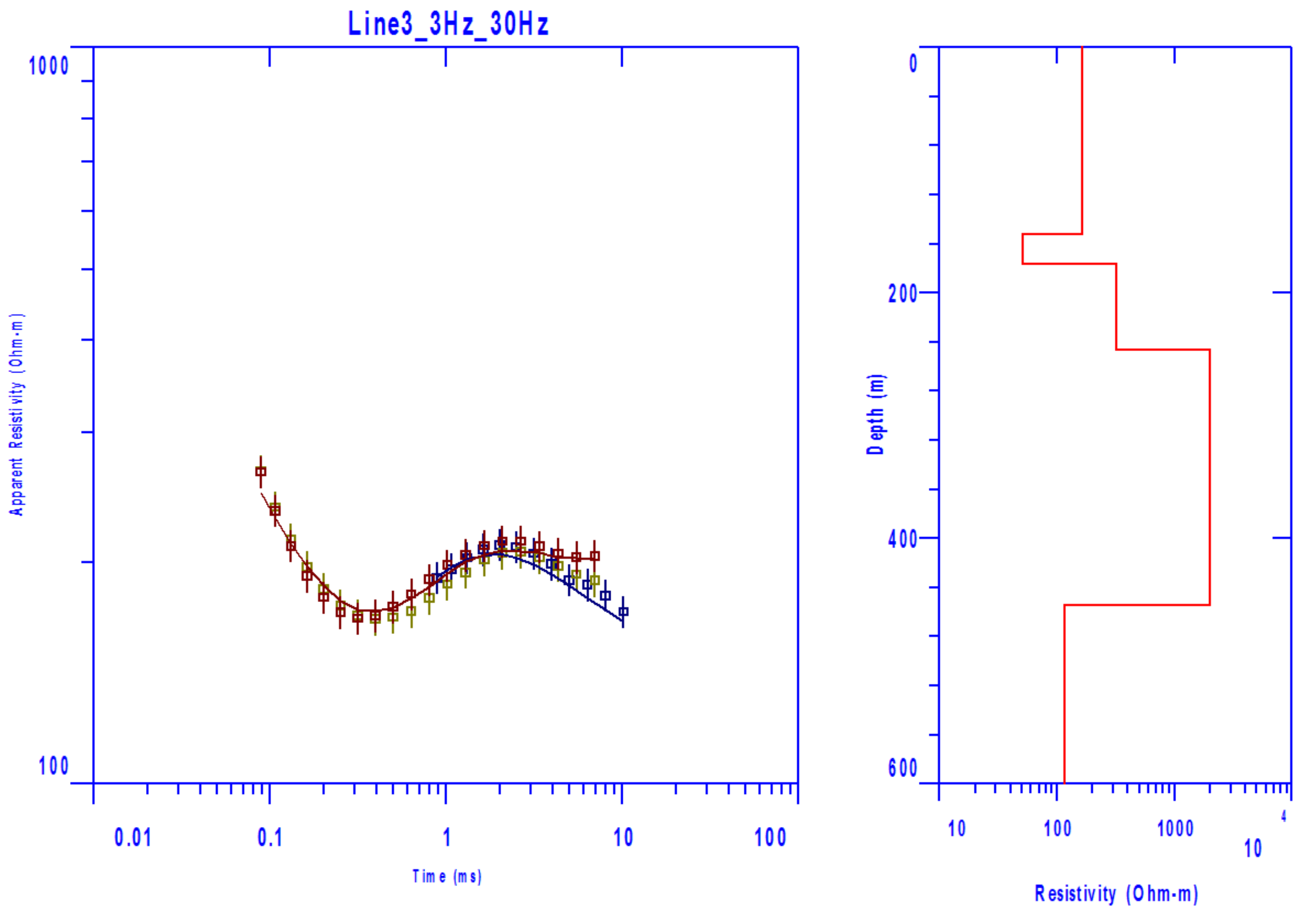

Figure 11. One dimensional resistivity profile at EM-57 survey site three

The fourth survey site was several kilometers north of Sites 2 and 3. There were five surveys conducted at this site, however one was neglected on account of inconsistent survey size. The geologic layer at the surface where the surveys were conducted was identified as the Lewis shale. Figure 12 shows the one dimensional resistivity model beneath Site 4. The first layer has a resistivity of 280 Ωmeters and is approximately 75 m thick. The second layer is the largest layer in the model at 470 m thick, with a resistivity of 140 Ωmeters. The underlying layer of the model is located at a depth of approximately 550 m and has a resistivity of 105 Ωmeters. The RMS error for this model is 3.39%. The resulting model at this survey location was interpreted to be the Lewis shale to a point beyond the depth of investigation. The top of the Mesaverde is visible around 600 m but that is also the depth of which the instrument can no longer take reliable measurements.

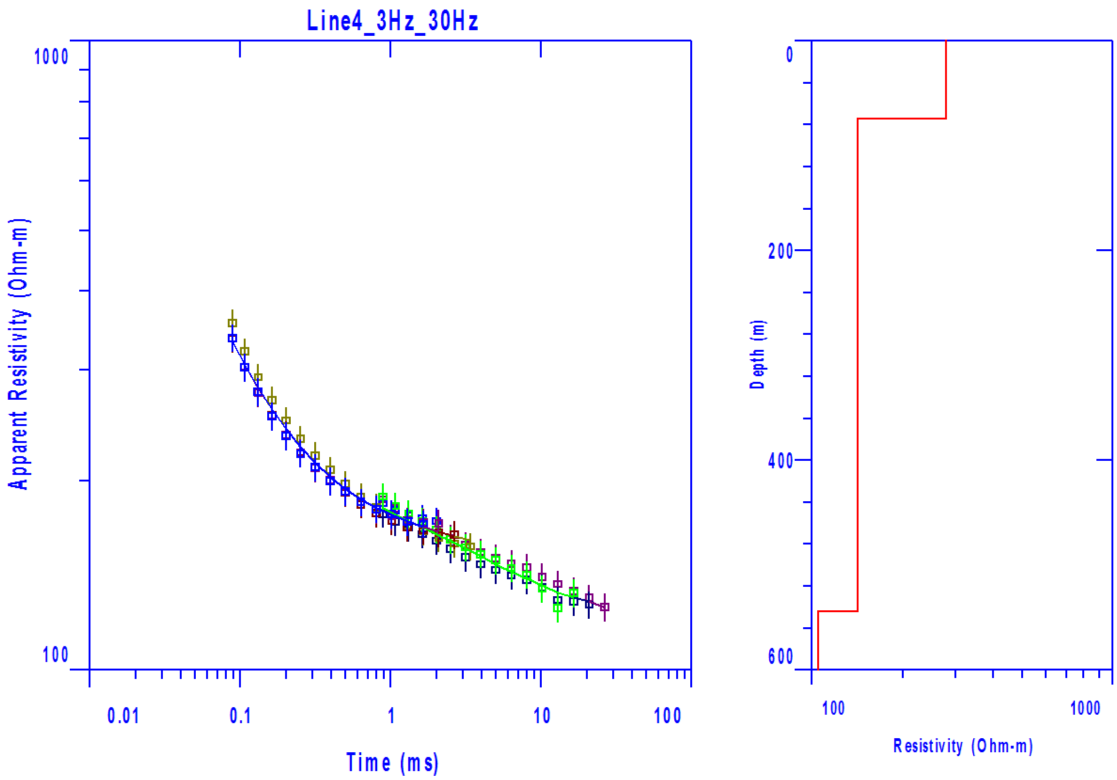

Figure 12. One dimensional resistivity profile at EM-57 survey site four

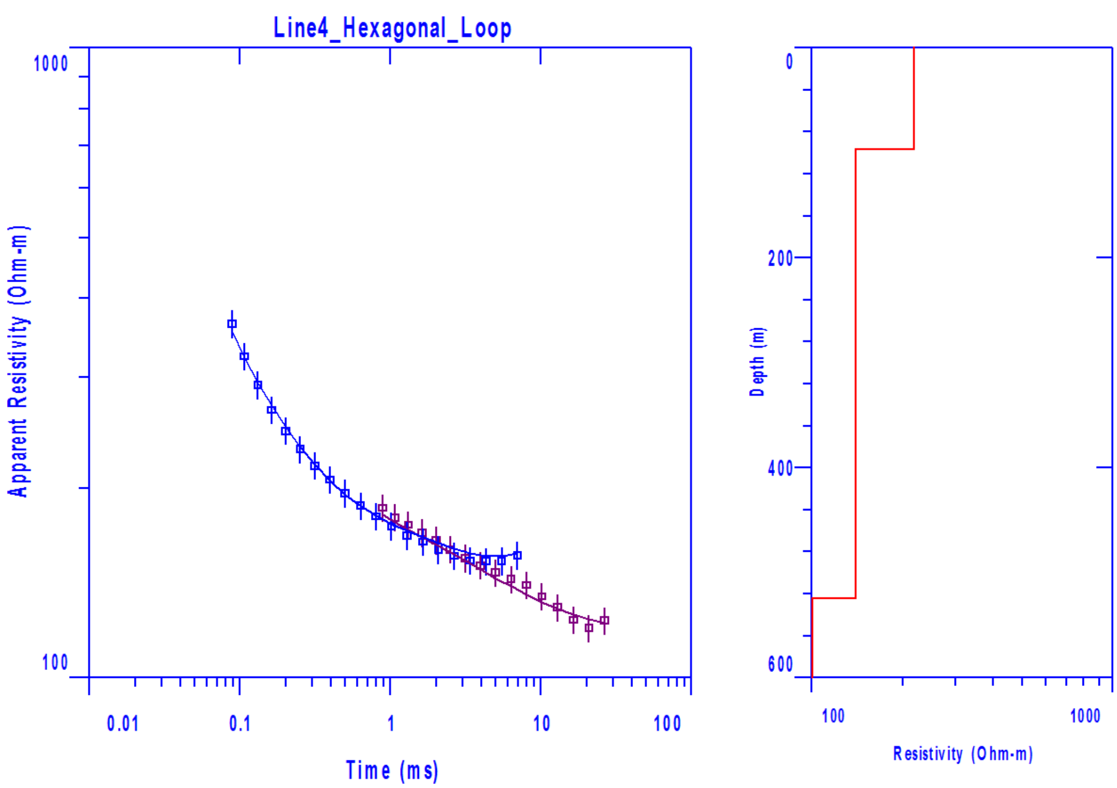

Figure 13. One dimensional resistivity profile at EM-57 survey site four. Hexagonal transmitter loop.

The larger, hexagonal survey conducted at the fourth site provided the benefit of added resolution at depth; however, the resulting resistivity model differs very little from the other four normal 100x100 meter loop surveys at the same location. Figure 13 below shows the resistivity profile at depth. The upper layer is approximately 100 meters thick with a resistivity of 220 Ωmeters. The second layer has a resistivity of 140 Ωmeters and is 430 m thick. The underlying layer has a resistivity of 100 Ωmeters. The RMS error for this model is 2.69%. This model confirms the interpretation from the smaller loop surveys conducted at Site Four.

3.3. Sources of Error. In the field, many factors can affect the quality and reliability of acquired data. For TEM in particular, the 60 Hz frequency emanating from power lines can have adverse affects on the data collected. The EM-57 is equipped, however, with built-in noise processing which can effectively remove this effect at the time of data acquisition. Another source of error in the field is the survey setup: the transmitter loops were constructed using a combination of measuring tapes and handheld GPS units. If the measuring tapes were not pulled completely tight or they did not measure a straight line between two loop corners, the flags would ultimately be closer than 100 m apart. Furthermore, the handheld GPS units are only accurate up to one meter. The presumed transmitter area of 10,000 square meters is therefore an approximation of the actual size. Other errors that may have influenced the data include noise caused by the generator and the background telluric noise.

3.4. Summary. TEM plays an important role in characterizing the underlying electrical conductivity structure in the Chromo anticline. The method provides key information that can help characterize the subsurface in the 100-600 m range. The initial 100 m for the TEM surveys is considered erroneous and unrepresentative of the actual geology. TEM provides support in the construction of a stratigraphic column which can then be used to locate the transitions between geologic units. For the second and third survey areas, an unexpected resistive unit appeared after inverting our data for those sites. This resistive unit doesn't match with the predicted geologic model and should be the subject of further investigation.

4. Magnetotellurics

4.1. Data Processing.

4.1.1. *Description of Raw Data.* The raw data returned by an MT survey includes the orthogonal components of the electric field, **E** (V/m), and free Magnetic field, **H** (A/m). The frequency values for each measurement are also collected, but the results are originally provided as a function of time. In order to find the resistivity of subsurface layering, several steps must be taken in the form of preprocessing, processing, inversion, and interpretation. The preprocessing consists of digitally filtering the time series data from each site to show the collected frequency values of the EM plane waves over time. Large spikes and noise are also removed before processing. When the data is determined sufficient, the time series for each frequency filter is processed by calculating the ratio of orthogonal magnetic and electric field amplitudes. As a result, 1D pseudo depth profiles of apparent resistivity and phase are plotted as a function of frequency. The apparent resistivity is determined as the average of resistivity values within the depth of investigation. In order to find a resistivity profile as a function of depth, the data must be run through an inversion program to determine a reasonable model that suits the 1D profile. The interpretation can be further tied to the known geologic structure and results from other methods nearby.

4.1.2. *Assumptions.* The geologic structure along the main line west of Chromo, CO is a broad, shallow dipping anticline. For the sake of simplicity and lack of time, the MT survey and processing parameters were chosen assuming a 1D layered subsurface. Thus, the assumption of zero coupling of the **E** and **B** fields in parallel directions is also implied ($Z_{xx} = Z_{yy} = 0$). Additionally, the inversion models and interpretation of MT surveys rely largely on the constraints of known geologic structure and resistivity values. The values applied to the interpretation were provided by Andre Revil in his paper concerning the plumbing system of the Pagosa thermal Springs in Table 2 [**11**]. Stratigraphic column data from the Colorado Oil and Gas Conservation Commission (COGCC) also provided local thicknesses of the geologic formations [**31**]. Well log data directly analogous to the MT sites were also referenced to focus on the geology specific to those locations (see Appendix 10.1).

Formation	ρ (**Ωm**)	**Thickness (m)**
Lewis Shale	20	650-700
Mesaverde S.S.	200	70
Mancos Shale	30-Oct	600
Dakota S.S.	400	70
Top Morrison	100	150
Bottom Morrison	300	140
Crystalline Basement	10,000	—

Table 2. Geological Restraints

Another assumption pertinent to the quality of data interpretation and processing is the vertical incidence of the electromagnetic plane waves at the site of acquisition. This is consequential of the sources originating at distances great enough to neglect oblique influences. Nearby sources of electromagnetic energy, power lines specifically, emit a constant signal at a frequency of 60 Hz that is picked up by the survey setup. If the survey is too close to power lines it decrease the signal to noise ratio.

4.1.3. *ViewMT.* When the ADU is finished recording, the data is exported to a field laptop for initial inspection to determine whether the measurements are reasonable. Seemingly legitimate data shows smooth trends in all four $\mathbf{E}_x$, $\mathbf{E}_y$, $\mathbf{H}_x$, and $\mathbf{H}_y$ channels for a time consistent with what was originally selected in the ADU parameters. If determined sufficient, the data files are then named accordingly and saved where they can be imported into Mapros.

4.1.4. *Mapros.* The data is imported into Mapros such that the roaming and reference stations are distinguished between as separate survey lines. Under each survey line, an MT site is created for each set of data where the **E** (electric) and **H** (magnetic) channels can be digitally filtered for 512 Hz, 128 Hz, 32 Hz, 8 Hz, 2 Hz, and 2 s. The time series for each site at all frequencies are then viewed and erroneous points are manually marked to be ignored during processing (see Appendix 5.5.1). Each frequency band is then selected and run through the program's default processing function which returns apparent resistivity and phase curves as a function of frequency (see Figure 14). Two processing functions are run for each site where the Overlapping Blocks and Ignore Marked Points options are selected. The first processing is a selective stack of the individual data set, while the second processing applies a correction with the associated remote reference site. If the quality of the data is insufficient, the frequencies with problematic noise are remarked for data anomalies in the time series. Once the resistivity and phase curves are satisfactory, the two processed datasets for each site are exported as ASCII files to be imported into Excel.

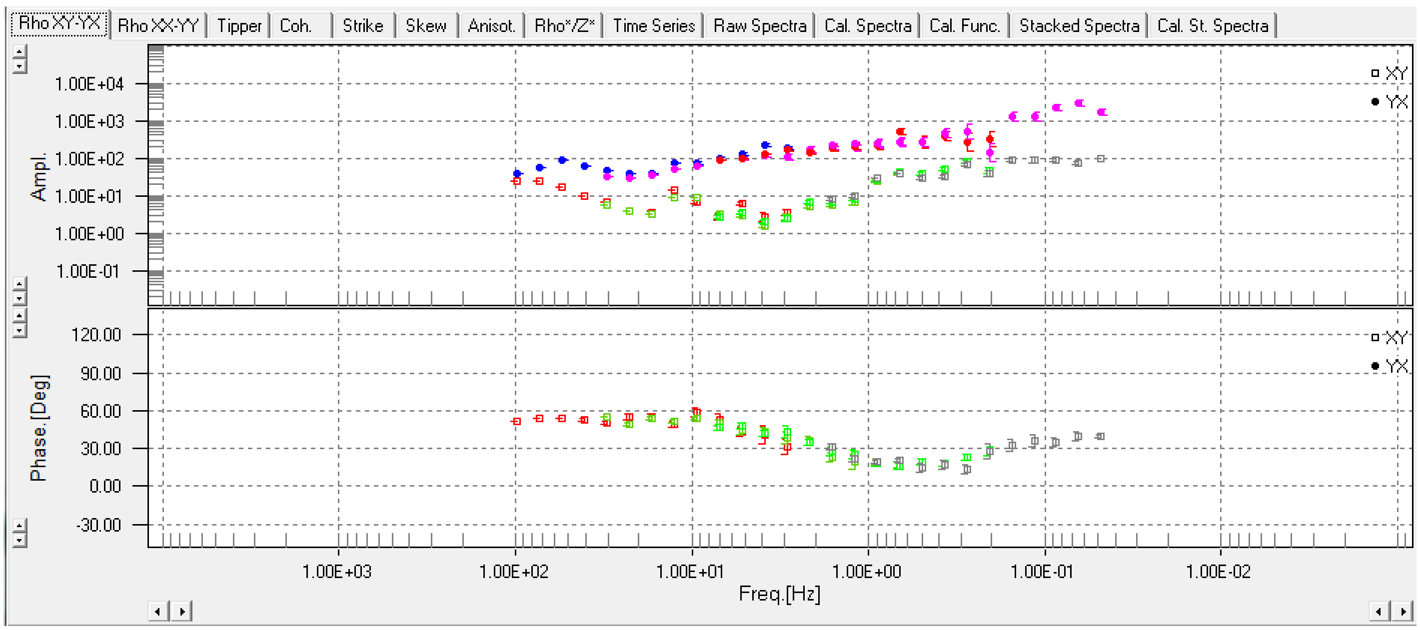

Figure 14. Apparent resistivity and phase curves vs frequency are plotted for Site 4 as a result of the Mapros processing function. The different colors are representative of the four frequency bands that were used in the inversion and interpretation. The hollow / filled data points differentiate between the yx and xy components of the apparent resistivity tensor.

4.1.5. *Excel.* Excel acts as a platform on which apparent resistivity, phase, impedance, and frequency data can be quickly plotted and manipulated by hand. The points in the ASCII file include 26 columns for each data point exported from Mapros (see Appendix 5.5.2). The frequency bands which were digitally filtered in Mapros are also clearly defined. A quick plot of apparent resistivity vs frequency for each band is plotted for both the select stack and remote reference data in a log-log scale. The dataset processed using the remote reference site is typically of higher quality, and therefore the select stack data is often disregarded. Between bands, there are often up to three overlapping data points that were calculated for the same frequency value in Mapros. The primary task in the Excel processing is to converge these points with a weighted average that best fits the resistivity and phase curves with minimal variance (see Figure 15). This averaging task is completed for each phase and resistivity dataset in order to plot a continuous curve as a function of frequencies. To achieve a relatively smooth plot, the significantly anomalous points in the data are further removed. For each data point in the phase and resistivity curves the standard deviation is calculated as the square root of variance. The error associated with each point is then defined as two standard deviations above and below the value of a data point (see Appendix 5.5.1) for a more in depth explanation). The phase and resistivity curves and the respective error values are then exported to Ipi2win for inversion.

Site 4:

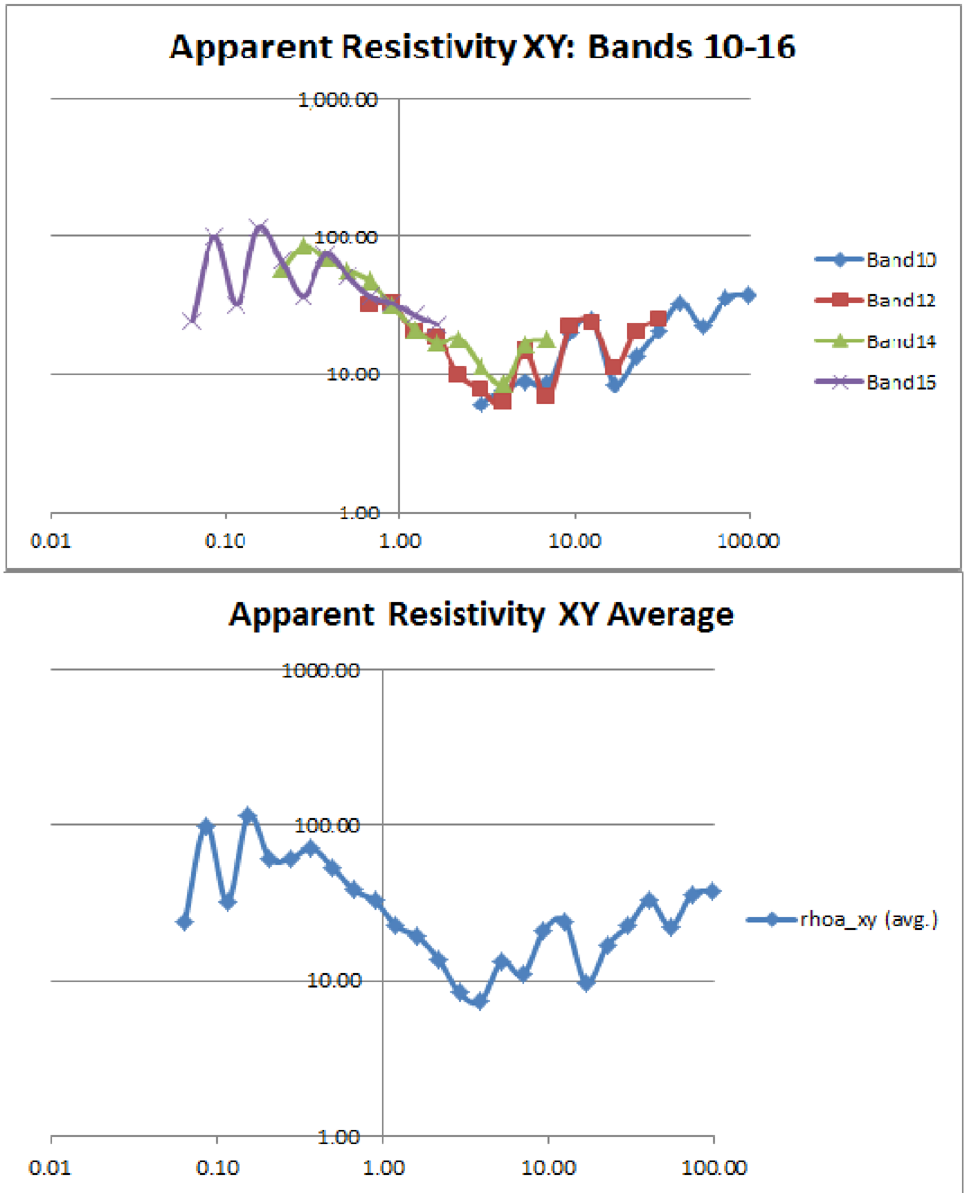

Figure 15. The xy apparent resistivity curve is plotted for the four applicable frequency bands. (a) shows the raw plot of the data at site 4 while (b) shows the post-averaging resistivity curve.

4.1.6. *Ipi2win.* Ipi2win acts as a one-dimensional inversion program on which a model of the subsurface according to apparent resistivity and phase data can be determined. To import data into the program, it must first be written in the specified Ipi2win format in Excel. This format includes columns of the square root of the period (a modified form of frequency), resistivity, the error associated with resistivity, phase, and the error associated with phase. As a result of Ipi2win acting strictly as a 1D platform, the $\mathbf{E}_x/\mathbf{B}_y$ datasets are distinguished from the $\mathbf{E}_y/\mathbf{B}_x$ datasets as separate files. The data (error bars) are then plotted beneath a resistivity vs depth model (blue) along with apparent resistivity and phase curves that are determined by that model (red). Figures 16-20 show examples of the generated plots. The objective of processing in Ipi2win is to fit the model to the data such that the predicted structure is geologically plausible. In this inversion, the amount of layers is limited in the subsurface to six at sites 4-6 and four layers at sites 1-3. These values were determined by site position relative to the anticline. Ipi2win offers an inversion option that builds a geologic model to best fit the resistivity curve with the specified amount of layers. Due to unrealistic depth and resistivity values, the inversion built models are not included in the results. Models are also built by manually entering layer thickness and resistivity values to best fit the curve. Once an initial model is constructed, the structure is modified one parameter at a time to adjust the fit of the curve. The final models included below are a compromise between the incorporation of a geologically plausible explanation and the fit of the forward model relative to apparent resistivity and phase data.

4.2. Results.

4.2.1. *Modeling Results.*

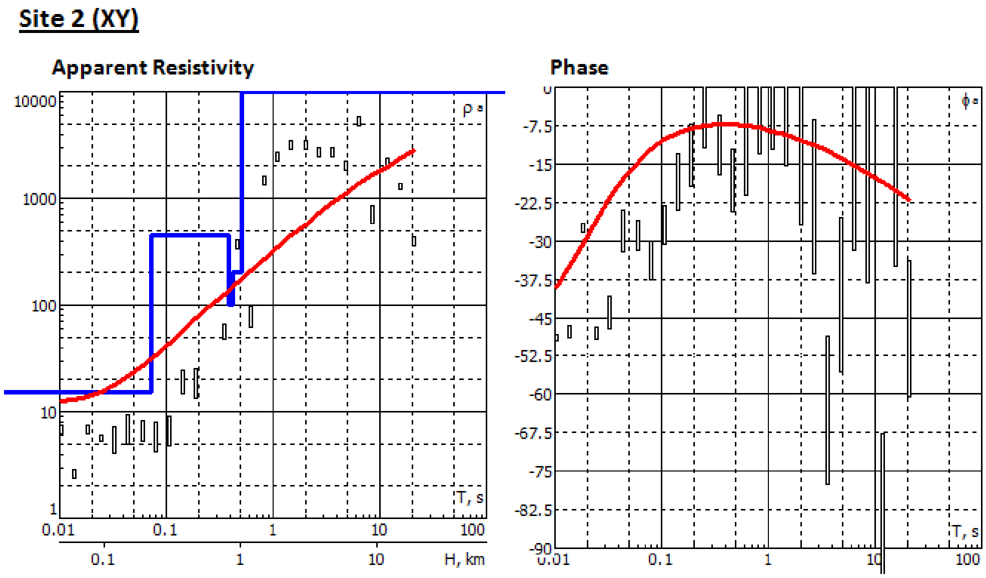

Figure 16. The geologic model for site two is predicted. ρ_{axy} (a) and ϕ_{xy} (b) data are represented by the hollow error bars, and the subsurface layering structure and associated resistivity values are shown in blue. Red shows the forward model associated with that geologic structure.

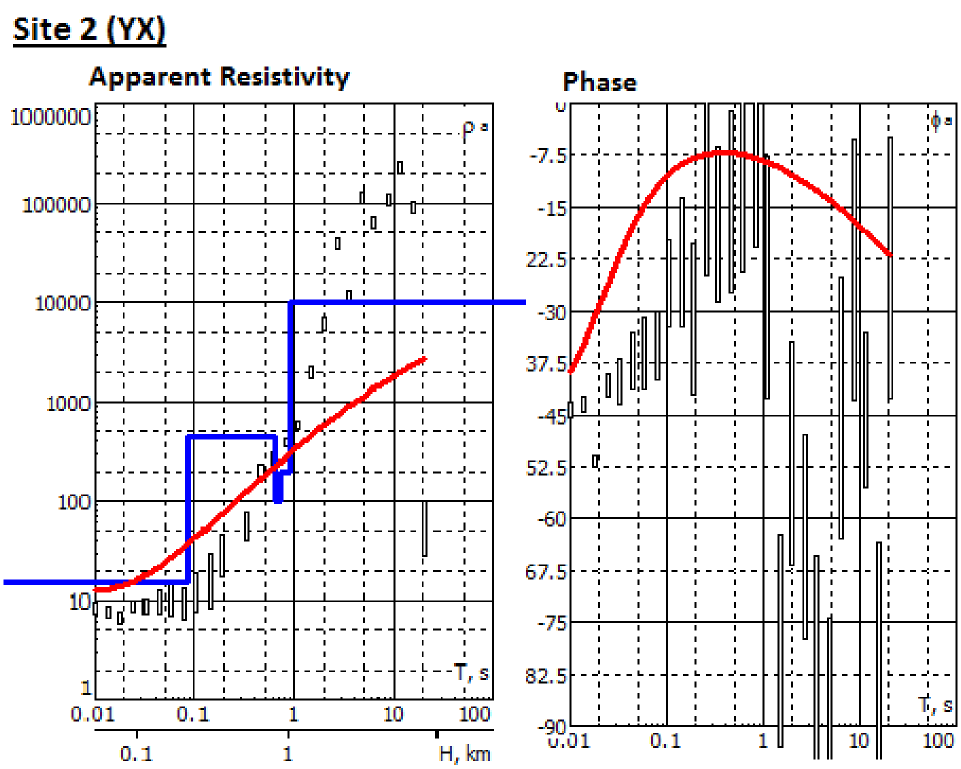

Figure 17. The geologic model for site two is predicted. ρ_{ayx} (a) and ϕ_{yx} (b) data are represented by the hollow error bars, and the subsurface layering structure and associated resistivity values are shown in blue. Red shows the forward model associated with that geologic structure.

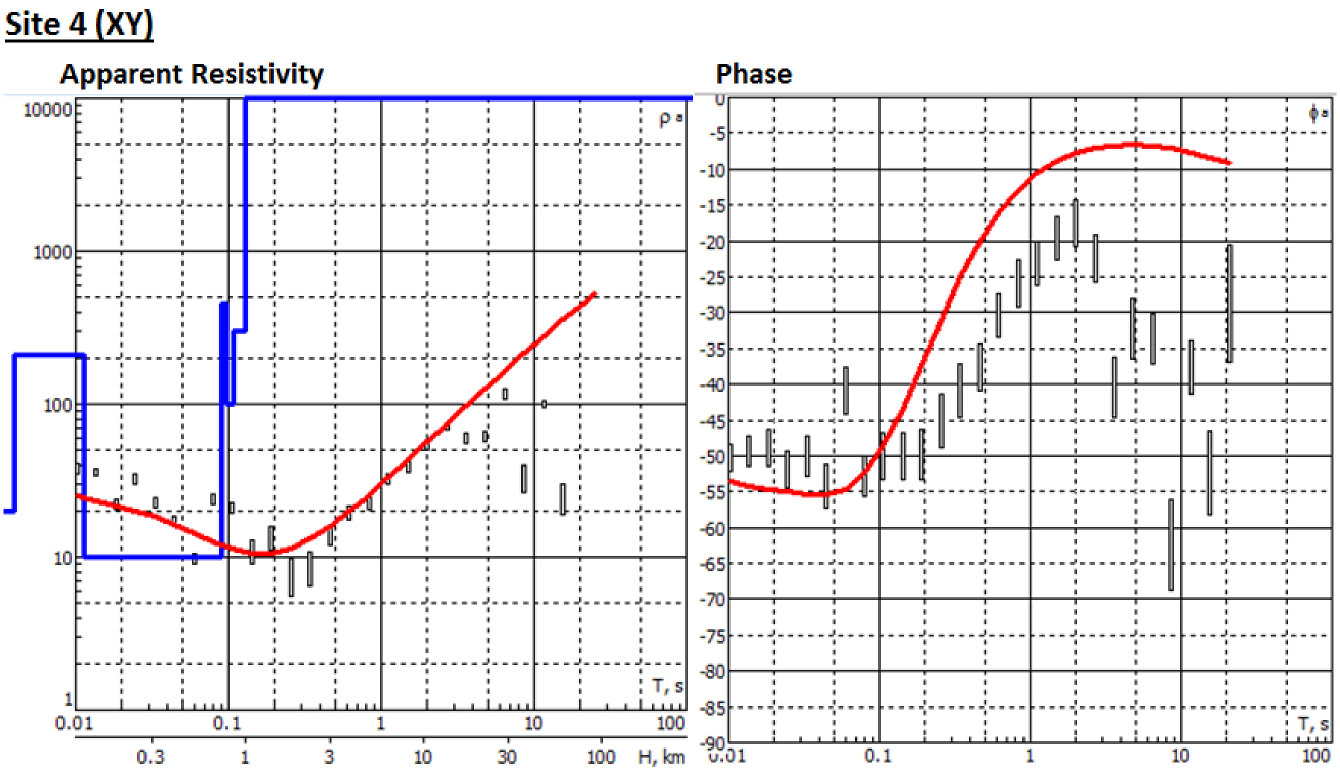

Figure 18. The geologic model for site four is predicted. ρ_{axy} (a) and ϕ_{xy} (b) data are represented by the hollow error bars, and the subsurface layering structure and associated resistivity values are shown in blue. Red shows the forward model associated with that geologic structure.

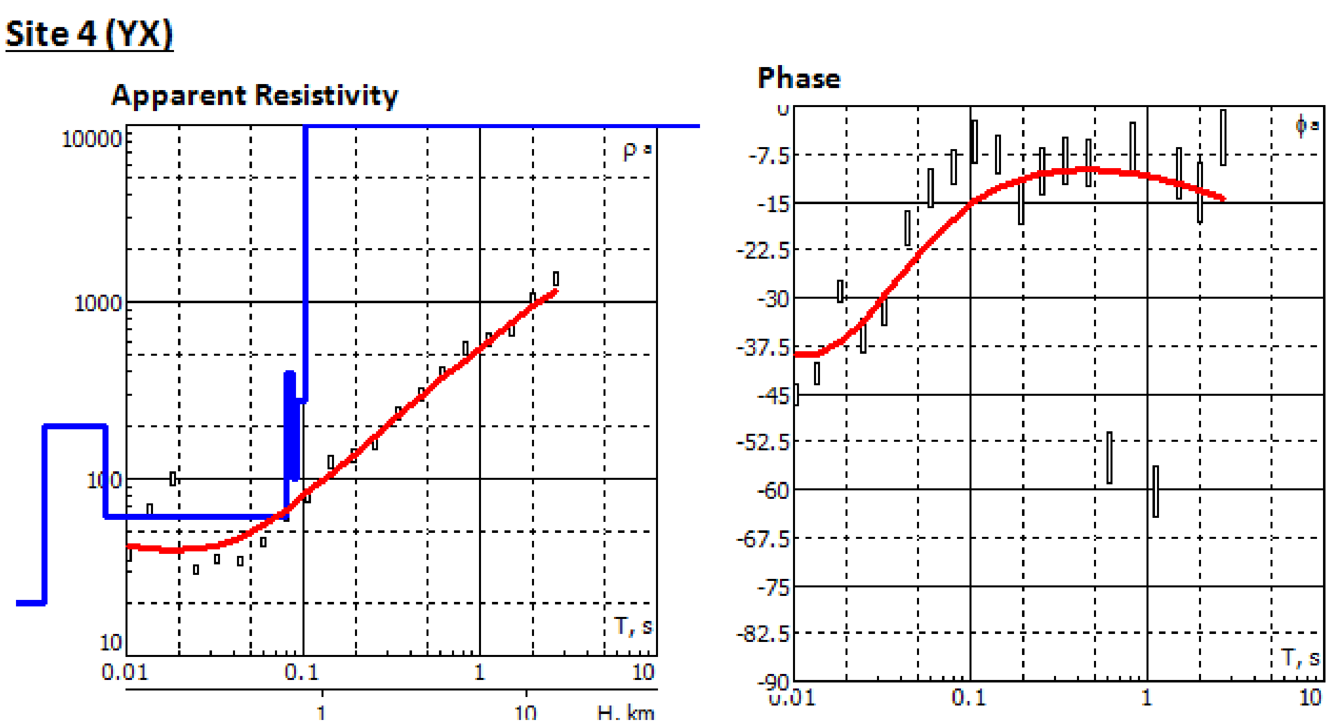

Figure 19. The geologic model for site four is predicted. ρ_{ayx} (a) and ϕ_{yx} (b) data are represented by the hollow error bars, and the subsurface layering structure and associated resistivity values are shown in blue. Red shows the forward model associated with that geologic structure.

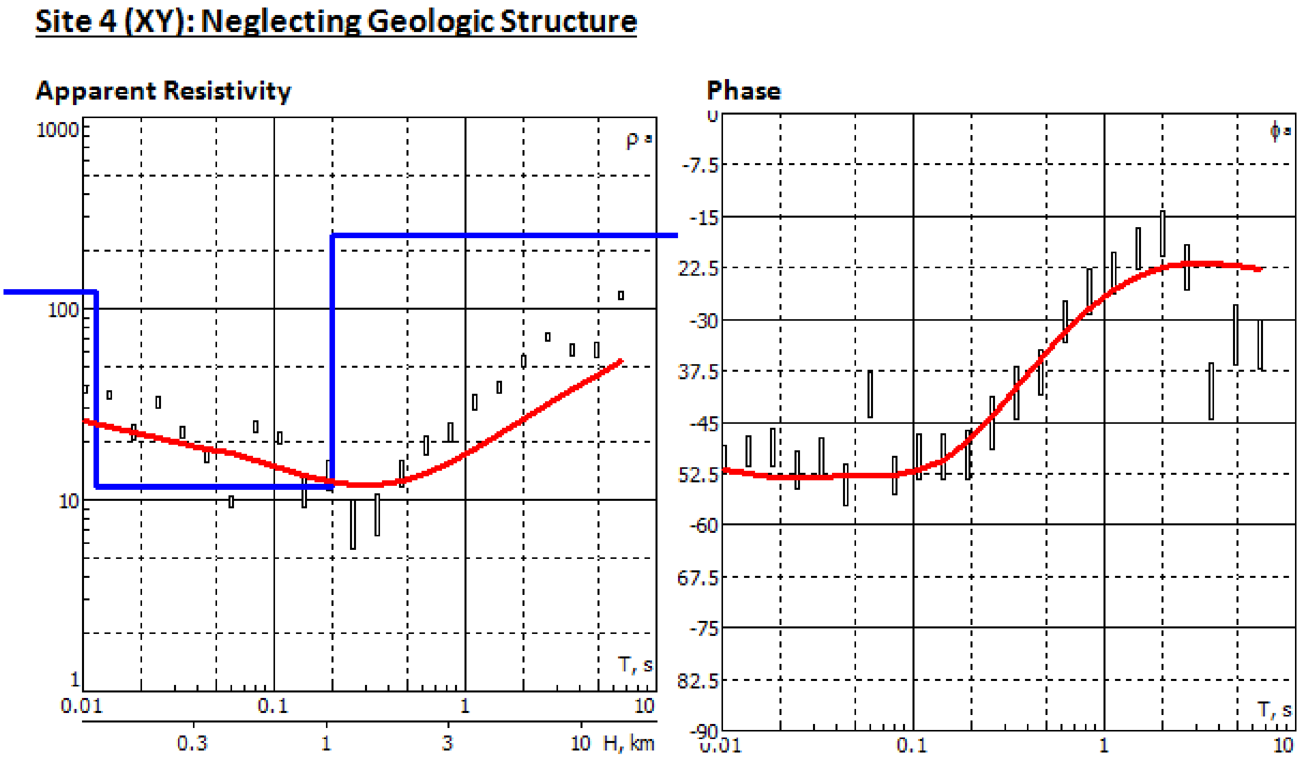

Figure 20. The following 1D model was created to fit the yx component of the Site 4 data, disregarding geologic structure. This illustrates that MT interpretation is limited by its vertical resolution and shows the necessity of having to constrain the data with the geology.

4.2.2. *Interpretation.* The interpretation of the apparent resistivity and phase curves collected at Site 2 and Site 4 are provided in Figures 16-19 where three curves are included in each plot. The original measurements and associated error are shown in black, a 1D geologic structure with regards to resistivity and depth is shown in blue, and the resulting forward model of the layered structure is shown in red. The final models of Site 2 and Site 4 are largely constrained by stratigraphic columns and nearby well log data (see Table 2 and Appendix 10.1). The known resistivity values of these formations were also referenced in the inversion process. Tables 3 and 4 also show the final values associated with the geologic structure that best fits the processed data.

Formation	Resistivity (Ω*m)	Thickness (m)	Depth (m)	Top Depth (m)
Mancos	15	220	220	0
Dakota	450	60	280	220
Top of Morrison	100	70	350	280
Bottom of Morrison	200	140	490	350
Basement	10000			490

Table 3. Site 2 Interpretation

Formation	Resistivity (Ω*m)	Thickness (m)	Depth (m)	Top Depth (m)
Lewis	20	50	50	0
Mesa	210	75	125	50
Mancos	10	600	725	125
Dakota	450	60	785	725
Top Morrison	100	70	855	785
Bottom Morrison	300	140	995	855
Basement	10000			995

Table 4. Site 4 Interpretation

The results of these surveys serve the purpose of confirming the predicted geologic structure of the anticline local to Chromo, CO. The inversion model was initially constructed based on layering assumptions at two distinct locations on the anticline. The model was then modified to better fit the data. In the case of Site 4, the xy and yx data are not well correlated (see Figures 18 and 19). This is likely due to the presence of a 2D structure at the site location. The xy data was used to construct the geologic model because the apparent resistivity and phase curves made more sense with regards to prior geologic information. Figure 21 shows a plan view image of Site 4 which lies between a large normal fault to the east and Archuleta Mesa to the west. The effects of these formations are seen in the yx data as a result of the perpendicular orientation of the Ey channel with respect to the 2D structures. Vertical interfaces experience charge build up along geologic boundaries that couples with, and therefore increases, the electric field of the perpendicular orientation. This charge build up results in exaggerated apparent resistivity values in the Ey/Bx direction because of the east/west orientation of the Ey channel. The xy and yx data at Site 2 show nearly equivalent results, showing that the subsurface, as predicted, can be described as a 1D layered earth.

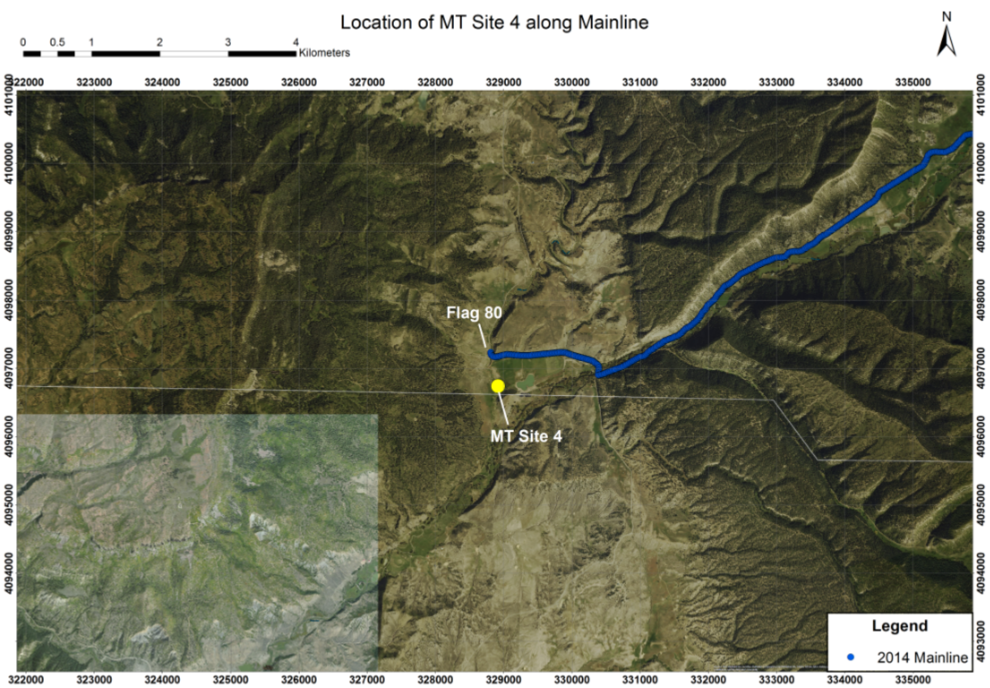

Figure 21. The location of Site 4 relative to bounding topographic structures to the east and west is shown. The geologic boundary is seen as the contrast in vegetation density.

4.2.3. *Error and Uncertainty.* MT surveys are designed to collect and measure all electric and magnetic field signals at a given site. Consequently, the effects of power lines, lightning, and nearby cars are all picked up by the electrodes and magnetometers. By linking the reference and remote reference data in processing it is possible to remove a significant amount of noise, with some erroneous points remaining in the results. In Mapros, there is a tool which allows a user to eliminate data points that deviate from the consistent trend in each channel. While not all noise can be effectively removed, taking out obvious anomalies further constrains the standard deviation of the data.

Human error adds a significant component to the uncertainty in MT field acquisition and processing. In the field, uneven ground and obstacles often prevent precise placement of electrodes and magnetometers. The equipment was also succumbed to inclement weather and wildlife, which led to disconnected channels at site 3 and several battery failures at the reference site. Consequently, several hours of roaming data were lost and remote referencing for the first two sites could not be applied in processing. The tedious tasks associated with data manipulation in Mapros and Excel make an additional contribution to human error in the final results. In Mapros, there is a level of judgement required to remove noise while not eliminating legitimate signal. The processing in Excel and Ipi2win requires the user to select the best fitting data points and forward model by hand, which adds an additional level of judgement to the result.

As a result of the 1D layered earth assumption associated with this interpretation, 2D and 3D structures in the subsurface contribute an additional error in processing. When telluric current passes through a 2D structure it causes electrical charges to build up on the interface. Consequentially, a secondary electrical current is generated and influences the measured electromagnetic fields. Depending on the nature of the 2D anomaly and survey orientation, the structure attributes to a static shift between the ρ_{xy} and ρ_{yx} curves generated in processing. In order to understand the shift, if a 2D model is assumed, a rotational matrix is applied to orient the data according to the structure. In the case of this survey, the measures to understand static shifts were neglected as a result of limited time and the assumptions made in processing. A program that could model 2D magnetotelluric surveys would be able to better model the subsurface and better support the other methods used.

4.3. Processing Summary. The apparent resistivity and phase curves generated by the 1D geologic model fit well with the recorded field data. The $\mathbf{E}_y$ channel at Site 4 is an exception and can be explained by a 2D effect caused by the bounding features of Archuleta Mesa in the west and large normal fault in the east. The non-unique character of magnetotelluric data leads to significant uncertainty in a stand-alone model. These results are useful nonetheless such that they are capable of supporting the data found by local efforts. The depth of individual layers will likely provide the most support for identifying horizons in the deep seismic section and density contrasts in gravity data along the main line.

5. Direct Current Resistivity

5.1. Processing.

5.1.1. *Raw Data.* The raw data is displayed as apparent resistivities at pseudo-depths in Figure 22. In this image it is difficult to definitively interpret the subsurface along the main line. There is evidence to suggest more than one layer in the subsurface, one of which is more conductive. The depth of investigation is approximately 220 m so it is possible that details of the layers beneath this conductive layer will not be imaged. The excess noise present, and a topographic correction not put into place, will cause an inaccurate interpretation based off this image. For these reasons, it is critical to process raw data before making interpretations.

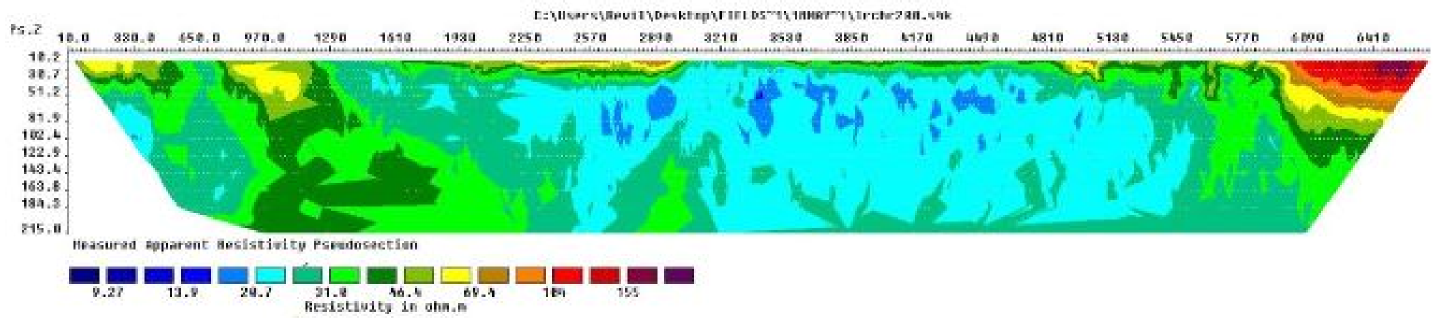

Figure 22. In this figure we see a pseudo-section plot of the raw data. High resistivity is indicated by red values and low resistivity is shown with blue values. In this image it is difficult to discern what the subsurface looks like.

5.1.2. *Data Reduction.*

(1) Reject the negative resistivity values.
(2) The topography needs to be added to the end of the data file.
   (a) Type a '1' on the line below the end of the data, hit 'Enter', type the number of elevation points, hit 'Enter', insert the topography data next.
   (b) Make sure the four zeros that indicate the end of the entire file are after the topography data.
(3) Open RES2DINV.exe (inversion software) and import the .dat file that was created during the downloading process. To do this click "File" → "import data file" →
(4) To remove data points that are not acceptable click on "Edit" → "Exterminate bad datum points". Look at the data and select the datums that appear as spikes or outliers. Exit the display window and save the new data file as a .dat file with a different name.
(5) Run an inversion to examine the changes in the data. Once this inversion is complete there will be an opportunity to remove more data points using a histogram depicting percent error values. To utilize this data reduction method go to the display window by clicking "Inversion" → "Display inversion". Click "Edit Data" → "RMS Error Statistics" to display the histogram. Move the vertical green line on the histogram to the desired highest value of percent error, and all the data to the right will be removed. Upon exiting the histogram window save the new .dat file with a new name.
(6) Reload the new .dat file from step 4 and run the inversion again. Steps 3 and 4 can be repeated as many times as it takes to get a data set you are content with.
(7) Removing the data points with high percent error does not account for large quantities of bad data. This is most effectively done with a smoothing or despiking filter.
   (a) Note that this can be done as preprocessing as well. In this case we used both a despiking filter and a median filter to preprocess the data.
(8) Invert the data again and analyze it to see if further processing is required.

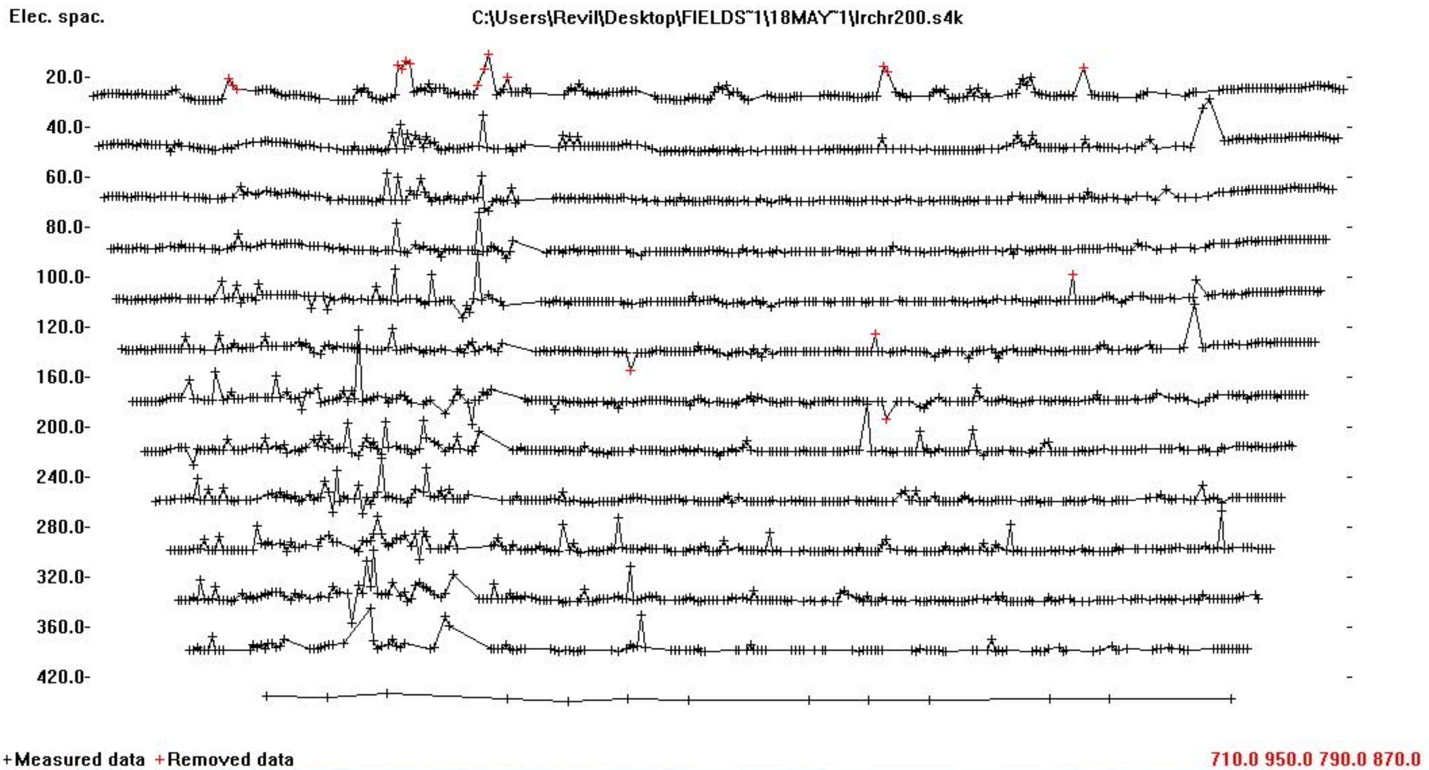

Figure 23. This is a figure of the "bad data elimination" screen. This is an image of our main line DC resistivity data. This screen was used to manually remove bad data.

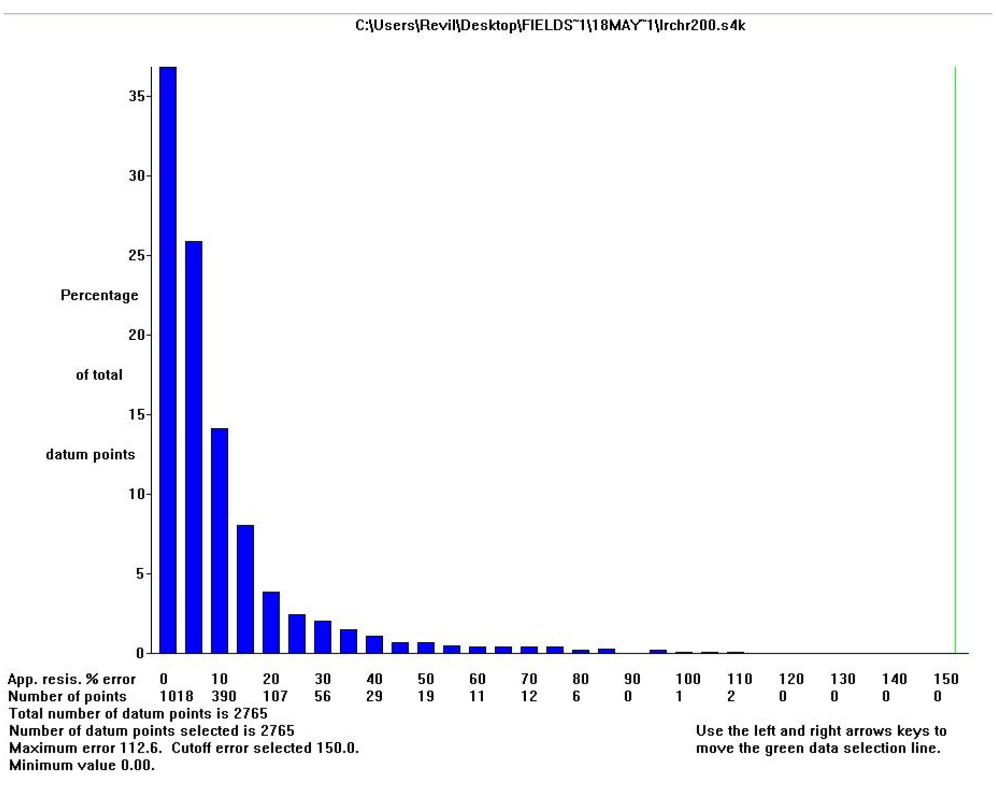

Figure 24. This is a figure of the histogram representing the distribution of the apparent resistivity data points based on their associated percent error values. The data points with high error values should be removed. It is up to the user to decide what the acceptable error values are.

5.2. Results and Interpretation. After processing the DC Resistivity data we obtained the results shown in Figure 25.

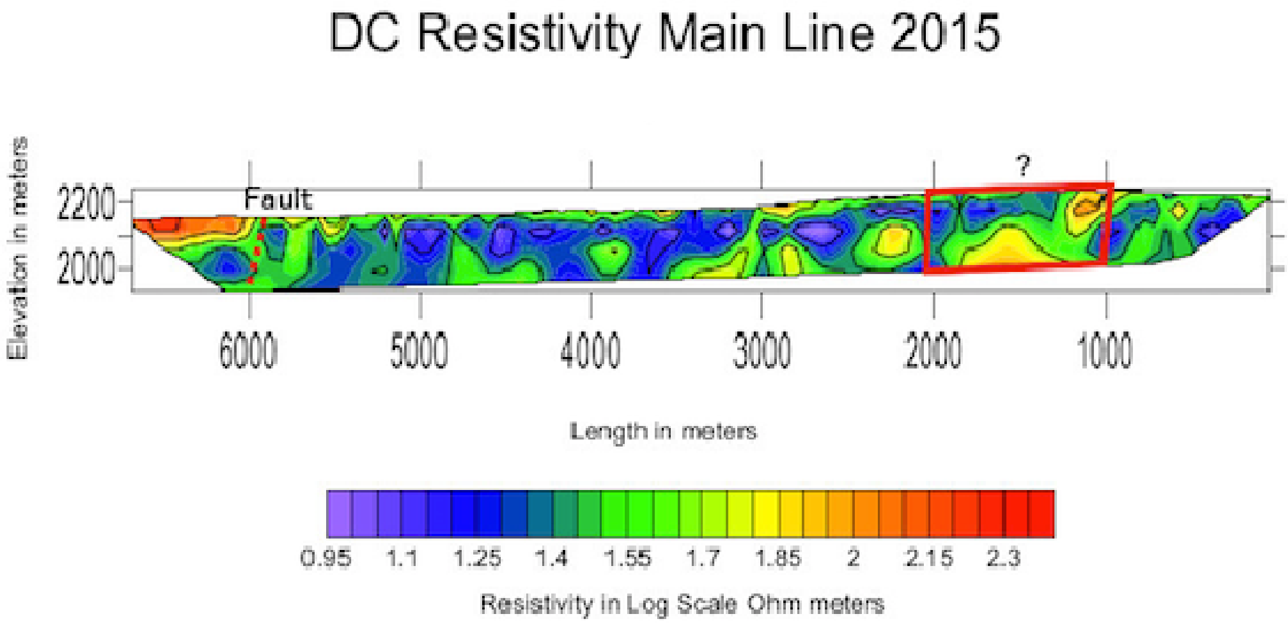

Figure 25. This is the final inversion of 2015 main line. Areas of high resistivity are illustrated by red and low resistivity is shown by blue. On the west side of pseudo-section there is an area of high resistivity that is out of alignment with the rest of the subsurface which indicates a fault. There is also a region of high resistivity that is likely the result of noise during data collection.

The westernmost part of the line shows an increase in resistivity that contrasts with the highly conductive material next to it. This indicates a fault and is concurrent with a known fault at the same area. This fault dips into the Mancos shale, the more conductive layer visible in Figure 25, and the more resistant Mesaverde is brought down into the subsurface. The majority of the line is found on the Mancos shale, which has a resistivity from ten to thirty Ωm. There are some more resistant areas present, but most of the area is approximately the same. However, the area that is highlighted in Figure 25 negatively impacts the inversion of the data. This set of data was collected on a day that had a large downpour of rain, resulting in a large amount of noise in the data. As such, this data either had a large resistive intrusion, or the entire area was overcome with noise. Referencing the geology showed that a large intrusion is unlikely, and the Dakota Sandstone Formation does not reach that depth. The data was filtered and despiked, but there was noise leftover. Highly conductive layers also make it difficult to image the underlying layers, so anything under the Mancos Shale is difficult to interpret. The depth of investigation is 220m, and does not leave the Mancos for the majority of the line. The layer of Mancos Shale is seen dipping lightly to the West, as would be expected in an anticline.

The Mancos shale has a range of resistivities due to the saturation of the clay. This range varied as the week progressed due to times of increased rainfall followed by the soil drying out. The range of the Mancos Shale resistivity matches that found by the other EM and MT groups, as well as the range of the Mesaverde resistivities.

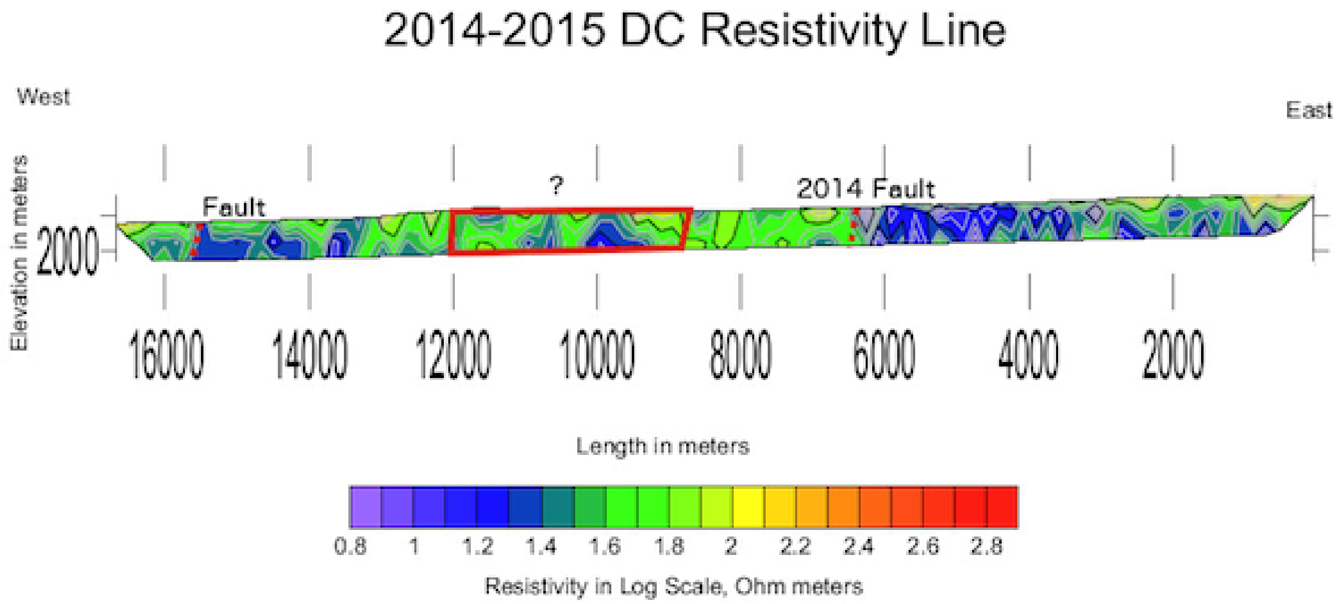

Figure 26. This image is the final combined 2014 and 2015 main line interpretation. There was a gap between the two data sets that was interpolated during the inversion process shown in the red box, as well as two different faults that were identified based on the change in resistivity.

The 2014 line covered the area from 9000 m to 0 m, and found many interesting subsurface features. The one that stands out the most is the steeply dipping fault found around 6050 m, which shows a change in resistivity from the underlying Mancos to the Mesaverde. The area directly to the east of the fault has a low area of resistivity, which seems to be due to a fractured zone. This zone allows for water to move through the layers, and creates a lower resistive area than is found in the rest of the plot. This fractured zone lines up with Stinking Springs, a known hot water seep, and so lends credence to this hypothesis. The box that is marked from 9000 m -12000 m shows an area of high error. The area from 9000 m -10000 m was not covered by either survey, and so was interpolated by the res2Dinv software. This is fine unto itself, however, the area that the inversion directly correlated to is the high resistance area near the fractured zone to the East and the high resistance area from a lot of noise to the West. This area has an unknown interpretation, as both of the bounds were much higher than the rest of the underlying structure. There is a common resistivity seen in all of the Mancos layers in that area, but the overall error for the inversion in that section is unknown. The two highly resistive units to the East of the line, near the surface, were interpreted to be noise caused by houses along where the line was plotted, and more resistive highs can be seen near the surface from 12000 m to 13000 m. Figure 26 shows that these two areas of resistivity exist, but were stretched by the full line inversion.

5.3. Sources of Error. In any experiment there are always possible sources of error and uncertainty. First of all there is the chance of error being introduced from the instrumentation itself. This would most likely be a systematic error that would be included in all of the measurements. Another error from equipment is the contact resistance between the electrodes and the ground, which can be reduced by pouring salt water on the soil around the electrodes. Factors outside the survey that can affect the results include powerlines, metallic fences, pipes, and other conductive objects. The frequency of the powerlines in the survey area can be inputted when setting up the DC survey so that the recording instrumentation, the ABEM Terrameter, can handle them appropriately. Conductive materials cannot be accounted for as easily, they might induce spontaneous potentials and provide short circuit paths for the current. Additionally there is uncertainty that comes from measuring a potential field since the value obtained is a weighted average of the overall effects resulting from the composition of the subsurface. Similarly, the exact location of interfaces and changes in geology in the subsurface is not known. This means that when we invert the data as means to interpret it there will be several possible solutions each with some degree of uncertainty. This is especially relevant if the subsurface is anisotropic (contains fractures, joints and layers) [**32**].

5.4. Summary. DC Resistivity locates a known fault on the western portion of the line shown in Figure 25, as well as illustrates the dipping of the Mancos Shale due to the anticline. Furthermore in Figure 26 there is a fractured zone that would allow water to move through the layers and corresponds to Stinking Springs, a hot water seep site. There also appears to be a highly conductive layer, the Mancos Shale, which makes deep imagining more difficult because of its higher conductivity. Overall DC Resistivity data yielded valuable information on locating structures in the subsurface along the main line. It can be jointly interpreted with other methods in an attempt to gain further information on the subsurface structures observed.

6. Self Potential

6.1. Error and Noise. There are several sources of noise associated with the data collected by self potential, or SP, surveys. First, and most easily corrected for, are the electrode drift and reference corrections. The survey design includes reference station measurements from which a correction for linear electrode drift can be applied. SP voltage measurements also depend on consistency of base and roaming electrode application. To make sure all of the values are in reference to the same base electrode, all data is shifted to correspond with the measurements collected at the selected base. Cultural noise from power lines, buried metal, pipe corrosion, and electrical grounds can also influence the data [**33**]. Noise from power lines is corrected for using a 60 Hz filter which removes most but not all of the associated noise. Differences in soil temperature, chemistry, and moisture add an additional component of background noise. Wet soil leads to positive influences in voltage measurements, and chemicals foreign to the electrolyte lead to electrode polarization. Telluric currents generated by the earth's magnetic field are also a source of noise in SP surveys. If these currents are consistently picked up by the survey they can be averaged out and removed [**33**]. According to several studies, an inverse topographic correlation may exist within the SP data [**34**]. This correlation has not been studied in depth and may be site dependent. Theoretically, the correlation makes sense because topography determines shallow groundwater flow direction, and groundwater flow produces a potential. The correlation might be demonstrated on the left side of Figure 27.

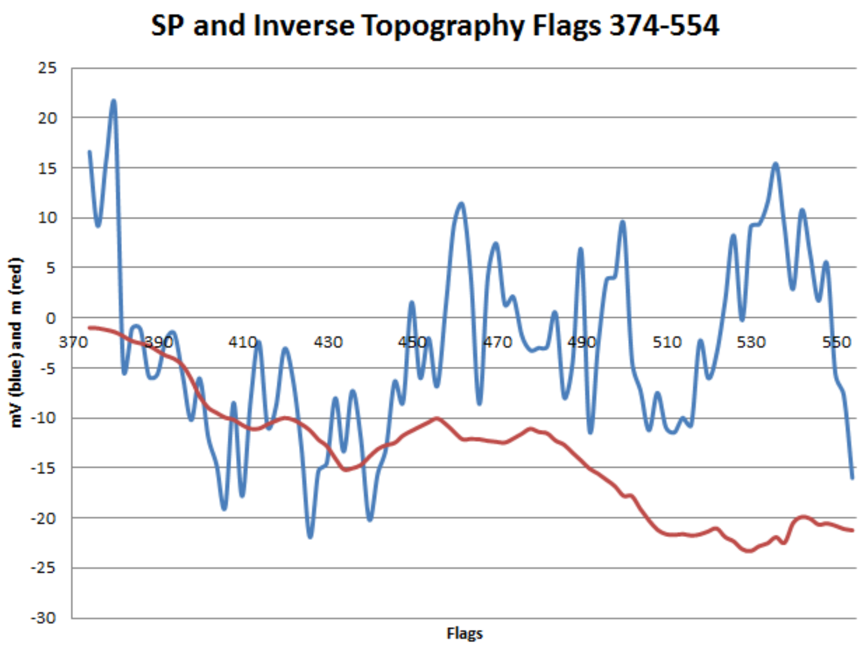

Figure 27. This figure shows the inverse correlation between SP signals and topography. The red line is the negative topography while the blue line is the SP signal. One can see on the left side how they correlate. On the right side, there is a positive SP anomaly.

6.2. Processing. Self Potential data only has two necessary corrections: the electrode drift correction and the base electrode correction. The drift correction is required on account of instrumental drift while the base electrode correction remedies the issue of different reference points for overlapping lines. Since the measured physical property is voltage differences, there needs to be a common base electrode when combining lines.

6.2.1. *Drift.* The drift correction needs to be completed prior to the base electrode correction. Assuming that all the measurements were within the same time intervals, the linear drift correction can be completed. The equation used for the drift correction is included below:

$$V_{corrected} = \Delta V + n\frac{\Delta V_{final} - \Delta V_{initial}}{N-1} \tag{1}$$

where $\Delta V$is the uncorrected measurement, n is the current indice (starting at zero), N is the total number of measurements, and ΔV_{final} and $\Delta V_{initial}$ are the voltages measured when the electrodes were touched together at the end and the beginning of the survey.

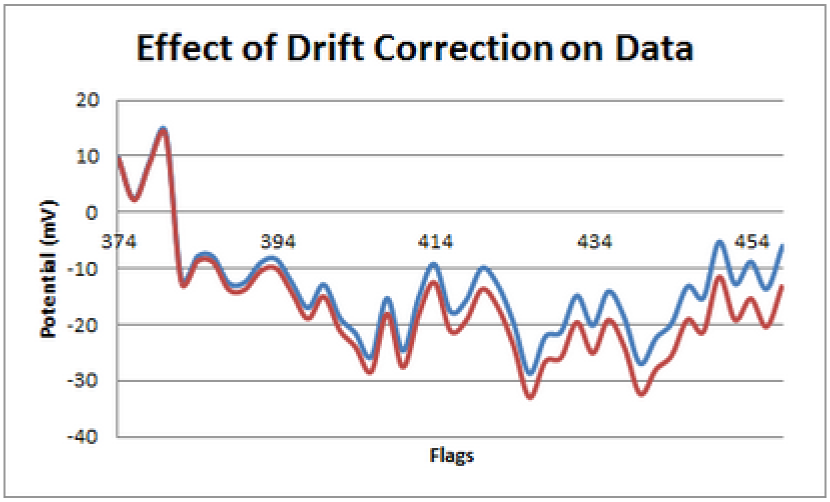

Figure 28. This figure shows the effect of the electrode drift correction. The red line is the corrected data while the blue line is the raw data.

6.2.2. *Base Electrode Correction.* The measurements in an SP survey are relative so it is important to ensure that overlapping lines have measurements that are mornalized to the same value. If two lines overlap, all of the values on one line need to be shifted such that the overlapping electrodes have the same value. In Chromo, four SP surveys were performed on the main line including two sections of overlap that were merged to form two larger data sets.

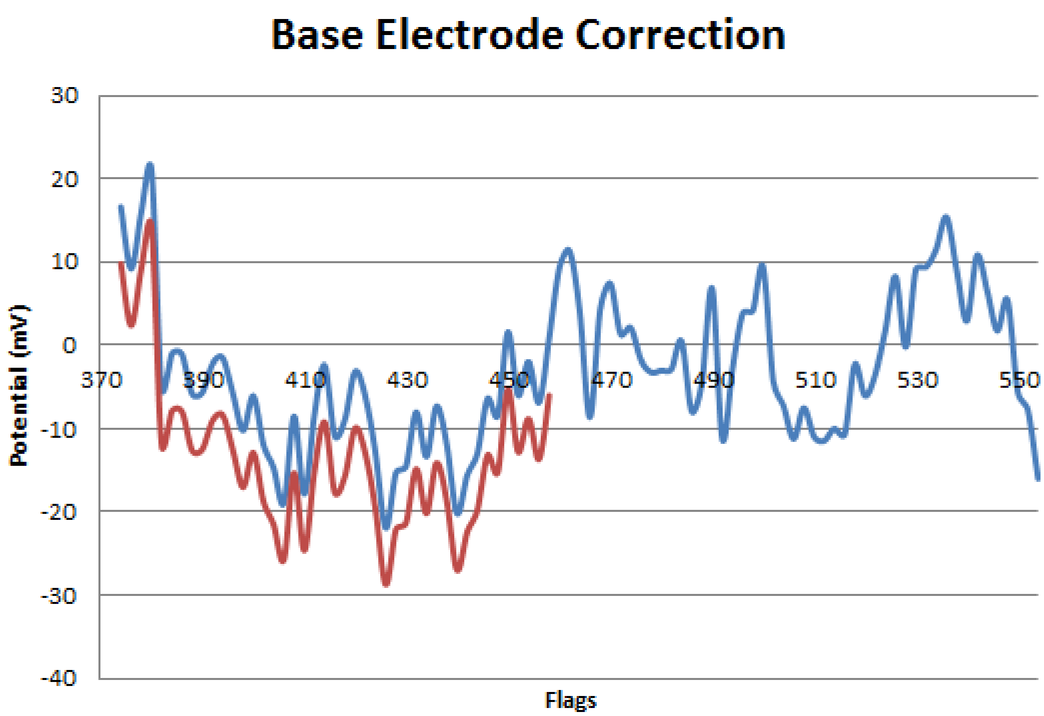

Figure 29. This figure shows the necessity of the base electrode correction. The red line is the raw data from the line between flags 374 and 458.

6.3. Results and Interpretation. Interpreting SP data can prove difficult since an anomaly can be structural, thermal, biological, topographical, or chemical. This means it is essential to gather all known data before attempting to analyze SP data. It is likely most of the SP data gathered in the survey heavily relates to groundwater and moisture content, given the amount of rain that occurred during the data acquisition. Therefore, it is important to know topographic and geological information before analyzing the data. In terms of groundwater flow, positive anomalies represent regions of upflow while negative anomalies represent regions of downflow [**35**].

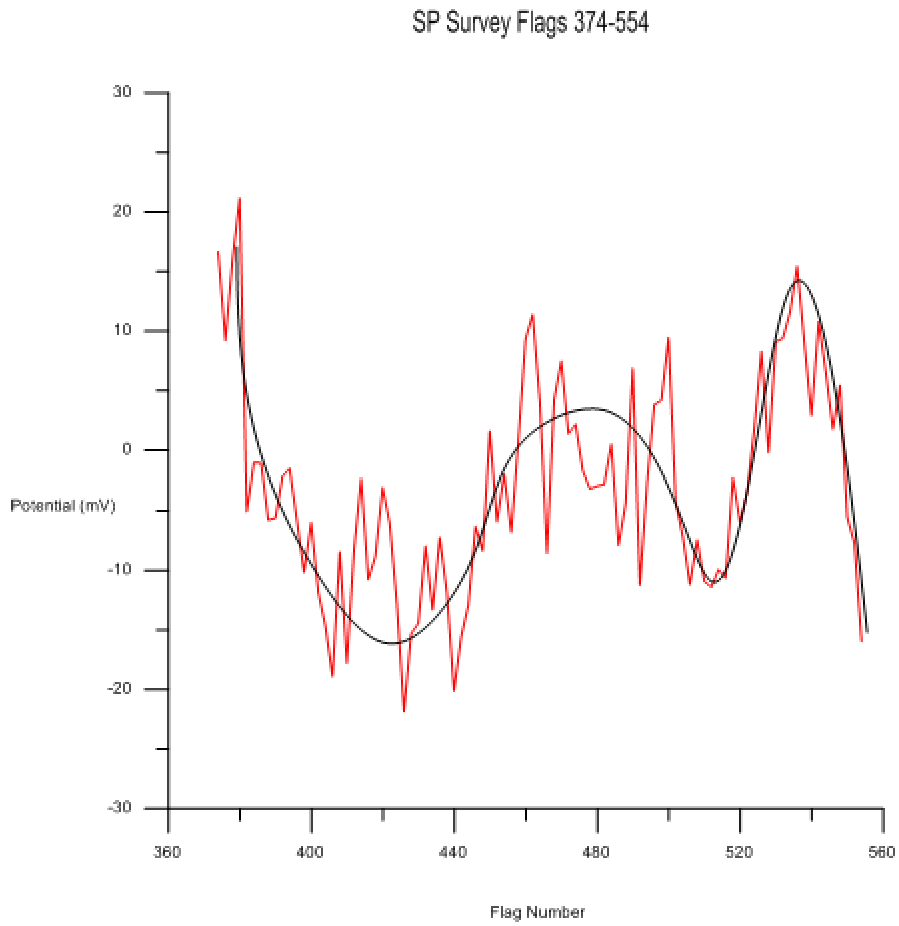

Figure 30. This figure shows corrected data for the SP survey between flags 374 and 554. A trend line has been added to show the relative anomalies.

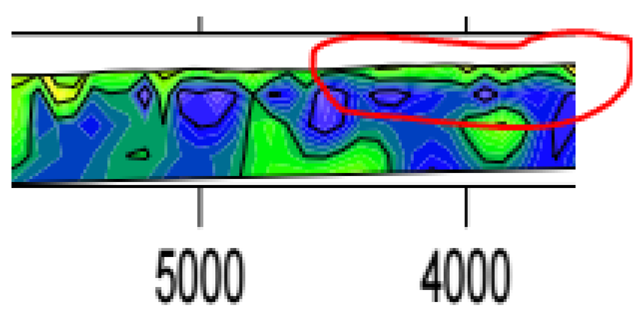

Figure 31. This image depicts the DC resistivity inversion data between flags 374 and 554. One can see a near surface resistive body near flag 540 which corresponds with the sharp positive anomaly in the SP data.

Most of the SP data is choppy so trend lines are drawn over it to pick out the anomalies. The first few anomalies are explained by the inverse topography correlation shown in Figure 27. While this is not the strongest correlation, the geological cross section and DC resistivity inversion do not give better explanations for the presence of these anomalies. The final anomaly near flag 540 is much sharper than the others. Nothing in the geologic cross section gives an indication of what it could be, but the DC resistivity inversion shows hints of a near surface resistive body. Alternatively, there could be a small fracture present in this area. If water flowed up this fracture, a positive anomaly would be generated.

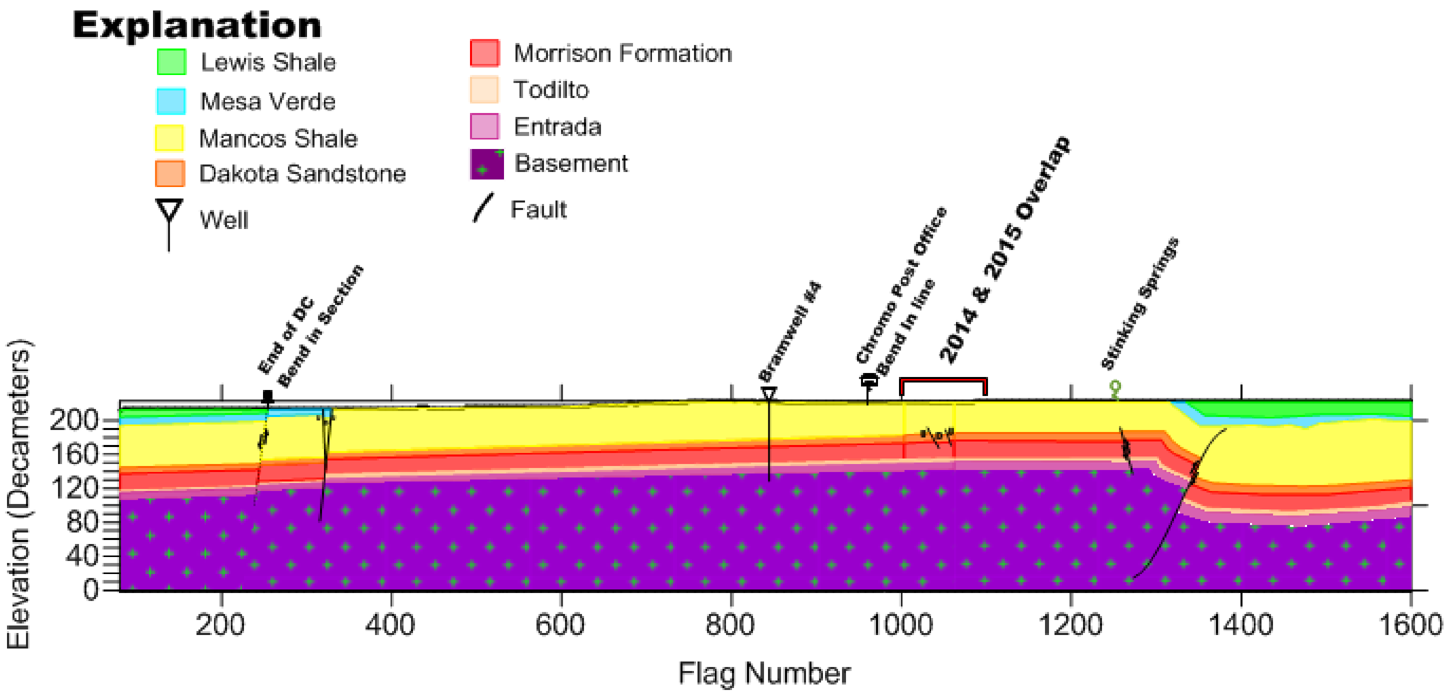

Figure 32. This figure is the geological cross section of the Chromo area. Nothing geologically significant exists between flags 374 and 932 besides the well around flag 840.

The data for the second survey along the main line (Figure 31) is even more scattered than the first. By eliminating a questionable data point, two positive anomalies can be identified. One of these anomalies could also correspond with a resistive spot seen in the DC data at 1000 m. The first anomaly around flag 790 looks like it corresponds to a larger resistive spot that is deeper in the subsurface around 1700 m. This larger resistive spot could be the Dakota sandstone, or an intrusive body, or simply an artifact produced by noise from the rain. The fact that the SP survey picked up a resistive anomaly as well makes the noise explanation less likely.

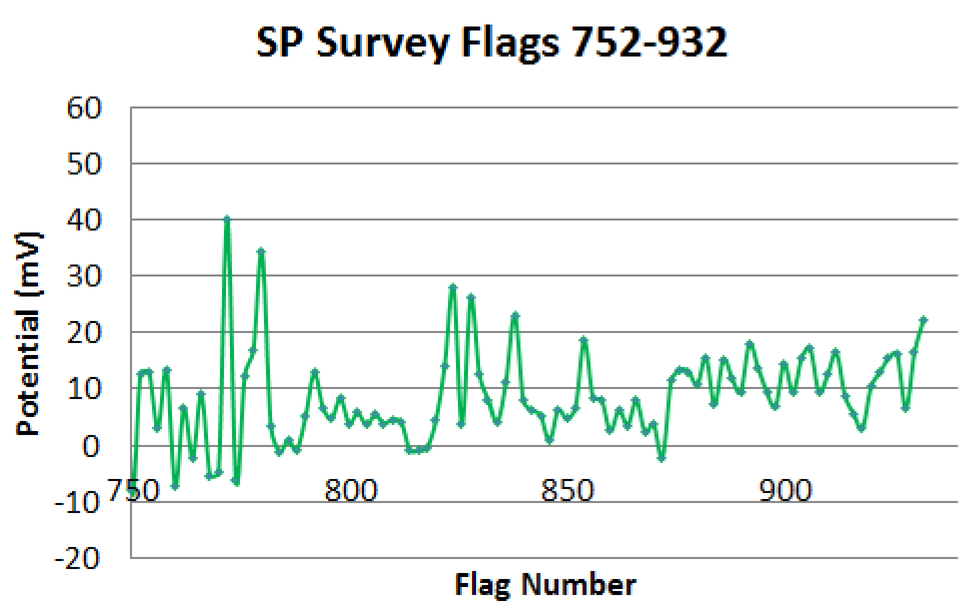

Figure 33. This image is the corrected data between flags 752 and 932. One can see two positive anomalies around flags 770 and 830.

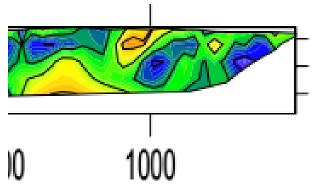

Figure 34. This image depicts the DC resistivity inversion data between flags 752 and 932. The two large resistive bodies correlate with the positive anomalies in the SP data.

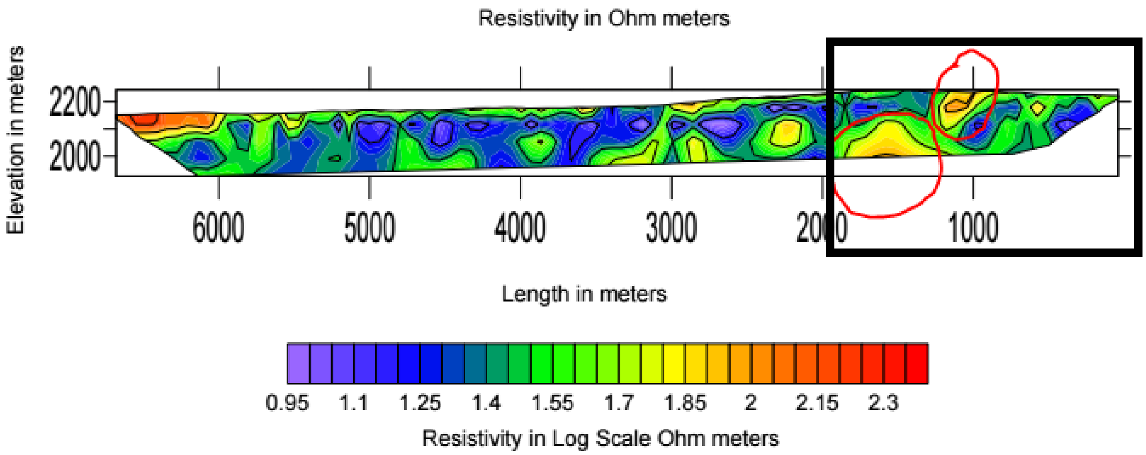

Figure 35. This image is the DC resistivity inversion of the 2015 main line. The black box shows where Figure 34 exists in the main line. The red circles show where the two resistive bodies are.

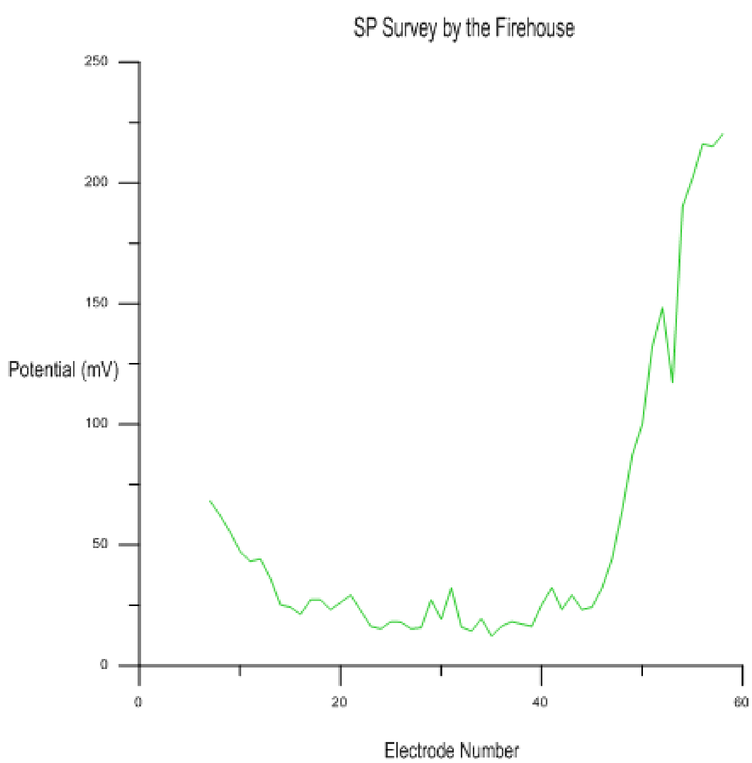

Figure 36. This figure shows the SP data of the Stinking Springs area. The large positive anomaly on the left side of the graph is most likely water rising to the surface.

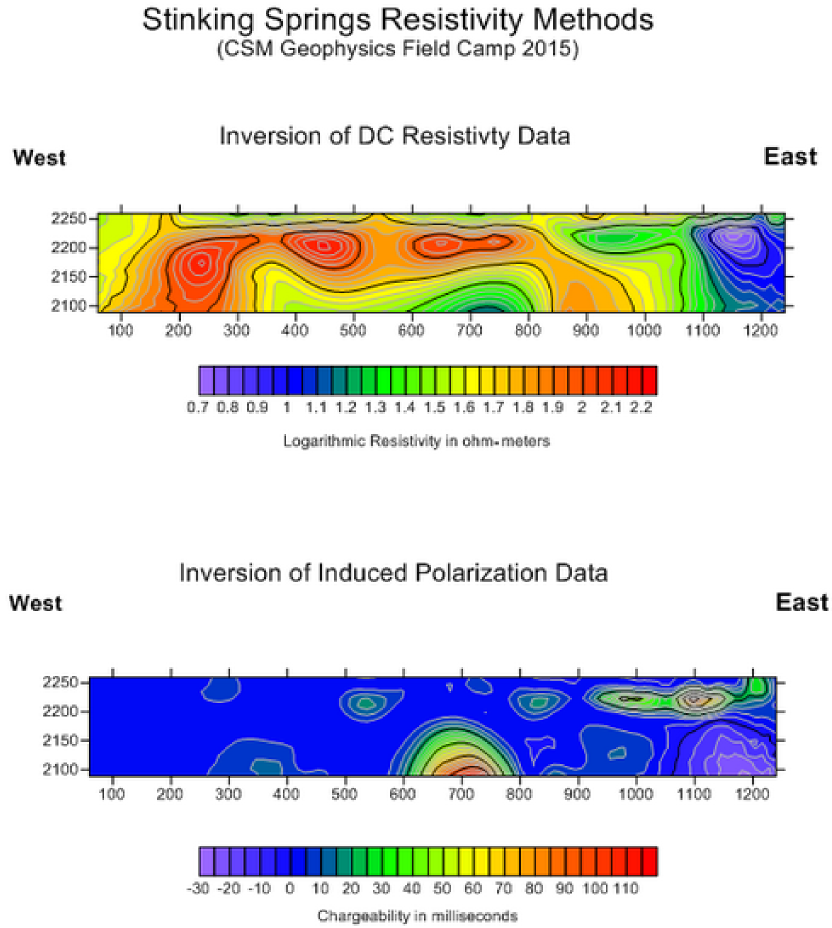

Figure 37. This figure shows the DC resistivity and IP inversions of the Stinking Springs area. The area of high chargeability in the middle of the IP inversion is most likely the source of the springs.

At the survey over the Stinking Springs, there is a large positive peak at the west side of the survey in Figure 36. The DC inversion of the same area (Figure 37) shows a layer of very resistive material on the west side of the survey, perhaps the Dakota sandstone. However, the resistive patches in the DC inversion are much more extensive than the large SP anomaly. Therefore, the large positive peak probably corresponds to where water is flowing to the surface. This makes sense since there is a known spring in the area. The IP chargeability inversion shows an area of high chargeability in the center of the survey, which might be the source of the spring. Since the water did not travel straight up to the surface, there could be a fracture through which water travels to the surface.

6.4. Conclusion. Ideally, the weather would have been perfect during the survey in Chromo. However, this was not the case. Different days brought different intensities of rain. The soil moisture is inconsistent across the different lines which consequently brings a certain amount of noise to the data. Other sources such as buried metal objects may have produced a signal, causing more error. The interpretations of the data are based on geologic and topographic knowledge as well as the DC resistivity inversions. For future surveys it would be beneficial to conduct a magnetic survey before conducting an SP survey so that objects that might create an SP signal will be found. This would allow for a more accurate characterization of groundwater flow. Overall, the SP data gathered showed where water is travelling to the surface at Stinking Springs. The data also backed up the validity of the large resistive body shown in the DC inversion. For future work, it would be interesting to conduct an SP survey at the recon site so the water flow in that region could be characterized.

7. Induced Polarization

7.1. Processing. The first step in processing the Induced Polarization data is to download data from the instrument or recorder. The ABEM Terrameter System SAS-4000 was used to run, record, and store the survey. Data is never erased from the ABEM unless extra storage space is needed. When system initializes it displays a “bot-rate”. It is critical that the bot-rate on the computer and the bot-rate on the ABEM match. The columns hold information on the starting electrode location, the electrode spacing, apparent resistivity, and apparent chargeability for the array. Running the inversion requires that the data be free of negative values in both the

resistivity column and the chargeability column. Negative values are removed from the resistivity and IP data. Then, both resistivity and IP data are analyzed for noisy or outlier data which may complicate inversions. These data points are removed or modified to increase the data quality.The program runs an inversion on the DC resistivity data and then uses those values to aid in the implementation of the inversion of the IP data, specifically to ensure that the values in the IP inversion use inverted resistivity values and not apparent resistivity values. At this point, a quick interpretation of the inversion is performed to determine if it is a reasonable representation of the data and the geology. If the inversion looks suitable, the files are then exported as .xyz files. Post-inversion data needs to be transformed from chargeability to normalized chargeability because the latter will

have a noticeable increase in contrast along the survey line. In MATLAB or Excel, the .xyz file was opened in order to calculate normalized chargeability. Each individual cell of the inverted chargeability was divided by the corresponding cell of the inverted resistivity data. The new .xyz file was loaded into Surfer 12 and created an image with it. It is important to note that Surfer 12 does smoothing and interpolation when the data is transformed into a grid file.

7.2. Sources of Error. There will be several sources of error and uncertainty encountered while using the Induced Polarization method. Obvious sources of noise are man-made. This includes things like power lines, buried pipes, and conducting fences. Power lines can create noise at specific frequencies, commonly 60Hz in the United States. These can create coupling within the subsurface that may affect the IP survey by increasing, decreasing, or redirecting the injected current. Pipes can cause large amounts of noise if they are parallel to your survey line or if they are cathodically grounded. The current will choose the path of least resistance and these pipes will be that path in these situations; this is sometimes referred to as channeling. Fences will also cause similar effect as buried pipes. There are 3D effects to consider, however in a 2D model perpendicular fences and pipes are not as concerning. Obviously it is wise to avoid these sources of noise, however that is not always possible. The locations of these sources of noise should be recorded and used in the interpretation and processing of the data.

Another source of noise will be weather and soil conditions. The lightning strikes will produce a surge of electricity that interferes with the control of the ground current. Telluric currents caused by electromagnetic waves from solar winds interacting with the ionosphere along with the natural currents in the subsurface will cause noise. The last source of noise due to weather and soil conditions is caused by rain falling and saturation increasing in the topsoil. The moisture will lower contact resistance and provide paths for channeling to occur in the near surface. There is not a lot that can be done about the above sources of noise because we cannot control the weather. However, noting the presence of these noise sources and try to explain the effects in the data.

Other sources of noise are caused by survey setup and equipment. A difference in the strength of contact resistance at each electrode causes uneven current flow. Electrodes may be placed within saturated ground, which decrease contact resistance and decreases voltage measurements at the A and B electrodes. The overall apparent resistivity of the circuit would be deceased as a result. This is avoided by placing the electrodes consistent with the survey design and simply taking note of the variations in soil conditions for each electrode. Electrodes can also become disconnected from the due to damaged wires within the DC cable. Electrodes #4, #58, and #64 were disconnected during our IP survey. This results in data gaps and causes the inversion program to perform more interpolation on the data

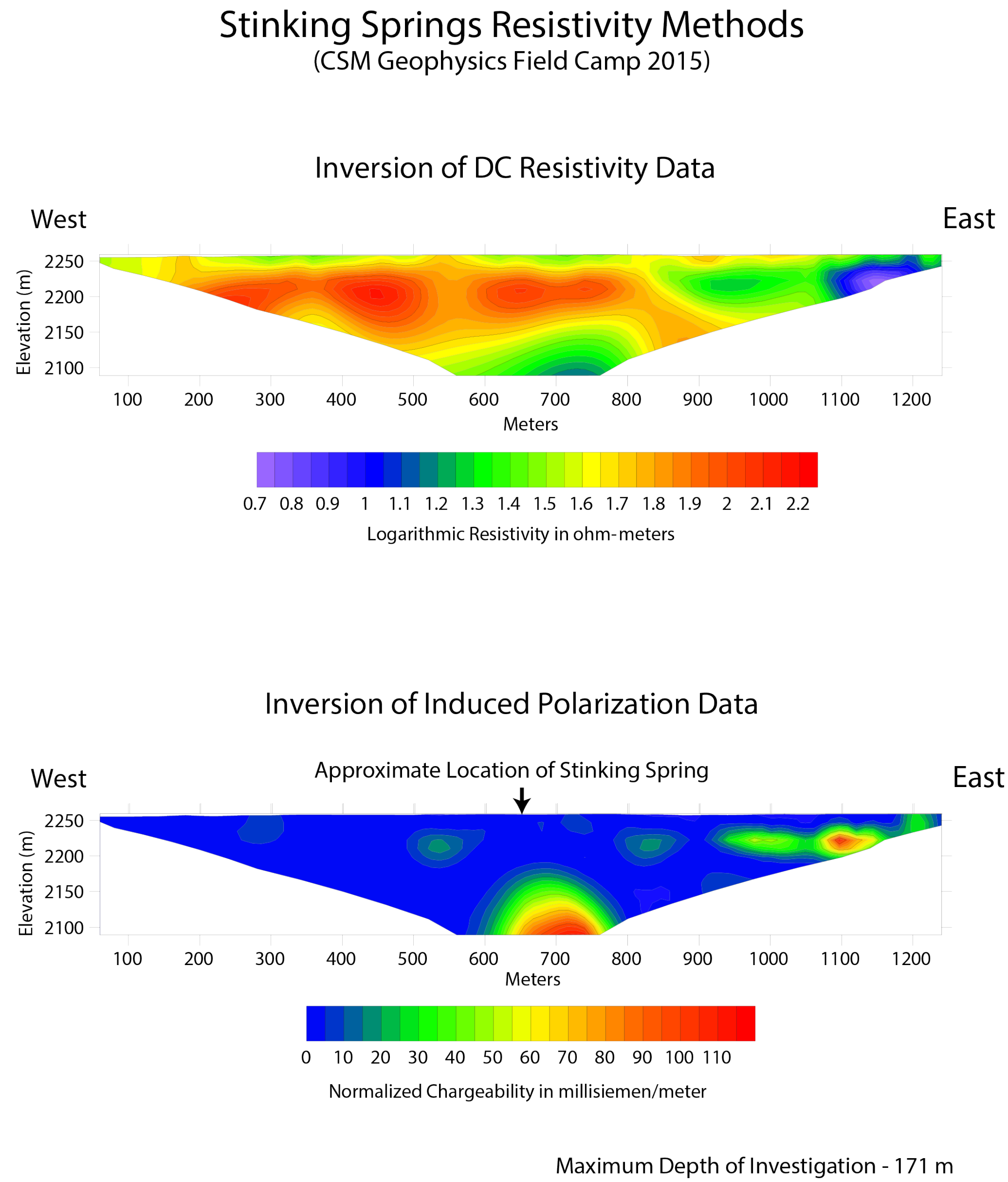

Figure 38. Inversion results from the induced polarization survey. The top figure shows DC Resistivity inversion, plotted in Ωm, and the bottom figure is plotted in normalized chargeability

7.3. Summary. Examining the inversion of induced polarization data, the most notable feature is the positive anomaly located at the extreme depth of investigation. This area of high normalized chargeability could be caused by saturation along with the presence of biofilm, both of which would contribute to the larger measured values of partial chargeability. This anomaly could also be a product of noise, occurring at depth due to a loss of resolution and accuracy. Data manipulation could also contribute to the contrast of the anomaly. In attaining normalized chargeability, the partial chargeability is divided by inverted values of resistivity, causing normalized chargeability and resistivity to have an inverse proportionality. This can be observed in comparing the resistivity inversion to the normalized chargeability. There are also small lenses of high resistivity occurring at an approximate 40m depth. These anomalies could be sourced by lenses of clay, delineated by the normalizing of chargeability. This depth could also correspond to the water table of the region as pore saturation would be relatively large at the water table, increasing measured partial chargeability. The inability to discern noise from valid data along with a lack of alternative geophysical methods to verify results, a conclusion cannot be made with good confidence.

8. Deep Seismic

8.1. Processing.

8.1.1. *Description of Raw Data.* Deep seismic raw data is in SEG-D format. Each shot will only show the result in one location, and the pre-correction data is noisy resulting features being covered. From the raw data we can see strong reflections and the relative depth (the raw data is in time, but time and depth are related). Also, we can see the dominant frequencies for each shot, which is helpful for de-noising. The raw data is also not matched with the geometry, and it contains mismatched trace information. By correcting the data and applying other techniques such as denoising, signal enhancement, and stacking, the reflections are much clearer on the image and easier to interpret.

8.1.2. *Software Used.* SeisSpace ProMax seismic processing software is used to analyze and reduce the raw data. The program supports an effective user interface that allows users to visualize data reduction as it takes place. SeisSpace is a common software used in industry and with the help of two professionals, Robert Basker from Landmark Services (Halliburton) and Hugo Garcia from Chevron, the program is effectively used to produce the final product.

8.1.3. *Integration of Data.* The overall goal of this year's deep seismic team is to acquire, process, and interpret seismic data from the Chromo region. Because the 2015 seismic line overlaps with the 2014 line, it's possible to combine the data from the two surveys. Integration of more than eighteen kilometers of seismic data allows us to better define Chromo's geology. The general combination of both datasets is a challenging task, as the geometric and seismic parameters are not identical. The first main issue to be corrected is the total listening time of each shot. In 2014's survey, four seconds of data was observed, while in 2015's survey two seconds of data was observed. The difference in listening time is corrected in a SeisSpace flow function that filters out data readings that are longer than 2 seconds, allowing both data files to have identical listening times. After adjusting the listening time, the last part of the merging process is to analyze the overlapping section of seismic data, which occurred from flag 1100 to flag 1000 (1000 m). The 2D land geometry modules from SeisSpace are used to merge the locations of the overlapped shots and receivers into single values. The final files contain both the 2014 and 2015 data with identical properties and spatial geometry.

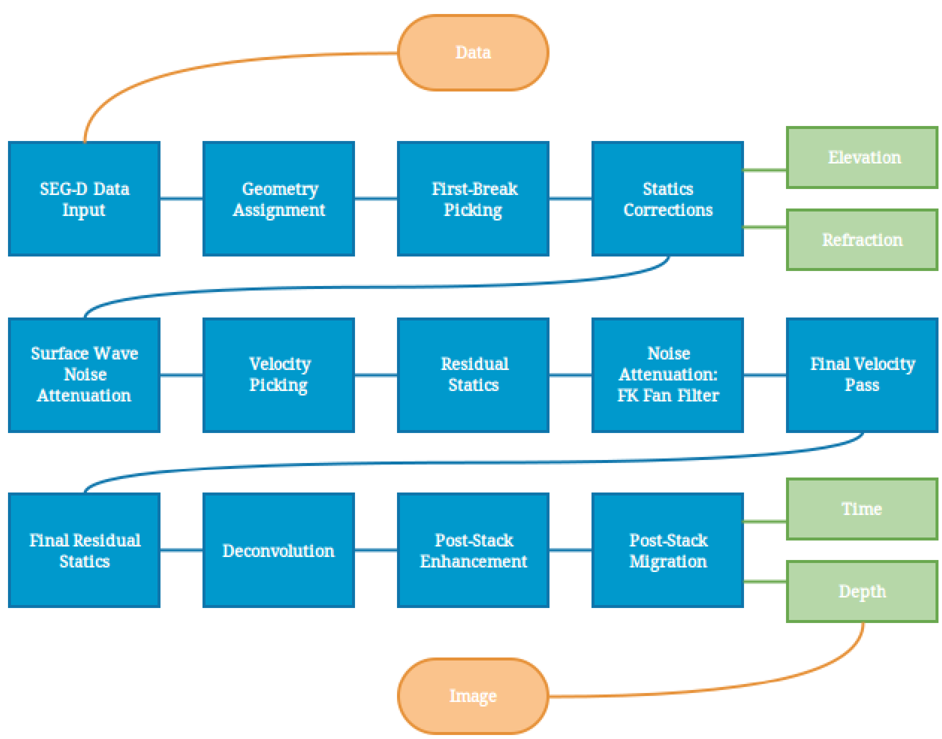

Figure 39. Seismic data processing flow overview.

8.1.4. *Geometry.* After importing the corrected spatial data into the geometry toolbar, the SEG-D data files are linked to match the spatial geometry database. The final troubleshooting quality control with geometry is completed to verify each shot that was taken in the field matched the correct flag location: observer notes are referenced for manual corrections in source locations and each trace is visually reviewed to ensure precise relative positioning. Midpoints are calculated for the provided source and receiver locations. Irregularity of the seismic line path requires the use of a crooked line spreadsheet flow, which prompts users to define multiple linear segments along a non-linear survey. Five smaller best-fit line segments are chosen to describe the path of the line. Midpoints are displayed on the survey map and it becomes apparent that midpoints don't reside directly along the line. To account for this, a five-meter bin interval is set for each segment of the crooked line. At every bin location, all midpoints lying along a five hundred meter line perpendicular to the bin are compiled and assigned to the bin location. Geometry has a large impact on fold, which describes how many traces are contained in a common midpoint gather. Data quality increases where fold is high, as noise is correlated out of the image. High fold is observed near the midpoint of each line segment chosen for the survey.

Parameter	**Value**
CMP Interval/Bin Length	5 meters
CMP Bin Width	500 meters
CMP Range	01/24
Maximum Fold	163
Receiver Interval	10 meters
Source Interval	20 meters / 10 meters
Maximum Offset	2400 meters
Receiver Range (Flag number)	80-1900

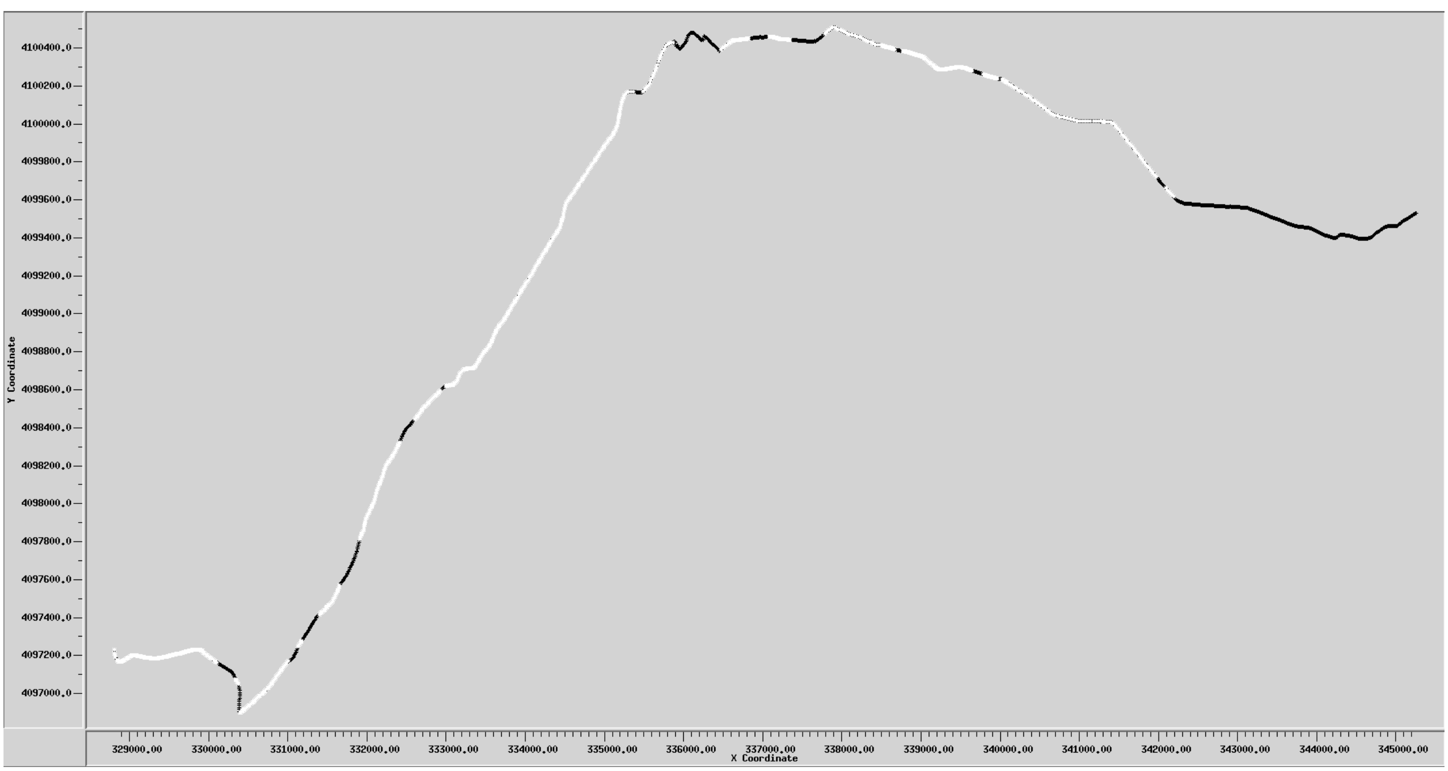

Figure 40. Receiver stations of 2014 and 2015 lines in black; source stations in white.

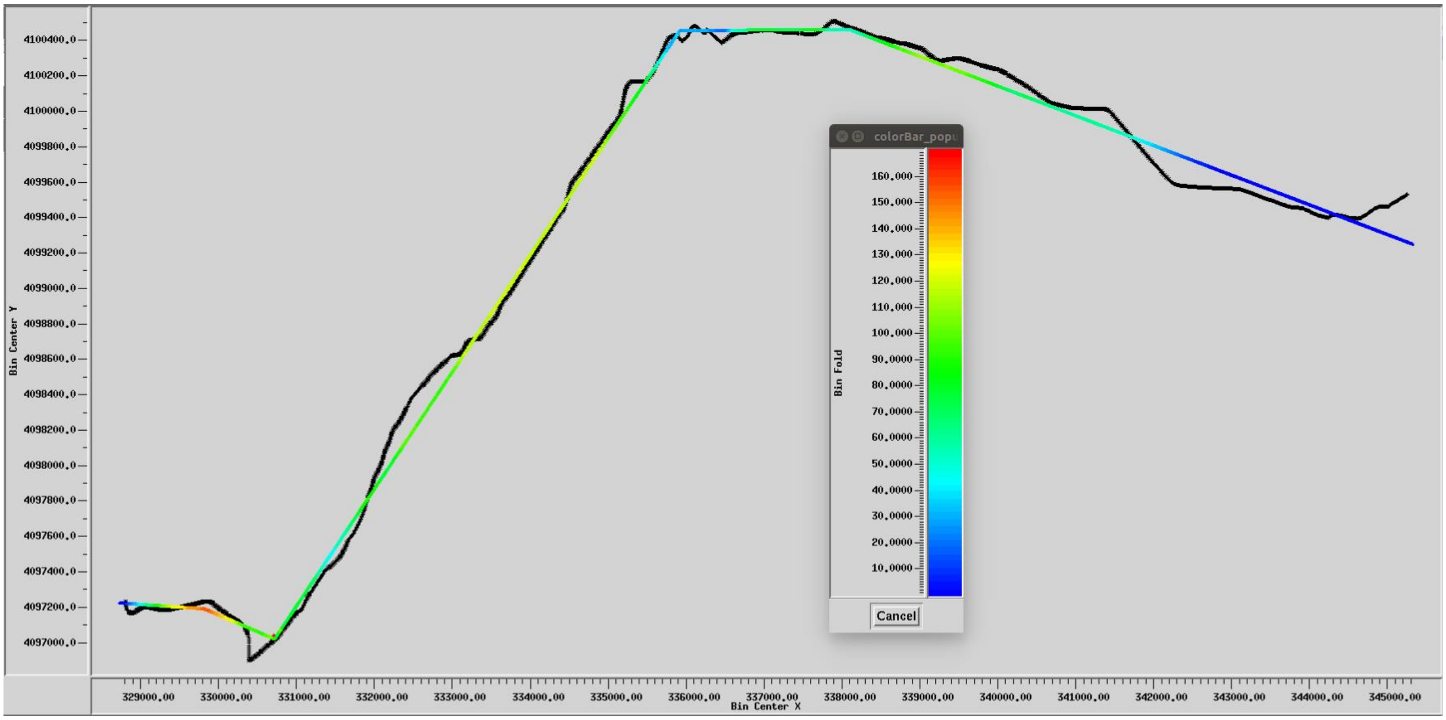

Figure 41. Fold values along the 2014-2015 seismic line with crooked line geometry.

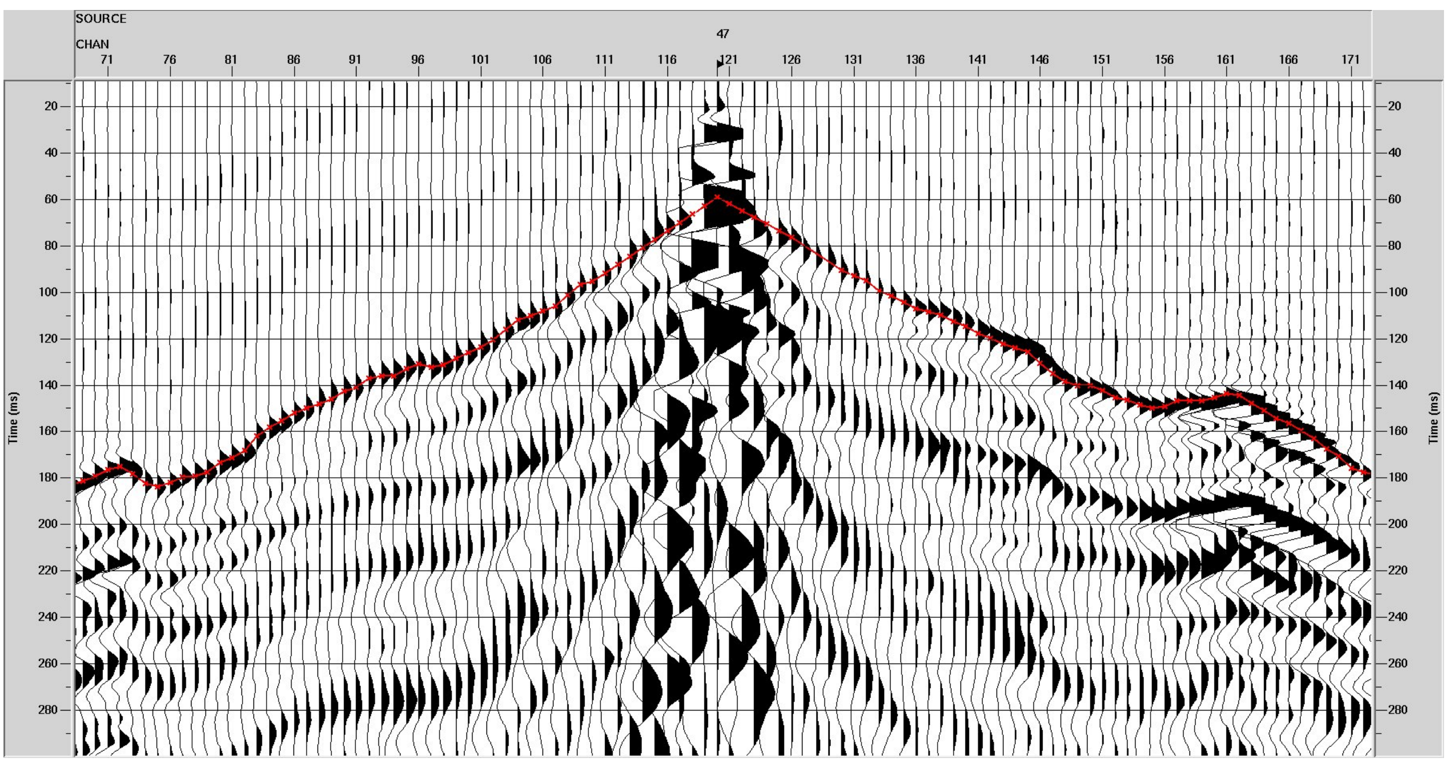

Figure 42. Shot gather with the first break header trace.

8.1.5. *First-Break Picking.* First-break picking refers to the identification of refracted arrival times of P-waves in the near-surface low velocity layer. This process is a prerequisite to statics corrections because it provides the software with the refraction velocity in the subsurface. SeisSpace requires that the user specifies parameters to narrow its automated first-break pick. These parameters are based on the user's assumptions of the velocity in the near surface layer, the envelope width that illustrates the amplitude distribution, the power ratio stabilization factor, and the type of source used in the survey. Using these parameters, the program is set to automatically identify the arrival time, but false first-break readings occur within traces exhibiting low first-arrival amplitude. Automatic picking accuracy depends on the geologic structure, source type, and the signal to noise ratio. If the subsurface structure is too complex, the program will identify false breaks. Consequently, it's necessary to manually correct false picks for some traces [**36**].

8.1.6. *Statics Corrections.*

8.1.6.1. *Elevation Correction.* The SeisSpace elevation statics tool shifts all data up to a constant arbitrary datum, effectively mimicking a flat surface. The tool allows for corrections in elevation differences between traces, calculates differences in times to a specific reflector, and then corrects for those differences. This process removes small perturbations/distortions caused by topography in reflectors.

8.1.6.2. *Refraction Calculation.* Thin, low velocity layers near the surface of the earth (10-50m depth) relative to the bedding beneath cause delays in reflection arrivals. Velocity values for these layers are found manually through first-break picking. Time delays are calculated based on a 1000 m/s velocity assumption for the low velocity layers. Shallow velocities are then replaced with the velocity of the first break picks. Reflections become more continuous within a shot record after the correction.

8.1.7. *Surface Wave Noise Attenuation.* After the refraction correction, reflection events in most part of the seismic record are still unidentifiable due to noise from surface waves. A surface wave noise attenuation correction is then applied to the data. The program is adjusted to remove surface waves with a velocity between 2500-3500 m/s and frequencies below 100 Hz. The result of this correction is a better resolution of true reflectors, which gives us the ability to perform a velocity analysis.

8.1.8. *Initial Velocity Analysis.* Velocity analysis is performed on common midpoint (CMP) gathers, and the objective is to find NMO curves that best fit the data, which allows us to obtain the NMO velocity. A semblance plot is used to find the areas with the highest amplitude stacks, and points are picked within these high energy areas to find a stacking velocity profile for that particular CMP. Constant velocity CMP stacks are shown in the software interactive window, in order to aid velocity picking (Figure 43). Changes made to the seismic stack after velocity analysis and static corrections can be analyzed through comparisons of Figures 44 and 45.

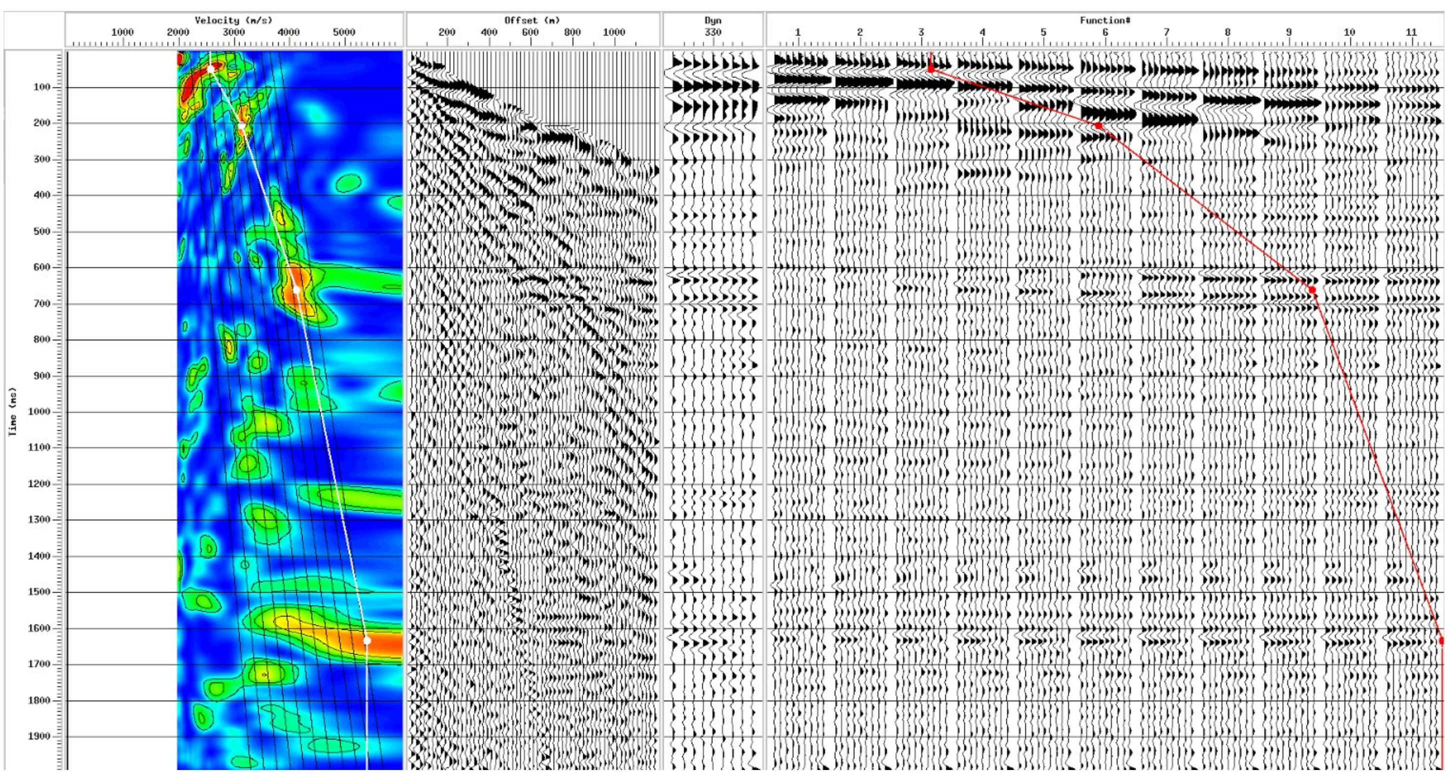

Figure 43. A Velocity Analysis window with a semblance plot, CDP, and CVS.

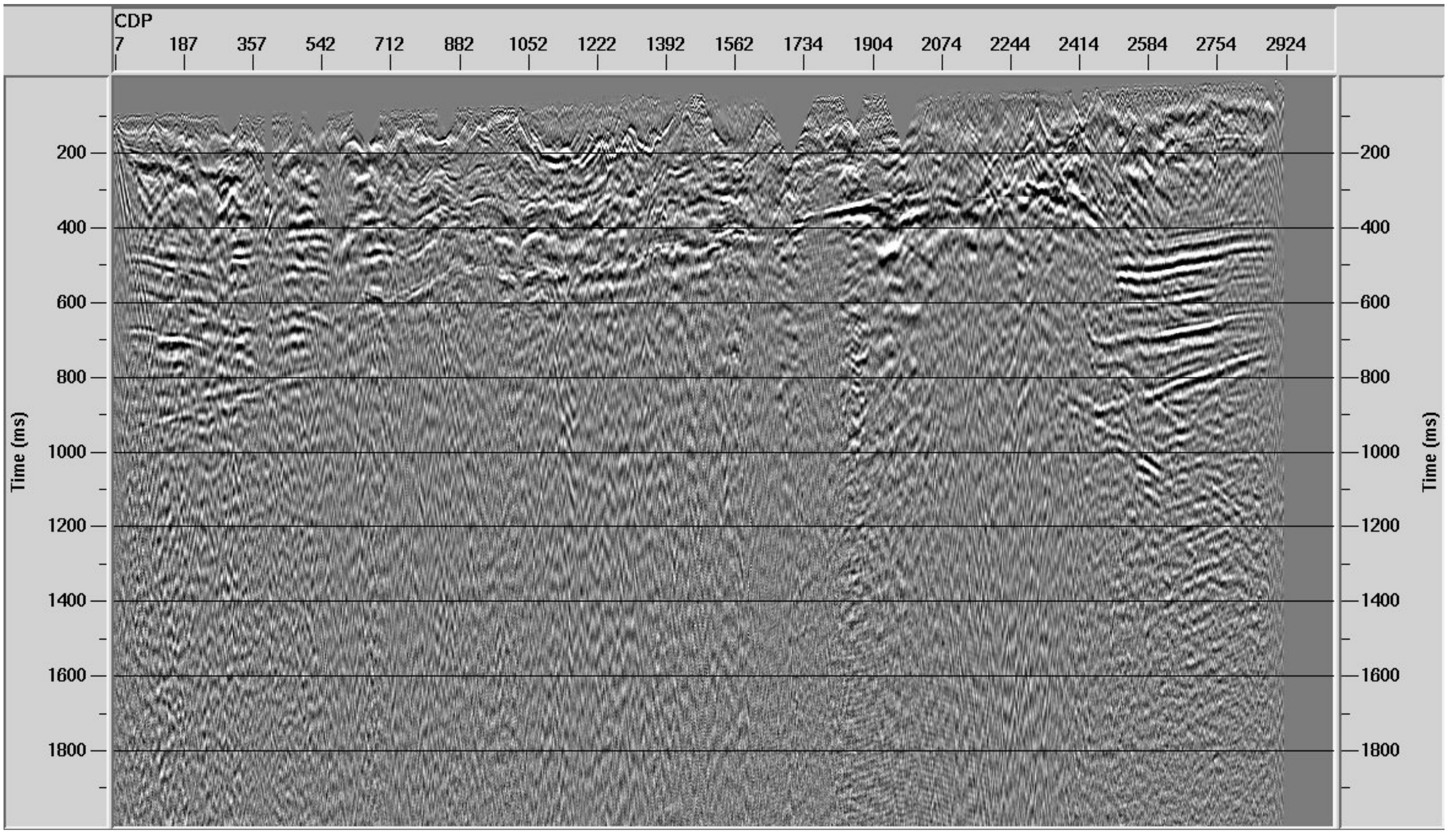

Figure 44. Seismic stack before velocity analysis and static corrections.

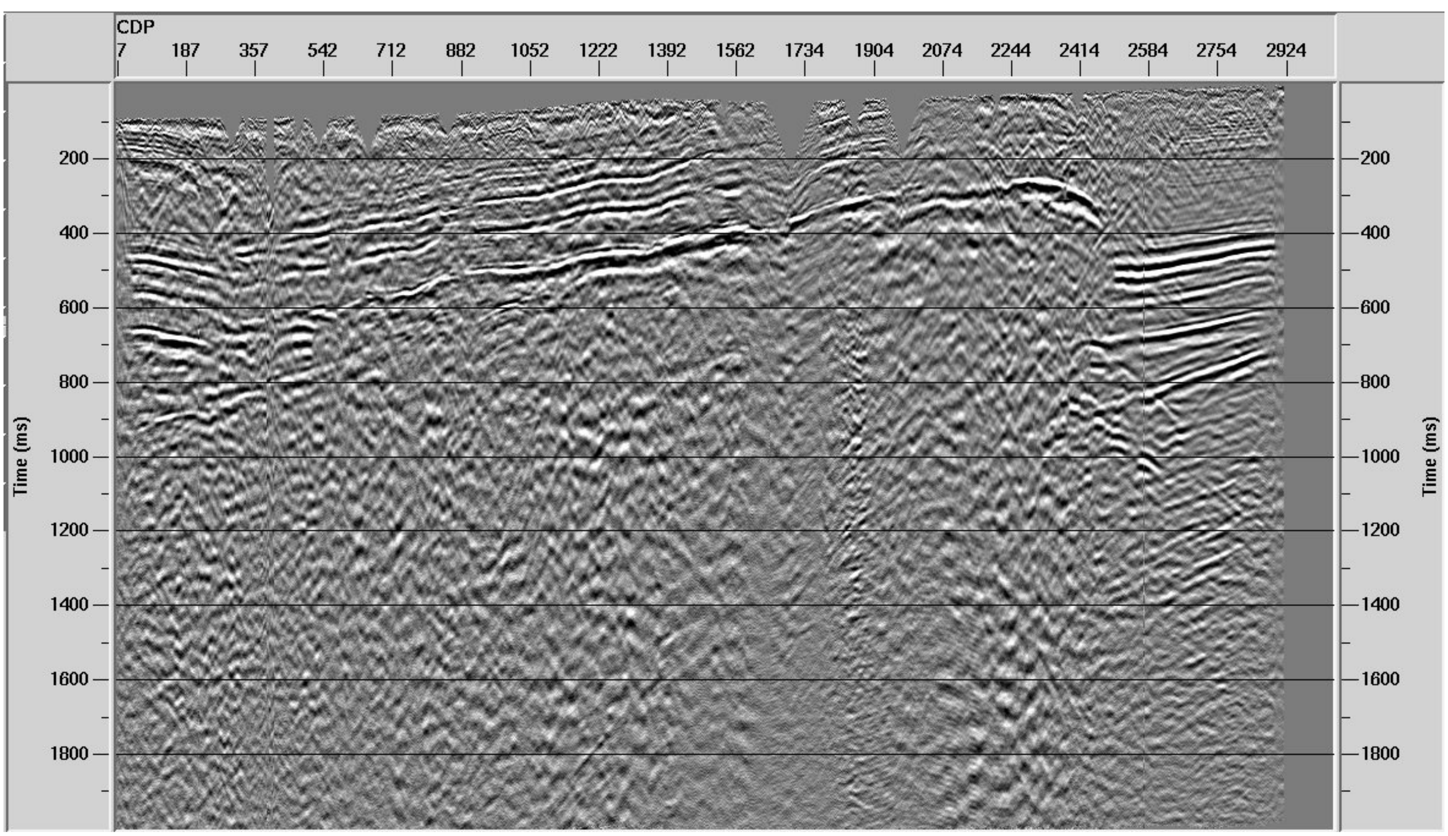

Figure 45. Seismic stack after velocity analysis and static corrections.

8.1.9. *Residual Statics.* Elevation corrections employ a simple near-surface model based on a constant datum. This leads to inaccuracies in the model that can be easily seen after the NMO correction: various adjacent traces in the data do not properly align as shown in Figure 46. These misalignments are static time shifts in the data caused by near-surface velocity anomalies or topography. The purpose of residual statics is to correct for these small errors in near-surface models and find the correct geometry of the reflectors. Application of residual static corrections will improve the final model compared to using only the constant datum static correction [**37**].

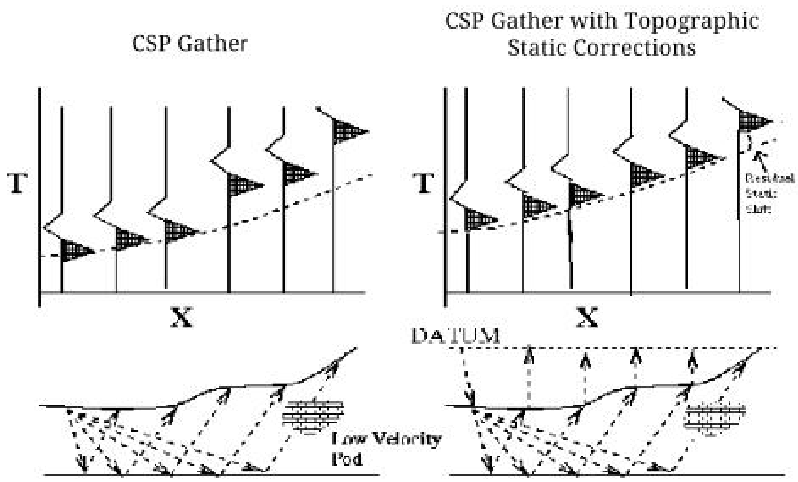

Figure 46. Image of residual static misalignment in traces [**38**].

8.1.10. *FK Fan Filter.* FK Fan filter is a noise suppression process. By using FK fan filter, data can be transformed into the frequency-wavenumber (FK) domain. In the FK domain, signal and noise can be separated by a dip filtering technique. After separation, noise is eliminated by filtering out the dip that represents noise. SeisSpace requires the user to draw polygons or lines around portions of the FK display with high noise. If the dip limits chosen are too harsh, the output data will look over-filtered [**39**].

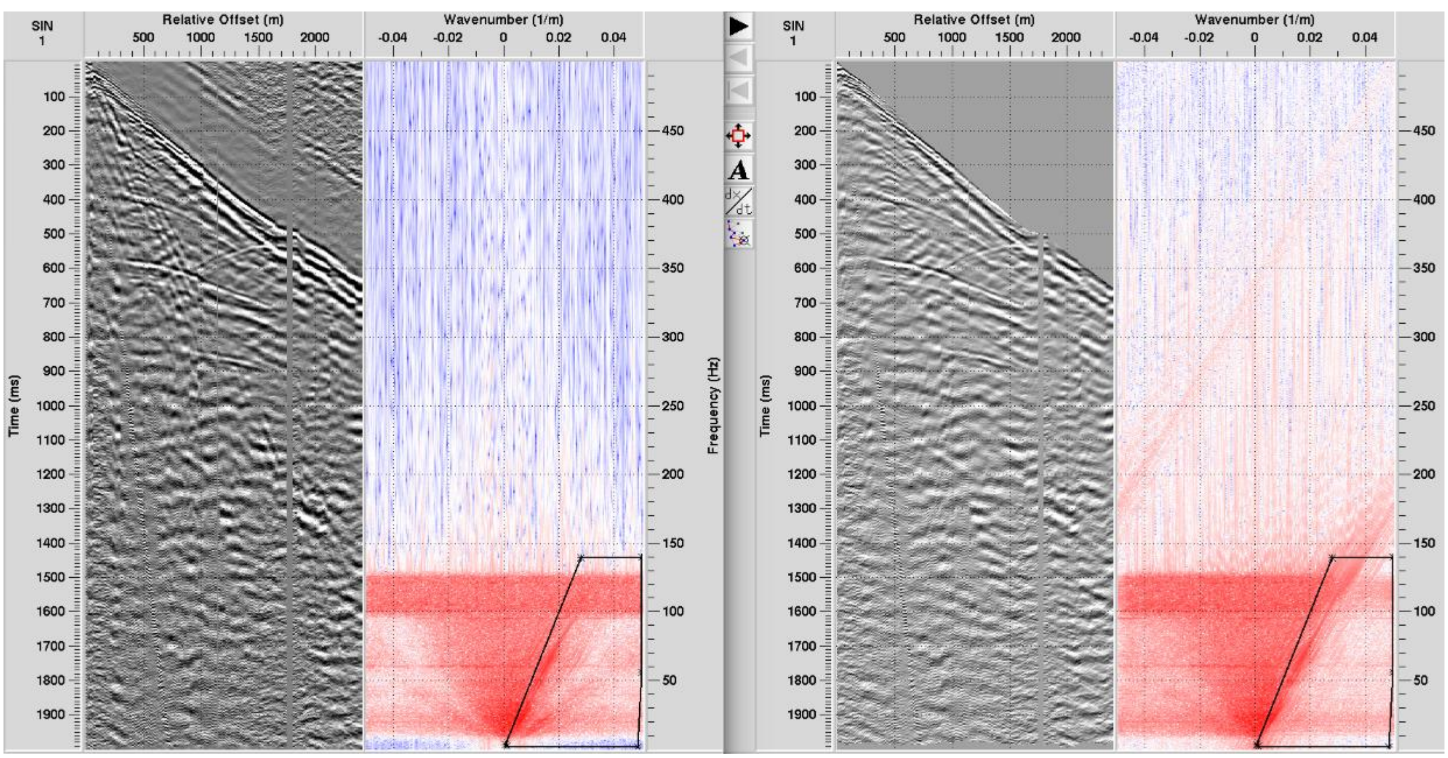

Figure 47. Shot record in TX and FK domain, before and after FK filter using the drawn polygon.

8.1.11. *Final Velocity Analysis.* A final pass of velocity analysis is implemented, and the velocity picks are found in the same way as in the initial velocity analysis. This final stacking velocity is a more accurate value as it is obtained after performing noise attenuation and residual static corrections, and if properly smoothed, this velocity is used as input for time migration.

8.1.12. *Deconvolution.* Deconvolution is the process that filters the source wavelet from the seismic data, in order to obtain the earth's reflectivity response. Assuming the earth reflectivity is aleatory and the source wavelet is stationary, the autocorrelation of the seismic signal at various time gates leads to an estimation of the source wavelet, that can be deconvolved from the seismic trace. Also called spiking deconvolution, this process broadens the frequency range of the seismic data, improving temporal resolution. The wavelet for each reflector in the seismic section will be sharper, distinguishing reflectors better for later seismic interpretation [**39**].

8.1.13. *NMO Correction and Stacking.* A normal moveout correction (NMO) is a processing technique in which reflection events of the pre-stacked data, which are approximately described in a hyperbolic shape, are flattened within a common midpoint gather. After completing this correction, all of the reflections appear at the same time for all offsets: any travel time delay due to offset has been removed. This correction, however, does not affect the direct arrivals seen in the raw data, as they behave in a linear fashion. SeisSpace provides a workflow function that accomplishes this moveout. The two dimensional geometry of the main seismic line diminishes the necessity of corrections accounting for the 3D dip velocities with NMO, however the stretch mute percentage still needs to be altered. After completing this procedure in SeisSpace, the data is sorted to CMP gathers, and all traces within a gather are stacked (summed) to create a stacked section.

8.1.14. *Post-Stack Enhancement.* A stacked section usually still contains some unwanted features that the pre-stack processing is not able to treat. In order to remove more noise from a stacked section, some post-stack enhancement techniques are applied. The most common one is called FX Deconvolution.

The FX Deconvolution algorithm transforms the seismic data to the frequency domain. A series of frequency-spatial gates (FX) are created based on user parameters. For each one of these gates, a predictive filter is computed along the spatial axis for each frequency. Anomalous samples relative to the predictive filter are removed and replaced by samples predicted by the filter. Then, the seismic data is transformed back to the spatial-temporal domain by an inverse Fourier transform. The output from the FX Deconvolution algorithm shows a stacked section with enhanced reflectors, attenuated incoherent events and less random noise [**40**].

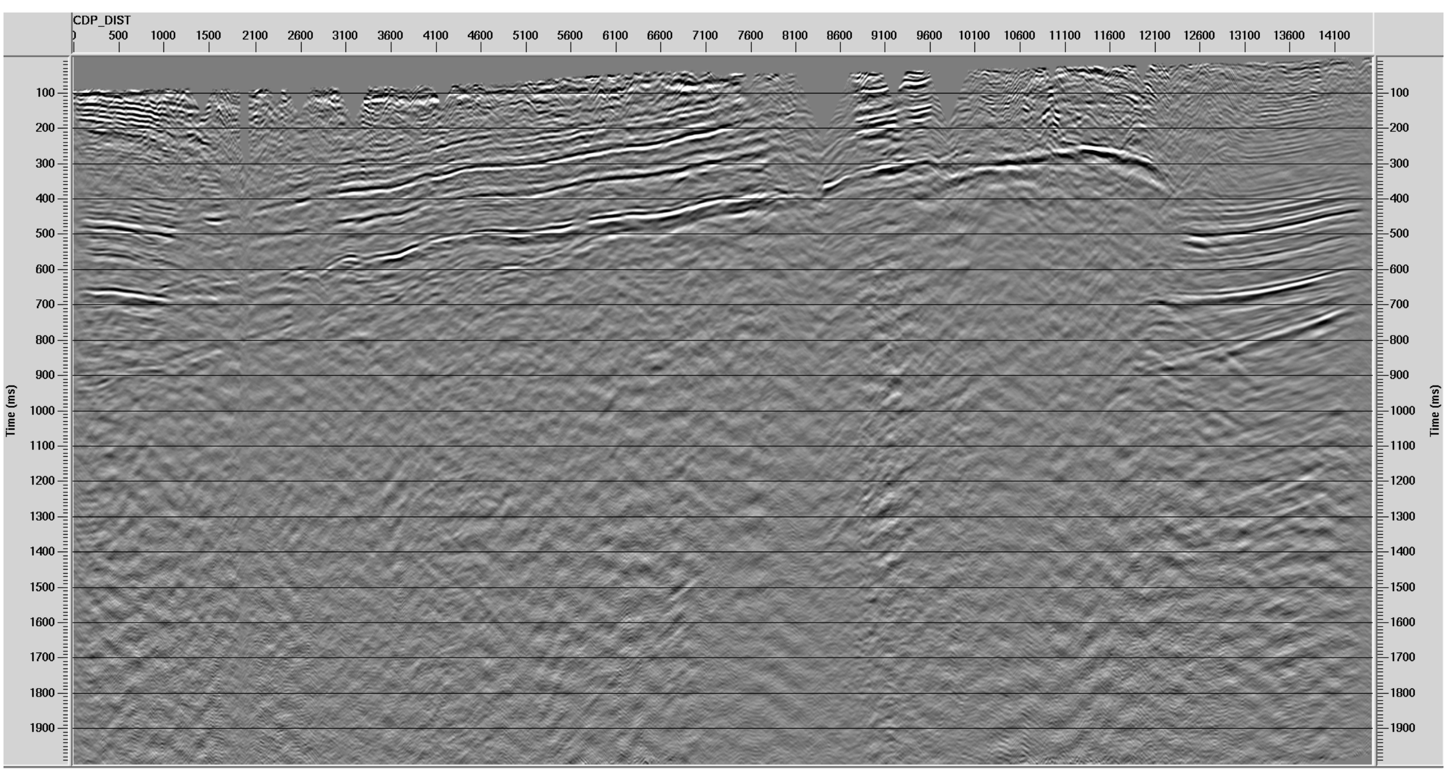

Figure 48. Stacked section after post stack enhancement.

8.1.15. *Post-Stack Time Migration.* Post-stack migration is a seismic processing method that aims to replace reflectors in their correct positions and collapse diffractions present in the seismic data. Post-stack migration is needed due to the fact that variable velocities and dipping interfaces cause the data to misplace reflector in a time seismic section. Post-stack produces optimal results when the geological dip and lateral velocity variation are relatively small. Therefore, this migration is applied when the seismic data has very few complex structures.

The RMS velocity obtained by the most current velocity analysis is smoothed in order to avoid large lateral velocity variations. For a reflector with a certain dip, its location and dip is changed based on its local velocity. Therefore, in the FK domain, each dip event is phase shifted in frequency and wavenumber (which corresponds to a spatial-time relocation of the event) based on the local RMS velocity. This migration implemented in the FK domain is commonly called Stolt Migration [**41**].

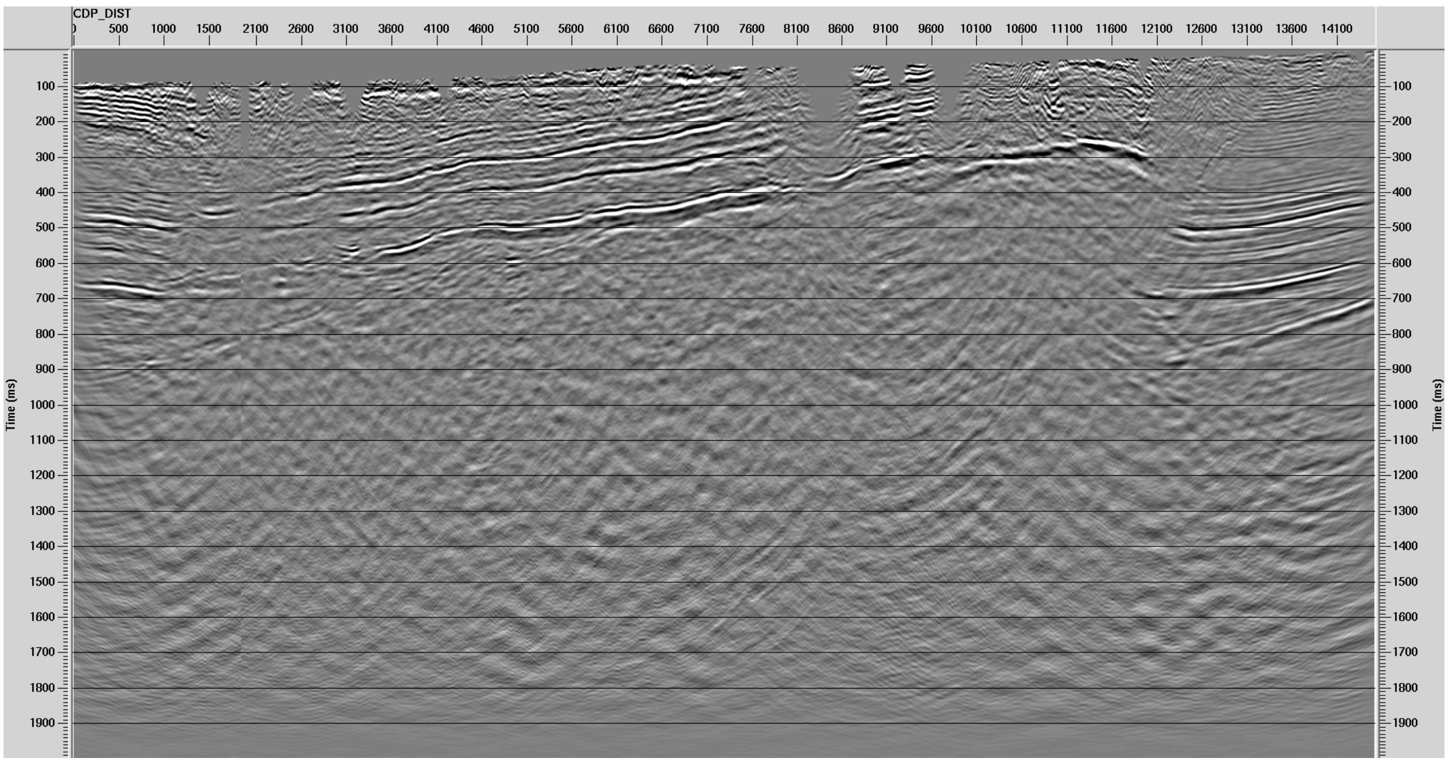

Figure 49. Post-stack time migrated section using Stolt migration.

8.1.16. *Post-Stack Depth Migration.* Depth migration is the process in which an interval velocity model is used to produce a section that displays the vertical axis in the units of depth. This process of converting from time to depth will allow us to correlate between the other surveys that were performed along the main survey line. In general, depth migration is more useful in industry and practical situations since it handles lateral velocity variations. It also allows outside geology and well information to be directly correlated to the seismic data, which helps in different types of geophysical projects [**42**].

The post-stack depth migration used here is an implicit finite-difference (FD) migration. The RMS velocity is converted into an interval velocity in depth. The migration algorithm implements a downward continuation, extrapolating the seismic data on the surface to each depth step by an approximation of the wave equation using the interval depth velocity. This downward continuation is implemented in the Fourier domain. Once a wavefield is formed, which contains the data at each depth step, a seismic image is formed at zero time (t=0) [**43**].

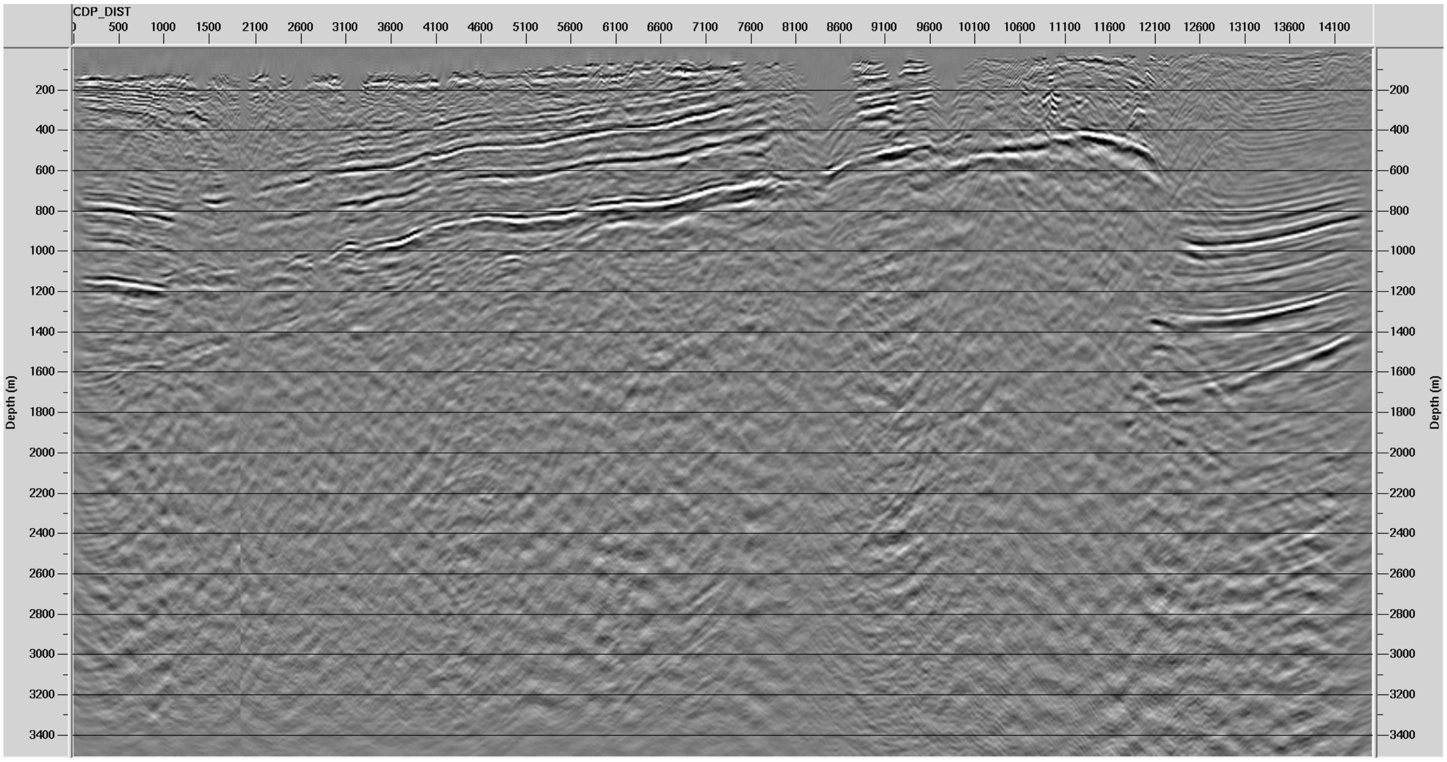

Figure 50. Post-stack depth migrated section, using implicit finite-difference migration

8.1.17. *Assumptions.* The final products shown here, which are the migrated sections, have been through a processing flow that have underlying assumptions that are needed to highlighted here before any further interpretation:

- CMP Locations are scattered nearby the main line. We assume that the skid (distance between the real CMP points and the center of the processing CMP Bin) does not affect considerably the processing (See Geometry subsection).
- The velocity analysis is based on a simple NMO correction, which assumes a series of horizontal homogeneous isotropic layers above a certain time. Better corrections requires additional terms in the NMO equation that consider seismic anisotropy, which are not used here (See Initial Velocity Analysis subsection).
- Spiking deconvolution assumes a stationary source wavelet throughout the entire record length, and also assumes the earth's reflectivity is aleatory. Another assumption is that the level of noise in the seismic trace is low (See Deconvolution).
- During stacking, the main assumption is that a CMP (Common Mid-Point) corresponds to the projection on the surface of a CDP (Common Depth Point). This is only valid if we consider horizontal homogeneous isotropic layers in the subsurface. For a reflector with a certain dip, the CDP will be located not vertically down from its CMP (See Stacking).
- Post-Stack Time Migration assumes that lateral velocity changes are small. It also assumes smoothly varying velocity in time (See Post-Stack Time Migration).
- Time-depth conversion applied on a time migrated section is sort of inaccurate, placing reflector not exactly at their true locations by a considerable range. From industry experience, this range can even be of couple of hundred meters.
- Post-Stack Depth Migration can handle lateral velocity variation. As it only migrates the stacked section, its main underlying assumption is that for a certain CMP gather, traces from different offsets corresponds to the same CDP (See Post-Stack Time Migration).

8.1.18. *Summary.* Overall, by following the seismic processing flow, an image that started with very few structures and horizons is transformed into a final image that could undergo geological interpretation. Many different techniques were used to enhance the quality of the seismic section. Some of the most influential processes in the workflow were elevation and refraction statics, surface wave noise attenuation, residual statics, and post/pre-stack migration. The process that had the greatest impact on the improvement of the seismic data is refraction statics, as shallow velocities near the surface have a large impact on the quality of the section, by producing significant time delays. The other techniques are able to enhance the general fault and fold features, while removing smear and tightening the horizon reflector amplitudes. SeisSpace provides the necessary user interface and functions to properly follow and process the raw SEG-D data into a presentable image of Chromo's geological subsurface.

8.2. Results. The main features of interest in the final 2D seismic cross section are two large faults occurring at the beginning and end of the line, and a fold structure interacting with the thrust fault. In general, the post-stack time migration did an effective job making the geological structures and horizons appear in higher resolution. The post-stack depth migration is useful for practical engineering purposes, such as geothermal, oil, and gas drilling projects. Using both of these final seismic sections supplemented with background geological analysis, horizons, faults, and folds can be estimated at specific locations in the subsurface.

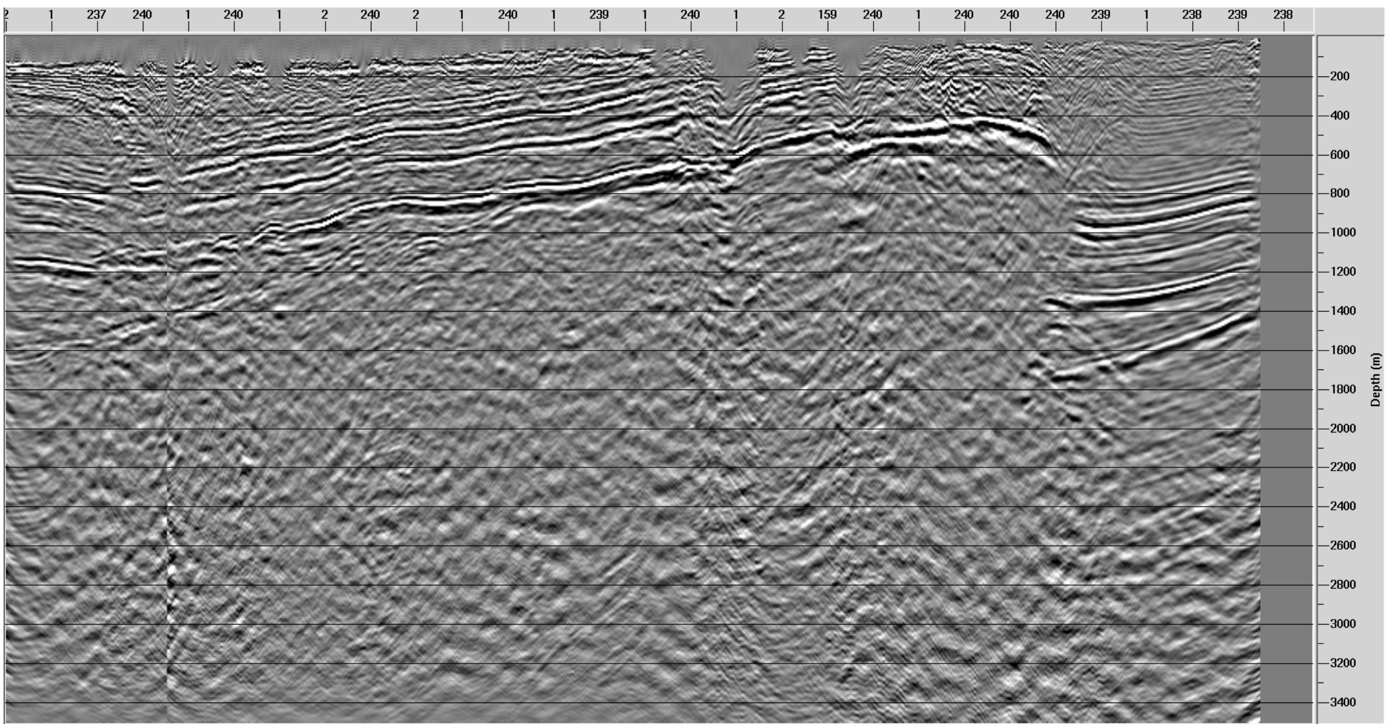

Figure 51. Poststack depth migration seismic section

Looking at Figures 51 and 52, a grayscale seismic section has been overlain with the geological layers present in the Chromo area. Layers within the seismic section are distinguished by strong, continuous reflectors spanning horizontally across the image. Analysis of these reflectors combined with knowledge about local geology leads to interpretation of geologic bedding. There is a regional, asymmetric anticline present in the image: the axial plane appears to be dipping to the left, at approximately 6 degrees. This anticline was produced by a large uplift in the Precambrian Basement layer. This can be confirmed by the thinning from SW to NE of the Pre-Jurassic layer. After this older geological event, sedimentary layers were deposited in a marine setting, unaffected by the uplift event. It appears that the thrust fault was then activated, causing around a 450m throw of the geological layers to the NE. On the SW side of the seismic line, a normal fault appears to be active, causing a 70m throw. Faulting features are typically present in seismic imaging where reflections truncate and appear again at a shifted depth or direction. The processed seismic image exhibits events near flags 235 and 1394 that confirm faulting activity in the area, as shown by Figure 51. Along with these two large fault systems, there are multiple fracture planes present in different areas of the section. The Kirchhoff pre-stack time migration section does a better job displaying these faults and fractures, as seen in Figures 53 and 54. The final seismic images did an excellent job displaying the geology and specific structures in the subsurface of Chromo.

Observations of Figure 55 reveal an obvious discontinuity of all the reflectors around flag 235. The beds also change dipping directions from west to east. This indicates a major normal fault that goes all the way into the basement rock. In the center of the seismic section (Figure 51) there are a number of smaller faults present. We interpret this region as a fracture zone, which agrees with the interpretation from last year. The fault on the east side of the image was interpreted last year as a reverse fault with a dipping angle for about 60°. The fault was also interpreted to change the direction near surface drastically. By applying the processing techniques we can clearly see on Figure 55 that the fault is indeed a reverse fault, but the dipping angle is much larger making the fault almost vertical. The fault is also consistent from the surface to the basement rock. This interpretation is geologically more realistic than the result last year.

In reference to fluid flow, patterns that produce hot springs at the surface may be present. The two large faults and multiple fracture patterns create a feasible fluid transportation system.

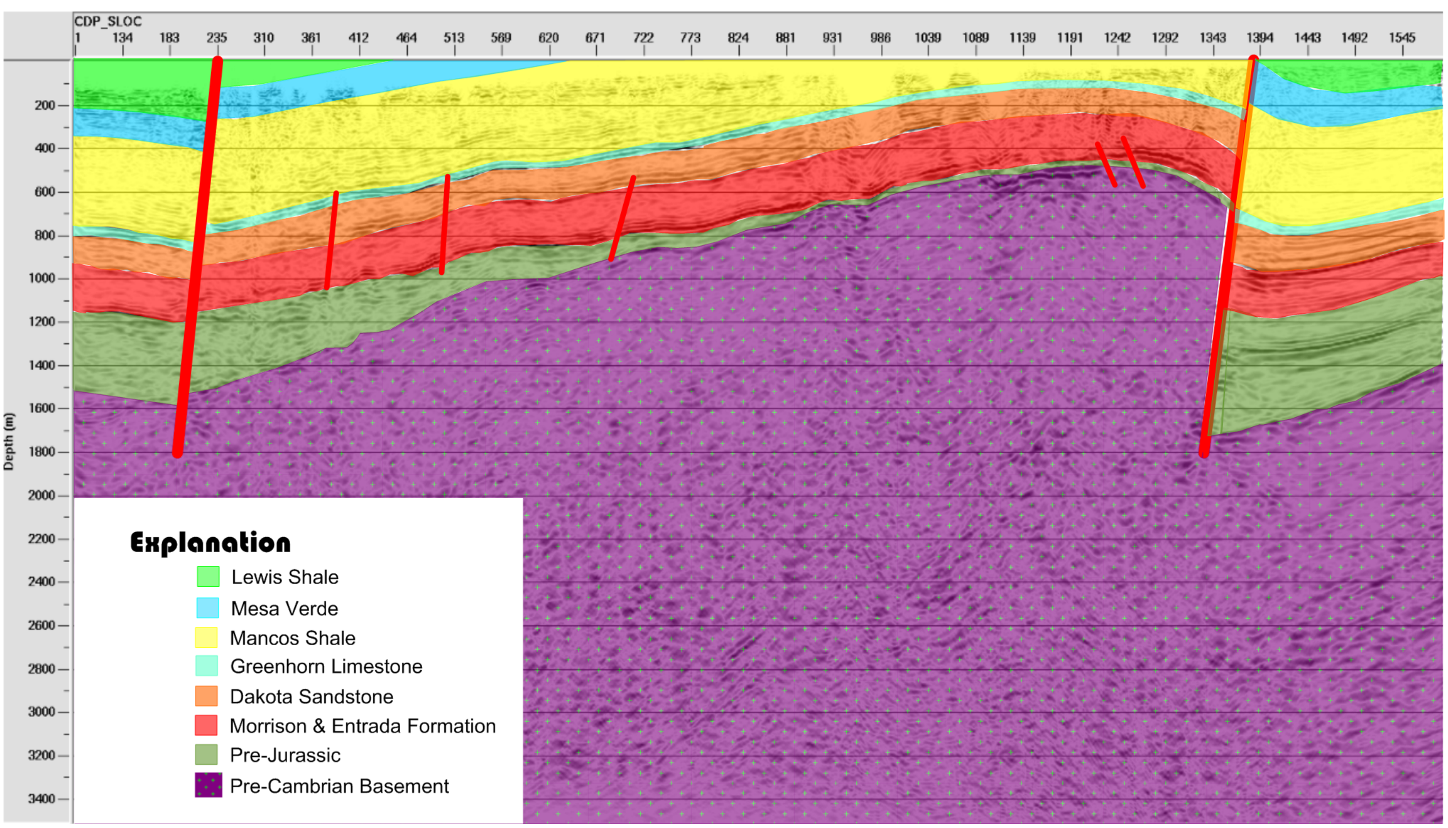

Figure 52. Poststack depth migration seismic section overlain with geologic layers

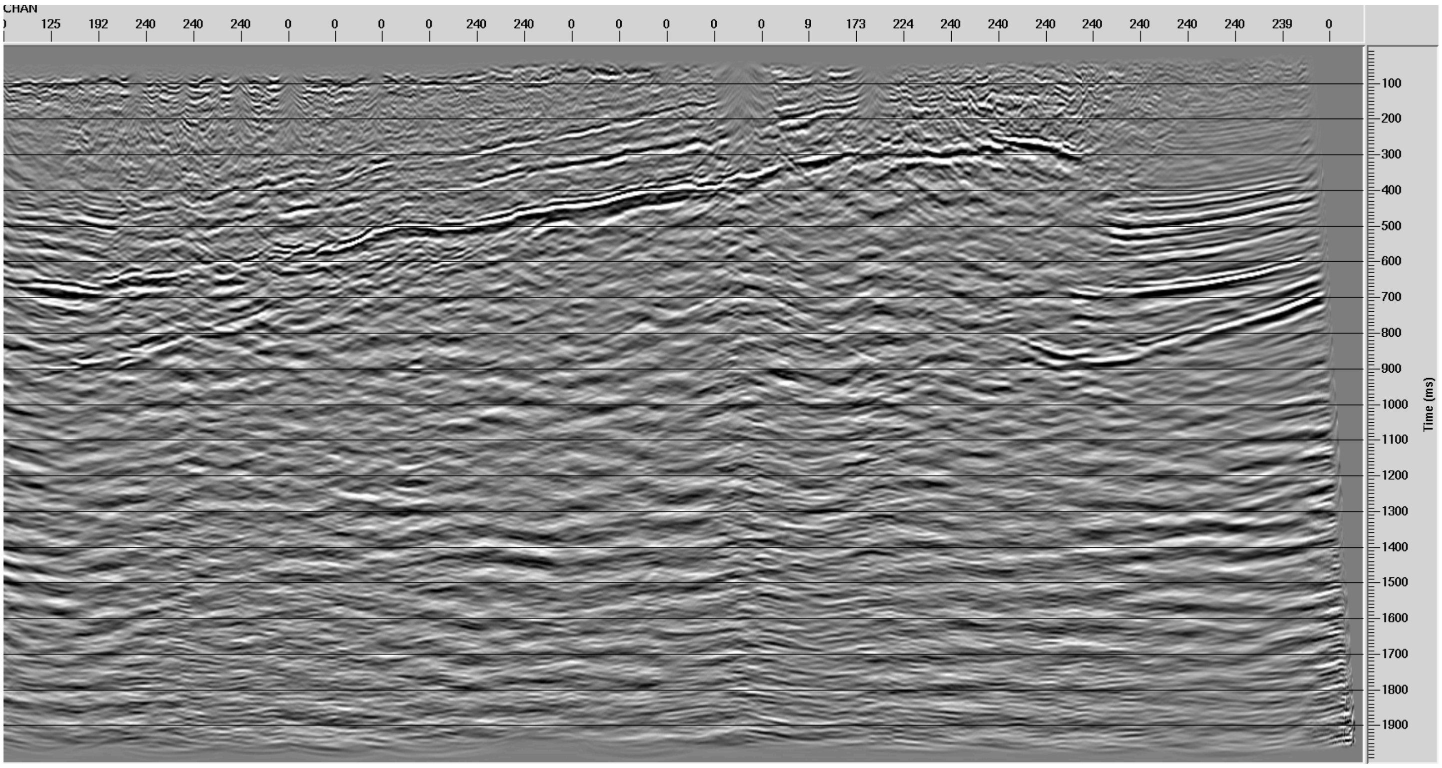

Figure 53. Kirchhoff Pre-Stack time migration seismic section

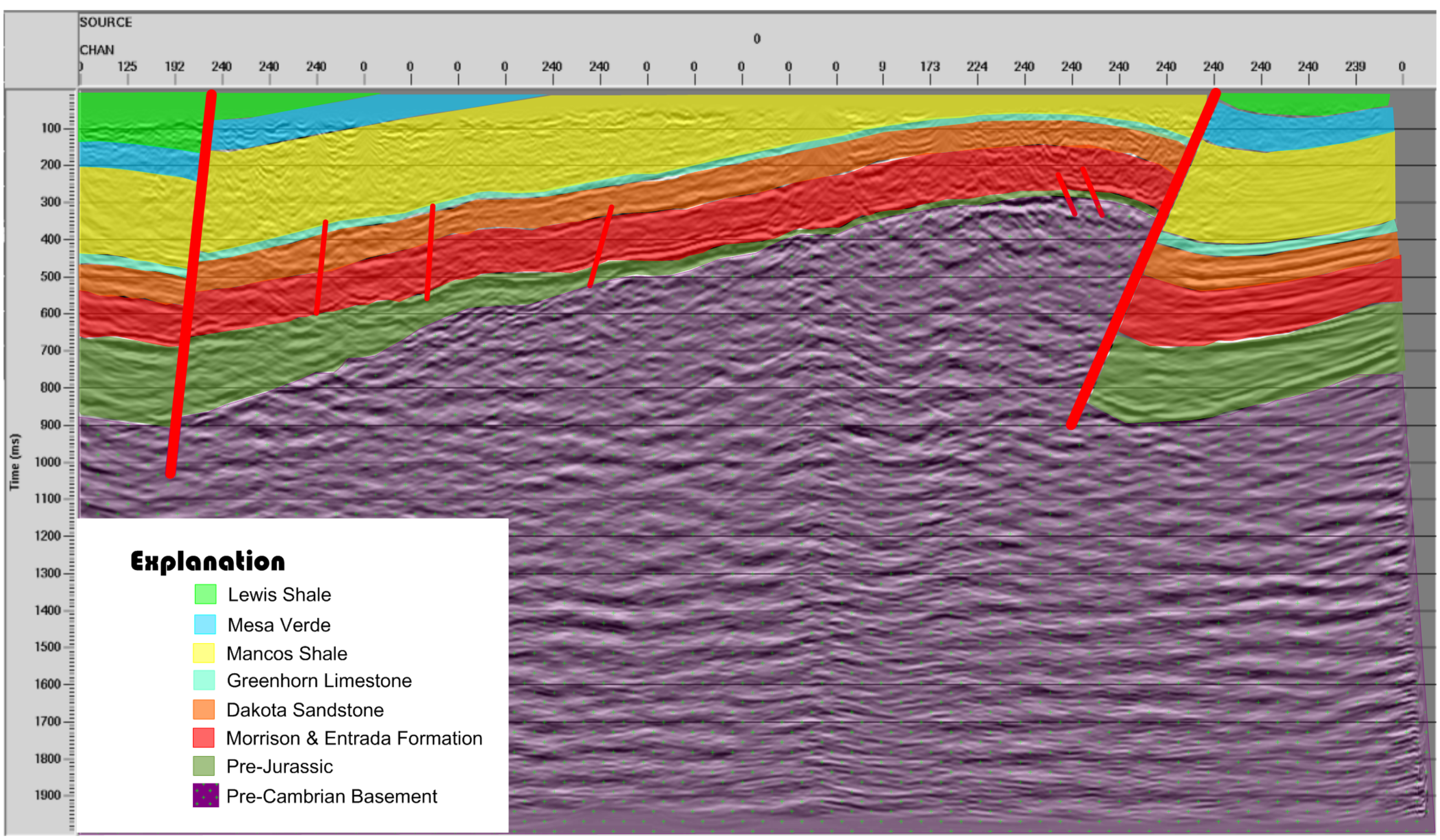

Figure 54. Poststack time migration seismic section overlain with geologic layers

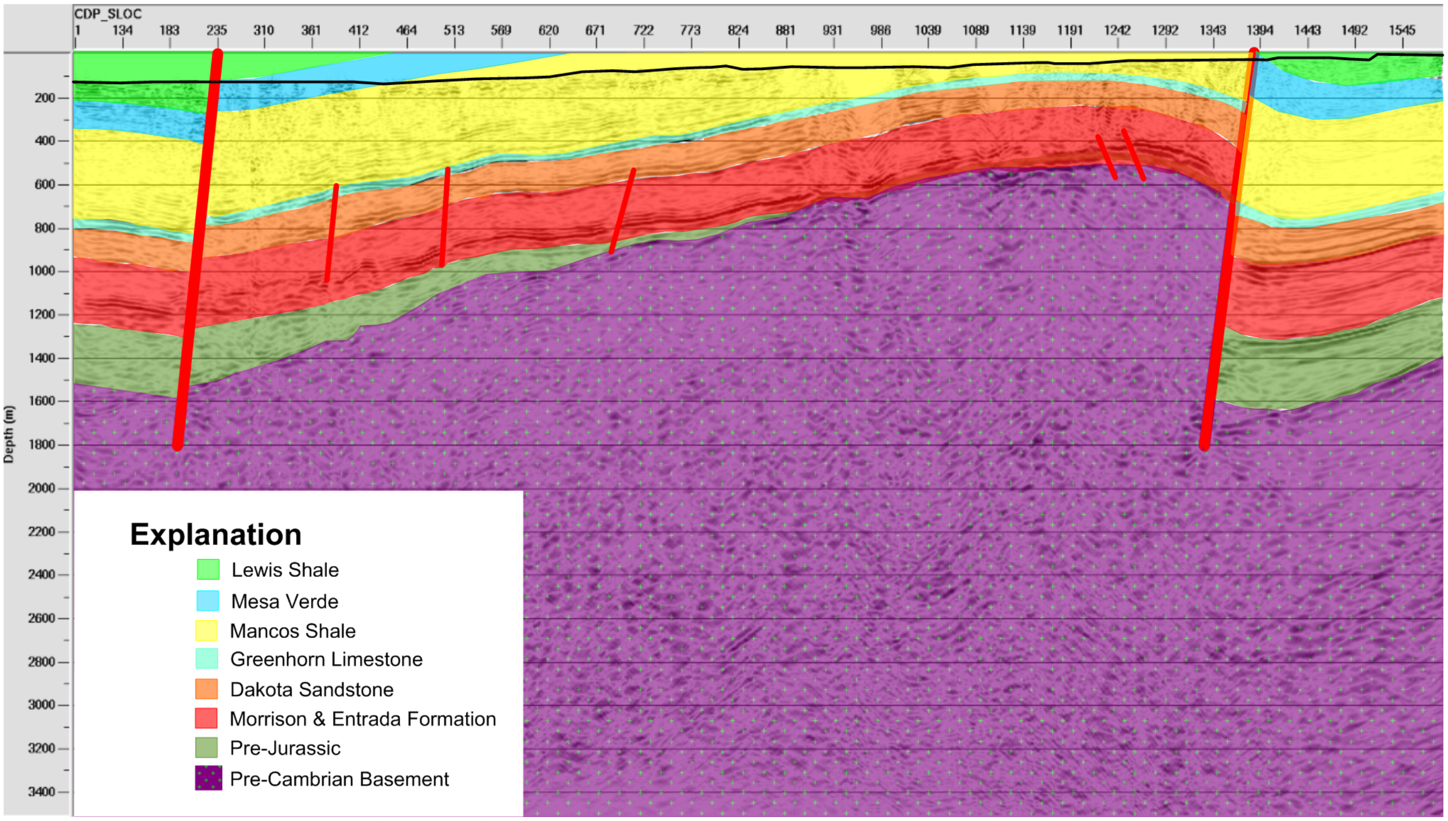

Figure 55. Final interpretation

8.3. Sources of Error.

8.3.1. *Survey Errors.* Common problems experienced during both cable layout and acquisition include: bad connection between cables and geophones, inclement weather, trouble planting geophones, lack of communication between doghouse and field workers, influence of nearby crew, and various human errors.

For seismic surveys, bad weather, such as rain, can cause serious problems to the data acquisition. Rain drops can hit the geophones and cause spikes on the data. Such traces often need to be removed, which reduces data resolution and quality. Rain also creates mud which decreases the coupling between the vibroseis and the ground and causes delays in the shooting process. During the survey, there were several days with heavy rains that caused delays in shooting and potentially affected data quality.

Permit permissions and vibroseis truck regulations limited the continuity of the survey. Regulations prohibit vibroseis trucks from shooting within 100m of local structures including houses and bridges. This is the cause for the main shooting gaps including the discontinuity across Highway 84. In addition, the road crossed paths with large open pipes, local water wells, rivers, and several other structures that made collecting the data not possible in these locations. These gaps compromise data resolution.

One of the biggest factors in the data that significantly affected the processing were bends in the line. There are two locations in which the road has a curve great enough to greatly affect source-receiver geometry. The majority of the line runs northeast with large bends near the end points. The first curve is at the southwest end of the line where the road turns sharply to the west. The second is after the discontinuity across Highway 84, where the line runs due east on County Road 382. Consequently, a crooked line geometry needed to be applied while processing the data. Although these are the two biggest errors in the straight line, the nature of the topography also leads to small effects in the data when processed as a straight line. Furthermore, the ground surface changed conditions through the entire main line, and some areas did not allow complete penetration of the ground. It was unavoidable that some geophones were not planted vertically especially when surface ground was not flat.

Another error in the recording of the data was incorrectly connected cables. The geophone connection process was simple but required a large amount of work. It was common that some connections were loose or skipped altogether. Doghouse controllers were able to confirm the connection between cables and geophones as well as the conditions of geophone plantings prior to data acquisition. Unfortunately, connection errors were mistakenly overlooked on a few occasions, resulting in erroneous geometry of the data for portions of the line.

Other errors in the survey include the disruption of data collection as a result of interference from other crews. The seismic main line was occupied by other groups such as DC survey group, Gravity, and GPS during recording times. Along with this, several vans and trucks drove on the line during the survey collection, creating minor vibrations along the road. This may have caused slight effects on the geophones that were actively collecting data.

The last potential error in the data is that the Vibroseis truck was driven by students for a majority of the time, who had no prior experience of operating such equipment before. When attempting to line up the truck pad with a flag location, many inexperienced students did not always stop the truck in the exact locations; as a result, the real shooting locations might not match the accurate shooting locations. These errors are generally irrelevant in comparison to the seismic survey scale and considering the real shooting locations have known positions.

8.3.2. *Programming and Interpretation Errors.* Corrections applied to data in order to make the final image are subject to error. Many of the tools applied in SeisSpace, such as crooked line geometry parameters, first break picking, the velocity picking based on semblance, and FK Fan filters, require user judgement. This potentially creates the largest source of error in processing because if the user chooses velocities that are not accurate then the stack will have poor resolution. For the geometry parameters, the traces will not line up as expected if source and receiver positions aren't accurately corrected. The FK Fan filter is a tool in SeisSpace that diminishes noise, but the user draws polygons around the areas with high noise. If the user includes an authentic signal in the polygon, the authentic signal will be filtered instead of noise. In the static corrections we apply a simple model for the elevation. All of the traces are shifted to a single elevation datum to mimic a flat surface. This creates uncertainty in the exact location of the trace in the subsurface and leads to a loss of resolution. When applying surface wave attenuation to the data, the velocities and frequencies chosen to remove can take away valuable traces in seismic section. This is where the resolution of the final stacked image will be lower quality due to the removal a important information.

One of the most important errors that can occur during this process is the interpretation of the seismic section. The interpretation of geological features is primarily based on geologic knowledge of the interpreter. When facing less obvious seismic responses, different people can express different opinions on the same section. The processed image is of better quality than the raw data, but the center of the stacked image still contains discontinuities. This may be caused by faults, but it can also be interpreted as data quality issue. Also, some faults presented on the image have very steep dip angles, the misinterpretation of the fault types may change the entire interpretation of the local geology.

8.4. Conclusion. Deep Seismic provides high resolution and great investigation depth, and therefore is an important part of our field camp project. Our goal was to use deep seismic as well as other geophysical methods to better understand the subsurface structures west of Chromo, CO, and to understand the geothermal flow within the area. We started acquiring data from the west end of last year's main line in order to connect two years' data together. With the generous help from Sercel and Dawson Geophysical, we were able to acquire data for 1014 flags in total, though there were several skipped flags due to nearby structures. Using deep seismic method, we located a main fault on the west side of the area that extends into the basement rock as well as smaller faults along the main line. These observations in addition to the fault identified last year may be the main transportation system of fluid and therefore may be the source of the geothermal energy in the area.

Upon returning to Golden, students worked in the lab processing the field data. We worked under the guidance of experts, Robert Basker and Hugo Garcia, to complete our processing in SeisSpace. The processing was able to combine the 2014 line with the 2015 line and convert the raw shot data into an interpretable image that showed both the faults and geologic boundaries in the subsurface. We are very fortunate to be able to experience the entire seismic method from start to finish and it has been a valuable experience.

Based on the results from seismic processing, we can recommend modifications in possible future deep seismic acquisitions in order to deliver a better final product. Larger offsets should be used, since it increases the depth of investigation and seismic velocity resolution for deeper areas, and we believe the areas where main faults exists will better imaged. The shot gaps that existed in our acquisition due to obstacles or building should be avoided next time. From processing, we realized that using a crooked line geometry enables us to accept shots that were recorded with large deviations from the main lines. Therefore, whenever obstacles or building appear on the main line, instead of no shot record, a shot record away from the obstacle or building should be recorded. The main line should be designed to be as straight as possible, with few large bends, and small deviations within a range of dozen meters that can be handled by crooked geometry.

9. Hammer Seismic

9.1. Processing. Hammer seismic data is processed using Madagascar [**44**]. In principle, it is better to focus on refraction analysis since hammer seismic data contains few reflection events. In this case however, we can utilize reflections since the data contained on the Main Line has relatively longer coverage and denser source and receiver arrays.

The data consist of three files, one 2D line (Line 3000) and two roll-over 2D lines (Line 3100 and Line 3200).The raw field data contain test shots and false shots, these are removed along with other unwanted shot gathers. An example of Line 3000 shot gathers after editing is shown in Figure 56. The shot gather contains 72 geophones with 1 m spacing. Two types of geophones were used to record the data. The first 60 are 10 Hz geophones and the last 12 are 40 Hz geophones, this equipment change causes the event jumps around traces at 60 m.

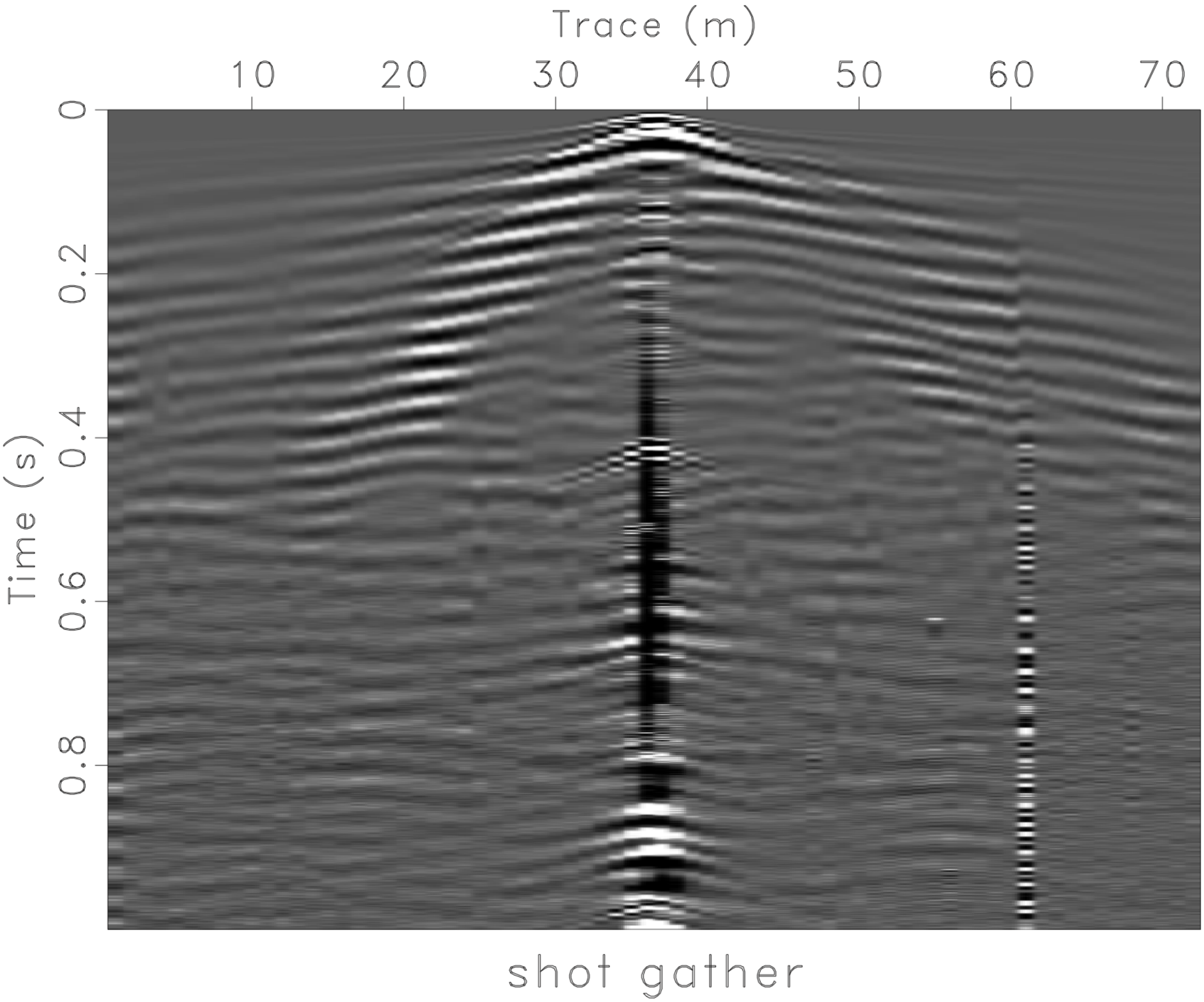

Figure 56. Shot gather

Line 3100 and Line 3200 are rollovers of the Line 3000. The data is processed by integrating the three lines and entire line with rollovers. Line 3200 has coarser shot spacing than Line 3000 and Line 3100; therefore, the program sfremap1 is used to interpolate Line 3200 to 1 m shot spacing before the lines are integrated. Since each shot gather has different offset ranges and Madagascar requires regularly sampled data, the offset range is extended in each shot gather to -119.5 m to 119.5 m. An example of the integrated shot gather is shown in Figure 57.

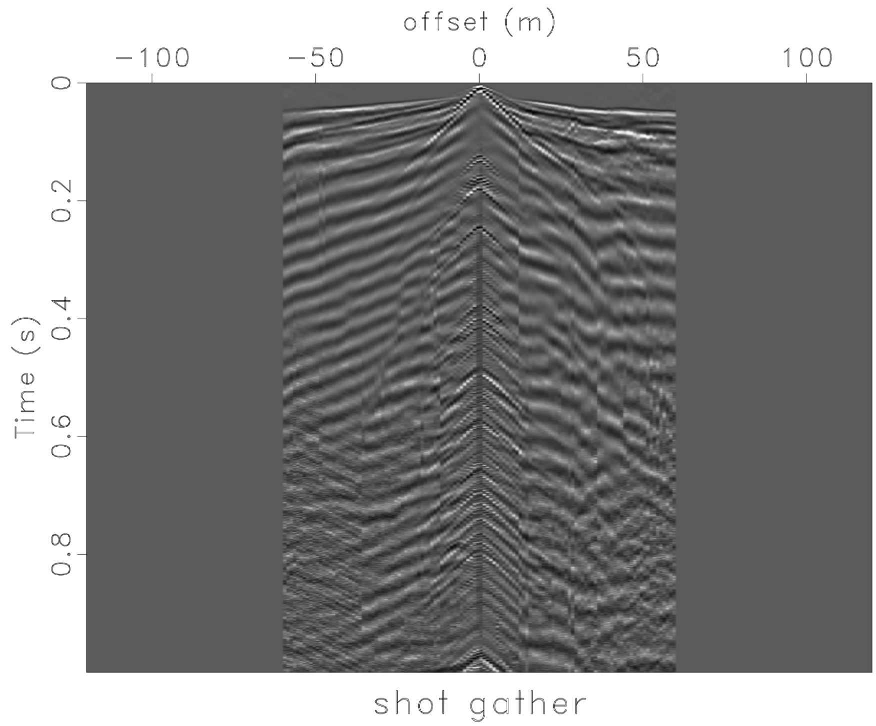

Figure 57. Shot gather

The shot gathers do not show useful reflection events, and are sorted to common midpoint gathers using the program sfshot2cmp. Since the offset axis is coarsely sampled, the negative offset is flipped to positive offset and interleaved with the original positive offset. This step has an assumption of reciprocity. Figure 58 shows a typical common midpoint gather. The CMP gathers are looked at directly to interpret the data. Since the data is dominated by the low frequency surface waves, high-pass filters were applied. Three CMP gathers are plotted in Figures 59, 60 and 61. The red circled areas in Figures 59 and 60 are possible reflections. They appear however to have different arrival time which indicated that the reflecting layer is probably dipping. The common offset sections are also looked at and are shown in Figure 62, 63 and 64. The circled areas in Figure 63 and 64 are possible dipping layers.

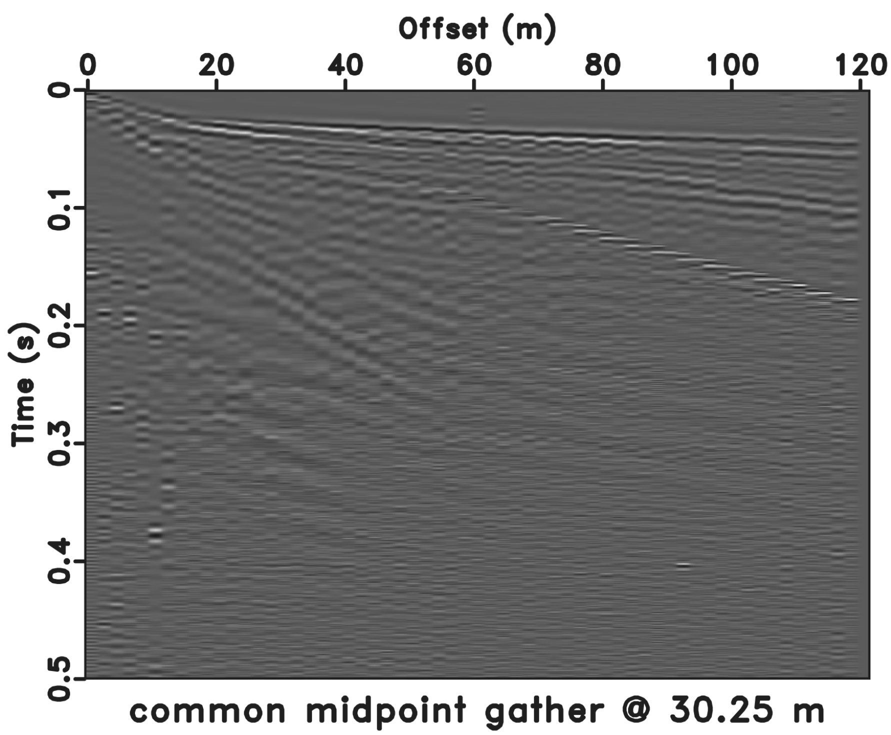

Figure 58. Common midpoint gather at 30.25 m

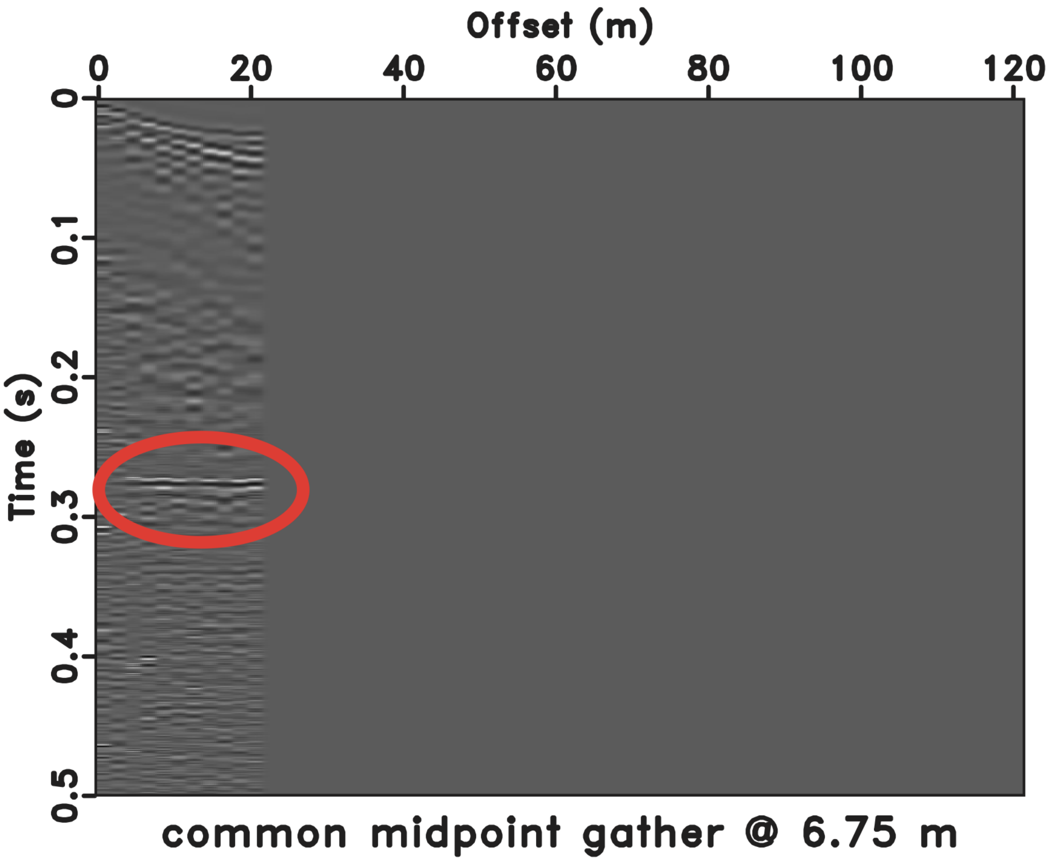

Figure 59. Common midpoint gather at 6.75 m

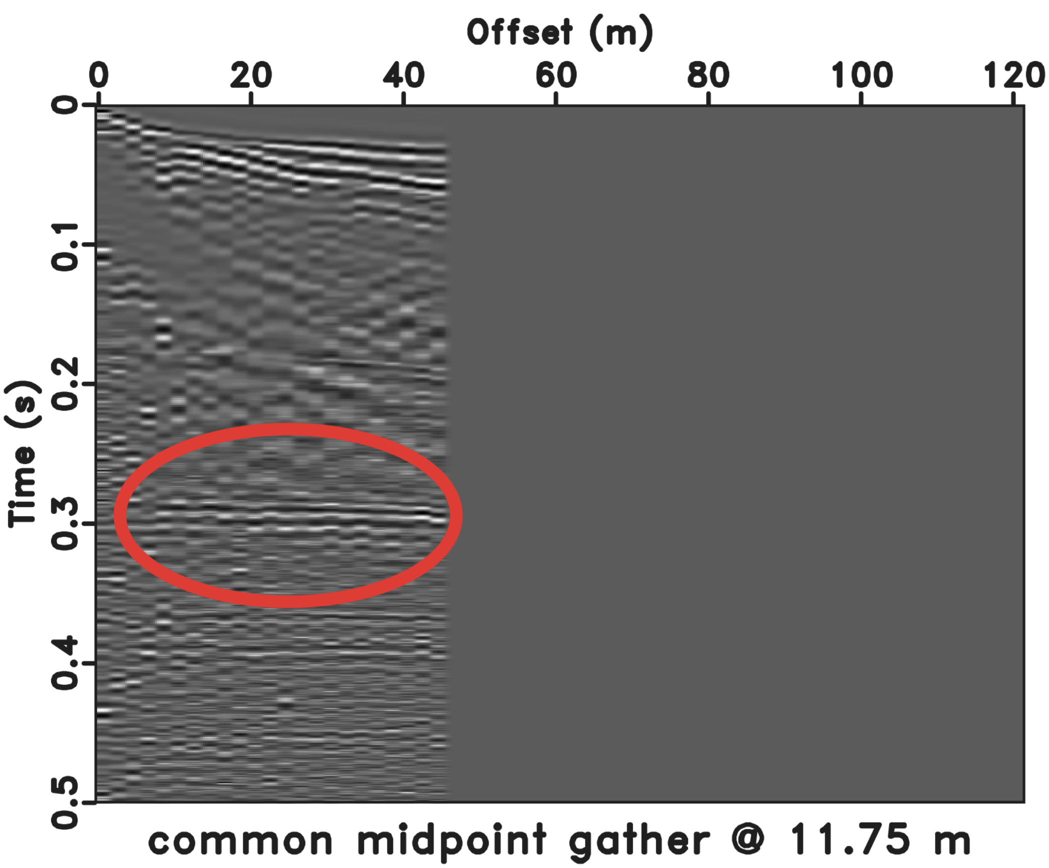

Figure 60. Common midpoint gather at 11.75 m

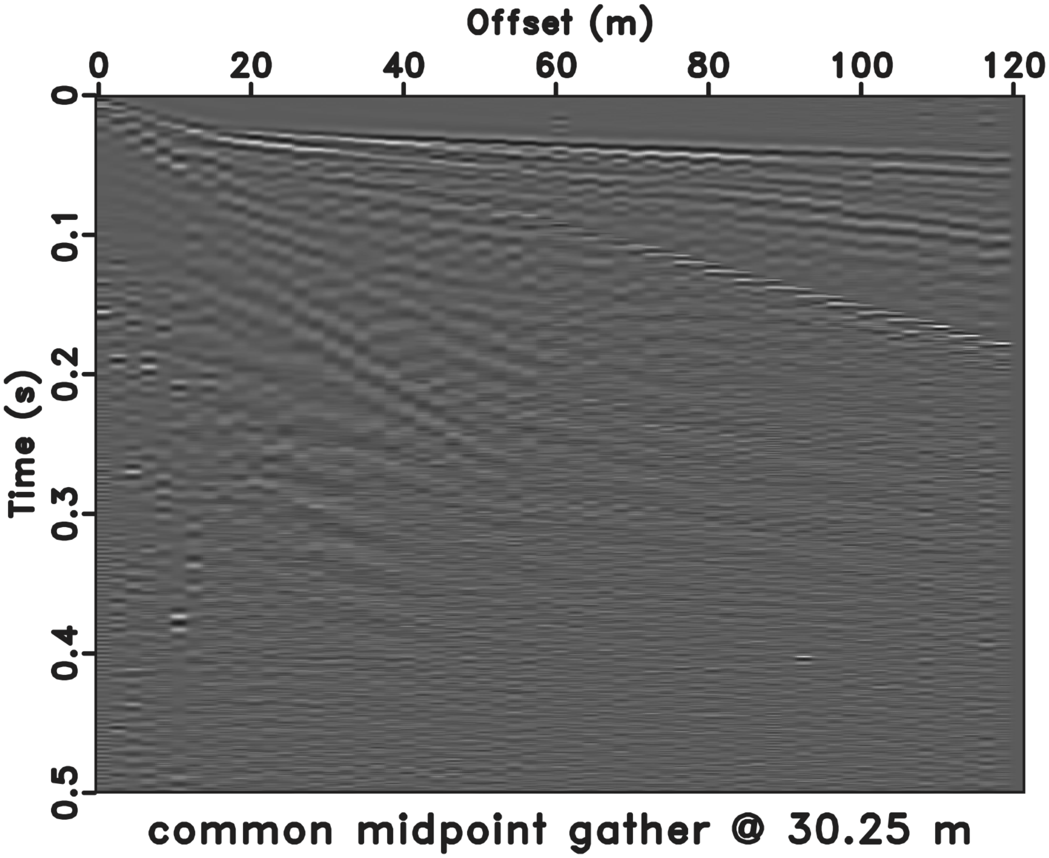

Figure 61. Common midpoint gather at 30.25 m

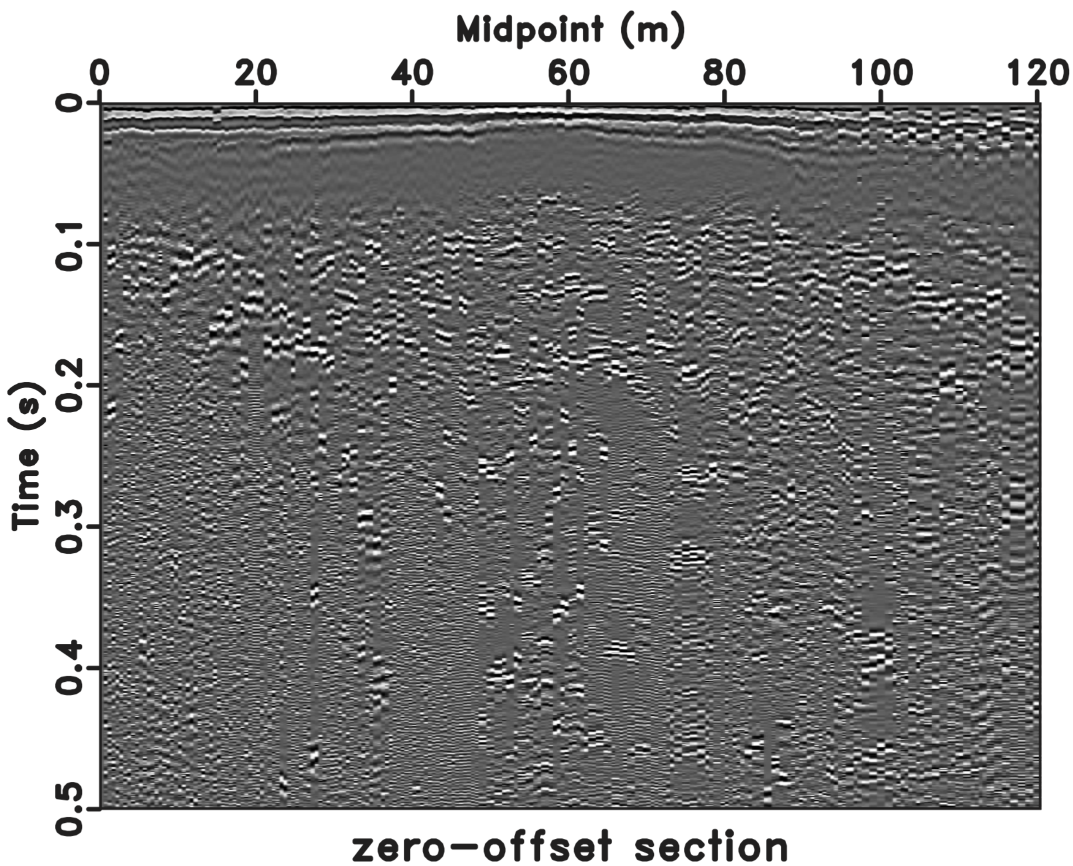

Figure 62. Zero-offset section

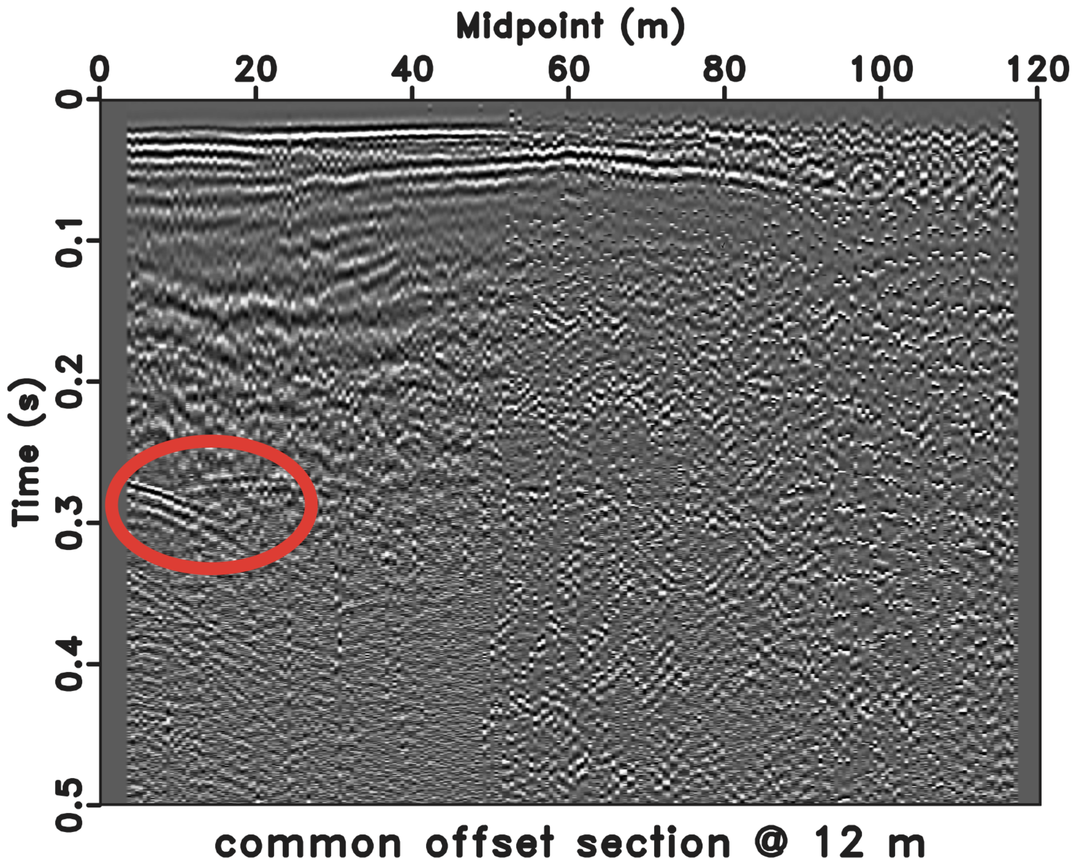

Figure 63. Common offset section at 12 m

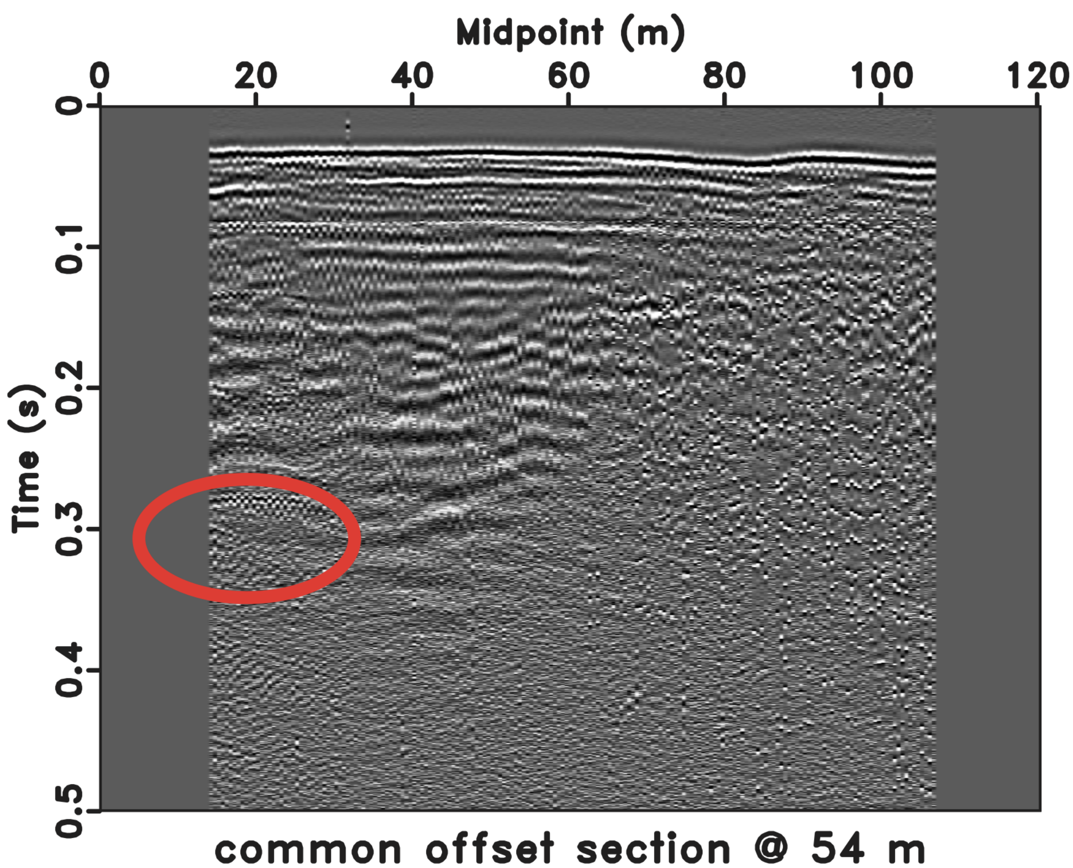

Figure 64. Common offset section at 54 m

Since the reflections are the events of interests, a normal movement analysis is performed and the semblance scanning plot is examined, which is shown in Figure 65. Velocity scanning is done for selected shot gathers and aim to produce a consistent velocity profile used for normal moveout (NMO) corrections. Time to depth conversions are done for the zero offset image based on the picked velocity profile.

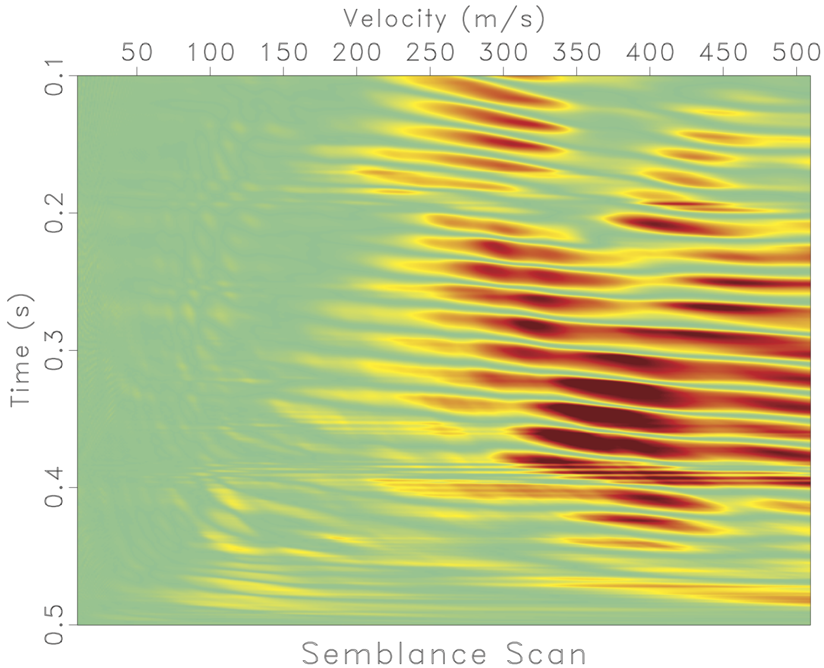

Figure 65. Semblance Scan

9.2. Results. After time to depth conversion, the final velocity image is shown in Figure 66. From the image, four layers are clearly seen. The first two layers are almost flat and the last layer has an dipping shape. These layer are very shallow and are only three meters deep. The deeper part of the subsurface is imaged with decreased resolution because hammer seismic energy can not go too deep into the subsurface. But, as seen in figure 63 and 64, some reflectors may be visible at relatively deep depths. Unfortunately, there are not enough reflectors to make an accurate velocity model in the pursuit of resolving these possible reflectors further.

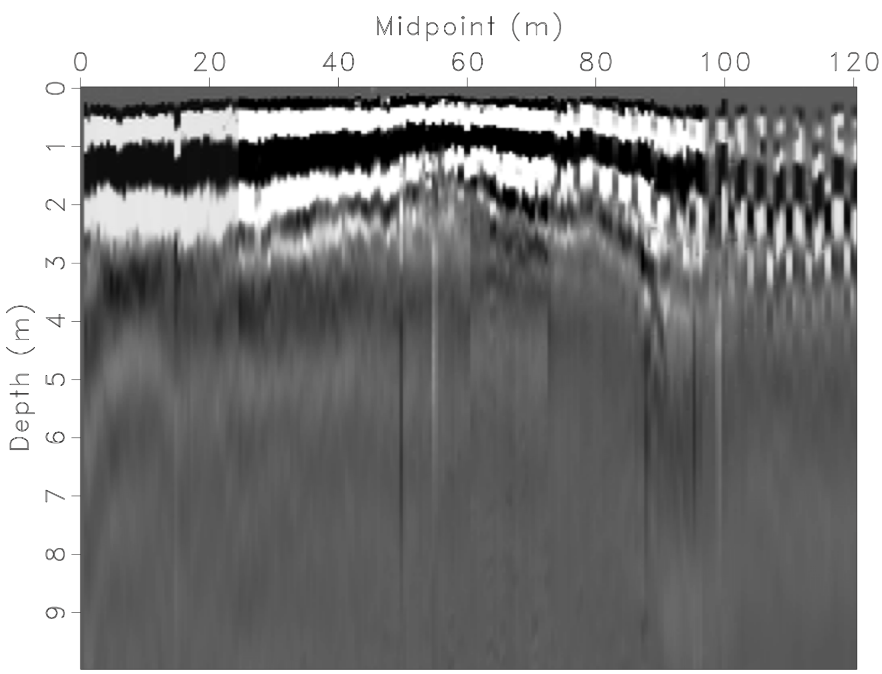

Figure 66. Final velocity

9.3. Sources of Error. The hammer seismic method mainly targets near-surface areas. Since the recorded data is often dominated by surface waves and refractions, applying the reflection analysis could be challenging. In the reflection analysis ground roll is regarded as noise, to be filter out. A bandpass filter requires knowledge of frequency content of the surface waves. The filter errors when wrong estimate of the surface wave frequencies are inputted. During the processing flow, methods like moveout analysis, semblance analysis, and time to depth conversion only apply to reflection data. Therefore, errors exist if these methods are applied to refraction data. The final step of processing, time to depth conversion, has the assumption of laterally homogeneous velocity, and the result can be improved by using more advanced time to depth conversion algorithms [**45**]. Migration techniques are not applied, so the reflectors in the final image may mislead the interpretations.

9.4. Summary. Hammer seismic data can help resolve near surface structures that may be missing from the deep seismic data. Rather than a refraction analysis, a reflection analysis is employed to find reflectors at near surface. From the final time-to-depth converted structural images four layers are visible. The top three layers are almost flat and the last layer has some dipping features. This survey on the main seismic line has revealed that hammer seismic is not the best method for imaging reflectors at large depths. Hammer seismic simply does not provide enough source energy to illuminate reflectors. Layers at very shallow depths can be seen but deep reflectors should be left to full scale seismic surveys. The following shows that processing methods besides reflection analysis can be used with hammer seismic to reveal valuable information about the subsurface.

SECTION 6

Reconnaissance Site

1. Introduction

For the past few years a student site has been an integral part of the Colorado School of Mines Summer Field Camp. The site has allowed students to demonstrate their abilities in creating and implementing a geophysical survey with any available instruments. In turn, this site further promotes confidence and experience within the field of geophysics. This year, the student site was rebranded as a “Reconnaissance Site” which signals a modification in the purpose of the survey. It was our responsibility to determine whether or not it would be desirable and feasible to do further work in this area.

The 2015 Reconnaissance Site was on US Forest Land (the San Juan National Forest) between the towns of Pagosa Springs and Chromo, Colorado. The site is located on Valle Seco Road off of Highway 84 and is about 16 km from Pagosa Springs (studied during the 2012 and 2013 field camps) and 28 km from Chromo (studied during the 2014 and 2015 field camps). Because of its central location, this area of permitted land has the potential to show geothermal connections, if any, between the two towns. It could also provide insight into the region’s geologic history. Four geophysical methods were chosen to characterize the area’s geologic features as well as any possible geothermal properties that might be present in the subsurface. These methods are electromagnetics, magnetics, hammer seismic, and DC resistivity.

2. Geology

There are many more intrusive igneous bodies present inside and around the permitted area of the Reconnaissance Site. These felsic dikes all typically strike to the northeast, and are relatively parallel. Most of the dikes are several kilometers long. Normal faults are also mapped running perpendicular to the dikes. The formation of interest, mapped as a Tertiary dike by geologists [**46**], and it extends roughly 2.8 km. The feature is present along a ridge which has a southwest portion higher in elevation and drops to the northeast. The southwest portion has an upper layer of Pictured Cliffs Sandstone; beneath this layer of sandstone is the Lewis Shale which is visible at the Reconnaissance Site. The dike visibly protrudes out of the subsurface and can easily be seen in geologic and satellite imagery. The dike is offset on either side of Valle Seco Road and there are several faults mapped in this general area.

3. Objectives

Students proposed questions to answer based on geologic maps, topography information, and brief in-person visits to the Reconnaissance Site. The big questions that we tried to answer were:

(1) What does the structure of the dike look like?
(2) Where is the actual location of the fault(s)?
(3) Is there fluid flow in this area?

After the questions were determined, the students next decided what geophysical techniques would be most useful to answer the questions. The area of interest was along Valle Seco Rd. where an igneous dike is mapped and a fault is shown near the road. There is surficial evidence of the fault because the two sides of the dike do not line up. However, the dike could also be two individual features. The instruments and methods chosen to study this area were based on the information they would provide as well as site constraints. The features we were to collect data over were covered in shrubs and cacti and would not conducive to large and/or heavy instruments.

Method	Purpose
EM 31 and EM 34	Describe subsurface conductivity changes.
Magnetics	Determine whether or not material is magnetic. Describe magnetic susceptibility patterns.
Direct Current	Define subsurface conductivity contrasts, particularly between the shale layer and the intrusion(s).
Hammer Seismic	Characterize the potential fault.

4. Magnetics

4.1. Survey. A geophysical magnetics survey works similar to a gravity survey in that it is a passive method that uses one of Earth's natural fields to find anomalies in the subsurface. In the case of magnetics, magnetometers utilize Earth's magnetic field to identify notable variations in magnetic susceptibility. It is a fairly common survey type due to its low cost and versatility. Furthermore, it can be easily implemented for standard geophysical investigations and is even useful for archaeological problems.

4.1.1. *Motivation for Survey.* When exploring the Recon Site location the survey crews discovered that there were small outcrops of the dike visible. Upon examining the outcrop further it was concluded the volcanic intrusion most likely contained the mineral magnetite, which as its name suggests is magnetic. Because of this the survey crews decided to conduct a magnetics survey on the dike. It was decided that the surveys would run perpendicular to the dike to give us the best view of its subsurface features. It was hypothesized this would give us a strong magnetic dipole response along the surface (see Section 6: Appendix for more information). The magnitude of the response as well as how quickly the response died as you moved away from the intrusion would give us an indication about the size and orientation of the dike.

4.1.2. *Survey Parameters.*

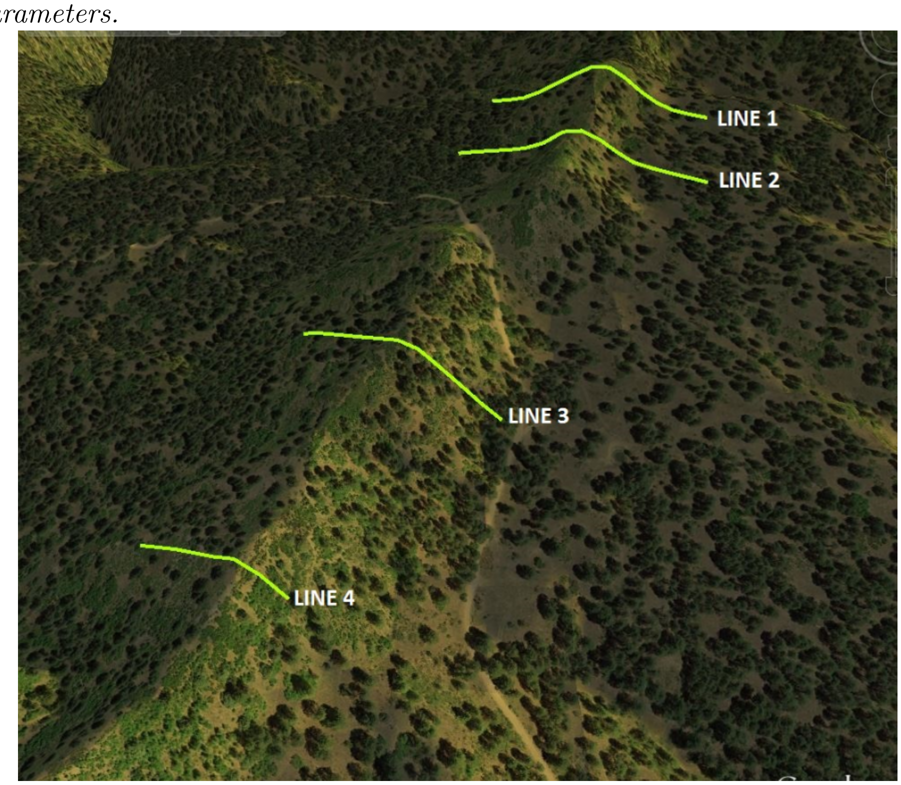

Figure 1. Google Earth image with 3x vertical exaggeration of the recon area

Magnetics surveys were conducted along Lines 1-4 shown in Figure 1. Line 1 was 150 meters long, Line 2 was 270 meters long, Line 3 was 190 meters long and Line 4 was 130 meters long. Each line ran roughly from east to west with a slight inclination to the north, to ensure it was perpendicular to the dike. Lines 1 and 2 were north of Service Road 653 and lines 3 and 4 were south of Service Road 653. Each survey was conducted by walking along the line with the magnetometer using a discrete data collection method. A discrete data collection method means data is collected when the user manually tells the device to do so. This is in contrast to a continuous data collection method where data is collected constantly along the line and a constant walking pace is assumed. A discrete data collection method was used due to the harsh topography and vegetation of the survey area. The time to walk between two flags varies greatly along the line because the environment is rapidly changing, which is not optimal for a continuous survey. On May 18 surveys were conducted along lines 1-4 with discrete measurements taken every 10 meters along the line. After preliminary processing, it was determined 10 meters spacing was not fine enough to accurately map the response of the dike. On May 20 another magnetic survey was conducted along Lines 1-3 with measurements taken every 2.5 meters. Line 4 was not surveyed on May 20 due to time constraints caused by poor weather and other survey crews in the area. Each day a magnetic base station was set up that was positioned off of the road further along to the north. The purpose of the base station will be explained in the data processing under diurnal corrections.

Notable sources of error during data collection stem from the natural region that the magnetic surveys were being conducted in. As mentioned above, the topography and vegetation of the area were very harsh. This hindered the surveyor's ability to walk in an exactly straight line at a constant pace. The topography, which included walking up and then down the large dike feature, caused the magnetometer to be closer and farther away from the ground depending on if you were going up or down the dike. This is explained further in Figure 2. Having the magnetometer closer to the ground leads to a higher reading because the magnetometer is closer to the source. It is best to have the magnetometer at a constant height above the ground but this was not possible with our survey location. This means that our data is slightly higher on the side of the dike where the surveyor was walking uphill and slightly lower on the opposite side where the surveyor was walking downhill which can be seen in Figure 3.

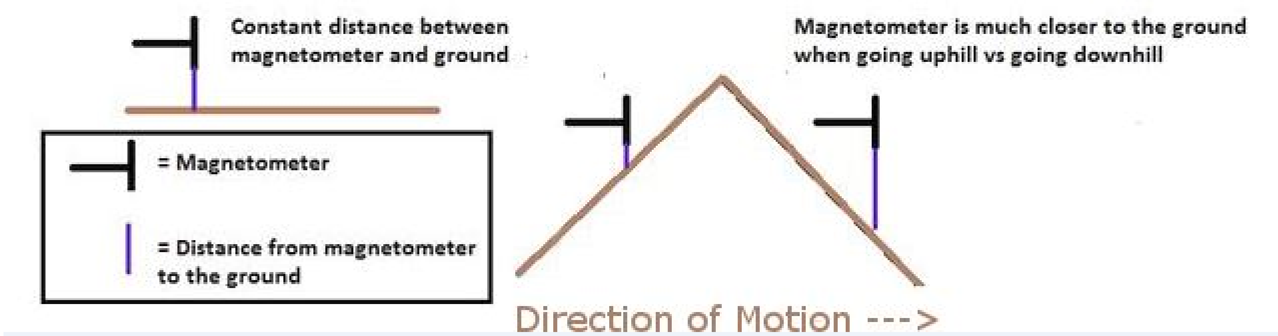

Figure 2. Distance of magnetometer to the ground over different topographies

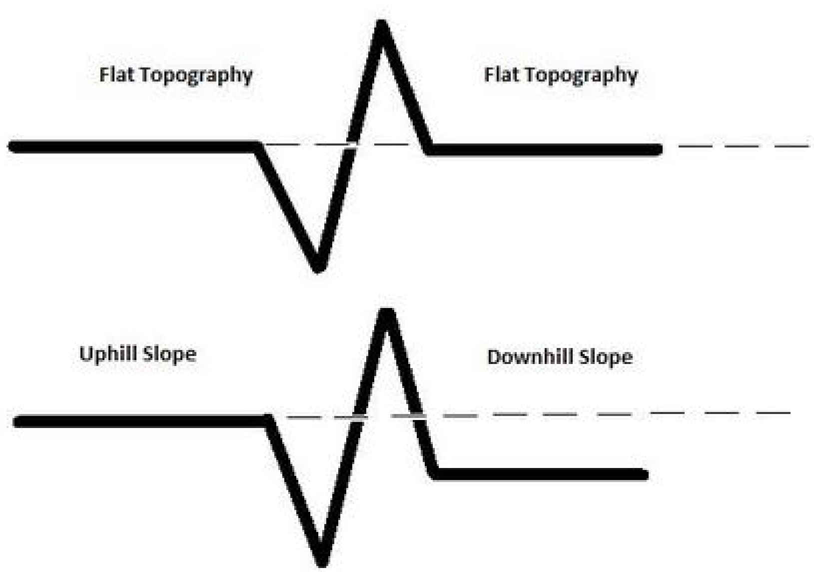

Figure 3. Magnetic response over flat ground vs hilly topography

There was also a barbed wire fence running parallel to the dike on its east side. Lines 1-3 crossed this fence on their far east end and the length of Line 4 on the east side was limited due to this obstacle. This had to be accounted for in the data processing and will be further explained in the data processing section for this survey method.

4.2. Goals of Investigation. The original goal for carrying out a magnetic survey in the Recon Site was to combine it with gravity data and create an inversion of the area to fully image it. Due to weather and time constraints however survey crews were never able to get any gravimeters up to the area. Instead focus shifted to simply trying to characterize the dike. Using magnetic data the processing group tried to determine the width, depth, dip, and magnetic susceptibility of the dike. Magnetics collaborated with other methods used at the Recon Site to help solidify the conclusions reached with this method.

4.3. Processing. The raw data is plotted with the program MagMap2000. The raw magnetic response recorded along each line can be plotted in a simple graph with flag numbers along the x-axis (units of meters) and the magnetic response along the y-axis (units of Tesla). The next step is to despike the data, removing any erroneous readings from the base station data, and apply a diurnal correction by using the base station data. A diurnal correction is a correction to remove the earth's background magnetic field so that only the magnetic response of the target is left. The base station is set up in an isolated location away from the survey and anything with a magnetic response (fences, cars, etc.). It is set to take a measurement of the magnetic field at a certain time interval throughout the day. The earth's magnetic field changes throughout the day and affects the reading of the magnetometer on the survey line. An erroneous reading in the base station data is one which does not fit the daily trend and is often characterized by a small spike an order of magnitude greater than the other readings. The diurnal correction takes the reading from the magnetometer and subtracts the base station reading that was taken at the same time. The reasoning behind this is that the magnetometer reading is a combination of the target's magnetic field and the earth's magnetic field. The base station reading is just the earth's magnetic field. Subtracting the two will give you just the target's magnetic field. This is explained in Figure 4.

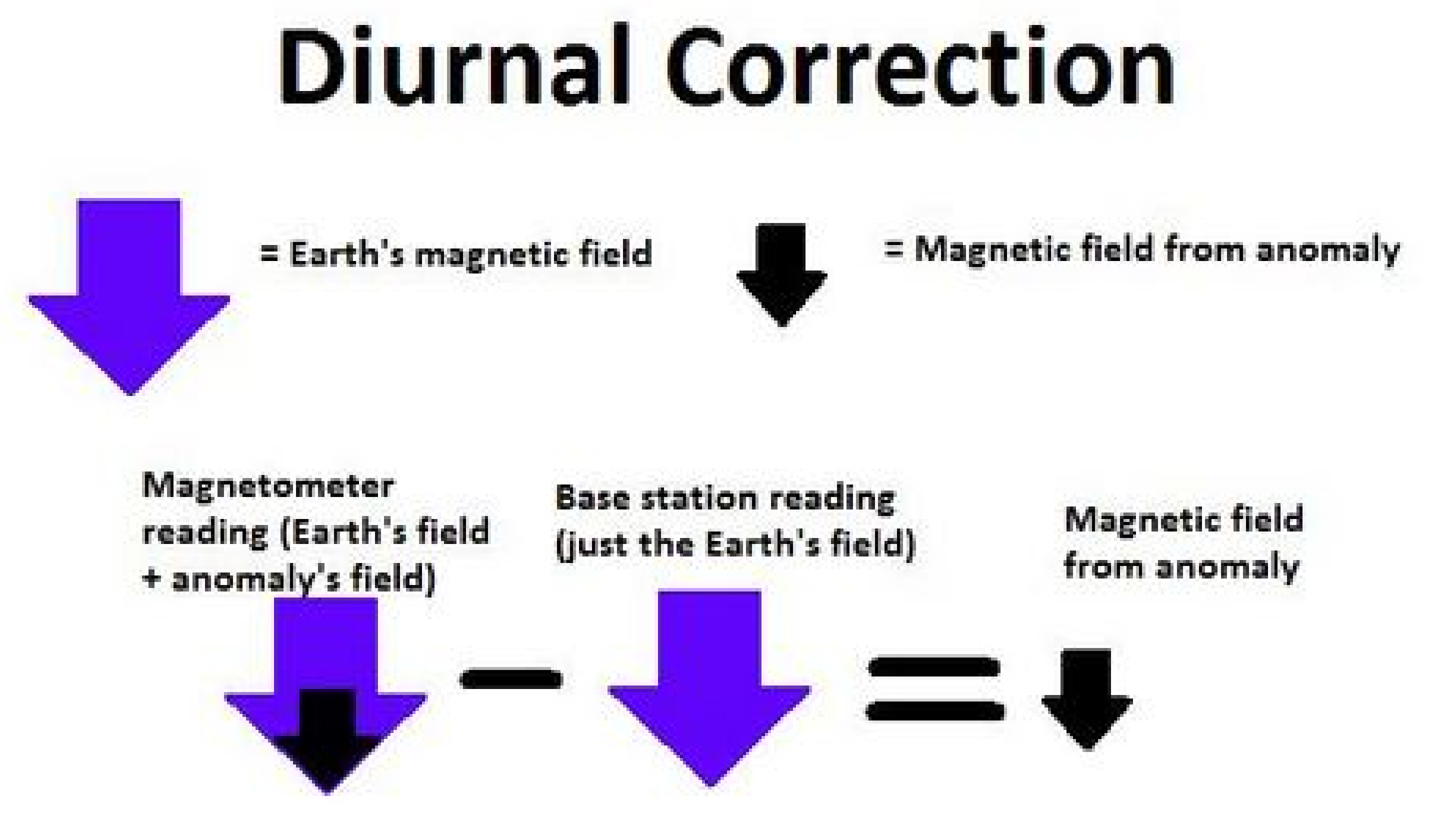

Figure 4. Diagram explaining a diurnal correction

The MagMap2000 program is set up to perform a diurnal correction. Once you have the base station data and survey data open in the program, simply exporting the data to a data file will prompt MagMap2000 to perform the diurnal correction automatically. The data is now corrected and in a format that is useable by excel and Matlab.

The data from each line is plotted onto individual 2D plots. Lines 1-3 crossed a barbed wire fence which caused a spike in our data. The response from the fence is removed from each line by looking at the flag location at which the fence crosses the line and removing the spike from the data at the corresponding flag number. Other bad data points are removed by observing the scale of the response and the response of each sensor; some of the data was on a significantly larger scale than our target anomaly and was also removed. Secondly if there is a varying response in the top sensor but not in the bottom, the top readings are considered to be bad data. These images are shown in Figure 5.

The next step is to interpolate the data. Interpolation is a method of processing where empty data spaces are filled in by looking at the nearest actual data point. There are many types of interpolation which vary in how they correlate actual data points to empty spaces. We experimented with multiple types of interpolation but concluded that most of them took too much liberty with the data and produced an image that was too far from our actual data to be trusted. To help the interpolation we decided to look at the analytic signal of the magnetics data. This changed the data from a dipole with negative and positive values to a monopole with just positive values. This allows us to interpolate just the monopole data and obtain a much more accurate representation of the data. To obtain the analytic signal of the data, we apply a Hilbert transform on the data.. A Hilbert transform is a linear operator that transforms your original signal into its analytic representation [**47**]. The Hilbert transform is essentially outputting the envelope of your signal. The produced signal is in the complex plane so the absolute value of it is need in order to plot the data. We also apply a moving average smoothing function to the data to give us a cleaner image. This resulting data is plotted in Surfer and a Kriging interpolation is then used to fill in the data for the recon area.

We also used a forward modeling script written by Dr. Yaoguo Li to forward model our raw magnetics data. The goal was to create a dike in the program that would produce a magnetic field on the surface that was the same as the one we recorded in the field. From this we could get an idea of the thickness, dip and magnetic susceptibility of the dike.

4.4. Results.

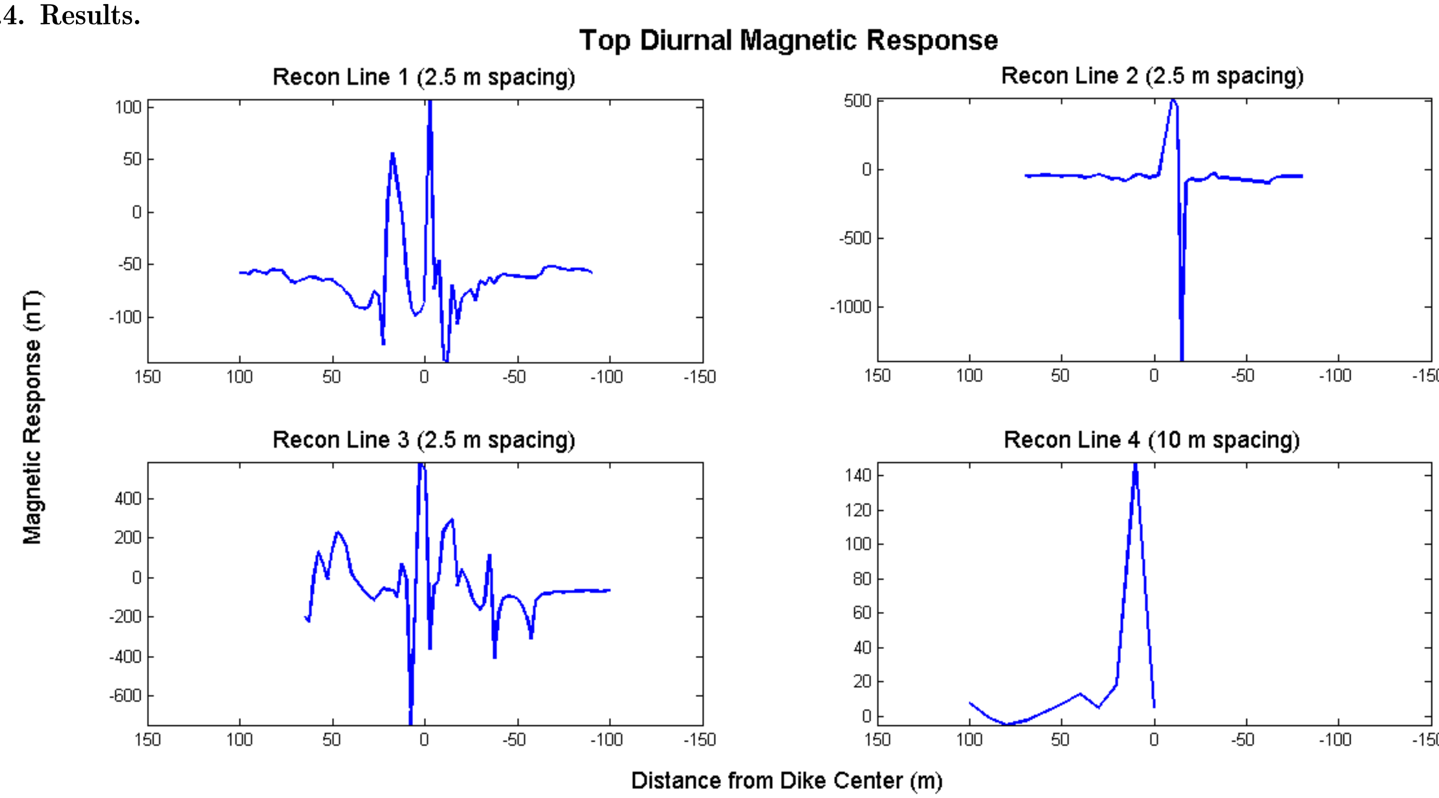

Figure 5. 2D images of the magnetic response from Lines 1-4.

Figure 5 shows the raw data obtained from the top magnetometer. There is a large response visible around the center of each line. Each line was positioned so that the dike was near the center. Line 2 produces the clearest dipole response while Line 3 seems to have the most noise. Note that Line 4 data was collected using 10m spacing versus 2.5m spacing which was used on Lines 1-3.

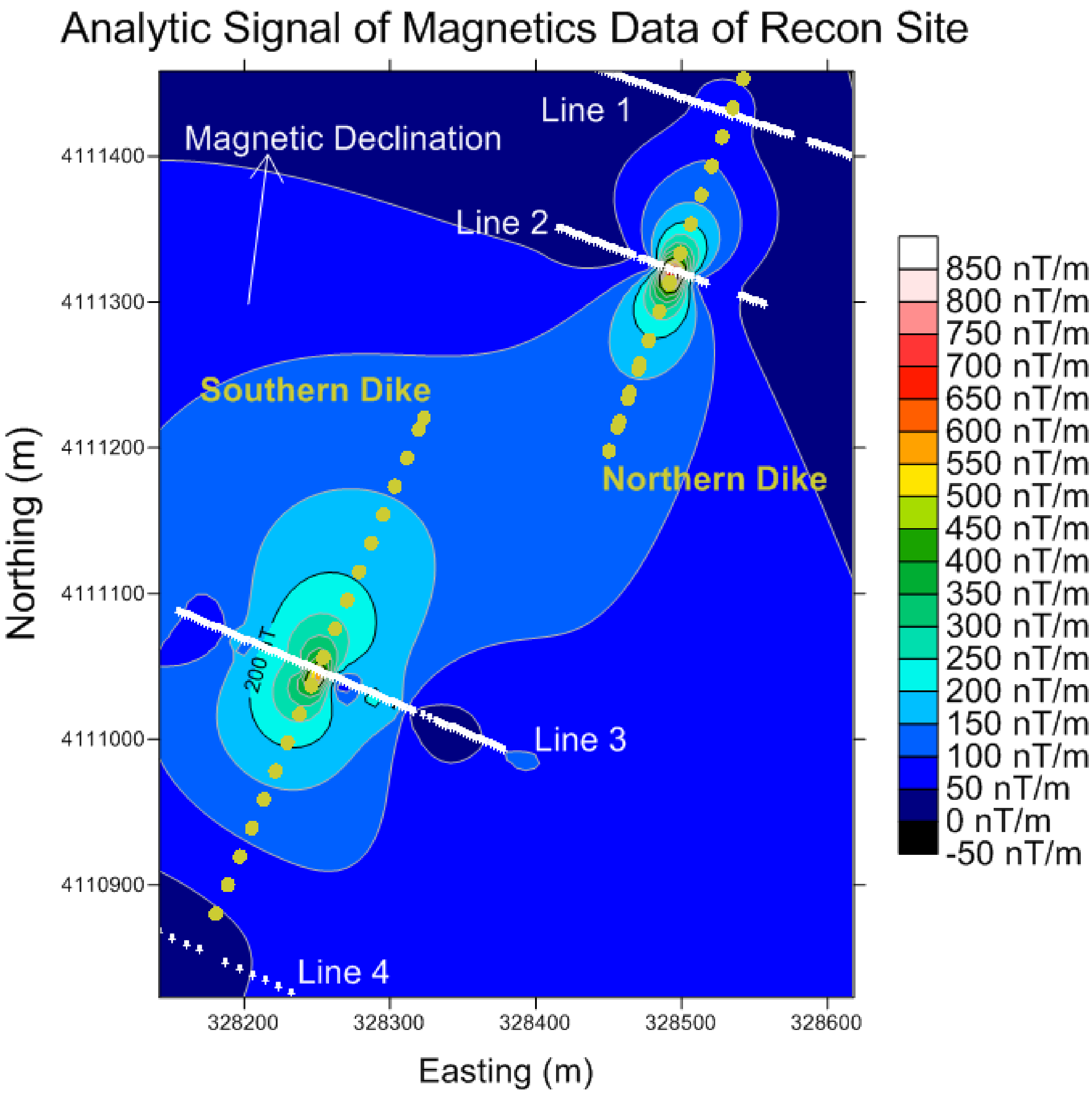

Figure 6. Contour map of the analytic signal of the magnetics data of the Recon Site.

Figure 6 shows the final analytic signal contour map of the recon area. Our image is limited by the amount of data collected. Despite the small amount of data, the trend from the Northern and Southern dike can be seen. Its full predicted presence is indicated by the dotted yellow line. These trends are confirmed by our surface observations of the dike and its North/South offset.

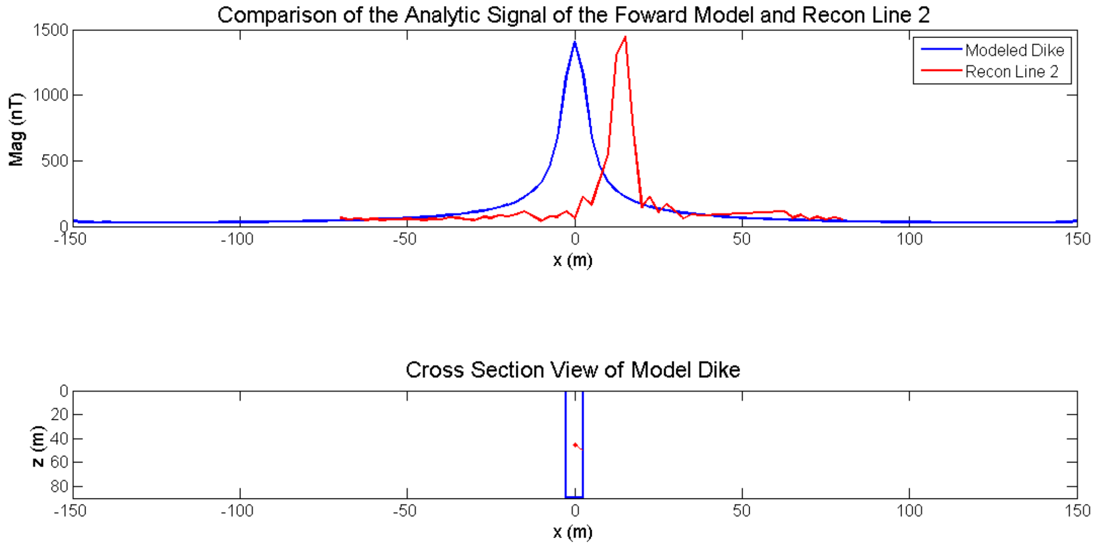

Figure 7. Forward model of a dike compared to magnetics data collected along survey Line 2

The results of the forward model show that a dike with a width of 5 meters, at the surface, with a dip of 90 degrees and a magnetic susceptibility of 0.085 produces a magnetic field very similar to the one observed along survey Line 2. Line 2 was chosen for the forward model because it had the least amount of noise in the data. No estimate for depth of the dike is made because in this forward model, changing the depth of the dike had no sizable effect on the surface magnetic field. Note that the two magnetic fields are offset in the figure because the forward modeled dike is centered at 0 while the dike in the field was not at the exact 0 mark of survey Line 2.

4.4.1. *Sources of Error.* A majority of the error in our data processing comes from our limited amount of data. The harsh terrain of the Recon Site coupled with several days of bad weather meant magnetics group only had three lines of data with dense station spacing and one line of data with much less dense station spacing. These lines were also around 100 meters apart from each other, giving us very sparse data. This meant that the processing group had to interpolate our data to get an idea of what the bigger picture was. Interpolation is good but not perfect because it is assuming data will follow the trend of the actual data you have. It cannot predict the presence of unexpected anomalies in your survey area. It will also look any noise in your data as an actual trend in your data and will continue that trend into the interpolation.

There was noise present on the west side of Line 3 which was unexpected. Looking at the topography through Google Earth, it looks like there might by a subtle feature underneath the survey line at that point in the line. Its presence was not obvious in the field which is why it was not investigated further. There were some noticeable divergences between the top and bottom sensors along some of the survey lines. It was concluded that the bottom sensor must have been malfunctioning or was exposed to more sources of noise since it was closer to the ground. To resolve this, data from the top sensor was used to make all of our figures.

4.5. Summary. The results show us a strong magnetic dipole response along the dike. On each survey line when the magnetometer crossed the dike, a dipole was recorded. This raw response is shown in Figure 5. After experimentation with the interpolation programs in Surfer and Matlab, we decided to look at analytical signal of the data to help get a better interpolation. After the interpolation of the analytical signal, we produced Figure 6. There is a clear trend in the data around the location of the northern and southern portion of the dike where the survey line crosses. A dotted yellow line was placed on the image to show the pattern expected if more data had been collected. From this image it can be seen that the dike is magnetic and follows a linear trend that propagates northeast and southwest. The forward modeling showed that the dike has a 90 degree dip from the horizontal, a width of 5 meters and magnetic susceptibility of 0.085. The depth could not be confirmed with our forward model. The 5m width of the dike is confirmed by findings of the hammer seismic survey however there is some uncertainty in that number. The dike is most likely not to be any wider than 5 meters but it could possibly be slightly thinner than 5 meters.

5. Electromagnetics

5.1. Reasoning. The EM31 and EM34 were used to construct a resistivity map over the geologic features found in the San Juan National Forest Reconnaissance Site. The major question resulting from the initial geologic survey pertained to whether the feature was a dike or sill. If a dike, the feature would display high resistivity readings due to its resistive volcanic intrusive material, resulting in a drastic resistivity change from the surrounding Lewis shale and Mesaverde sandstone. A resistivity reading is needed in order to characterize any faults found in the area that could possibly indicate water flow in the area [**48**]. Water flow through the faults would display weak resistivity readings due to the strong ionization of the water. While TEM and DC resistivity would produce the same value as the EM31/34, they lack in ease of use because of the difficult terrain. Therefore, the reconnaissance site was the main area of interest for the EM31 and EM34 survey crews.

5.2. Parameters of Survey. In order to characterize the resistivity of the dike, four survey lines were laid out perpendicular to the dike, all varying in length due to terrain restrictions such as dense shrubbery and a barbed wire fence. The lines ran Northwest to Southeast, flagged every 10 meters (see Figures 8 and 9) and numbered 1 through 4. Line 3 , in particular was flagged parallel to a fault already mapped in the USGS data prior to the survey setup. After the surveys on lines 1-4 were completed, a geologic feature, termed the "mound", was flagged every 5 meters for the EM34 to survey in order to determine similarities between the mound and the dike. The final EM31 survey was conducted along the road between the northern and southern dike to observe any potential fluid flow in the area.

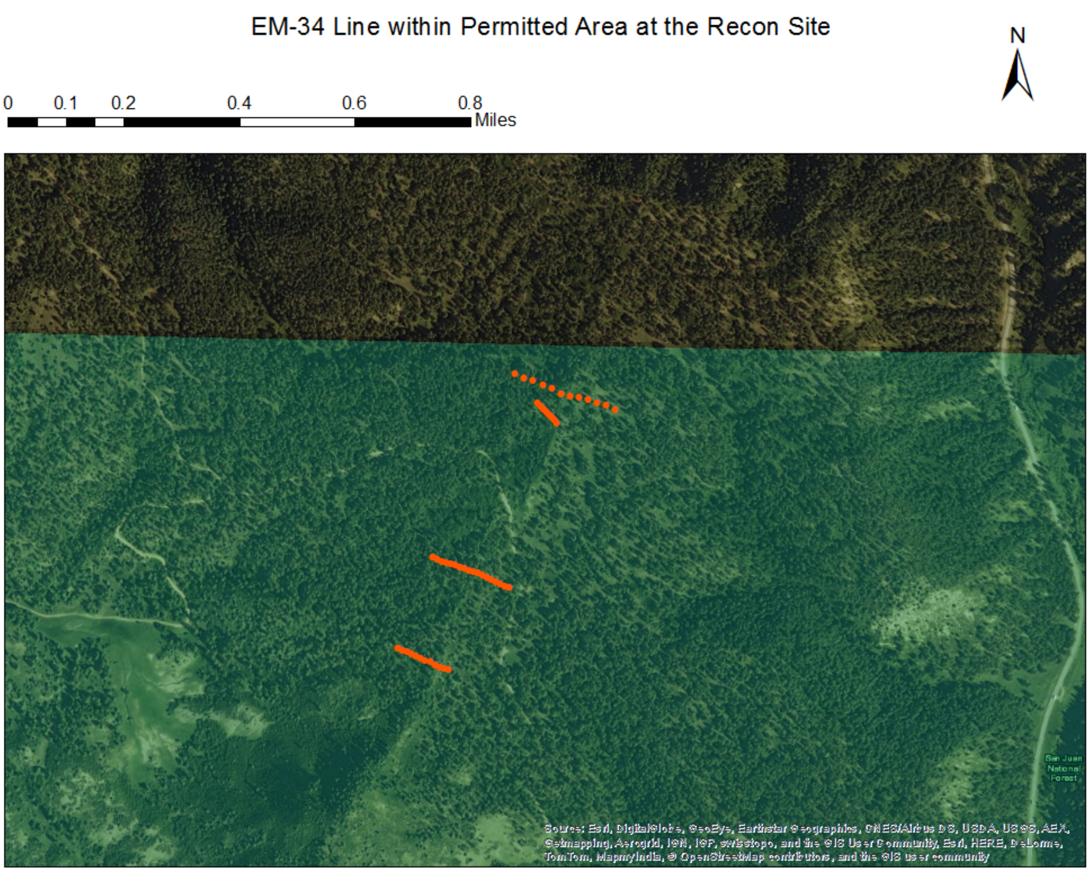

Figure 8. GPS coordinates of the EM34 line surveys.

Survey Flag Parameters		
Location	Length (m)	Flag Spacing (m)
Line 1	250	10
Line 2	270	10
Line 3	190	10
Line 4	130	10
Mound	60	5
Road	138	2

Table 1. Survey flag parameters for Recon Site

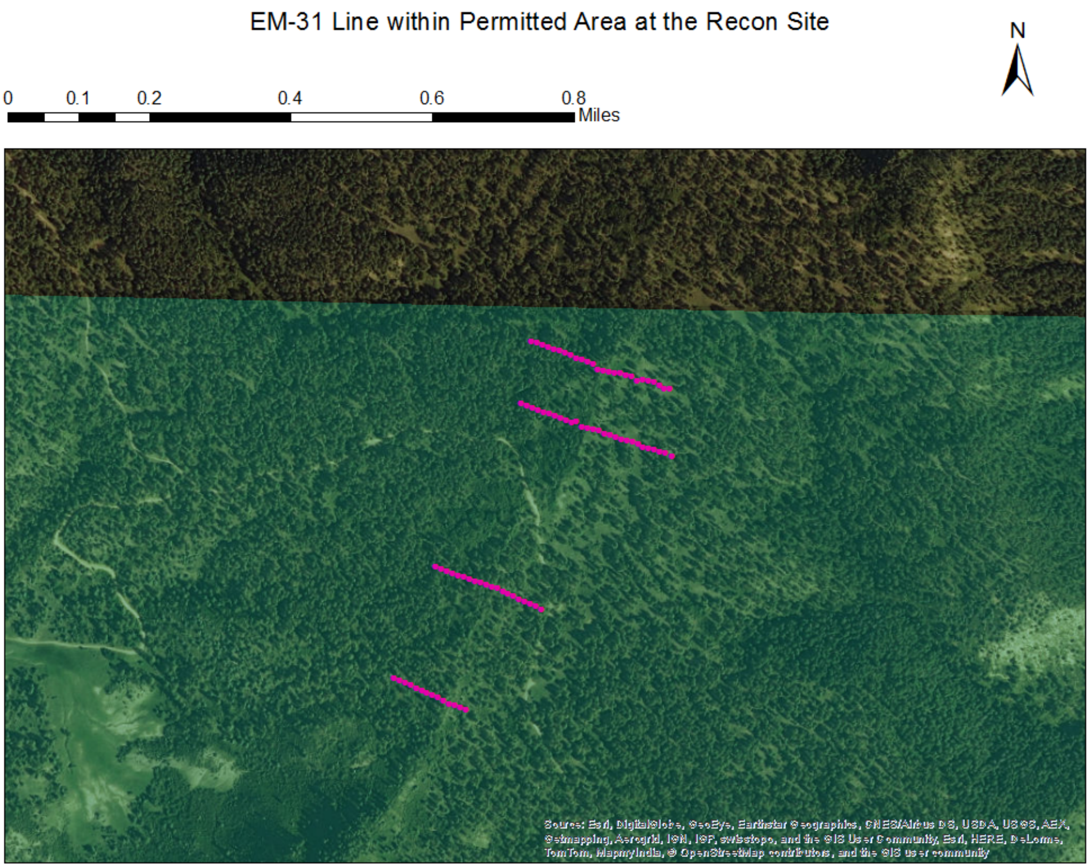

Figure 9. GPS coordinates of the EM31 line surveys.

Initially, the EM34 took measurements every 20 meters along Line 1 at 20 meter transmitter/receiver separation. After analyzing the data, it was determined that the spacing for each flag measurement would need to be reduced to fully capture the resistivity of the line while still maintaining the transmitter/receiver separation of 20 meters. Therefore, for lines 3 and 4, measurements were taken every 10 meters. The road and Line 2 were ignored for the EM34 due to weather and time restrictions.

One major parameter that the EM31 required consideration for was the option between discrete or continuous measurements. Due to the dense vegetation found in the reconnaissance site, discrete measurements were taken rather than continuous measurements because of . The difficulty of maintaining a constant walking velocity necessary for continuous measurement makes it an unreasonable parameter for this particular survey.

5.3. Assumptions. To process the data, assumptions had to be made regarding the EM31 and EM34 surveys. One major assumption applied to the UTM location points which we assumed were accurately measured by the handheld GPS and not affected by the adverse weather; therefore, Table 1 is assumed to be accurate. Another major assumption made at the Recon Site is that the dike was once a single continuous geologic feature that has been shifted and separated over time. It is also assumed the parameters within the EM31 and EM34 operating systems are correct, and the instruments were used properly and functioning without any error. The final assumption made for data processing is that the Kriging analysis predicted reasonable representations of the resistivities between the survey lines.

5.4. Sources of Error. One of the major sources of error in the EM31/34 surveys resulted from the frequent rain storms that occurred during the surveys. The poor weather caused setbacks in survey planning, and consequently accurate completion of certain survey lines. The EM34 was not used for measurements over survey Line 2 and the road, while the EM31 did not complete a survey over the mound. Another major source of error results from the EM31/34's sensitivity to other electromagnetic objects, such as: powerlines, barbed-wire fences, cattle guards, and cars. If these objects are detected by the EM devices, the data will predict false anomalies. The user could also create errors in the EM31 data when setting the parameters in the control box. The EM34 requires the data to be recorded manually, so errors could occur from misread numbers, poorly recorded data, or inputted incorrectly into excel. Another error could be in the separation and conductivity correlation. For an accurate conductivity reading the separation must be between +/- 300. Errors could result if the separation is out of the range for accurate conductivity readings.

5.5. Data Processing.

5.5.1. *Physical Property Measured.* The EM31 and EM34 measure the resistivity of rocks and sediments found in the shallow subsurface. Resistivity is defined by Ohm's law, and is measured in units of Ohm meters (Ωm). Because the resistivities are known for the many different geologic layers, it is possible to make geologic interpretations based off the calculated resistivity readings.

5.5.2. *Steps Toward Data Reduction and Software Used.* To begin data processing for the EM31/34 the GPS coordinates of each measurement taken need to be determined, because only the beginning, middle, and end of each line were recorded while in the field. The three UTM coordinates of each line are loaded into Google Earth, with a path connecting the three points. Google Earth provides a latitude, longitude, and elevation for each location on the path. Using the survey design, the distance between measurements is known (see Table 1). Every conductivity measurement is converted to resistivity using the inverse of conductivity and multiplying by 100 to produce Ohm meters (Ωm). The resistivity, location, and elevation is then saved. Once the locations of each measurement are determined, Surfer 12 is used to create different resistivity maps of the region. In order to use the program, the data first had to be loaded into two separate worksheets and saved as a .dat file. Both files contain the easting and northing coordinates, with one worksheet containing the elevation data and the other the resistivity data. Outliers in the resistivity data are adjusted to match the surrounding resistivities. Both worksheets are transformed into a grid using a Kriging spatial analysis. The Kriging analysis gives the best linear unbiased prediction of intermediate values. The grid of the UTM coordinates and elevation is loaded as a 3D surface overlain with a contour plot of the resistivity grid. Two overall maps are created; one of all EM31 data and one of all EM34 data to depict an overall view of the topography affects with the resistivity measurements. Two more contour plots are created of the resistivity values taken by both the EM31 and EM34. These plots depict a 2D map using northing, easting, and resistivity. All four maps create an overview of the resistivity characteristics of the dike.

5.6. Final Products.

5.6.1. *EM31.* Figure 10 and Figure 11 below show the results from the EM31 survey taken over lines 1 through 4 and the road found between the dikes. Areas with low resistivities can indicate the presence of fluids due to the ionization of water as it flows through fractures. As the density of the ions in the fluid increase, the amount of resistivity measured by the EM31 will decrease.

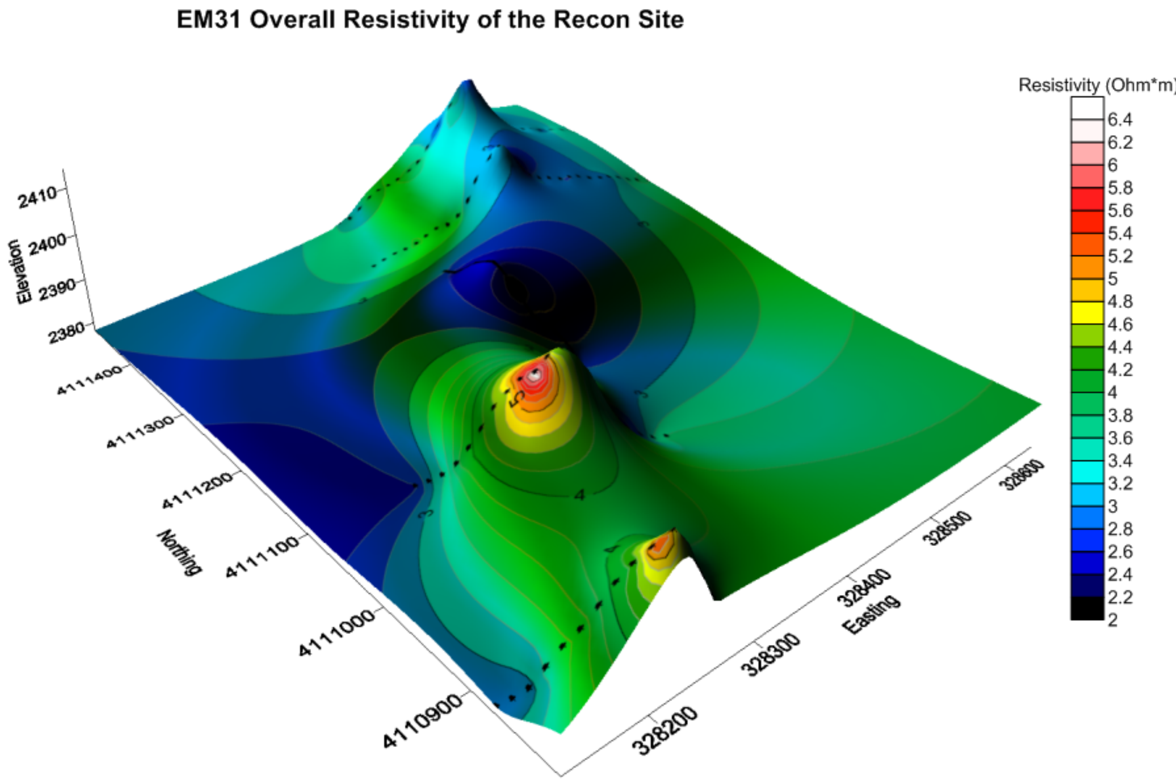

Figure 10. Resistivity contour plot overlain the topography of each EM31 survey conducted at the Recon Site. The survey lines are seen as the black pin locations.

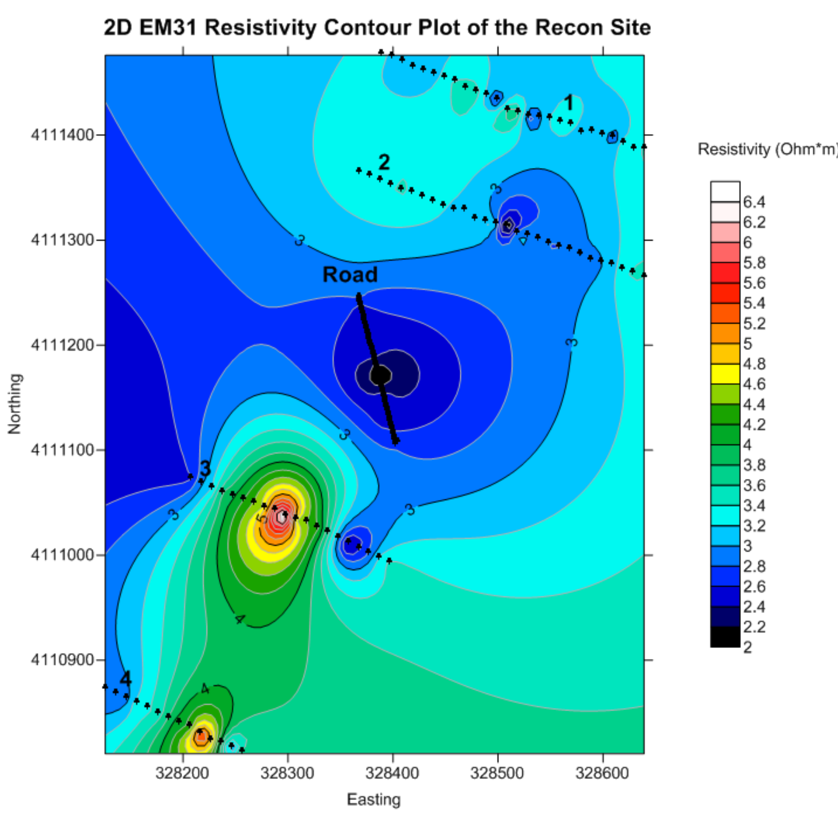

Figure 11. Resistivity contour map of the EM31 data collected over each survey line at the Recon Site. The survey lines are seen as black pins on the map.

In Figure 11, survey lines 1 and 2 indicate resistivity readings ranging from 2 -3.4 (Ωm) across the northeast portion of the dike. Survey lines 3 and 4, however, indicate higher resistivity readings of approximately 4.4-6.4 (Ωm) across the southwest portion of the dike. This is an unexpected result due to the assumed continuous material properties of the dike. This discrepancy could be the result of the Kriging interpolation used in processing.

Figure 11 also shows the variable resistivity between the high measurements of survey line 2 and the low measurements of survey line 1. This difference is potentially a result of weathering patterns. Despite the high resistivity readings found at survey line 1, there is still evidence of the contrast between the dike and the surrounding shale and sandstone. This could be due to the absence of the weathered dike material, or other geologic processes making the anomaly less apparent. The lower resistivity readings at survey line 2 indicate potential water flow east of the region due to the contact of the intrusive dike and surrounding Lewis shale and Mesaverde sandstone.

The road survey measured lower resistivities of about 2.6-2 (Ωm), which could be a potential fault zone running parallel to the road. Evidence of this fault is found in the offset of the southern and northern dike, and is a possible conduit for fluid flow. The presence of a fault zone is reasonable due to past mapping of faults in the region [**46**]. The effect of the frequent rainstorms during the time of the survey may have also affected the consistency of the EM data. As a result, Figure 12 shows the resistivity readings not following the gravitational trend of water flow from a high to low elevation.

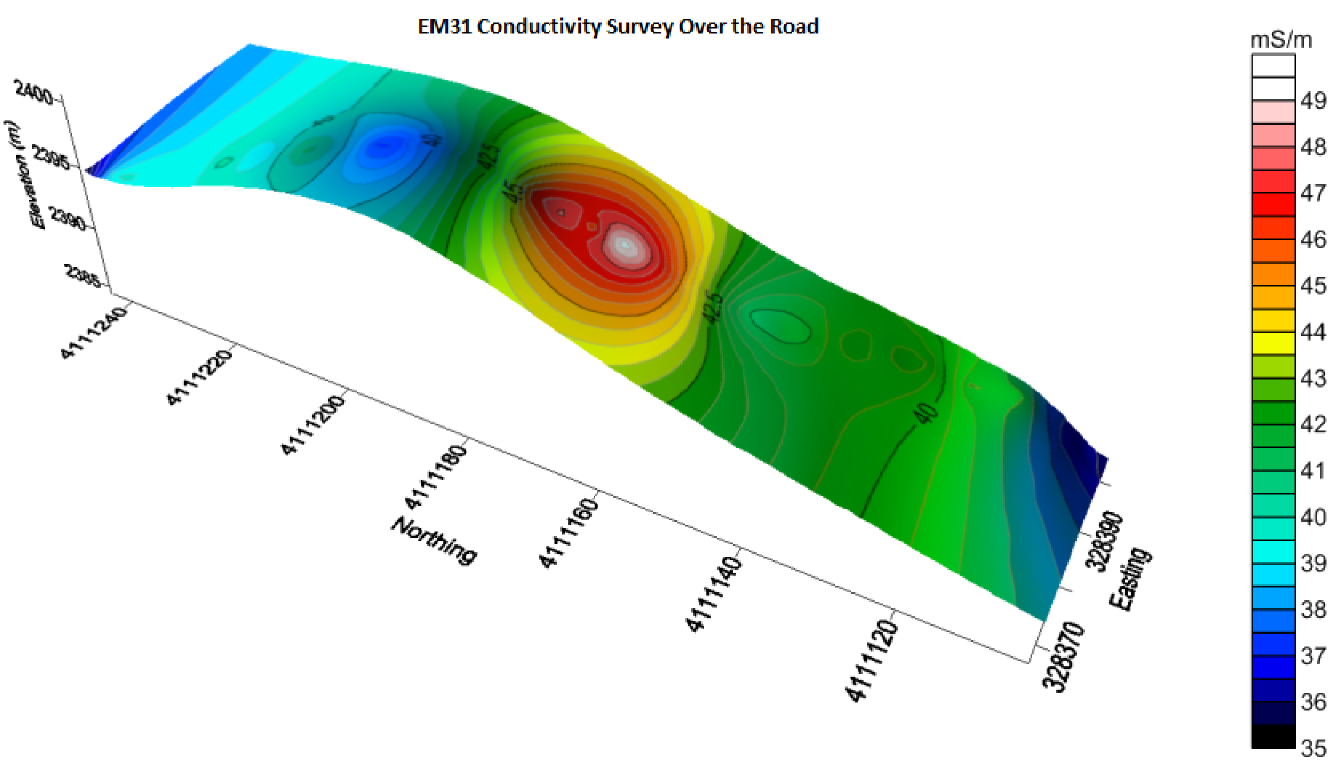

Figure 12. EM31 resistivity plot of the road survey.

5.6.2. *EM34*. Figures 13 and 14 below plot the results from the EM34 survey taken over lines 1, 3, and 4, and also the mound near the northern dike. The EM34 resistivity data differs from that of the EM31 because its measurements can record at greater depths due to the longer loop separation.

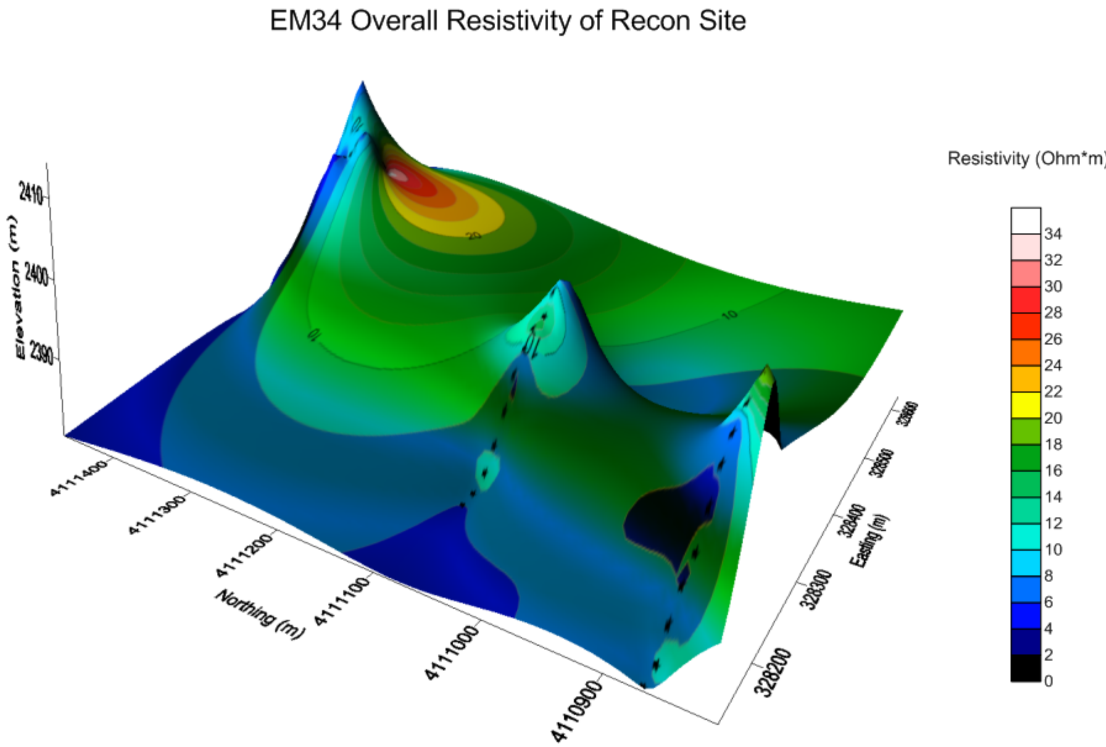

Figure 13. Resistivity contour plot overlain the topography of each EM34 survey conducted at the Recon Site. The survey lines are seen as the black pin locations.

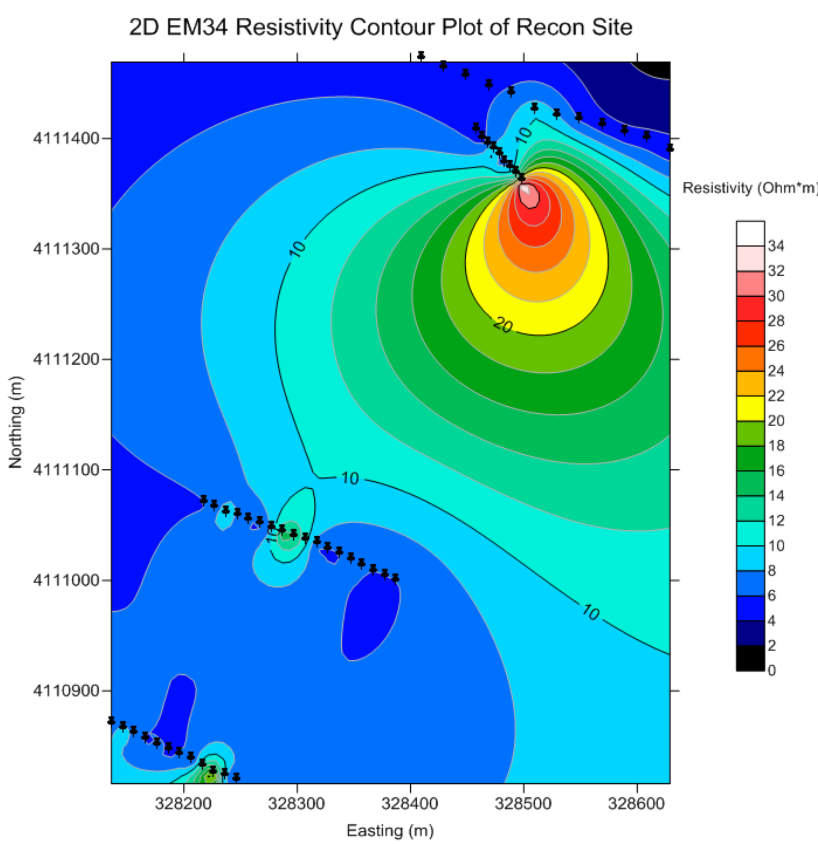

Figure 14. Resistivity contour map of the EM34 data collected over each survey line at the Recon Site. The survey lines are seen as black pins on the map.

Figure 14 above shows mid-resistivity readings along line 1 ranging from 16-20 (Ωm) on the edges of the dike, with higher resistivities from 18-20 (Ωm) measured in the center of the dike. The mound survey measures resistivities increasing from 18 to about 34 (Ωm). Across line 3, a pattern forms of mid, mid-high and mid-low resistivities. The center of the plot, near the top of the dike, has resistivities ranging between 6 to 2 (Ωm). On either of the side of the high resistive zone slightly lower resistivities are seen ranging from 15-17 (Ωm). To the east of the dike the more conductive region continues ranging from 6-4 (Ωm). To the west, a mid-high resistive zone is observed at about 12-14 (Ωm). At line 4, another small pattern with slightly low resistivities ranging from 2-6 (Ωm) embedded between two slightly higher resistivities can be seen. To the east a much higher resistivities range from 14-18 (Ωm), and to the west mid resistivities are measured at 6-10 (Ωm).

5.7. Combined Results. Comparing the EM 31 data to the EM 34 data results in a difference in resistivity seen in the northeast corner of Figures 11 and 14. If these two dikes were once connected then it would be expected that the two anomalies would produce similar resistivity responses. However, this is not the case seen in Figures 10 through 14 above. The greater depths imaged with the EM34 make the dike appear more resistive whereas the shallower depths of the EM31 shows an electromagnetic response that is more conductive. A probable cause of this could be weathering. As the surface of the dike erodes and fractures, water seeps in, and makes the resistive rock appear conductive in the EM31 data. The EM 34 shows resistive dike material due to its deeper investigation thus it is able to see the material that is not affected by weathering. In the southwest corner of both Figure 11 and Figure 14, high resistivities can be seen; however, the resistivities for line 4 are slightly more east than they are in Figure 11, a difference that is attributed to the EM34 seeing deeper down the dike.

The anomalous high resistivities found at the road by the EM31 (see Figure 11) can also be explained by the rainy weather that occurred the day before the survey. Large amounts of mud were observed along the sides of the road, indicating moisture in the area that has potential to give false conductivity responses. Several days later the DC resistivity team collected data along that same road, and the data showed a low resistivity anomaly in a similar area of the road where the low resistivities are seen. This correlation could once again be due to the rain that was seen over the course of the field camp. Faults can appear as low resistivity features within a high resistivity environment. Since this low resistivity, as seen in Figure 15, is surrounded by slightly higher resistivities, a fault could be present. However, without further DC resistivity and seismic data, this conclusion is uncertain.

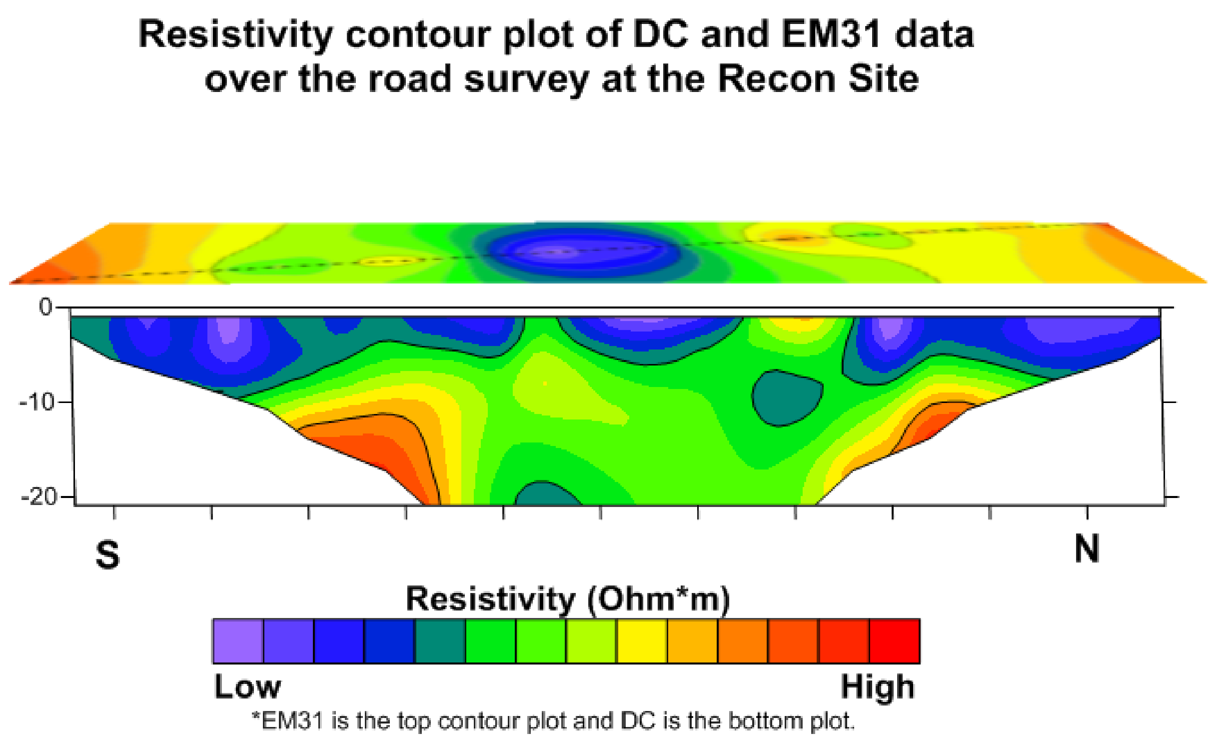

Figure 15. Combination of the DC Resistivity (below) and EM (top) survey lines over the road.

5.8. Sources of Error. Two sources of error are associated with the data processing; the Kriging analysis and the lack of UTM measurements taken in the field. The Kriging analysis predicts intermediate grid points between measured data points. The predictions could produce false anomalies or nullify existing anomalies. This is particularly true with the EM34 results because a large gap of data is missing between line 3 and the survey conducted over the mound creating highly conductive regions in the northwest portion of the map where no data was collected. The analysis also predicts less conductive regions towards the east of the dike because the anomaly located near the mound is very resistive. This anomaly dominates the region between the mound and line 3 because the Kriging analysis determines the intermediate values 14. Therefore, the impacts from the Kriging predictions are substantial because the analysis predicts a large portion of the maps produced. The second source of error in data processing is associated with the amount of UTM coordinates taken at the Recon Site. Only three UTM coordinates; the start, middle, and end of each line were recorded for the four lines. In order to line up each resistivity with a coordinate for plotting in Surfer 12, the coordinate of each resistivity reading is calculated using knowledge of the survey set up and the recorded UTM coordinates. The set flag spacing and the assumption that line should be a straight across the dike made the calculations possible. The coordinates taken in the field and the mathematically calculated coordinates have the potential to be inaccurate. This is due to the fact handheld GPS units have accuracy within 5m. The impact from errors when calculating the UTM coordinates could result in the location of anomalies at incorrect positions causing incorrect data interpretation.

5.9. Summary. The electromagnetic survey conducted over the reconnaissance site in the San Juan National Forest resulted in the resistivity profile over the dike of interest and the road. Through the use of Surfer software and Kriging prediction analysis, the data sets collected by the EM31 and EM34 were interpreted for water flow and dike characterization. As seen in Figures 10 through 14, there is a possible fault zone due to the low resistivity readings found at the road. However, it is still uncertain if the lower resistivities found in the areas are simply due to the wet conditions or water flow through a possible fault. The dikes displayed higher resistivities, representing the resistive material of the igneous intrusive rock. Further investigation in this area would be useful in determining the impact the frequent rain storms had on the data and interpretations.

6. Direct Current Resistivity

6.1. Physical Property. As the name implies, DC Resistivity is a method that looks at the physical property of resistivity. It is considered an active electrical method in that a current is put into the ground where it then goes through the subsurface allowing for a difference in the electric potential to be measured between two electrodes. It is from this that we are able to obtain a value for the apparent resistivity based on the mathematical theory explained in the DC Resistivity section of the appendix. Resistivity itself is defined as a measurement of how much an object opposes the flow of electrical current.

6.2. Reasoning. When determining what methods to use, it was important to consider the terrain of the survey area, accessibility of the area, and what types of geologic features are of interest. The reconnaissance site appeared to have two possible geologic features: one or more dikes and a fault. The terrain in the area had several mounds covered with lots of trees, bushes, and rocks. These features made it difficult to utilize any methods that required heavy or bulky equipment. The ABEM Terrameter SAS 4000 is a very small, lightweight piece of equipment, and it can be utilized with smaller, lightweight reels which made it easy to transport to and use at the reconnaissance site. DC Resistivity not only gives resistivity data useful for understanding the rock properties of the area, it can be used by other methods, such as seismic to further their understanding and help in the interpretation of their own data sets. The interpretation of resistivity data can also be used in conjunction with other methods such as spontaneous potential and induced polarization in order to help clarify subsurface features.

6.3. Survey.

6.3.1. *Survey Parameters.* Array Type: Wenner-alpha
Electrode Spacing: 4 m
Number of Electrodes: 32
Power Line Frequency: 60 Hz
Midpoint: 16
Maximum Current: 200 mA
Total Acquisition TIme: 3.5 seconds
Primary Acquisition TIme: 2.0 seconds
Initial Delay Time: 0.3 seconds
Maximum Number of Stacks: 2
Error Limit/ Standard Deviation: 5%

6.3.2. *Decision Process for Parameters.* In order to obtain the best possible results in a DC Resistivity survey it is crucial to consider what types of features are likely to be present. At the reconnaissance site we anticipated seeing some horizontal layers as well as a dike. From surface outcrops we expected the dike to be close to vertical. A Dipole-Dipole array would be ideal if the survey line was set up to image the dike itself; however, we aimed to look at the interplay between the horizontal layers and the dike. This led us to choose a Wenner Array for this site as well.

At the reconnaissance site there was difficulty in creating longer survey lines without encountering obstacles that would make it difficult. For this reason the shorter CVES cables with 16 electrodes was utilized and a grid was set up with 4 meter electrode spacing along a road.

We kept the acquisition time and maximum current the same as it was for the main line DC resistivity survey and the reasoning behind the selection of these parameters is explained in the Geophysical Investigation of the Main Line DC Resistivity section.

6.4. Execution. At the reconnaissance site we collected data on the apparent resistivity of the area using a Wenner Array. Our main objective was to examine the relationship between the horizontal layers present in the subsurface and the intrusive dikes that were observed on the surface. A standard deviation of five percent was deemed to be an acceptable amount of error in each measurement and we found that overall the standard deviation was well under that limit. To further help reduce the amount of error in the data we also programmed the ABEM to perform up to two stacks of each measurement in the event that the five percent standard deviation was not met.

6.5. Data Reduction. To begin with, we added topographic data to a copy of the raw data file. We then inverted the data using res2dinv without any edits made, only the topography taken into account.

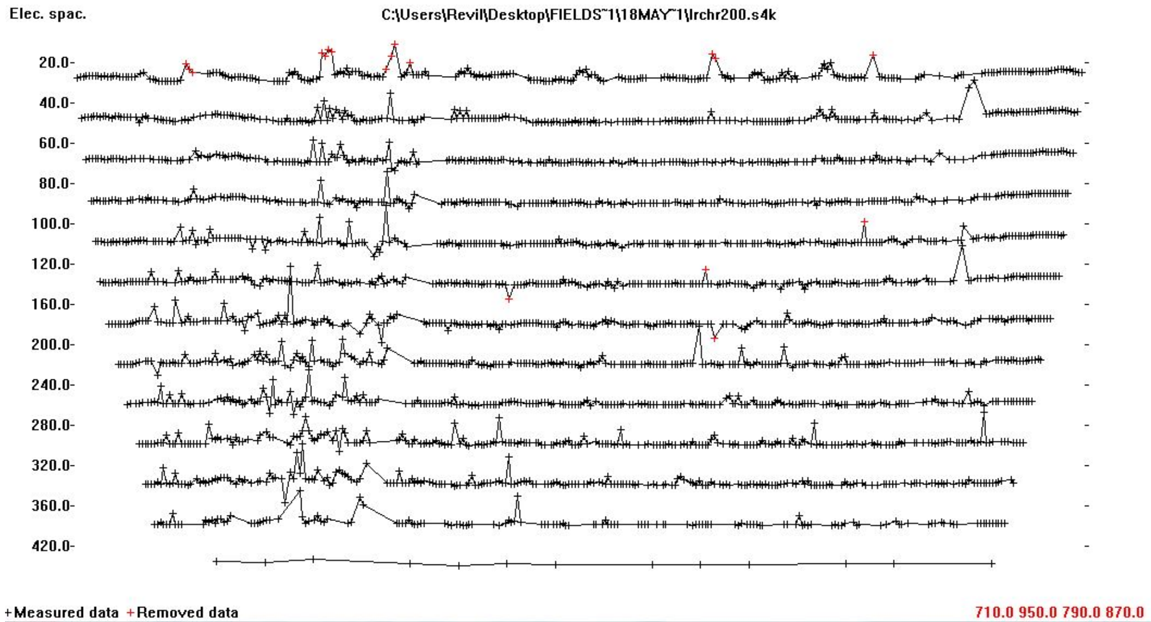

Figure 16. Inverted the data using res2dinv

With an initial image, we then did some quality control. We examined the data file and determined if any of the data points had a notably high standard deviation. After examining our results we found that the data was of excellent quality and that there were no outlying points that needed to be removed. Our next step was to then put this data into the software Surfer12 in order to generate an image that was easier to interpret and had color schemes that transitioned from one resistance to another more gradually than the image created by res2dinv. The more detailed image clarifies the results so that they are more geologically feasible and therefore better for interpretation.

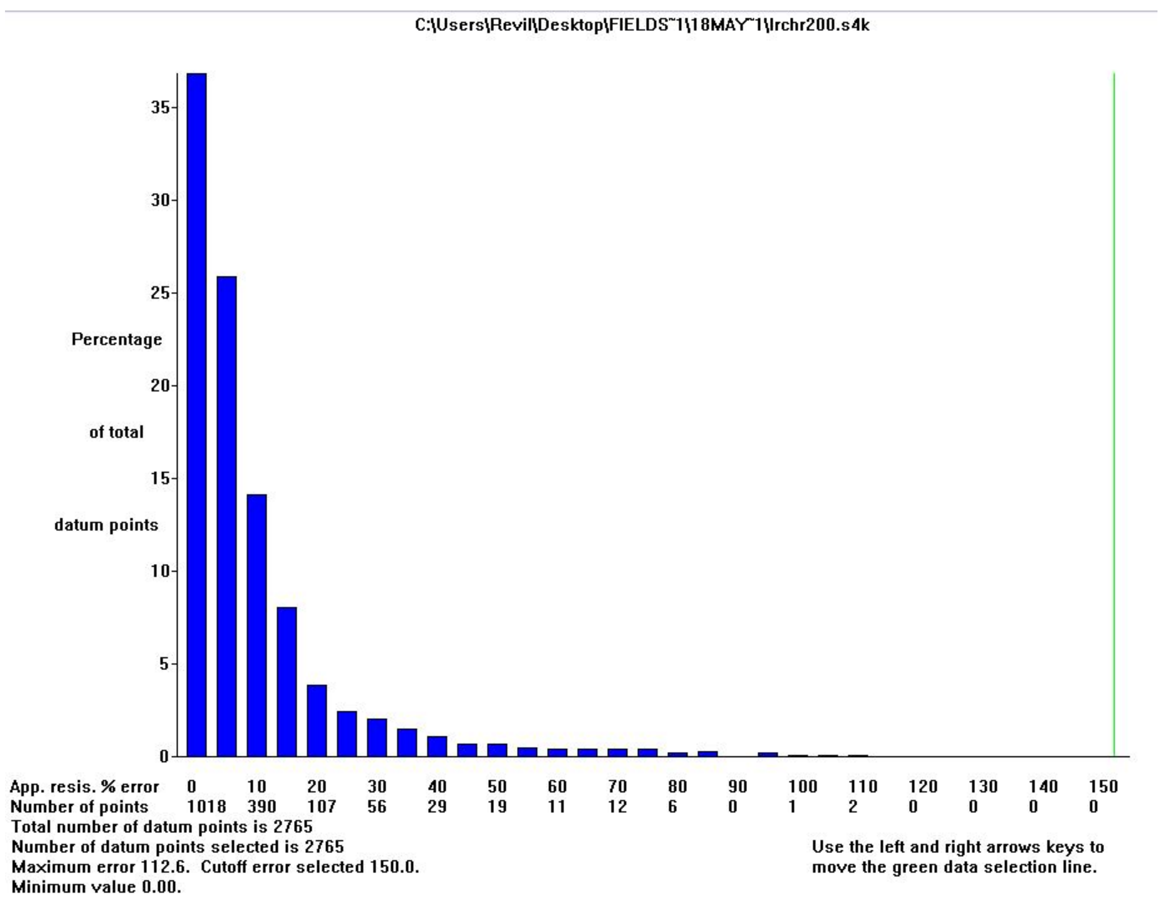

Figure 17. Recon site with topography

The final inversion is shown in Figure 17. Notice how there seems to be more conductive material on the surface. This is likely not a direct property of the rock, but due to a collection of water from the recent rain. The image also shows a layer of 1.7 Ωm resistivity material. Theret intrudes into this layer that has a resistivity of at least 2 Ωm.

6.6. Sources of Error and Noise. The sources of error in this survey are similar to those of the DC survey on the main line. They include errors from instrumentation, contact resistance, and conductive objects short circuiting the current. More information on these can be found in the main line DC Resistivity data processing sources of error section. The methods used to handle any error that might occur involve programming the ABEM so that it has a limit on the maximum standard deviation and if this limit is reached or exceeded, the ABEM will then do one more stack of the measurement until the designated maximum number of stacks of data is reached.

6.6.1. *Impact on Results.* In this particular data set the error was quite low, remaining beneath five percent standard deviation for every measurement. If there were to be error introduced into the data from any source, as long as that error is not a systematic error we would expect it to appear as a spike in the data which we would remove before doing the final inversion.

7. Hammer Seismic

7.1. Survey.

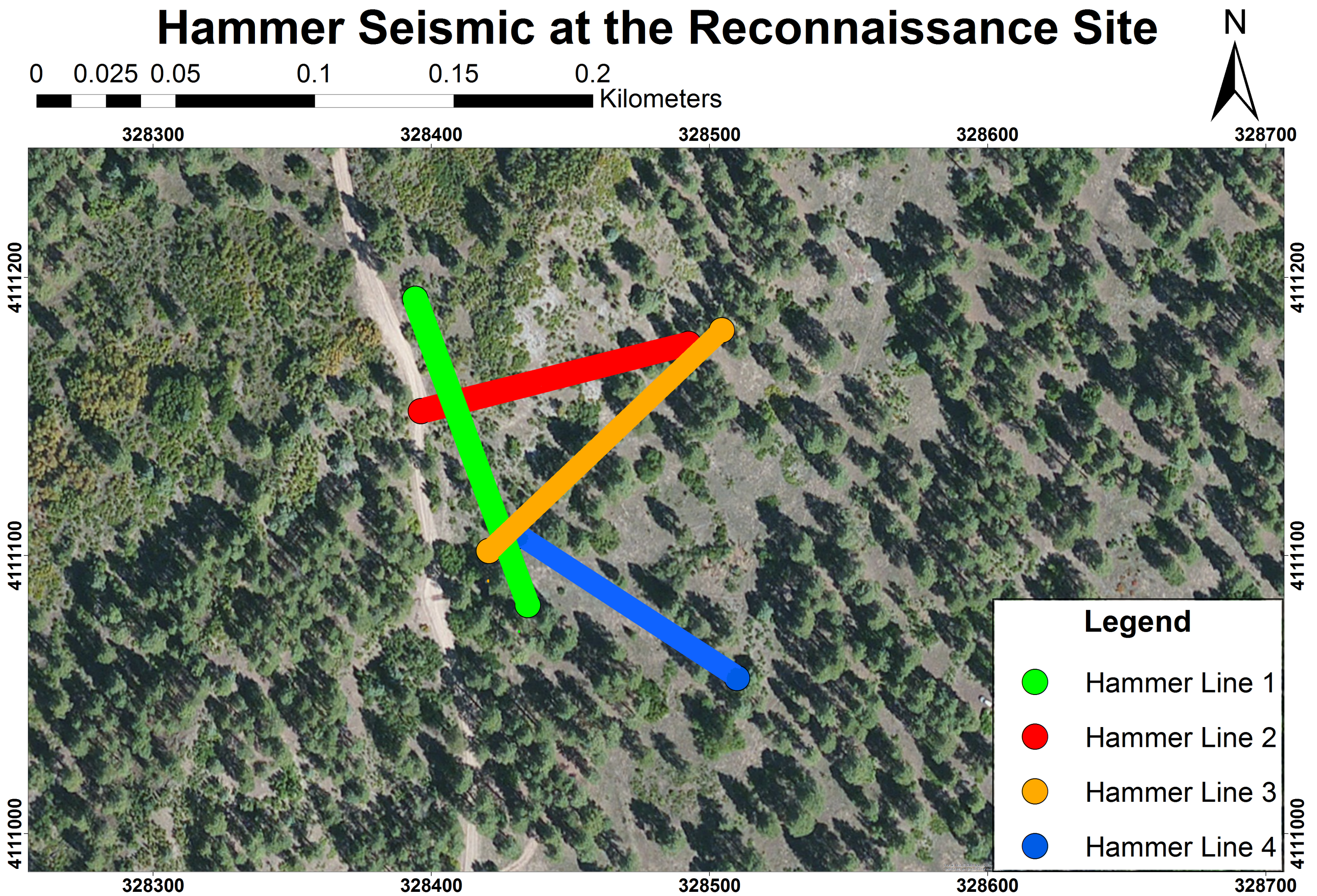

Figure 18. Hammer seismic lines at the Recon Site

Line	Location	Length	Receiver Spacing	Shot Spacing
1000	Recon Site	120 m	2 m	6 m
2000	Recon Site	120 m	2 m	8 m
4000	Recon Site	120 m	2 m	4 m
5000	Recon Site	100 m	2 m	4 m

TheRecon Site has two specific geologic structures of interest, the first being a dike that was observed at the site and the second is a potential fault that appeared to offset the dike on either side of the road. These were the targets of the four surveys performed at the Recon Site and explains why the logic behind the orientation of the lines 1-4. The purpose of the 1000 line was to image the fault that separated the dikes, supposedly crossing it in the middle to west end of the line. The 2000 line was used as a control experiment, not crossing the dike or fault. The 4000 line ran roughly perpendicular to the dike, crossing it and potentially the fault. And The 5000 line ran oblique to the dike and potentially crossed the fault. The conditions at the Recon Site consisted of thick brush, a steep slope along the dike, mud and a barbed wire fence. Therefore these surveys were not completely linear, to work around and through the conditions at this site. These lines had more sparse receiver spacing (every 2m) and shot spacing (every 4-8m), and also increased the stacking at the end of the lines to 5 per shot, while only doing three along the middle of the line. We assumed the dike was no more than 10 meters thick and that we knew the general shape of the dike we believed our spacing would be adequate to give good resolution of the targets. However, we were concerned that the fault would not show up because there was Louis Shale on either side of it.

7.2. Goals of Investigation. The hammer seismic survey at the reconnaissance site consisted of four separate lines: 1000, 2000, 4000 and 5000. The four lines interact or overlap at different angles to best characterize subsurface layer depths, thicknesses and fluid content. Line 1000 was placed to image the fault that is causing the offset between the two dikes at this location. The fault here should be expressed in the thick, near-surface shale layer, which will not be easy to detect on a seismic image. In order to help locate the fault on line 1000, line 2000 was created. Line 2000 is perpendicular to 1000 and oblique to the fault, without crossing it. If the fault is represented as a disturbance on the 1000 line, the absence of that disturbance on the 2000 line will support conclusions regarding the fault. The 4000 and 5000 lines were created with a similar geometry to complement one another. The 4000 line starts on what we believe to be the top of the dike and will characterize the size and velocity of the dike while the 5000 line was positioned to image the fault.

7.3. Processing.

7.3.1. *Refraction Analysis.* Refraction waves seen in hammer seismic shot gathers can be used to create a layered model of the subsurface. Refraction waves travel along interfaces between two layers of earth with contrasting velocities before returning to the surface. By examining the arrival time and the velocity of the returning refraction wave, the depth and velocity of the layer contact can be calculated.

Before picking velocities, shot gather images have to be filtered and modified to best image the refracted waves. In the field, the receivers recorded data for 1.0 second. After looking at the initial shot gathers, a window size of 0.08 seconds was applied to zoom in on the refractions with changing velocities. Because these images still have a lower than ideal resolution, an automatic gain control (AGC) of 100 was applied. The AGC averages the amplitude of the energy in each shot and ‘smooths’ the data to allow finer details to emerge from the noise.

From these filtered images, refracted waves can be seen with three different velocities on each shot. The first step in creating a layered geology model is to calculate these velocities based on their changing slopes. 19 shows an example of the changing slopes, and how they were selected. The three velocity values correspond to three layers in the subsurface that the waves have traveled through. The steepest line corresponds to the slowest velocity and shallowest layer from the survey.

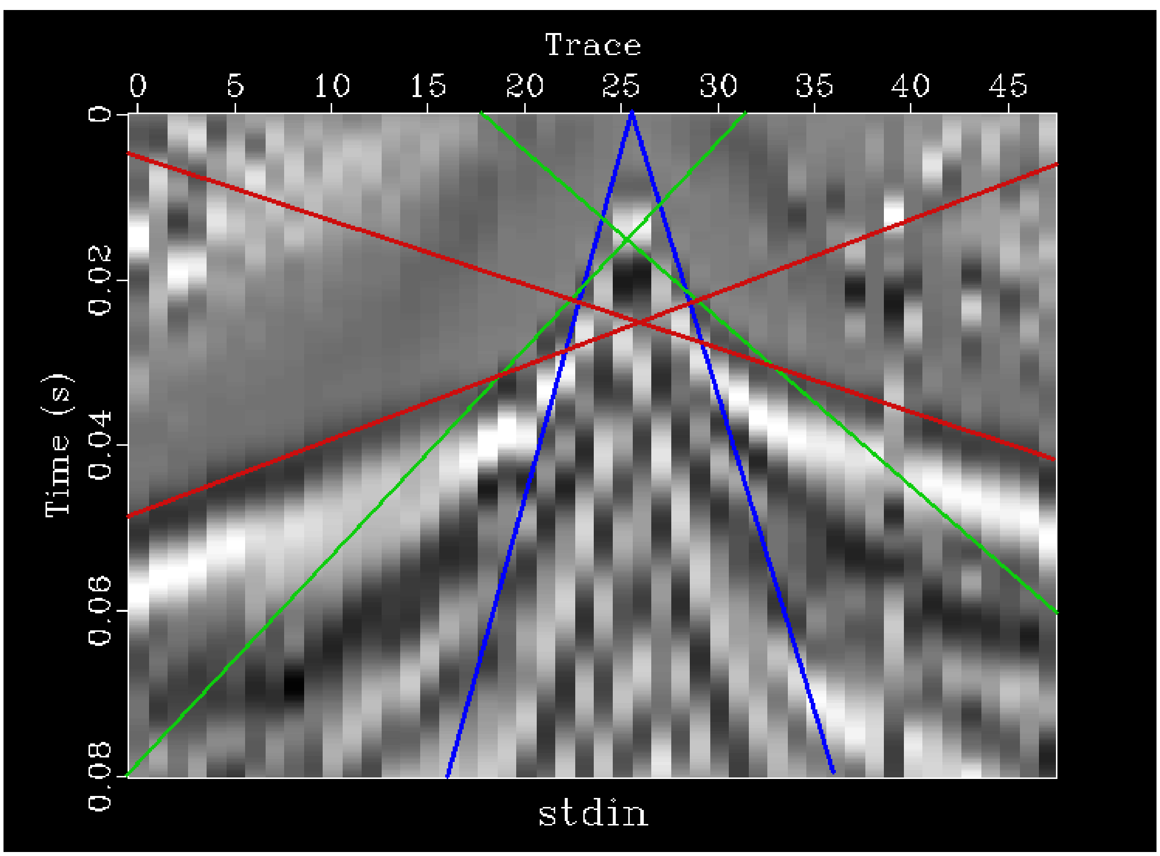

Figure 19. Velocity lines drawn on the 26th shot gather from the 1000 line

The velocity calculation process is done on three separate shots from each individual line. A shot that clearly images the changing slopes is selected from the beginning, middle, and end of each line, with separate values being measured for both sides of the center shot. Once the velocity values from each line are collected, horizontal layers are assumed and the first thickness is calculated with Equation (2)

$$h_1 = \frac{t_i}{2} \frac{V_2 V_1}{(V_2^2 - V_1^2)^{\frac{1}{2}}} \tag{2}$$

Where h_i is the thickness of the first layer, V_1 and V_2 are the velocities of the first two layers and t_i is the time at which the velocity line crosses the zero offset line directly beneath the shot location. The thickness of the second layer is calculated using Equation (3) for each velocity value.

$$h_2 = (t_{i,2} - \frac{2h_2({V_3}^2 - {V_1}^2)^{\frac{1}{2}}}{V_3 V_1}) \frac{V_3 V_2}{2({V_3}^2 - {V_2}^2)^{\frac{1}{2}}} \tag{3}$$

The thickness values across each line are then converted to depths from the surface and interpolated between to form a cross section of the survey area. Assuming flat layers in the subsurface simplifies our calculations, but small dips in the layers can be observed by the changing thicknesses from line to line.

7.3.2. *Guided Forward Model.* Forward modeling is a powerful tool in geophysics that allows us to see the data we would expect to acquire from a certain survey under certain conditions. To do this we make an Sconstruct file that specifies the survey parameters and velocity model, then run it in Madagascar to produce a shot record from given parameters and velocity model. A model representing the expected geology of this area is built in an attempt to replicate a survey taken across the dike at the Recon Site. The geology is represented by a velocity model, created using the velocities and depths calculated in the refraction analysis. The first model is a basic layered-cake model of flat lying formations, we then add a region of faster velocities according to the assumed size and orientation of the dike. Finding the model that best represents our data requires us to adjust the size, location, and velocity of the dike, until we make a model we are happy with 20. We are only comparing one shot from the actual survey to one shot record from the forward model so we choose a shot position above the dike and that also had a good shot record in the real survey. 21 shows an actual shot gather compared to a shot gather produced with the forward model.

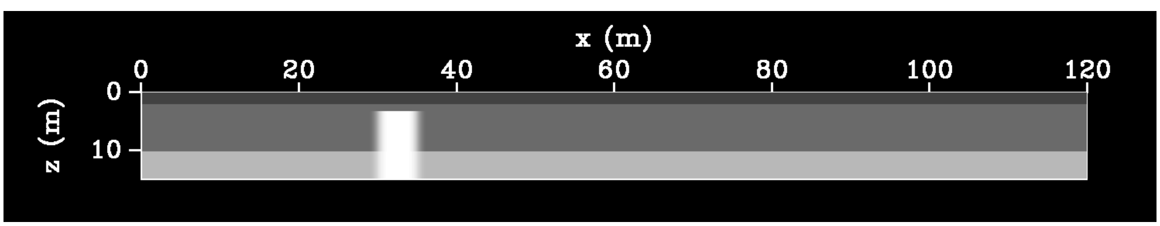

Figure 20. Three layer forward model with dike intrusion

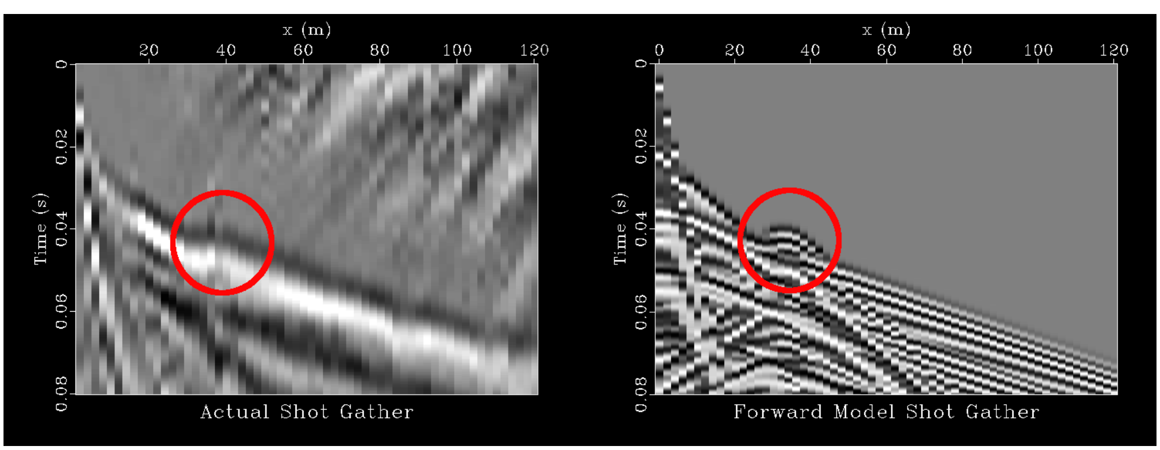

Figure 21. Same shot gather from actual data and from forward model. Both showing 'bump' dike anomaly.

The true shot record from the 4000 line had an anomaly, "bump", between traces 15 and 20 that we were unable to explain. This anomaly was not present with the layered-cake forward model, so we assumed this anomaly must have been caused by the dike. The next model included the dike allowing us to infer the position of the dike.

7.3.3. *Dispersion Analysis.* Another way hammer seismic is used to investigate the subsurface is by analyzing surface waves. Every shot gather contains surface waves that travel relatively slowly along the surface of the earth. Because of their large amplitudes and long wavelengths, surface waves are typically considered noise and get removed during processing. These waves however hold information about subsurface velocities that can be explored using dispersion curves. Even though surface waves do not penetrate the ground, subsurface characteristics still affect how quickly the waves travel on the surface. Surface waves at different frequencies interact with varying depths in the earth, causing them to travel at different speeds on the surface. In general, lower frequency waves respond to subsurface conditions deeper in the earth compared to high frequency waves. The velocity of surface waves at specific frequencies reveal how deep those surface waves are interacting with the subsurface. A plot of this relationship between frequency and velocity is known as a dispersion curve (dispersion curves actually use slowness in place of velocity). These dispersion curves can be manipulated to illustrate how fast waves travel at varying depths in the subsurface.

Dispersion analysis was performed on the 4000 line on three shot gathers; the far west end, the center, and the east end. Upon initial evaluation, the velocity of the surface waves at the center shot gather appeared to be different on the left and the right side of the shot. For this reason a separate analysis was done on the east and west side of the center shot. The west end, the center looking west, the center looking east, and the east end make four different locations for dispersion analysis. The 4000 line likely crosses the dike near the west end. Dispersion analysis could reveal velocity changes that correspond to the faster igneous rock that make up the dike.

A dispersion curve can be created from any of the four shot gathers. The slope of the surface waves is found for the full frequency spectrum of any given shot gather. These slopes represent time vs. distance values which need to be converted to slowness vs. frequency. A Fourier Transform converts time to frequency and a Radon Transform converts distance to slowness. Figure 22 is an example of a shot gathers that has been transformed into a dispersion curve.

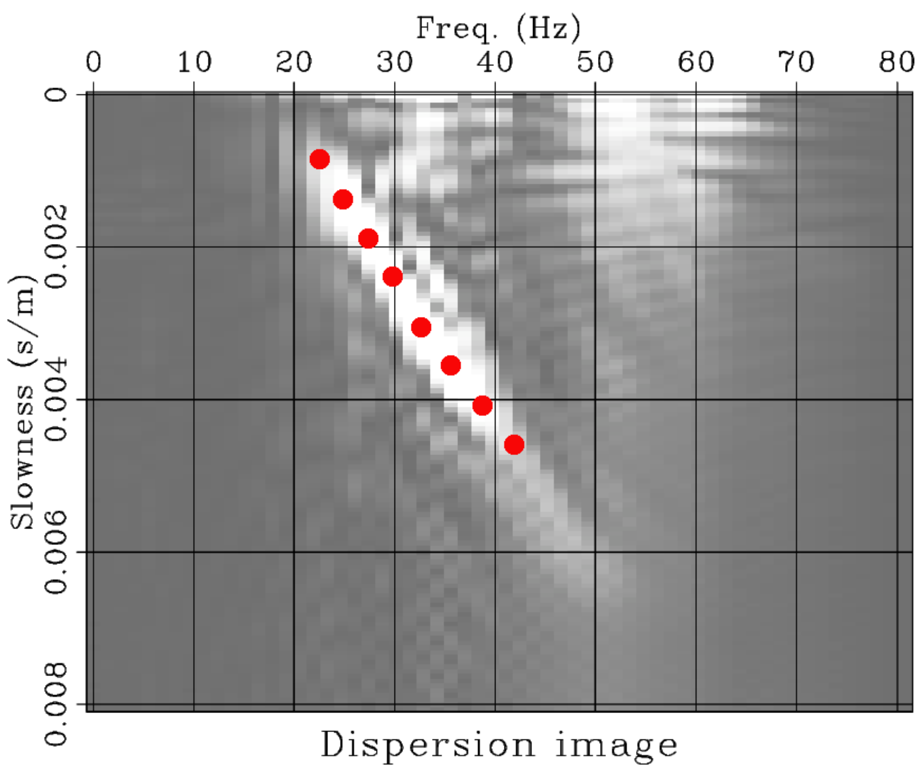

Figure 22. Transformation from shot gather to dispersion curve

Once a dispersion curve is made, some final alterations can be done to relate wave velocity to depth. On a dispersion curve, pick around ten data points that make a general line down the white, high amplitude curve. Figure 22 is an example of a few points picked on a dispersion curve from the east end of the 4000 line. This is a set of slowness to frequency values which can be converted to velocity and depth values. Velocity is the inverse of slowness and depth is velocity divided by frequency over two. Using this simple conversion each point can be converted to a depth and velocity relationship. Plotting depth against velocity beneath the respective shot gather reveals a velocity profile of the subsurface. Figure 23 plots the depth and wave velocity relationship of each dispersion curve generated from the 4000 line.

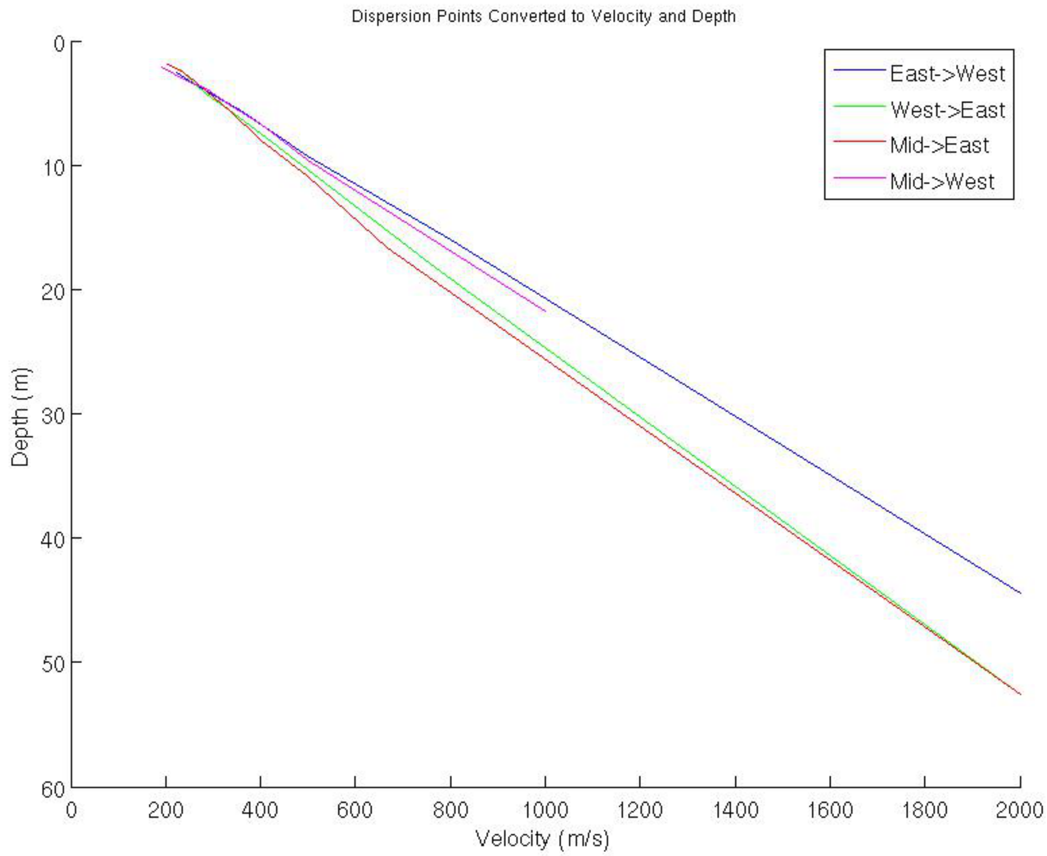

Figure 23. Picking slowness vs. frequency points on a dispersion curve

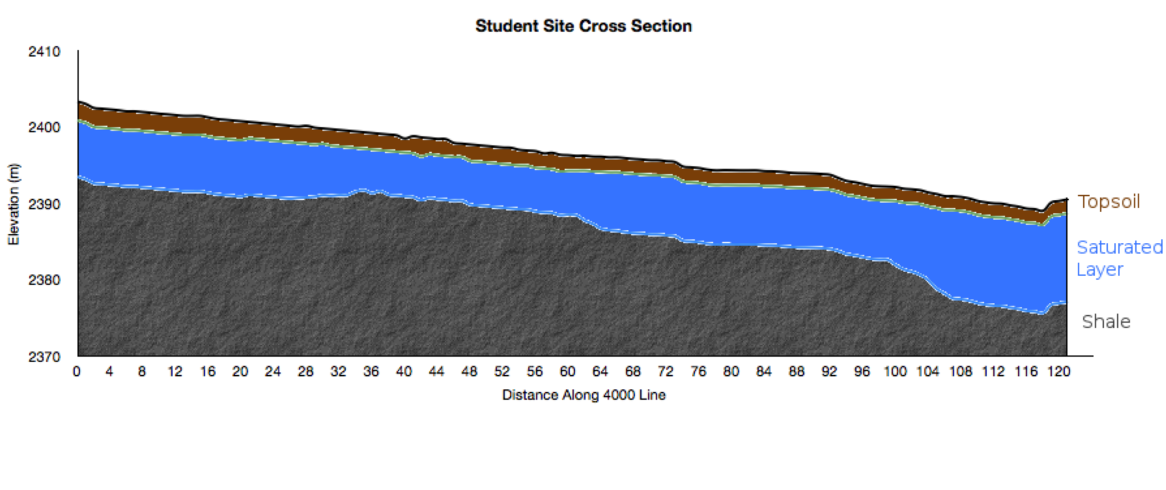

Figure 24. All four dispersions converted to depth vs velocity

The four dispersion analyses on the 4000 line reveal velocity information at four different locations; the west end, the middle looking west, the middle looking east, and the east end. A rough estimate of the velocity profile along the entire 4000 line can be done by interpolating the wave velocities between these locations. The inpaint_4nans.m function in matlab can be used to interpolate between the known velocity values. 24 is the final generated velocity image. The blue circles on the image represent the actual depth and velocity values from the transformed dispersion plots. The west and east ends, have velocity values from their respective shot gathers and dispersion plots. But, notice that the velocity values for the center shot have been offset to the left and the right of the center line. This is because two dispersion plots were created from the center shot gather. Both east and west looking velocity values could not be displayed on the same line in the image. To solve this issue, the velocity values were offset ten meters to the east and west, respectively. Exactly how far from the center the velocity values should be is hard to determine. They were gathered at the center point but since they look in one distinct direction they tell information about the subsurface on one side of the center shot. It was found that offsetting 10-20 meters from the center created almost identical interpolations. Any closer than 10 meters created a large anomaly on the center line that can be attributed to issues with the interpolation function. 24 is a rough estimate of velocity values in the subsurface generated from four separate dispersion analyses.

7.4. Results. The refraction analysis, forward model, and surface wave analysis have all helped reveal information about the subsurface at the Recon Site. The goal for all four lines was to image the dike and potential fault. Refraction analysis was able to identify three layers with distinct velocities. These layers were found with fairly consistent depths and velocities under all four lines. Figures 24 shows the relative depths below the topographic surface. Figure 25 illustrates the paths of the refraction waves and the velocities of each layer.

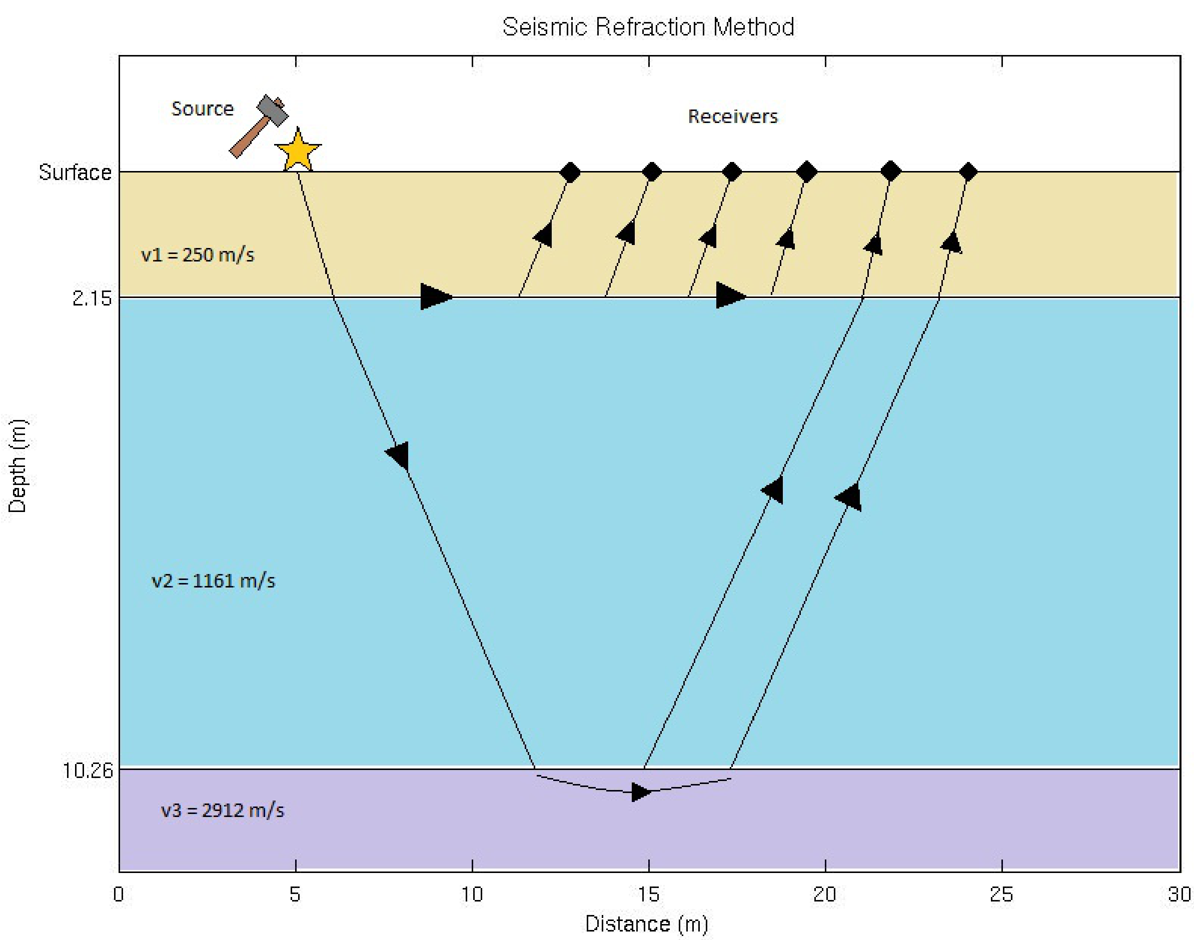

Figure 25. Cross-section along 4000 line, based on thicknesses calculated from velocity model

The depth and velocity information from the refraction analysis was used to create a forward model in Madagascar. The forward model replicated shot gathers seen in the field confirming that the interpretation of the subsurface is accurate. A dike intrusion was also inserted into the forward model at a location predicted by the

dike's surface expression. This produced an anomaly in the forward model shot gathers that was also seen in the shot gathers from the field. This supports the idea that the dike continued into the subsurface below the line in question.
Surface wave analysis was able to produce another velocity profile of the subsurface. Figure 26 shows the velocity profile beneath the 4000 line up to around 45 m deep. This profile shows an area of high velocity that may correspond to the dike seen on the surface. The forward model used with the refraction analysis predicted the dike coming closer to the surface and being further in the line. Since the surface wave analysis was a fairly rough interpolation, it is not surprising that the dike location is not exact. The important point gathered from surface waves is it confirms, with refraction analysis, that a high velocity area exists below line 4000 that corresponds to the dike.

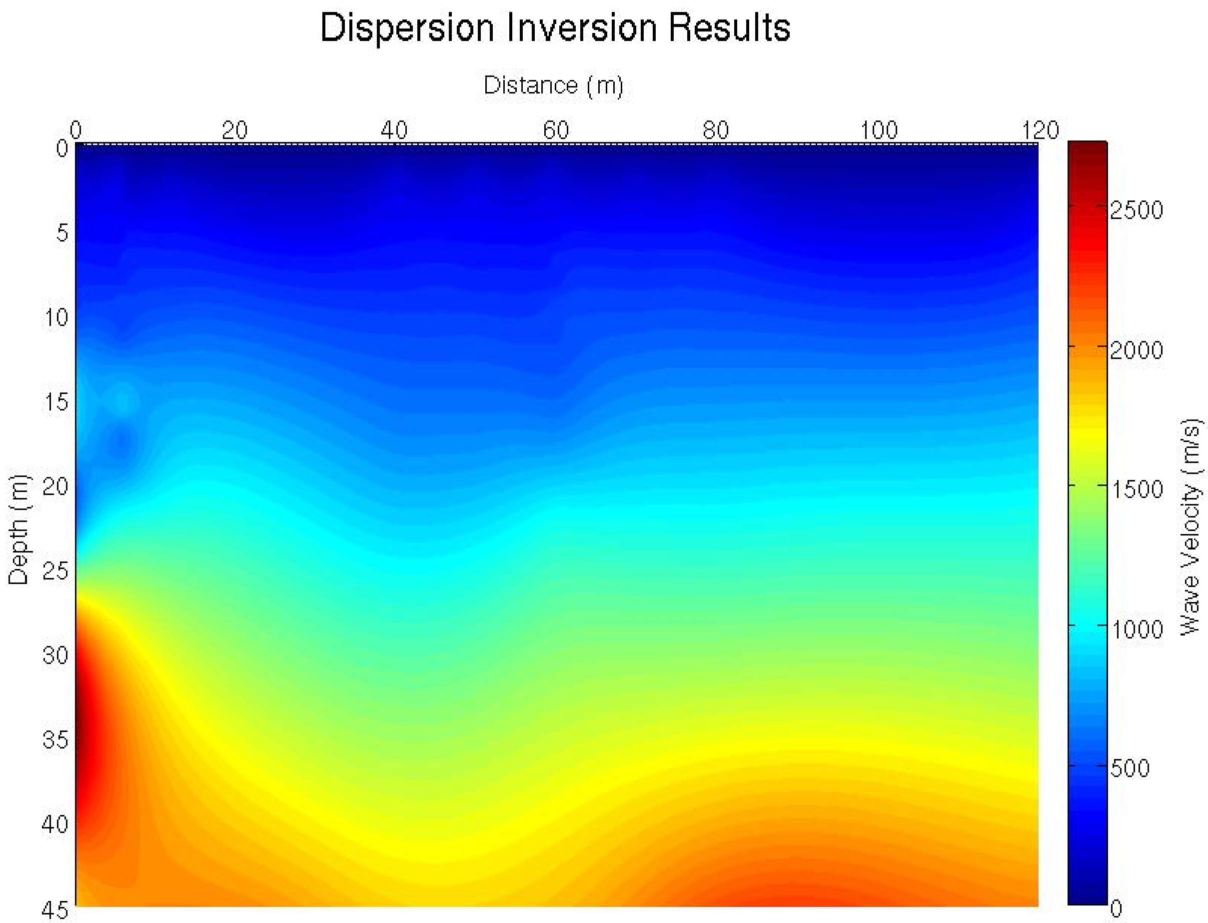

Figure 26. The refracted wave paths through our three-layered model

7.5. Sources of Error. The shallow depth of investigation for hammer seismic means that the data collected is very easily influenced by noise. Our surveys in the reconnaissance area could've been affected by people walking nearby, cars driving on the road, and even small animal burrows. The raw data is also subject to human error, such as inconsistency in the hammer strike, and uneven spacing between the geophones. The depth and velocity values used in the forward model were the product of the refraction analysis discussed above. This process has a lot of room for human error, especially when drawing the slopes of the surface and refracted waves, as a slight change in slope would change the depth of the interface. Also the size of the dike in the forward model is five meters thick, but the actual thickness is unknown and could change to as low as two meters thick. The five meter thickness was chosen because the velocity of the dike required to see an anomaly at a two meter thickness was unrealistic. This forward model was more of a qualitative investigation. When running it originally without a dike, the anomaly in the actual shot gather, circled in 21, does not show up. However this anomaly is present when the dike is included.Similar errors exist for our dispersion analysis. The velocities were hand-picked, causing human error. The final image was roughly interpolated over the 120 meter line with data from only the beginning, middle and end. For this reason the location of the anomaly could vary immensely. These various sources of error and noise should be kept in mind not only for interpretation, but for future hammer seismic surveys as well.

7.6. Summary. Within the Recon Site, hammer seismic was used with the intention of imaging the dike and potential fault in the area. Four lines were shot and processed to search for these features. Analyzing the data from each seismic line has revealed that hammer seismic is not the ideal method for producing a high resolution image of subsurface features. None of the survey lines were able to illuminate the fault or dike with reflection analysis. Luckily, hammer seismic is an ideal survey technique for studying other aspects of the subsurface. Both refraction analysis and surface wave analysis can be used to produce depth and velocity models of the earth. These results can be used to roughly image the subsurface and identify anomalies with high or low velocities, like a dike or fault. Both of these techniques provided evidence of a dike beneath the surface along the 4000 line in a location that make sense with surface expressions.

While it was discovered that hammer seismic has its limitations, careful processing can be used to provide valuable information about the subsurface. The very low monetary and environmental impact makes hammer seismic a unique geophysical technique that can be very helpful in areas like the Recon Site.

SECTION 7

Discussion

1. Integrated Results

The non-unique character of geophysical data implies that no acquisitional method alone can be used to image the subsurface. In order to form a reliable model, it is necessary to apply knowledge of local geology or results from other methods to constrain the interpretation. A well-developed model takes all available information and previous models into consideration, where any discrepancies between results are explained by reasonable physical phenomenon or can be attributed to error in survey execution. If discrepancies are small, data can be reprocessed with new parameters to converge on the most plausible solution. The development of a reliable, comprehensive model requires cycling through this integration procedure numerous times. The objective of method integration is to construct a logical explanation of results from all available datasets and provide justification for any inconsistencies. The first effort made towards constructing a comprehensive model of the Chromo anticline was to draft a geologic cross section based on surface observations. Upon arrival to the survey site, students were oriented with respect to the surface geology. Outcrops of the Mesaverde are stratigraphically situated between the Mancos and Lewis shales and observed as an outward dipping ring surrounding the town of Chromo. These outcrops ascend into large cliffs to the west and are expressed as hogbacks in the east, indicating the presence of a breached anticline. The stratigraphy of this region is well defined by well logs that confirm the superposition of the Mancos, Mesaverde, and Lewis formations respectively. Knowledge of stratigraphy and surface observations alone provide insight to the geologic structure along the main line.

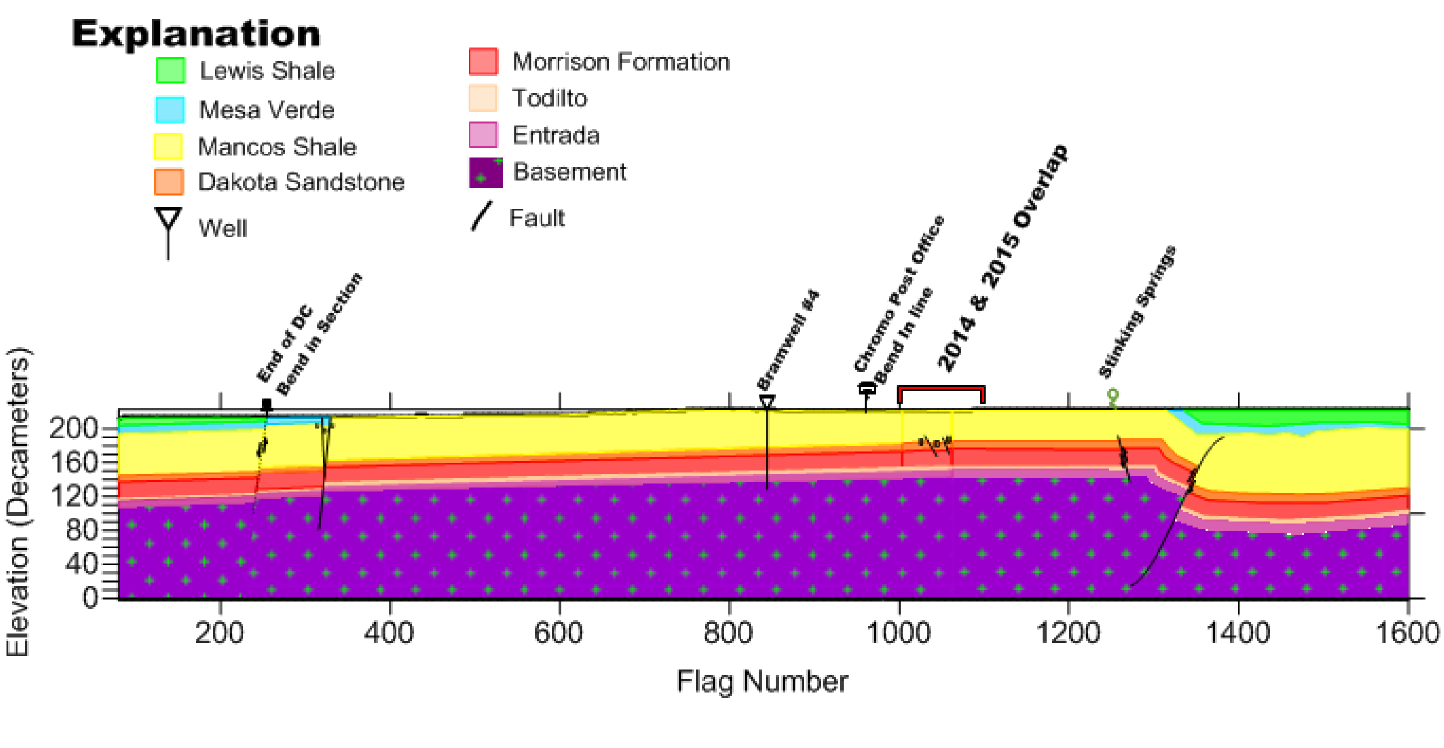

Figure 1. Geologic cross section of the Chromo anticline based on surface observations.

The primary result of the 2014 Field Camp was the identification of a large thrust fault and anticline crest centered on the geothermal feature of Stinking Springs. These findings were imaged using deep seismic acquisition, which is currently the most effective method that is used to determine geologic structure at depth.

Gravity surveys provide insight to a greater depth of investigation, but cannot be represented as a stand alone model as the results are largely non-unique. The forward model of the 2015 gravity data was therefore constrained to fit the reflectors in the interpreted seismic section. Discrepancies regarding the predicted gravity signal were illuminated as a result. The original interpretation indicated a significantly exaggerated anticline, indicating an overestimation of density as shown in Figure XX.

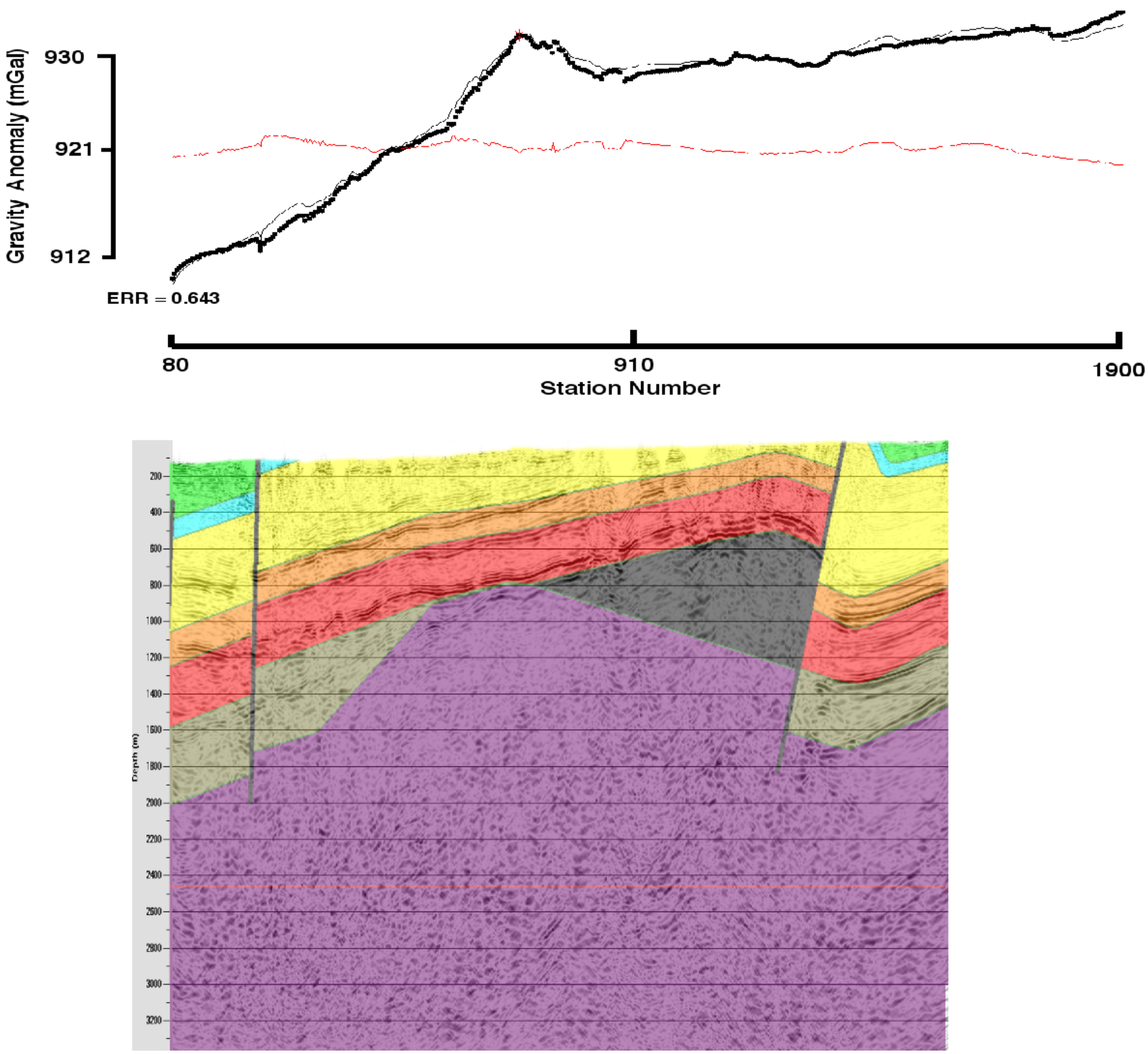

Figure 2. The bold black line is the free air/terrain corrected field data, the thin black line is the forward modelled gravity response, and the red line is the difference between the field data and modelled response. (Lower Image) Interpretation of gravity data using previous information provided by the seismic model and surface geology. This only incorporates gravity data along the 2014/2015 main line.

This discrepancy can be resolved by the presence of a low density, unconsolidated zone of sediment. This feature is predicted to be an anomalous, low density material along the hanging wall of the thrust fault. Two interpretations of this feature were considered. The first is that seismic processing did not properly distinguish a reflector and that the low density area is actually an extension of the Cutler Formation. A more likely alternative is that the basement reflector was properly imaged, but there exists a fracture zone with up to 10% reduction in density. This interpretation is supported by the presence of small faults on the basement reflector along the low density zone.

Electromagnetic methods are also integrated into our final results. The one-dimensional resistivity models of MT and TEM data are compared to the gravity and seismic results in Figure 3 below. These methods produce similar models, but are sensitive to different depths of investigation. The TEM survey has higher resolution at shallow depths but is not capable of detecting resistivity contrasts to the extent that is observed in an MT survey. The TEM model correlates well with the seismic, gravity, and geologic interpretation as it confirms that the Dakota Sandstone is saturated to the point that it maintains a lower resistivity value than the overlying Mancos shale. The MT surveys confirm these results such that a saturated Dakota sandstone is consistent the two 1D resistivity profiles.

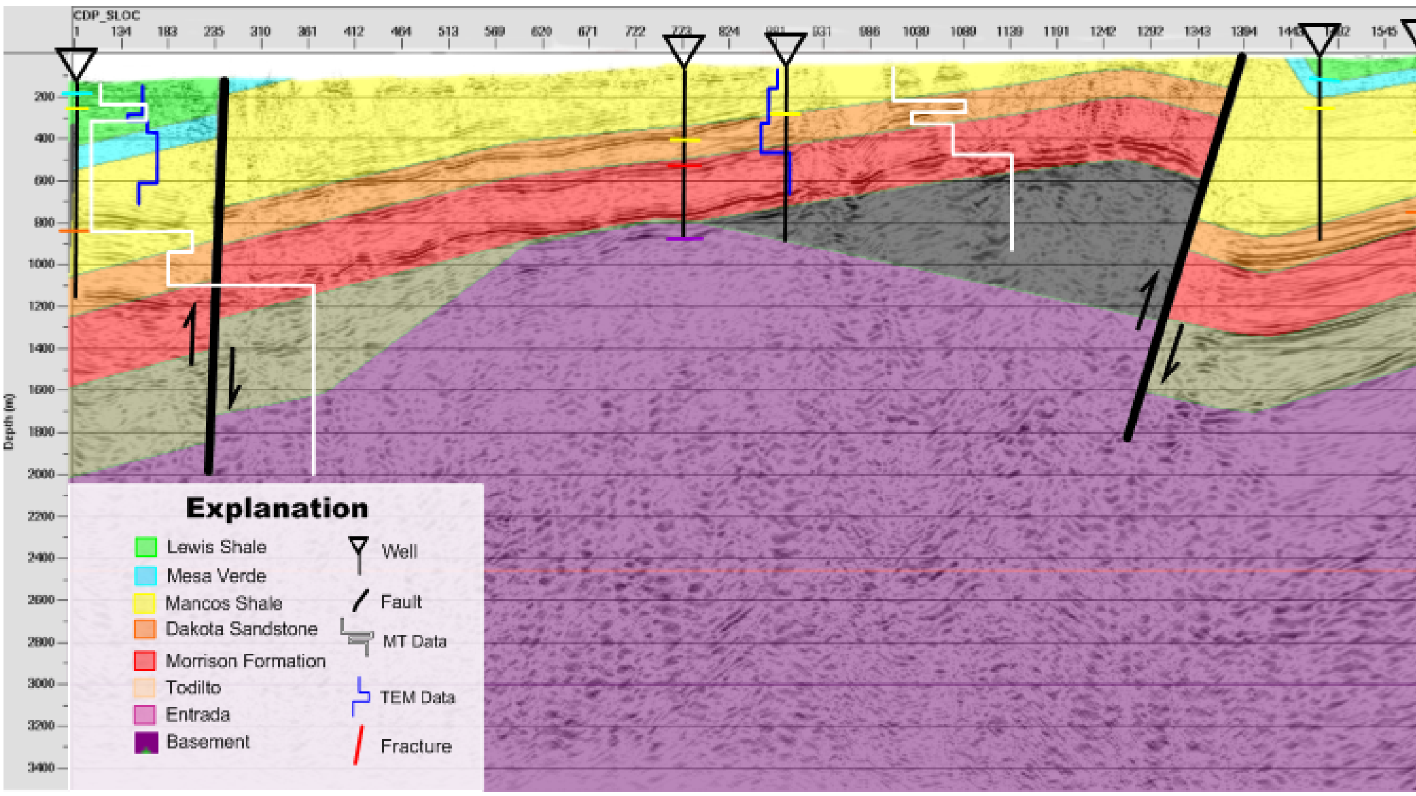

Figure 3. Final joint interpretation including data from well logs, seismic, gravity, TEM, and MT.

SECTION 8

Conclusion

The 2015 Field Camp survey was completed from May 10th to May 22nd. It sought to further characterize the structural controls of geothermal activity in Archuleta County and provide valuable information to the local community. During the survey, multiple geophysical methods were deployed onto the main line in Chromo, CO and at a reconnaissance site in the San Juan National Forest. The main line survey involved the acquisition of new data along County Road 391 in Chromo. The survey was designed to overlap with a previous study performed in 2014. This was designed with the intent of merging data sets in order to provide a larger characterization of the structure associated with the Chromo anticline. One of the first steps to the overall understanding was the application of a reconnaissance site. This portion of the investigation utilized more portable methods that could navigate the difficult terrain. The goal of exploring this auxiliary area was to determine if there is a possibility of linking the hydrologic systems from Chromo to the Pagosa area. When acquisition was complete, data processing followed back on campus. During processing, nearly all collected data were reduced into reliable information products and images. Interpretation of these results led to a description of geologic structure in the Chromo area which includes several newly discovered faults that do not reach the surface. The observed structure seen in the seismic and gravity results, when combined with electrical and electromagnetics methods, illustrate the presence of a low resistivity area at the depth of the Dakota sandstone. This is indicative of a saturated aquifer present within the Dakota formation. This formation is known to have a large porosity in comparison to the surrounding strata which further validates the notion of an aquifer that is conducive to fluid transport. However, there are obstructions to the preferential flow path within the Dakota formation. One such obstructions is the offset associated with the 2014 Field Camp Fault, which is large enough to shear the Dakota on both sides.This obstruction is at the same location as an inferred fracture zone which may provide a pathway for fluid to travel through the basement between ends of the Dakota formation. This occurs at a location coincident with the Stinking Springs on the surface. These interpretations and observations lead us to agree with the conclusions of previous field camps that the Dakota Formation is the primary reservoir for geothermal water in Archuleta County. We also suggest that geothermal heating primarily occurs at locations where faults offset the Dakota causing fluid to move through basement before returning to the unit or breaching the surface at a spring. This conforms to conceptual models of the broad structure in this region. The Archuleta Anticlinorium allows for accumulation of reservoir fluid at the crest of anticlines along its axis. The anticlinorium also results in an extensional tectonic regime which results in numerous conduits for fluid transport along the same axis. These faults have larger fracture zones and are more likely to penetrate into basement material when they are reactivated faults. This provides numerous locations where water within the Dakota Formation is geothermally heated through contact with fractured basement rock to produce hot springs. The high temperature springs associated with the Archuleta County area most likely occur due to a combination of ideal fault geometry and local properties of the Dakota Formation. Further studies of geothermal activity in Archuleta County should seek to address how these factors influence spring temperature and volume output. It is a complex problem that depends on numerous interdependent factors and will require observations of many hot, warm, and cold springs for results to reach statistical meaningfulness.

SECTION 9

Appendix

1. GPS

1.1. Introduction. Scientific applications used within geophysical exploration require accurate survey location information in order to process data and produce interpretable images. The Global Positioning System (GPS) is a freely available tool that provides geospatial information. While both handheld and differential GPS (dGPS) receivers are heavily utilized, the high accuracy of differential GPS (dGPS) is often required to collect reliable geophysical measurements. The primary advantage of using dGPS is the accuracy of elevation data. Seismic, DC, IP, and gravity methods, which require corrections to create interpretable images, are highly dependent upon precise, consistent GPS measurements.

1.2. Background and Theory. The Global Positioning System (GPS) is a navigation system created and maintained by the U.S. government. Originally designed for military use, satellite navigation was made available to the public in 1994. The signal was intentionally degraded for another six years, when deactivation of the feature, called Selective Availability, improved error from 100 m to the current 3-5 m range [**27**]. GPS measurements provide location information relative to a projection and coordinate system, both of which are important to consider in data acquisition. Choosing the wrong system can result in location shifts of hundreds of meters [**28**]. Attempts to represent the earth's surface in comprehensible ways, with minimal distortions, have resulted in an enormous range of coordinate systems. A map projection allows for the representation of the curved surface of the earth on a plane, cylinder, or cone. There are hundreds of different types of projections, but one of the most common is the Universal Transverse Mercator (UTM) projection, which uses a 2D Cartesian coordinate system. Taking a spherical surface and mapping it onto a plane causes distortions, which are typically only evident over large areas crossing multiple zones. Different coordinate systems may be used in different parts of the world, depending on which system provides the best fit. The most commonly used reference system in the United States and Canada is the North American Datum of 1983 (NAD83), which combines a standard coordinate system with a particular datum. A datum is a chosen reference point, line, or surface. In the case of GPS, the datum is a reference spheroid that is positioned to provide the best representation of the shape of the earth. The positioning is set by matching a point on the spheroid to a point on the earth's surface (i.e. the origin). There are several commonly used datums, all of which vary by origin and tilt. Each datum displays a different shift of the latitude-longitude coordinate system, meaning coordinates for a specific point on the earth's surface in one datum will not be the same as those in another datum. Consequently, it is very important to work consistently with one datum.

1.3. Practical Implementation. GPS is comprised of 24 or more satellites flying at medium-earth orbits, broadcasting their locations at precise times [**27**]. Once a GPS receiver (handheld or differential) acquires radio signals from at least four satellites, it uses the travel time of each signal to calculate the distances from the GPS unit to each satellite. It then calculates its position in three dimensions on the surface of the earth through trilateration. GPS receivers show heights relative to a spheroid (an idealized second-order approximation of the earth's surface, which has an equatorial radius that is 22 km longer than the polar radius) or to the geoid (a shape representing Earth's surface as a mean sea level, if the planet had no continents) [**28**]. A handheld GPS unit communicates directly with the satellites without referencing a base station and yields measurements with an average accuracy of three to five meters. In contrast, differential GPS (dGPS) requires two receivers: a base station and a rover. Ideally, the base station is placed at a fixed position where the precise location and elevation are known. A comparison between the benchmark and the location determined by the base station receiver yields an error correction that is applied to every measurement taken by the rover and can result in an accuracy on the order of centimeters. If the base station is occupying a known geographic location, accurate (or absolute) locations for each measurement taken by the rover can be determined. If the base station is not occupying a known geographic location its is determined by a GPS receiver, and the accompanying error means that measurements taken by the rover are locations relative to the base station. This problem of relativity can be overcome by taking a known point with the rover and performing a static shift.

2. Gravity Theory

2.1. Introduction. The gravity geophysical method utilizes the earth's natural gravitational field to detect variation in gravitational acceleration. Density contrasts in rock units affect the measured gravitational field. For example, high density materials have a stronger gravitational pull and associated acceleration due to their larger bulk mass. Ultimately, gravity measurements relate directly to changes in subsurface geology and can be used to characterize broad structural trends including faults and folds. The gravity method can help provide a local

description of the subsurface structure by incorporating other geophysical information such as surface geology, stratigraphy and density values. This description can be used to justify interpretations provided by other methods such as deep seismic or electrical methods. Additionally in comparison to other geophysical methods, gravity is relatively inexpensive and does not require a huge crew to operate. Relative gravimeters are also fairly small, so transportation and location of surveys pose little hindrance to their use. To measure precise changes in

gravitational acceleration we use a gravimeter. There are two types of gravimeters: absolute, and relative. An absolute gravimeter measures the absolute local gravity by measuring the speed of a mass as it falls in a vacuum. They are generally large devices that require extensive time to operate, but this reading is extremely accurate. A relative gravimeter can be used to take measurements at various locations quickly. This type of gravimeter contains a spring which is stretched differentially based on the earth's gravitational field at a specific location. The displacement of the spring changes as the gravitational field changes, so the relative displacement of the spring is proportional to gravitational acceleration.

2.2. Background.

2.2.1. *Theory.* The gravity method utilizes Newton's Laws to relate gravitational acceleration of physical properties of the system. First, Newton's Law of Universal Gravitation (shown in Equation (4)) states that two objects are attracted to each other with a force proportional to the product of their masses.

$$F = G\frac{m_1 m_2}{r^2} \tag{4}$$

The above equation relates the masses of two bodies m_1 and m_2, the distance between them r, and the resulting force put on that body F. The third quantity, G, is an empirical value derived from experimentation with a value of 6.673x10-11 $\mathrm{Nm}^2/\mathrm{kg}^2$. This value is know as the Gravitational Constant. Newton's Second Law relates the force on a body to acceleration and is illustrated in Equation (5).

$$F = ma \tag{5}$$

In this equation, F is the force applied to a body, m is the mass of the body, and a is the acceleration of the body. It relates the force on a given body with its mass and acceleration. Combining Equations (4) and (5) relates the acceleration and physical parameters of the system. The relation is described in Equation (6).

$$g = \frac{GM}{r^2} \tag{6}$$

Equation (6) can be used to determine the acceleration at any point on the surface if the distance from Earth's center is known. This equation gives us the basis for the gravity method using a relative gravimeter.

2.2.2. *Units.* The units of acceleration in Equation (6) are $\mathrm{m/s}^2$, but the gravity anomalies considered by the gravity method are on a smaller scale. In gravity surveys, units of Gals are used where $1\mathrm{Gal} = 10^{-2}\mathrm{m/s}^2$. It is important to note that most gravimeters display gravity measurements and respective standard deviations in units of $\mathrm{milliGal} = 10^{-5}\ \mathrm{m/s}^2$. All corrections in gravity data are in units of milliGals.

2.2.3. *Corrections.* There are a number of corrections that must be applied to raw gravity data before meaningful anomalies can be observed. These are generally applied in a predefined order. The corrections required for this data in order are tidal/drift corrections, the free air correction, the latitude correction, the Bouguer correction, and the terrain correction.

2.2.3.1. *Tidal/Drift Correction.* Tidal/drift corrections remove the effect that Earth tides have on gravity data. These tides are the deformation effect that the Sun and Moon have on the earth. This deformation of the earth also affects the gravity field, which over time can introduce error **[28]**. To counteract this we take a base station reading at the beginning of any survey, and then take another one every couple of hours. At the conclusion of each survey day, we once again return to the base station for a final reading. This process, called "closing the loop" gives us data we need to accurately correct for tidal/drift effects. This correction uses the following Equation (7).

$$g_{dc} = g_{obs} - \frac{g_{b2} - g_{b1}}{t_{b2} - t_{b1}} * (t_{obs} - t_{b1}) \tag{7}$$

In this equation, g_{dc} is the drift corrected data, g_{obs} is the observed data, g_{b1} and g_{b2} are the two base station readings, t_{obs} is the time of the observed reading, and t_{b1} is the time of the first base station recording..

2.2.3.2. *Free Air Gradient Correction.* The free air correction adjusts variations in gravity readings result partially from changes in elevation along a survey line. These variations must be accounted for, requiring a precisely known elevation at each reading. A change in elevation at any point cause variations in the distance between the measurement location and the center of Earth's mass. An increase in height will result in a decrease in gravitational acceleration relative to the base station, as described in Equation (6). The increase in height correlates to a negative effect on the gravity measurement, so the free air correction will be positive. This relation between gravity measurements and topography is observable on plots of drift corrected data with topography data as there will be an inverse relationship. The following Equation (8) describes the change due to free air that must be applied to the data[**28**]:

$$\delta g = (0.3087691 - 0.0004398 * \sin^2 \lambda)h + 0.000000072125h^2 \tag{8}$$

Due to the negligible variation in latitude, this equation can be reduced to the following simplified form:

$$\delta g = 0.3086 * elevation \tag{9}$$

Note that elevation is measured in meters, and the resulting δg value will be in units of milliGals, as the constant 0.3086 has units of $1/s^2$. The free air correction requires accurate elevation values at each point where measurements are taken to ensure the correction properly accounts for changes in elevation. Therefore if accurate elevation data is missing, the measurement is meaningless.

2.2.3.3. *Latitude Correction.* If the gravity measurements are from an absolute gravimeter, the latitude correction can be completed by subtracting the normal gravity from the absolute gravity. The normal gravity can be calculated from the International Gravity Formula [**28**]. When a relative gravimeter is used, the latitude correction can be completed by using the north south gradient of the base station and Equation (10):

$$\delta g = 0.812 \sin(2\lambda) \tag{10}$$

This equation produces a correction in mGal per km of latitude change. Where there is very little change in latitude, this correction can result in values smaller than the measurement error of the gravimeter, so they can be neglected.

2.2.3.4. *BouguerCorrection.* The Bouguer correction compensates for uneven mass distribution from asymmetric terrain. To do this, imagine that the asymmetric area is an infinitely wide, flat plate. This plate can be made with a thickness h and a density ρ that produces a gravity field equal to Equation (11).

$$\delta g = 2\pi\rho G h \tag{11}$$

Assuming a crustal density of 2,370 kg m^{-3} gives a with a correction of 0.1119 mGal m^{-1}, which is fairly high [**28**]. A complication with the Bouguer correction comes from the fact that it assumes a plate with flat topography. The correction does not take into account any lower elevations, thus overestimating the correction. To correct for this we use the terrain correction.

2.2.3.5. Terrain Correction. The terrain correction is generally applied after the Bouguer correction. It accounts for any overcompensations that the Bouguer correction makes. The Bouguer correction may account for a mass it thinks should exist and does not, the terrain correction takes this problem and removes it [**28**]. There are a several ways to do the terrain correction. The original method was to use a *HammerChart* as seen in Figure 1. The chart divides an area into smaller sections and the average height of each section is calculated. The calculations are then looked up in a table that gives the corrections [**28**]. Since this must be done for each measurement location, it can become tedious depending on how many measurements are taken. The modern approach is to use a program to find the corrections, such as Geosoft Oasis Montaj and the Gravity and terrain Extension.

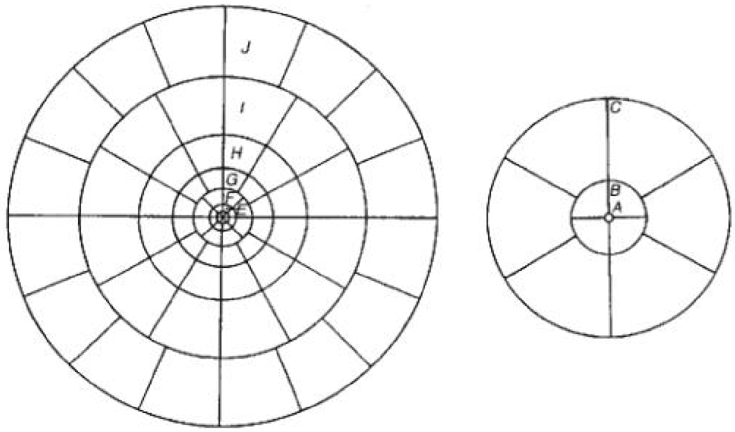

Figure 1. A basic Hammer chart [**49**]. This would be printed on transparent sheet and then placed over a topo map.

2.3. Practical Implementation.

2.3.1. *Relative Gravimeter.* The gravity measurements collected along the main line were recorded using the Autograv CG-5. This is a relative gravimeter, meaning that it measures changes in gravitational acceleration from station to station, whereas absolute gravimeters measure the local gravity in absolute units. Each

gravimeter has a "proof mass" which has a precisely known weight suspended by a spring with an empirically derived stiffness. As the gravitational field changes, the force on the proof mass changes accordingly, resulting in a change of the spring length. The amount of force required to move the mass back to its initial position provides a gravity measurement at a given station relative to other stations [**50**].

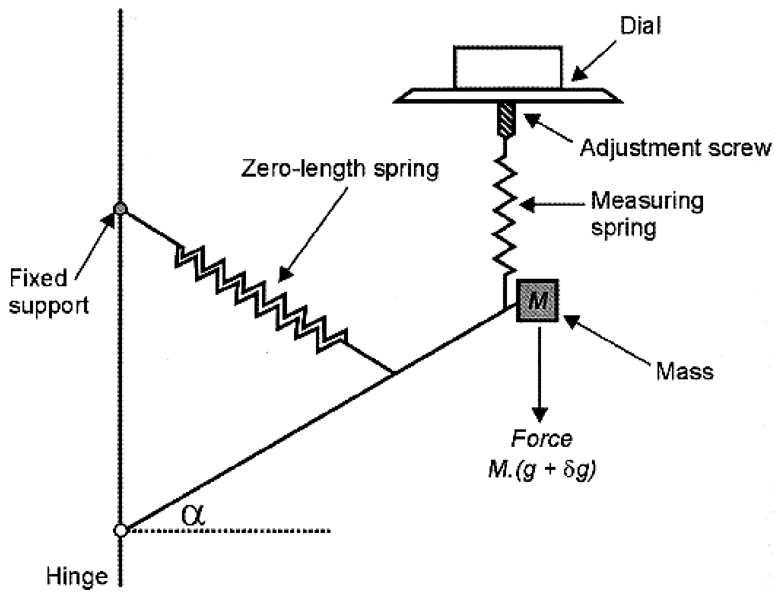

Figure 2. A very simple diagram of the inner mechanisms of a relative gravimeter [**28**].

After inputting several parameters including the time for each recording and the total number of readings at each point, the CG-5 takes several recordings accurate to within 5 μGal. With such a high degree of accuracy, noise is fairly easily introduced. Sources of noise include wind to people standing too close while taking the recording. Instrument tilt can introduce error because the mass will not be hanging straight down. Temperature can be a factor, as it will affect the stiffness of the spring. Seismic noise often involves shaking, and this will also affect the reading. Fortunately these are all automatically corrected.The CG-5 has a number of automatic corrections that are applied to the data including instrument tilt, temperature and a seismic noise filter [**51**].

3. Magnetics

3.1. Introduction. A geophysical magnetics survey works similar to a gravity survey in that it is a passive method that uses one of Earth's natural fields to find anomalies in the subsurface. In the case of magnetics, magnetometers utilize Earth's magnetic field to identify notable variations in magnetic susceptibility. It is a fairly common survey type due to its low cost and versatility. It can be easily implemented for standard geophysical investigations and is even useful for archaeological problems.

3.2. Background. Earth's magnetic field causes alignment of molecules within magnetic minerals which then generate their own secondary magnetic field. The components of the 'total' magnetic field are measured when recording magnetic data. The total magnetic field is composed of Earth's magnetic field with the secondary magnetic field superimposed. By removing the earth's magnetic field from the total field, all that is left in the data are the magnetic responses due to anomalies. This being said, there is still an important correction to be made when dealing with any magnetic survey data. To create accurate models, corrections for diurnal variation - changes in Earth's magnetic field associated with time of day - must be made. Additionally, magnetics can only be used effectively in certain environments. Rock types like shale and sandstone hinder useful implementation because they typically do not have a high enough magnetic susceptibility to distinguish between units. Igneous rocks on the other hand usually have a fairly high magnetic susceptibility and are easier to detect with a magnetometer. An ideal setting would be an area that includes a boundary between two rock layers of high and low magnetic susceptibility.

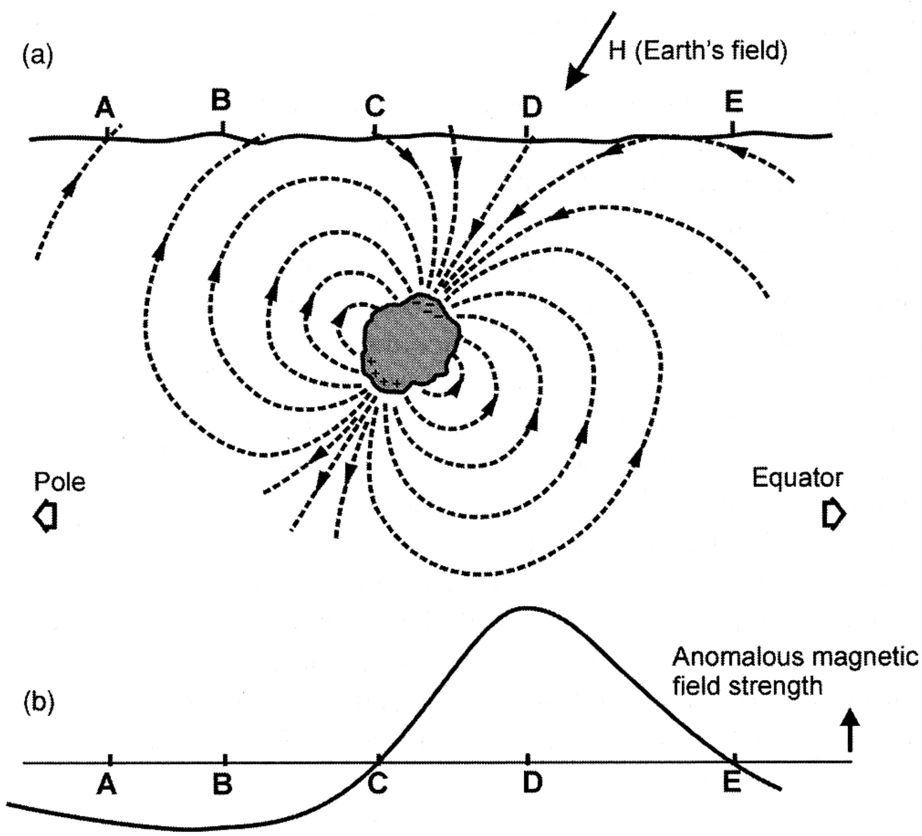

Figure 3. (a) Represents the magnetic field lines from an object below the earth's surface. (b) Represents the magnetic field strength that would be recorded by walking along the surface above the buried object [**28**].

Figure 3 shows how a magnetic anomaly below the surface produces a magnetic dipole field that is observable at the surface. The response in part (b) of the image can be obtained after applying a diurnal correction. During the survey the base station is set up isolated from the survey and anything with a magnetic response (fences, cars, etc.). It is programmed to take a measurement of the magnetic field at a certain time interval throughout the day. Earth's magnetic field will change throughout the day and will affect the reading of the magnetometer being used for the survey line. A diurnal correction takes the reading of your magnetometer and subtracts the base station reading for the same time as your magnetometer reading. This correction is required because the magnetometer reading will be a combination of the target's magnetic field and the earth's magnetic field. The base station reading is the background magnetic field, so subtracting the two gives only the target's magnetic field.

$$\vec{\nabla} \times \mathbf{E} = -\frac{\partial \mathbf{B}}{\partial t} \tag{12}$$

The cause of a magnetic field is described by Faraday's Law of Induction (12). Where **E** is the electrical field and **B** is the magnetic field. This equation shows that the movement of charges in space (given by the left side of the equation) is equal to the change of the magnetic field in time (given by the right side of the equation). This means that if you have a movement of charges (current) then you will have a magnetic field.

$$\vec{\nabla} \times \mathbf{E} = -\frac{\partial \mathbf{B}}{\partial t} \tag{13}$$

Gauss's law for magnetism (one of Maxwell's equations) explains that magnetic fields are not divergent (13). Over a closed surface the total magnetic flux is equal to zero. **B** is still the magnetic field and n is the normal vector.

$$\mu = \mu_0(1 + \kappa) \tag{14}$$

Magnetic susceptibility (κ) is the value of how easily an object is magnetized. It is related to the magnetic permeability (μ) and the magnetic permeability in a vacuum (μ_0) (14).

$$\mathbf{M} = \frac{\kappa \mathbf{B}}{\mu_0} \tag{15}$$

Magnetic susceptibility can also be used to determine the Magnetization (**M**) (15). Again, κ represents magnetic susceptibility, μ_0 represents the magnetic permeability in a vacuum and **B** represents the magnetic field. Equation (15) holds some characteristics that can be used to distinguish between different geologic rock layers.

3.3. Practical Implementation.

3.3.1. *Magnetometers.* There are two types of magnetometer that the crews have access to in the field: a proton precession magnetometer and a cesium vapor magnetometer. In a proton precession magnetometer polarizing current passes through a fluid filled container wrapped in a copper wire. This creates a magnetic field which causes hydrogen protons to line up. If the current is interrupted the protons align to the earth's magnetic field [**28**]. This alignment is then recorded. This type of magnetometer is particularly good at measuring changes in the earth's magnetic field which is why it is a very useful magnetometer to use as a base station.

The cesium vapor magnetometer operates using the properties of the cesium atom. When a small current is put into the atom it becomes excited and jumps to the next energy level. This creates a magnetic field which causes the protons in the atom to react. Photons are emitted and the change in photons is measured by the magnetometer [**52**]. This kind of magnetometer is more often used for locating anomalous sources in the subsurface, though it also ends up recording the earth's magnetic field as well. To obtain the magnetic field of just the anomaly, the data from a cesium vapor magnetometer can be subtracted by the data from the proton precession magnetometer.

4. Electromagnetics

4.1. Introduction. Electromagnetics (EM) is a useful geophysical method that manipulates the natural electromagnetic fields of the near subsurface. Using time-varying sources of current, secondary magnetic fields are induced in the subsurface, generating secondary currents that are measured by the different EM devices. These devices can either reside in the time domain or frequency domain, depending on whether the source is active or passive. A time domain EM survey observes the decay of the induced magnetic and electric fields, while a frequency domain observes the amplitudes and phases of the induced magnetic field. Frequency and time domain surveys differ in the way they measure the secondary magnetic fields in the subsurface [**53**].

The most commonly used frequency domain devices include the EM31 and EM34, which are considered active sources for the induction of the magnetic fields. For the survey sites, the EM31 and EM34 proved to be useful in the San Juan National Forest reconnaissance site. In contrast to the frequency domain method, the transient (TEM) time domain electromagnetic (TEM) method, temporarily alters the magnetic field in the subsurface and measures its diffusion at depth. This method is used to correctly identify electrically conductive subsurface anomalies. The method can also provide apparent resistivities for layered earth models at a greater depths than other electromagnetic methods.

4.2. Background. Electromagnetics is founded upon Faraday's law and electromagnetic induction, where an electric current generates a magnetic field, known as electromagnetic induction (see Equation (16)) [**54**]. Electromagnetic induction is a physical phenomenon that occurs when a time-varying magnetic field crosses a conductive anomaly in the subsurface (Figure 4) [**53**]. When this occurs, an electromotive force (EMF), or voltage, is produced within the conductive body, and can be mathematically calculated using Faraday's law (Equation (17)) [**53**]. Eddy currents are created around these anomalies and produce a secondary magnetic field, which then induces a secondary current. This current is measured on the surface via EMF. The EMF measurement can be calculated into an apparent conductivity reading, by dividing the measured electric potential (V) by the resistance of the receiver loop (see Equation (18)). This is used within the EM devices to convert the measured voltages into current for data processing. As the magnetic field diffuses at depth over time a layered resistivity model can be created (see Equation (19)) [**54**].

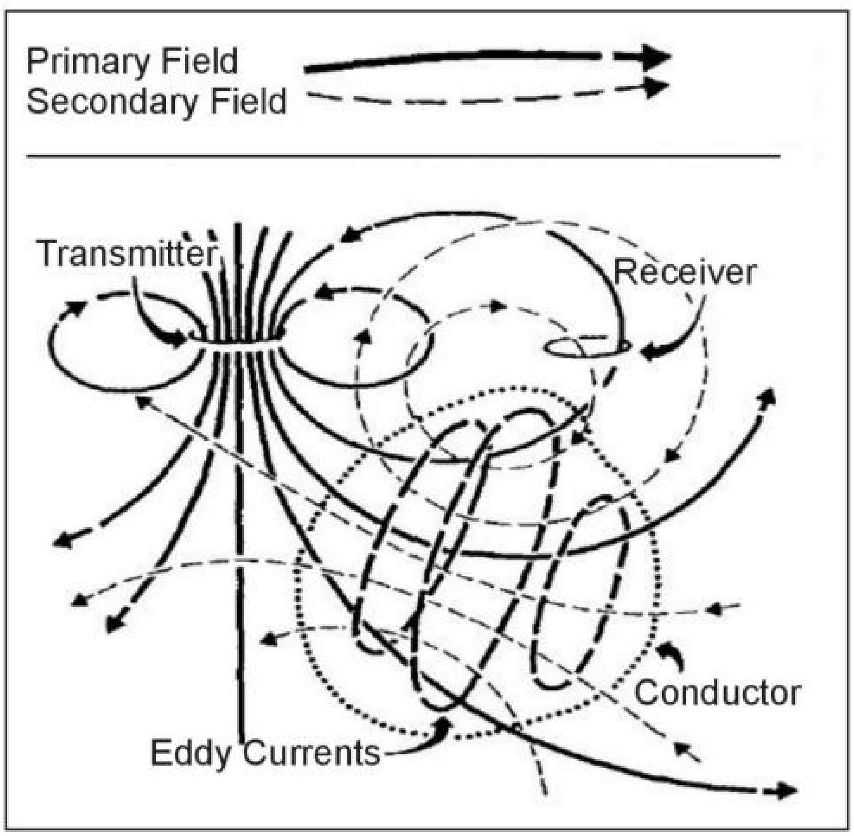

Figure 4. Physical depiction of the induced current reaction with the magnetic and electric field.

$$\nabla \times \mathbf{E} = -\frac{\partial \mathbf{B}}{\partial t} \tag{16}$$

Equation (16) mathematically represents the Maxwell-Faraday Law of Induction that states the magnetic field curls around an electric field.

$$\begin{gathered} EMF_c = M_{TC}\frac{dI_t}{dt} \\ EMF_R = M_{RT}\frac{dI_t}{dt} + M_{RC}\frac{dI_C}{dt} \end{gathered} \tag{17}$$

Equation (17) mathematically represents Faraday's Law of Induction for the target conductor and receiver end of the loop. EMF_c and EMF_R are the electromotive forces (or voltages) induced in the conductive body (C) and the receiver (R). M is the mutual inductance measured between the conductive body and transmitter (M_{RT}),between the receiver and transmitter (M_{RT}), and between the receiver and the transmitter (M_{RC}). $\frac{dI_t}{dt}$ represents the time-derivative of the changing current in the transmitter loop (I_t) and in the conductive body (I_c.

$$Ohm's\ Law$$

$$I = V/R \tag{18}$$

$$\sigma = \frac{\mathbf{J}}{\mathbf{E}} \tag{19}$$

Equation (19) shows the conductivity found by dividing the current density vector ($\mathbf{J}$) by the electric field vector ($\mathbf{E}$).

4.3. Theory. Electromagnetic induction is instrumented using EM31 and EM34 through the geometric pairing of transmitter and receiver loops. The transmitter emits a time-varying current at a specific frequency that will travel both above and below the ground surface. As a result of the injected current, the transmitter also produces a time-varying magnetic field at the same frequency and phase, crossing conductive bodies and producing an electromotive force. This creates a secondary current which produces a secondary magnetic field at a different frequency and phase than the primary field. This change is detected by the receiver and described further by Faraday's law (16) [**53**].

Once the secondary magnetic field is measured, the EM31 and EM34 convert the data into conductivity readings measured in milliSiemens per meter. This conversion allows the subsurface to be mapped, displaying the conductivity distribution across the survey area. The desired physical property when conducting EM surveys is resistivity, or inverse of conductivity. This relationship allows for the identification of different geologic structures in terms of geometry, size, and electrical properties [**53**].

Transient electromagnetics, (also known as time-domain electromagnetics/TEM) rely on nature's tendency to balance perturbations in naturally occurring magnetic and electric fields. A magnetic field perturbation at the surface will diffuse down and outward weakening into the subsurface until it is immeasurable (Figure 5) [**54**]. The magnetic perturbation creates eddy currents in the subsurface that create secondary magnetic fields (Figure 4). This process continues as tertiary magnetic fields create nearby eddy currents which create magnetic fields. This process repeats, and induced current loops gradually increase in size and decrease current flow as time progresses. The rate at which this diffusion occurs depends on the conductivity of the host rock. In electrically conductive media the perturbation will diffuse slower than it would in electrically conductive media since the potential of ohmic loss in conductive rock is greater than in resistive rock [**55**].

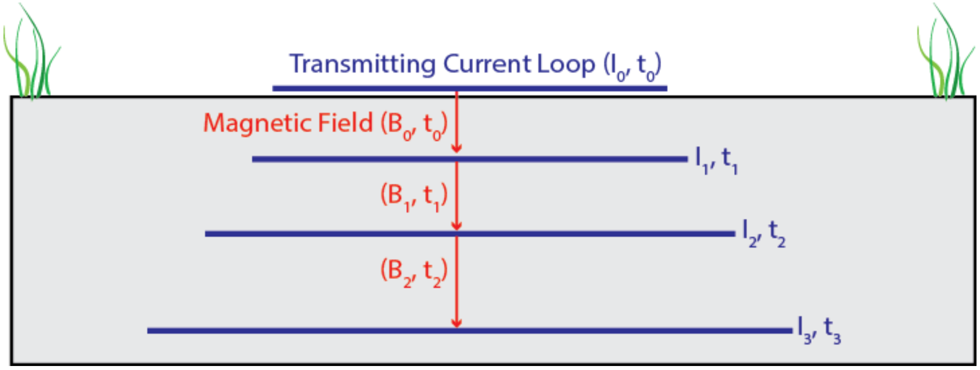

Figure 5. The transmitted current transmits current loops in the subsurface via the coupled magnetic field.

4.4. Practical Implementation. While the basic theories are consistent for both the EM31 and EM34, the devices themselves are constructed differently to enhance varying characteristics. The EM31 is a frequency domain instrument shaped as a long tube. The transmitter is located at the front end of the device, while the receiver is located at the end. A strap allows the user to balance the EM31 in the center where the main control console is placed. Based off the orientation of the device, either parallel or perpendicular to the ground, different in-phase frequencies and conductivities are read. The device can also be set up to take discreet (taken at each point) or continuous measurements. Discrete measurements are commonly used when the terrain is difficult and the user is unable to maintain a constant velocity, which is essential to take a continuous measurement. A limitation of the EM31 is its fixed distance between the coils which restrict the depth of investigation of the survey. For deeper surveys, the EM34 is used since the distance between coils can be adjusted [**53**].

The EM34 is designed to have two large coils (a transmitter and a receiver) connected by a 10, 20, or 40 meter cable. With this design, the depth of investigation can be determined based on the survey parameters. The receiver box, connected to the receiver coil, produces conductivity readings at each specific point; therefore, continuous measurements cannot be taken. Similar to EM31, the coils can be oriented in any direction, but to make data processing easier the ideal orientations are either the horizontal coplanar (vertical dipole) or vertical coplanar (horizontal dipole) direction in order to capture different in-phase frequencies and apparent conductivity readings (mS/m) [**53**].

In TEM surveys, a current loop is generated at the surface with a known current, which generates a magnetic field of a known strength (Figure 6). The current in the loop is then abruptly interrupted, causing the current to go to zero over a specific amount of time. This time known as the ramp time, and is calculated based off the amperage and area (Figure 6). When the current is shut off, the change in the magnetic field from the source induces a secondary current loops within the earth directly below the loop at the surface. A current from the secondary loops is induced in a receiver coil located on the surface. This current is measured via electric potential and converted into Equation (17). These measurements are used to generate a one dimensional apparent resistivity profile of the subsurface beneath the survey area.

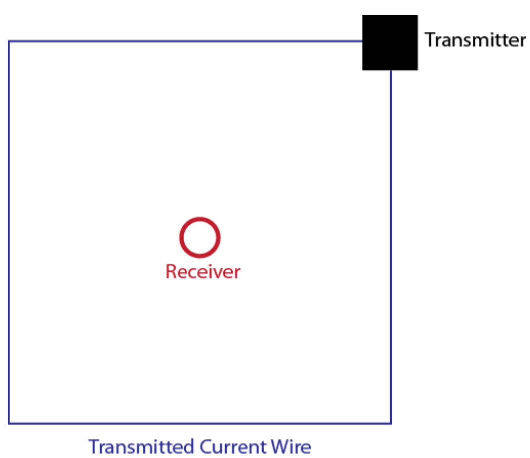

Figure 6. A plan view of a TEM survey.

5. Magnetotellurics

5.1. Introduction. Magnetotellurics (MT) is a passive method which uses the ratio of naturally occurring electric and magnetic fields to investigate the apparent resistivity of the subsurface. This method was initially applied to the 2015 field camp with the intention of identifying anomalous conductive areas associated with fluid reservoirs and transport flow. The lithology of a geothermal system commonly consists of a resistive host rock overlain by a more conductive zone of clay [**56**]. 1D pseudo depth profiles are plotted for two survey locations where the depth of investigation (DOI) is determined by plane wave frequency during the time of acquisition. The DOI is also related to the thickness and depth of resistive layers, providing for a non-unique interpretation of the processed data. The results of MT surveys can further be combined with methods sensitive to structure to help with the interpretation process.

5.2. Background and Theory. The sources of electromagnetic (EM) plane waves recorded in MT surveys are distant interactions between the Earth's magnetosphere and solar winds [**28**]. Upon interacting with the ground, EM waves generate telluric currents in the subsurface. The strength of the telluric current is related to the frequency of the plane wave where lower frequency waves correspond to larger amplitude and strength. The relationship of the telluric currents, electric fields, and magnetic fields are explained by Faraday's Law:

$$\vec{\nabla} \times \mathbf{E} = -\frac{\partial \mathbf{B}}{\partial t} \tag{20}$$

Where $\mathbf{B}$ and $\mathbf{E}$ represent the electric and magnetic fields respectively. In processing, Faraday's law in the frequency domain is utilized to plot the telluric response as a function of frequency.

$$\vec{\nabla} \times \mathbf{E} = -i\omega \mathbf{B} \tag{21}$$

Assuming a harmonic wave, and as the vertical location of the surface, this law implies that the ratio of $\mathbf{E}_x$ and $\mathbf{B}_y$ (or $\mathbf{E}_y$ and $\mathbf{B}_x$) is equivalent to the impedance. MT surveys record at varying frequencies, so that the electrical potential and orthogonal magnetic responses at the surface can be used to create impedance matrices. The associated apparent resistivity and phase can be calculated using these matrices. Furthermore, the apparent resistivity plotted against frequency, provides a pseudo depth plot of the subsurface.

The skin depth, or depth of investigation, of an MT survey is related to apparent resistivity and frequency of the plane wave:

$$\delta(\omega) = 503\sqrt{\frac{\rho}{\omega}} \tag{22}$$

The geologic formations in Archuleta County consist largely of shale, sandstone, and Precambrian crystalline rock. The apparent resistivity values therefore range between 30-100 ohm-meters in the sedimentary layers and 10,000 Ωm in the basement rock [**57**]. Assuming an average resistivity of 70 Ωm for the surface shale and sandstone layers, the depth of the investigation ranges between 200 meters for a maximum frequency of 512 Hz and 1500 meters for a minimum 8 Hz frequency. If a greater amount of time was dedicated to the survey, plane wave frequencies as low as 0.5 Hz could be measured to image depths of 6000 meters at this resistivity.

The local geology provides insight to the expected results of an apparent resistivity survey southwest of Chromo, CO. Sites one through three were set up above the shallow dipping Mancos shale which is underlain by the Dakota sandstone and Morrison formation. From these surveys, the detection of a conductive layer atop a resistive half space is expected. Sites four through six should show a similar response with a setup atop the shallow dipping Lewis shale that is underlain by the Mesa Verde Sandstone.

5.2.1. *Maxwell's Equations.* Maxwell's Equations are used to describe electromagnetic fields in a non-accelerated reference frame [**58**]. MT follows this assumption and therefore the following equations are obeyed in data acquisition and processing:

$$Faraday's\ Law:$$

$$\nabla X \mathbf{E} = -\frac{\partial \mathbf{B}}{\partial t} \tag{23}$$

$$Ampere's\ Law:$$

$$\nabla X\mathbf{H} = \mathbf{J} + \frac{\partial \mathbf{D}}{\partial t} \tag{24}$$

$$Gauss's\ Law\ for\ Electricity:$$

$$\nabla \cdot \mathbf{D} = \rho \tag{25}$$

$$Gauss's\ Law\ for\ Magnetism:$$

$$\nabla \cdot \mathbf{B} = 0 \tag{26}$$

where $\mathbf{E}$ is the total electric field (V/m), $\mathbf{B}$ is the total magnetic field (C/m), $\mathbf{D}$ is the free electric field (C/m^2), $\mathbf{H}$ is the free magnetic field (A/m), ρ is the electric charge density (C/m^3) and $\mathbf{J}$ is the current density (A/m^2). The constitutive relationships between the intrinsic properties and electromagnetic fields described in Maxwell's equations are also applicable to the MT method:

$$Ohm's\ Law:$$

$$\mathbf{J} = \sigma\mathbf{E} \tag{27}$$

$$\mathbf{D} = \varepsilon\mathbf{E} \tag{28}$$

$$\mathbf{B} = \mu\mathbf{H} \tag{29}$$

where is conductivity (mS/m), is the dielectric permittivity (F/m), and is the magnetic permeability (H/m).

5.3. Physical Assumptions of MT Method.

(1) All subsurface materials can be characterized as isotropic media, and all fields are considered conservative at a distance from the source.
(2) The electromagnetic fields measured at a site are generated by faraway, large scale effects in the magnetosphere and ionosphere. Consequently, at areas other than the poles and equator, these sources can be described as uniform, electromagnetic plane-waves that propagate vertically downwards at the surface of the earth [**28**].
(3) The dielectric permittivity of the subsurface ranges between that of air ($=$ 8.85 x 10^{-12}) and that of water ($=$ 7.08 x 10^{-10}) [**58**]. The value of also depends on the frequency of the electric and magnetic fields. Additionally, the magnetic permeability is equivalent to that of a vacuum ($=$ 4 x 10^{-7}).
(4) The survey parameters obey Maxwell's equations (23) - (26) of electromagnetics and Ohm's law (27).
(5) Recorded measurements are considered as volumetric averages of the conductivity of measured formations in the Earth. This is because the propagation of electromagnetic energy in the Earth can be described as a diffusive process [**58**].
(6) The electric and magnetic fields induced by the telluric current can be expressed in the form of harmonic waves:

$$\mathbf{E} = E_0 e^{i(\omega t + \mathbf{kr})} \tag{30}$$

$$\mathbf{B} = B_0 e^{i(\omega t + \mathbf{kr})} \tag{31}$$

where ω represents the angular frequency (rad/s), t is time (s), $\mathbf{k}$ is the wave vector (m^{-1}), and $\mathbf{r}$ is the position vector (m). Wave propagation is determined by the wave and position vectors while the oscillation depends on the angular frequency and time.

5.4. Mathematical Theory. According to Faraday's Law, the impedance tensor can be determined by the orthogonal components of measured electric and magnetic fields:

$$\begin{bmatrix} E_x \\ E_y \end{bmatrix} = \begin{bmatrix} Z_{xx} & Z_{xy} \\ Z_{yx} & Z_{yy} \end{bmatrix} \times \begin{bmatrix} \frac{B_x}{\mu_0} \\ \frac{B_y}{\mu_0} \end{bmatrix} \tag{32}$$

and correspondingly:

$$Z(\omega) = \frac{\bar{E}_x(0)}{\bar{H}_x(0)} = \frac{i\omega\mu}{\sqrt{i\omega\mu\sigma}} = \sqrt{\frac{i\omega\mu}{\sigma}} \tag{33}$$

Determining the impedance of a given layer relies on all of the geologic boundaries within the depth of investigation. As a consequence, the physical property measured on the surface is described as the apparent resistivity.

$$\rho_a(\omega) = \frac{1}{\omega\mu_0} \mid Z(\omega) \mid^2 \tag{34}$$

$$\rho_{\mathbf{a}} = \begin{bmatrix} \rho_{xx} & \rho_{xy} \\ \rho_{yx} & \rho_{yy} \end{bmatrix} \tag{35}$$

The apparent resistivity tensor is directly related to the real component of impedance tensor. In a 1D structure, the ρ_{xy} and ρ_{yx} show equivalent values at all frequencies. In the event of a 2D structure, the real component of the impedance is affected such that there is a static shift in the apparent resistivity curves at the frequencies corresponding to the structure.
The real and imaginary components of the complex impedance value can be distinguished as:

$$Z(\omega) = \sqrt{\frac{\omega\mu}{2\sigma}} + i\sqrt{\frac{\omega\mu}{2\sigma}} \tag{36}$$

and the phase can further be defined as the angle between the real and imaginary components in the complex plane:

$$\phi(\omega) = tan^{-1}\left[\frac{ImZ(\omega)}{ReZ(\omega)}\right] \tag{37}$$

In a uniform halfspace, the phase curve shows a constant value of 45 degrees at all frequencies. In the case of a 1D layered earth, the phase value increases as a result of a conductive layer below a resistive layer, and decreases as a result of the opposite scenario. The phase curve is significant such that it is unaffected by static shift as a result of 2D structures.

5.5. Data Processing.

5.5.1. *Mapros.*

Column#	**Content**
1	MT Site
2	Band
3	Frequency
4	Zxx (real)
5	Zxx (imaginary)
6	Zxx (variance)
7	Zxy (real)
8	Zxy (imaginary)
9	Zxy (variance)
10	Zyx (real)
11	Zyx (imaginary)
12	Zyx (variance)
13	Zyy (real)
14	Zyy (imaginary)
15	Zyy (variance)
16	Tx (real)
17	Tx (imaginary)
18	Ty (real)
19	Ty (imaginary)
20	ρ_{xy}
21	ϕ_{xy}
22	ρ_{xy} (variance)
23	ϕ_{xy} (variance
20	ρ_{yx}
21	ϕ_{yx}
22	ρ_{yx} (variance)
23	ϕ_{yx} (variance

Table 1. Mapros exported data column descriptions.

5.5.2. *Excel.*

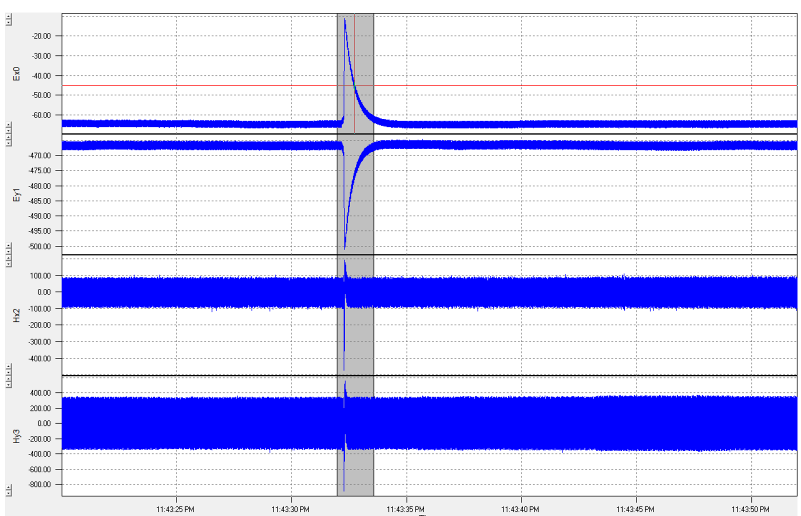

Figure 7. The raw data pulled from the ADU is plotted in Mapros. The four channels are representative of $\mathbf{E}_x$, of $\mathbf{E}_y$, of $\mathbf{H}_x$, and of $\mathbf{H}_y$. The amplitudes are displayed in units of volts per meter and Amperes per meter respectively. The gray mark is an example of noise removal in preprocessing.

A standard averaging algorithm is applied to develop the average apparent resistivity and phase curves. The phase curves are shown in degrees of angle on a linear plot. As a result, large jumps in the plots are observed when measurements approach values around +/- 180 degrees that are corrected for in the averaging process.

Variance values for the apparent resistivity and phase are averaged as well and converted to standard deviation using the following equation:

$$\text{std. dev.} = \sqrt{var} \tag{38}$$

A table was created to be read by the Ipi2win software including: the square root of period, apparent resistivity, apparent resistivity accuracy, phase, and phase accuracy. The square root of the period is inversely related to the frequency through the following equation:

$$\sqrt{P} = \frac{1}{f} \tag{39}$$

where P is the period and f is the frequency. The apparent resistivity and phase accuracy are defined using equations made from the developers of the Ipi2win software as follows:

$$\rho_a = \frac{\rho_{max} - \rho_{min}}{\rho_{max} * \rho_{min}} \tag{40}$$

where ρ_{max} is the average apparent resistivity value plus 2 times the standard deviation, ρ_{min} is the average apparent resistivity value minus 2 times the standard deviation, and ρ_a is the apparent resistivity accuracy (values should not exceed 1). The reasoning behind these max and min values is to encompass at least 95 percent or more of the data, assuming a gaussian distribution of the data.
The phase accuracy values are calculated using:

$$\phi_a = \phi_{max} - \phi_{min} \tag{41}$$

where ϕ_a is the phase accuracy, ϕ_{max} is the average phase plus 2 times the standard deviation, and ϕ_m is the average phase minus 2 times the standard deviation.
The values generated from these equations act as error bars for the data when displayed in the Ipi2win software.

5.6. Practical Implementation.

- Locate a large flat area very far away from all sources of electromagnetic interference for the base station.
- Set up the Analog-to-Digital Unit (ADU) in the middle, then place the magnetometers one meter away, facing north/south and east/west using a compass. The proper declination for the area must also be accounted for.
- Bury the magnetometers about 0.3 m down. Use a compass to ensure the correct orientation (north/south or east/west) and a bubble level to place the magnetometers flat beneath the surface.
- Connect the magnetometers and mobile GPS to the ADU. The battery should then be connected.
- Run a test to make sure the magnetometers are functioning and level.
- Set the system to run at the same time as the roaming system, preferably overnight.
- Secure any loose wires. Wires that move due to windy conditions will create noise in the data.
- Locate another large flat area (at least 100 x 100m) away from power lines and other interferences for the roaming station. Topographic features should also be avoided.
- Set up the second ADU in the middle and measure the electrodes out 50 meters to the north, south, east and west using a compass.
- Bury the electrodes 15 centimeters down in a vertical orientation at these locations.
- Place the magnetometers about 1 meter away from the center with one oriented north/south and another east/west.
- Bury the magnetometers about 0.3 m down. Use a compass to ensure the correct orientation (north/south or east/west) and a bubble level to place the magnetometers flat beneath the surface.
- Hook up the ADU to the magnetometers, the electrodes, and mobile GPS. The battery should then be connected.
- Hook up the laptop to the ADU and run a test to make sure the magnetometers are functioning and level.
- Set to record at the same time as the base station. This is preferably set during the night as this will also decrease the amount of noise in the data. The night is usually defined as 11:00 PM to 7:00 AM.
- After data collection, dig up all of the components, fill in the holes and move to the next location.
- Check on the battery at the base station in between each remote survey.
- When all remote surveys have been completed, collect all the gear from the roaming site and the base station. Fill any holes made to bury electrodes or magnetometers.

6. Direct Current Resistivity

6.1. Introduction. Direct Current Resistivity (DC) is an electrical method used in geophysics to image the conductivity contrasts in the subsurface. During a DC survey, a controlled current is injected into the ground. The interaction of the injected current and the ground is measured between two electrodes as a change in potential that can be used to obtain an apparent resistivity.

This method has proven to be useful for several applications including monitoring agricultural pollution, characterization of dikes, mapping of underground caves, mapping of groundwater accumulation for landslides, and characterizing seabeds [**32**].

6.2. Background and Theory. A DC resistivity survey examines the change in potential generated by running a current through an array of electrodes. There are two current electrodes, which carry induced electric current, and two potential electrodes, which the potential is measured across. Potential is measured as a voltage and is often referred to as the change in voltage. This potential can then be used to find the apparent resistivities at a pseudo depth underneath the array.

Current that passes through the electrodes is affected by the underlying surface structure and anomalies. The potential varies as the current interacts with the changing resistivities of the subsurface as is shown by the black lines in 9. As the array runs and is moved it measures the change in potential in relation to the spacing and placement of the DC array.

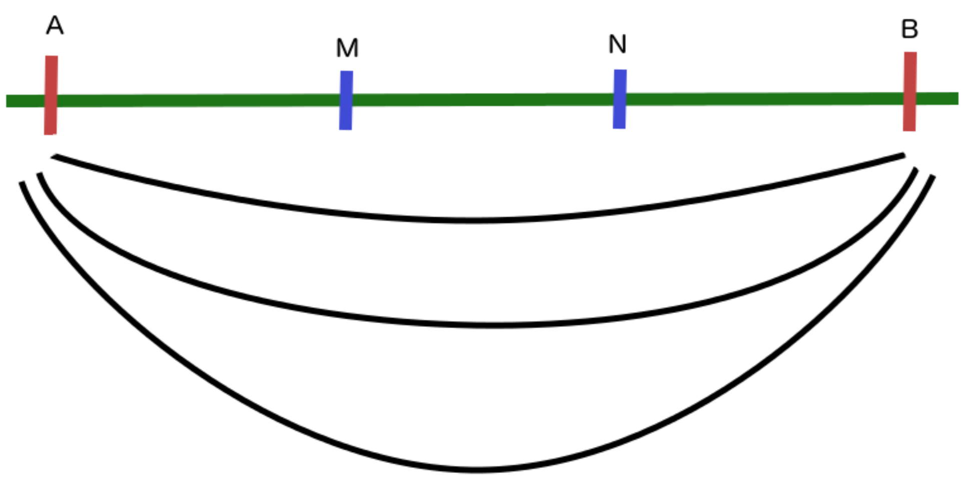

Figure 8. This is an example of current moving in the subsurface between the two current electrodes. The electrodes M and N are referred to as the potential electrodes which are used to measure the potential δV..

Resistivity depends on the fractures in a rock type, and fluid content. A list of example rock types and their resistivities is shown in Figure 8. Igneous rocks usually have high resistivities, while porous sedimentary rocks have low resistivities. Pure water has a high resistivity, but certain dissolved salts and other ions cause the resistivity to decrease. This can then be used to determine and map the resistivities of the structures in the subsurface. There are a wide range of resistivities, and as such a basic map of the subsurface can give an overview of what the possible layers lie underneath.

Approximate resistivity ranges for various rock<comma> minerals and water types in the base complex area (after Telford et al. (1976)).

Rock type	Resistivity (Ω m)
Clay and marl	1–67
Top soil	67–100
Clayey soil	100–133
Sandy soil	670–1330
Limestone	67–1000
Lignite	9–200
Sandstone	33–6700
Sand and gravel	100–180
Schist	10–1000
Granite	25–1500
Basalt	103–106
Quartzite	102–2 × 108
Surface water (in igneous rock)	30–500
Sea water	0.2
Saline water 3%	0.15
Saline water 20%	0.05
Groundwater (in igneous rock)	30–150
Weathered laterite	200–500
Fresh laterite	500–600
Weathered/fractured basement rock	100–500
Fresh basement rock	>1000

Figure 9. This is a table of approximate resistivity values for common rocks and minerals. It can be used to help interpret the inverted results by characterizing the different resistivities seen in the pseudo-section.

There are multiple survey geometries, called arrays, that can be used for a DC resistivity survey. Each one has its own advantages and can be used to focus on a certain area or depth.

The most common arrays are Wenner, Schlumberger, Pole-Pole, Dipole-Dipole, and Pole-Dipole. In each example, A and B electrodes are the current electrodes, and the M and N electrodes are the potential electrodes [**32**].

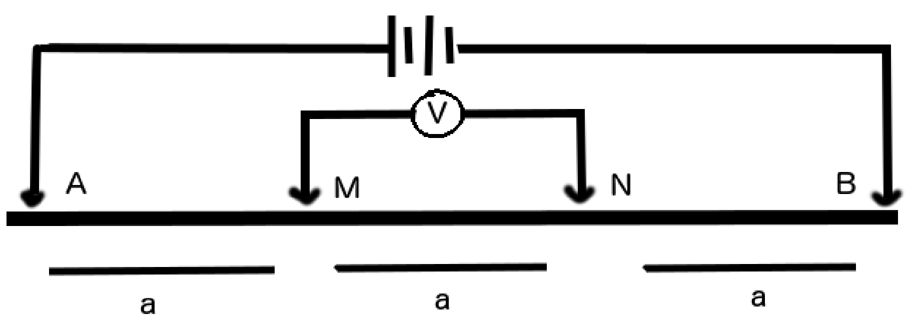

Figure 10. This image illustrates a Wenner array setup and spacing. The arrows indicates electrodes where A and B are the current electrodes, then M and N are the potential electrodes. The symbol ‘a’ is used to illustrate that each of the electrodes is equally spaced which is an important feature of the Wenner array.

A Wenner Array setup has four electrodes in a line, with equal spacing between all of them. The current electrodes surround the potential electrodes. This array is advantageous because it has a simple calculation for apparent resistivity; however, it is one of the most labor intensive. The primary benefits are a detailed view of near surface anomalies, and higher sensitivity to vertical changes in the subsurface (horizontal structures). The pseudo depth of a Wenner Array is approximately half of the spacing (a) and so the overall length of the array determines the depth of investigation [**59**]. This is the geometry that was used for all the DC surveys conducted at the 2015 Field Camp.

6.3. Mathematical Theory. DC Resistivity surveys and studies utilize Ohm's Law in vector form to calculate the resistance using the voltage and current.

$$\mathbf{J} = \sigma \mathbf{E} \tag{42}$$

where $\mathbf{J}$ is the current density vector (A/m^2), $\mathbf{E}$ is the electric field vector (V/m), and σ is the conductivity (S). This can be rearranged using the inverse relationship between the conductivity and the resistivity.

$$\mathbf{J} = -\frac{1}{\rho}\Delta\mathbf{V} \tag{43}$$

In this equation ρ is the resistivity measured in (Ωm), and V is the electric potential (Volts). This equation describes the quantity of current flowing through the area of a 2D surface that is oriented perpendicular to the direction of the current flow $\mathbf{J}$.

Assuming a simple model using one source electrode and one sink electrode and assuming the subsurface is uniform and extends infinitely we can then treat the current electrodes as a point source or sink. The total current will move from one electrode to another and in doing so cross the surface of a half sphere with an area is given by

$$V_{halfsphere} = \frac{1}{2}\pi r^2 \tag{44}$$

where r is the radius. This then gives us an equation for the current density of one electrode.

$$\mathbf{J} = \frac{\mathbf{I}}{\frac{1}{2}4\pi r^2} = -\frac{1}{\rho}\frac{dV}{dr} \tag{45}$$

If we assume that the resistivity, ρ, is constant we can integrate this equation in order to obtain

$$V(r) = \frac{\rho\mathbf{I}}{2\pi a} \tag{46}$$

where a is the distance from the electrode and I is the total current that flows between one electrode and another. Next we assume that the electric potential V is zero, infinitely far from the current source and a the electrode spacing is equivalent to the distances between the electrodes A and M, M and B, A and N, and N and B.

$$V_m = \frac{\rho\mathbf{I}}{2\pi}\left(\frac{1}{AM} - \frac{1}{MB}\right) V_n = \frac{\rho\mathbf{I}}{2\pi}\left(\frac{1}{AN} - \frac{1}{NB}\right) \tag{47}$$

$$V_{mn} = \frac{\rho\mathbf{I}}{2\pi}\left(\frac{1}{AM} - \frac{1}{MB} - \frac{1}{AN} - \frac{1}{NB}\right) \tag{48}$$

where

$$K = 2 * \pi\left(\frac{1}{AM} - \frac{1}{MB} - \frac{1}{AN} - \frac{1}{NB}\right) \tag{49}$$

In the DC Resistivity surveys conducted in Pagosa Springs, CO we utilized a Wenner Array for which the distance between electrodes is 'a' where: a = AM = MB = AN = NB. With this we can then simplify the equation for the apparent resistivity to obtain the equation used to determine the apparent resistivity of the Wenner Array.

$$P_w = \frac{V_{mn}}{\mathbf{I}}2\pi a \tag{50}$$

The geometric factor is a coefficient that accounts for the stratification of the subsurface, though it is important to note that materials closer to the surface have a greater impact on the measured resistance.
The depth that the Wenner Array can image is given approximately by the length of the electrodes divided by two [**32**].

$$\text{maximum depth} = \frac{AB}{2} \tag{51}$$

6.4. Practical Implementation. The ABEM Terrameter SAS 4000 was used to collect the DC Resistivity data. It was powered by a 12V battery and connected to steel electrodes through cable jumpers, CVES cables, and a switching/communication box.

6.4.1. *Equipment.*

- ABEM Terrameter SAS 4000
- External Battery Adapter
- RS 232 Cable
- Reels for Cables
- CVES Cables (Cables with Takeouts)
- Cable Jumpers (Connect Electrodes to Takeouts)
- Cable Joint
- Switching/Communication Box
- Communication Cables
- 1 -12 V Battery
- Steel Electrodes
- Hammer
- Tape Measure
- Oui Oui SP Chair

Figure 11. Here a group of Colorado School of Mines geophysics students observe the DC Resistivity equipment being setup. The ABEM Terrameter SAS 4000 and its switching box are the orange instrumentation and the yellow cables are the CVES cables that connect to the electrodes down the line.

7. Self Potential

7.1. Introduction. The self-potential (SP) method is a passive geophysical method used to measure naturally-occurring voltage variations within the subsurface. The SP method has a wide range of applications including mineral exploration, environmental remediation, and mapping groundwater flow. SP surveys are simple and relatively inexpensive because they use only two electrodes, a voltmeter, and a cable. The electrodes measure changes in voltage associated with currents caused by fluid flow, vegetation, mineral bodies, structural contacts, and thermal gradients.

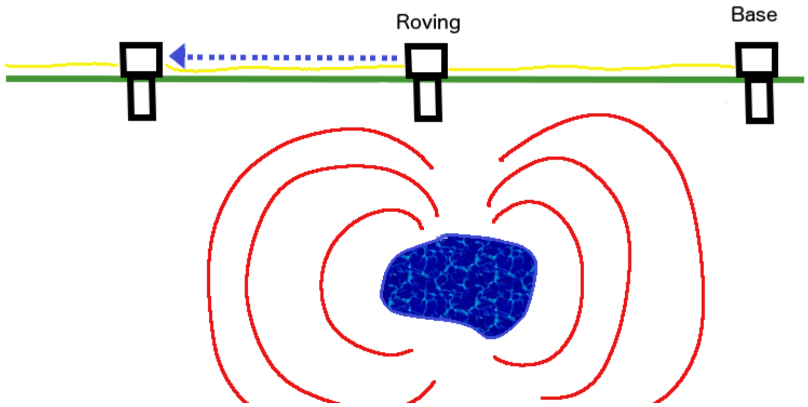

Figure 12. This figure shows a common setup for an SP survey with one base and one roving electrode. The roving electrode moves in equal intervals for each measurement while the base electrode remains static.

SP is useful in Chromo because it can be used to characterize groundwater flow and look for geothermal sources. Few methods indicate the presence of water, and even fewer indicate the direction of flow. Therefore, SP is an integral part in answering the question of whether the spring system in Pagosa connects to Chromo. Unfortunately, few SP surveys were conducted last year, so integrating the data sets from this year and last year might be difficult.

7.2. Background and Theory. Multiple sources generate a self-potential signal, however the bulk of SP signals come from two main sources: streaming potential and potential from oxidation-reduction reactions.

Streaming potential, also known as electrokinetic potential, is generated from fluid-flow through a porous medium. The charges in the moving pore fluid act as a current which generates an electric field and thus a voltage. The current behaves according to Ohm's Law.

$$\mathbf{J} = \sigma \mathbf{E} \tag{52}$$

The voltage is produced from its relationship with the electric field where ψ is the potential.

$$\mathbf{E} = -\nabla \psi \tag{53}$$

where ψ is the potential.

The charges in the pore fluid result from the electrical double layer on the boundary between the fluid and solid. The first layer of charge on the boundary results from chemical interaction of the materials. For example, in a sand grain, an Oxygen atom in the SiO_4 molecule faces toward the outside of the grain which creates a negatively charged surface. To stabilize the negative charge, positive counterions flow to the boundary [**60**]. These counterions compose the second layer, the Diffuse layer, of the double layer model. The first layer, the Stern layer, is made up of ions directly bonding to the mineral lattice of the grain [**60**]. The voltage across this double layer is called the zeta potential. The zeta potential is used to calculate the streaming potential (V_s) by the equation:

$$V_s = \frac{\varepsilon \rho \zeta}{4\pi\mu} P \tag{54}$$

where ε is the dielectric constant, ρ is the resistivity, ζ is the zeta potential, μ is the viscosity of the electrolyte and P is the pressure gradient [**33**].

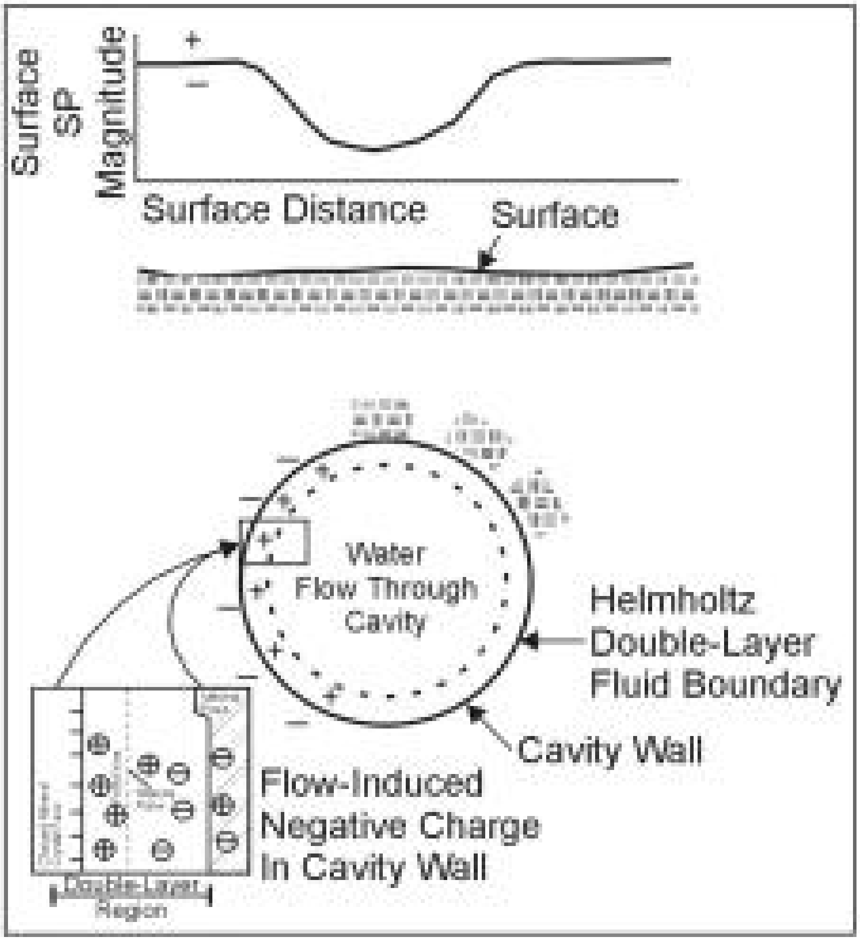

Figure 13. This figure shows the electric double layer and the voltages produced from the different layers. The center particle has a negative surface charge which is common in nature.

The second main source of SP signal occurs from redox reactions. Sato and Mooney (1960) explain this phenomenon with their popular geobattery model. In their model, an ore body sits with half its mass above the water table. Oxidation reactions take place above the water table where oxygen is more readily available. For example,

$$2Fe + O_2 \rightarrow 2FeO \tag{55}$$

or alternatively,

$$Fe \rightarrow Fe^{+2} + 2e^- \tag{56}$$

Reduction reactions take place below the water table.

$$Fe^{+2} + 2e^- \rightarrow Fe \tag{57}$$

Essentially, the ore body is acting as a galvanic cell (see Figure 14). Ions move through the ore body as they would in a galvanic cell and create a drop in voltage at the surface [**33**]. This model has been criticized and changed in the past 50 years but the general principle of redox reactions driving a current which acts as an SP source remains the same.

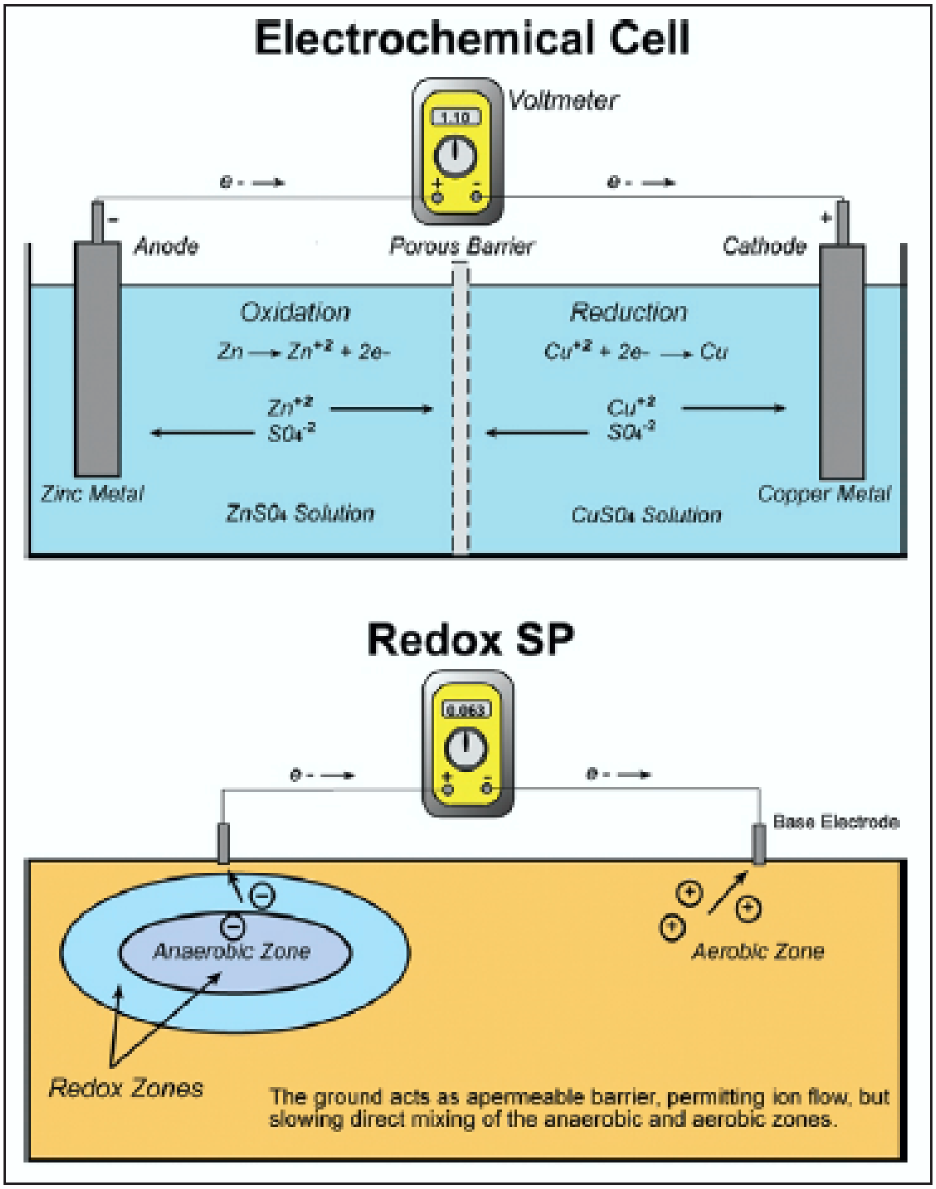

Figure 14. The top of this figure shows the classical galvanic cell with the anode and cathode. The bottom depicts an SP survey over a contaminant plume. Although they are shaped differently, the same chemical processes are taking place.

According to other studies, contaminant plumes with an anaerobic center also behave like ore bodies in that they generate a drop in voltage from redox reactions [**61**]. Although the usage of SP in the mining industry has decreased, the popularity of SP has increased in the environmental industry because of its ability to spot contaminant plumes.

Although less prevalent than streaming potential or redox potential, SP signals can also be generated in a geothermal environment through thermoelectric coupling. The thermal gradient creates a differential in the diffusion of ions in a fluid, known as the Soret effect, and generates a voltage gradient [**62**]. If the current density **J** reaches zero, the voltage gradient can be given by:

$$-\nabla V = S\nabla T \tag{58}$$

where S is the Seebeck coefficient, dependent on the material [**63**].

As shown in the figure below, the thermoelectric effect does not generate potentials as great as those due to streaming potential. However, when streaming potential is taken into account, SP is useful in characterizing geothermal systems and volcanoes.

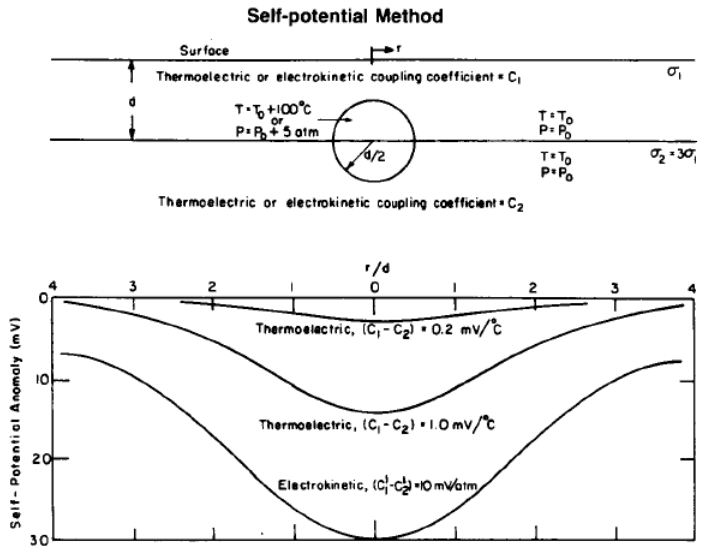

Figure 15. This figure shows the relative amplitudes of the SP signal produced from the thermoelectric effect and the electrokinetic effect.

Ion diffusion differentials also occur because of a difference in material. Charge will accumulate on the contact of a sandstone layer and shale layer since Na^+ ions can percolate into shale but Cl^- ions cannot [**33**]. This means an abrupt change in the subsurface geology can look like a potential anomaly. This demonstrates the need for prior knowledge of the geology of the survey area.

Another form of a membrane potential exists in the form of plant roots. Plant roots filter ions out of solution and can thus create a potential. Therefore, changes in vegetation can be observed in SP surveys [**33**].

From these sources of self-potential signals, we will be mostly concerned with signals due to streaming potential. Not only will these signals appear the strongest, but they will also teach us about the fluid flow in the area.

7.3. Instrumentation.

7.3.1. *Equipment.*

- 2 electrodes (Ag/AgCl)
  - 1 base electrode (does not move)
  - 1 roaming electrode (measures every 20m)
- Cable
- Voltmeter
- Shovel
- Hammer

One electrode serves as the static base and the second electrode takes measurements of the voltage differentials at regularly spaced intervals (20m).

7.3.2. *Procedure.*

(1) Touch the tips of the electrodes together at the beginning and the end of the survey to measure electrode drift using a voltmeter.
(2) Bury the base electrode.
(3) Take measurements with the roaming electrode every 20m in moist soil to reduce contact resistance. Switch the voltmeter switch to Off and back to Volts to reset the device and take the measurement.
(4) Take resistivity readings every 10 measurements.
(5) Enter measurements into a spreadsheet.

8. Induced Polarization

Conrad Schlumberger had the concept of induced polarization patented in 1939, having used the method to make field observations since 1913. Approached by the Soviet government, Conrad used the IP method to develop oil field logs in the USSR. A. S. Polyakov examined the ratio of the transient decay to the primary field and named this quantity chargeability. This method also used by the U.S. Navy for the detection of unexploded ordnance in 1942. Members working on the project eventually spread the method throughout various contexts of use. Physicist David Bleil joined this undertaking in 1943, afterwards exploring the uses for the IP method in mineral exploration. Bleil named the method induced polarization in 1953 in a geophysical publication. At that time, there were no geophysical methods that were sensitive to porphyry copper deposits. It was for this reason that IP gained significant attention when Newmont utilized the method to successfully delineating a massive porphyry copper deposit in Peru. In the last fifty years, industry and academia have made major technical advancements in the geophysical method of induced polarization. Although this method and the theorized physics governing it have been developing for over a century, having proven valuable in various contexts, it remains a frontier within the realm of electrical geophysical methods.

8.1. Background and Theory. Induced polarization is a geophysical method which uses electricity to measure the apparent chargeability and variation of the electric permittivity in the subsurface. This method requires the injection of a current into the subsurface using cables, batteries, electrodes, and an acquisition system. The current injected into the subsurface creates a polar accumulation of charge, or dielectric polarization. Dielectric polarization is the same physical behavior observed in capacitors, charging when provided a current and discharging when current is absent. Polarization in subsurface material is caused by the interaction of an injected electric field with an electrical double layer surrounding a charged material, such as a silicate rock or mineral and the fluids surrounding them. It has been previously theorized that several types of polarization dominated the signal determining the ability of a material to charge and discharge when supplied with an electrical current. Recent theories postulate that the polarization of fluids within material pore space dominates the signal determining chargeability. The source of fluid polarization in pore space is the polarization of the Stern and diffuse layer, previously referenced as electrical double layer. A material with a net surface charge will attract layers or shells of opposite charge. In the presence of an induced electric field, these layers undergo deformation, creating a polarization of charge. The dielectric polarization at the interface of this material propagates dielectric polarization into pore-space fluids. The Stern and diffuse layer and their reaction to an injected electric field can be seen in the figure below.

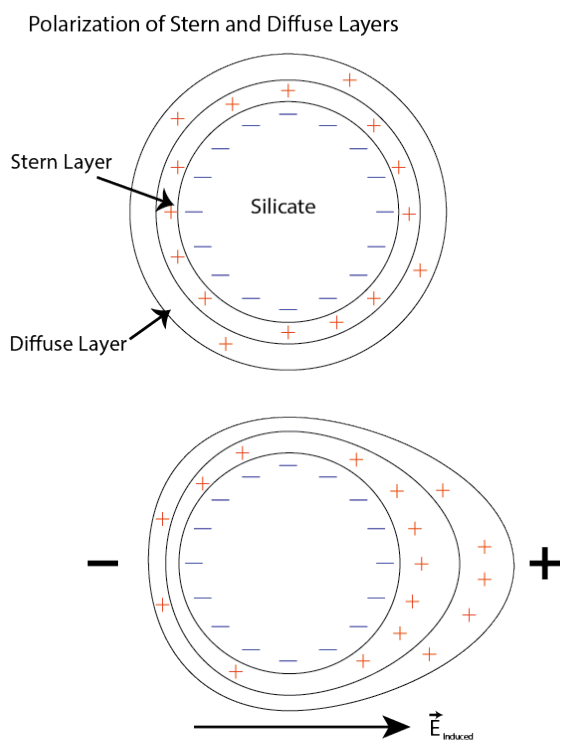

Figure 16. Polarizatin of Stern and Diffuse Layers

Chargeability is a material property measured in units of time. This quantity describes the ratio of the decaying voltage integrated over a window of time and the steady state voltage measured before interrupting the injected current. According to “Field Geophysics” written by John Milsom and Asger Eriksen, the formal definition for chargeability is described on page 141 as “the polarisation voltage developed across a unit cube energised by a unit current” [**28**]. This property often contrasts among rock and mineral types, making the method largely popular in the context of mineral exploration. As chargeability is largely determined by the polarization of the electrical double layer and the corresponding polarization of surrounding fluids, there exists a positive correlation between the volume/saturation of pore spaces and the measured chargeability. This correlation makes IP a viable technique in the examination of hydrogeological characteristics. Chargeability data in conjunction with resistivity data can be inverted to create images of the subsurface. These two properties can aid in the delineation of target media such as; current hydrologic storage in pore spaces (water storage), permeability, and rock/mineral type or boundaries.

8.2. Physics.

8.2.1. *Time Domain.* The induced polarization survey taken near Stinking Spring was designed to acquire time-domain data. Through analysis of the voltage decay curve, data gathered in the time-domain can be utilized to estimate the chargeability of subsurface cells. An electrical current is injected through the subsurface for a specified amount of time, in this case using a Wenner-Alpha array. After this time has elapsed a voltage measurement is acquired and the injected current is halted. After the interruption of current, a specified amount of time is used waiting for the effects of electromagnetic coupling to diminish. In response to ceased current, the voltage begins to decay and is measured or a specified time window, at interval. Because the full decay waveform is not measured, the values attained are called partial chargeability. Values of partial chargeability can then be inverted with corresponding resistivity measurements. The results of this inversion are then normalized through the division of the time elapsed in the measurement intervals. Beyond this, multiplying the inverted values of conductivity with inverted values of chargeability, cell by cell, can delineate materials with no inherent chargeability contrast.

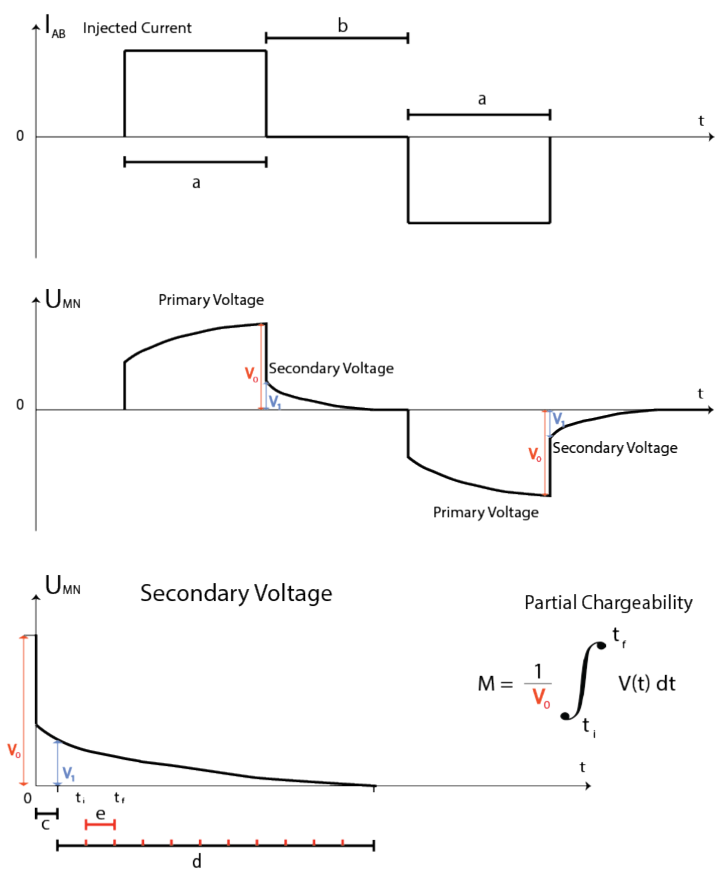

Figure 17. a - Primary acquisition time, b - Time on/off, c - Initial delay, d - Duration of measurements,e - Measurement interval

$$M = \frac{1}{V_0} \int_{t_i}^{t_f} V(t)dt \tag{59}$$

Where M represents the partial chargeability measured in milliseconds(ms), V_0 is the voltage measure directly before interruption of current measured in volts(V) and $V(t)$ is the decaying voltage as a function of time (V). The integration of $V(t)$ is carried out from the beginning to the end of the measurement interval.

$$M_N = \frac{\sigma}{V_0} \sum \frac{1}{\Delta t} \int_{t_i}^{t_f} V(t)dt \tag{60}$$

Where M_N is the normalized chargeability scaled with conductivity, measured in millisiemens per meter (mS/m). σ represents the conductivity in corresponding cell (mS/m), $\Delta_t = t_f - t_i$ is the time interval of measurement, measured in milliseconds (ms). V_0 is the voltage before directly before interruption of current, measured in millivolts (mV). $V(t)$ is the decaying voltage as a function of time (mV). This equation utilizes chargeability and conductivity estimates to discern materials that would otherwise have relatively small contrast in physical properties.

8.2.2. *Frequency Domain.* Frequency domain IP data was not acquired due to instrumentation constraints. As this type of IP survey was not conducted, only a brief overview of the physics governing this method will be provided. The collection of IP data in the frequency-domain can provide a robust range of calculated physical properties. By utilizing the phase lag data between injected harmonic current and the measured harmonic voltage response, complex electrical conductivity can be derived, which also yields information about complex electrical resistivity, complex permittivity and chargeability. Complex conductivity is composed of two components, in-phase conductivity and quadrature conductivity. In-phase conductivity corresponds to the real component of the complex conductivity and represents the current that was conducted through the media. Quadrature-phase corresponds with the imaginary component of the complex conductivity and represents the storage of injected current. Utilizing the physical properties implicitly measured by the lag in phase, interpretations of material composition and hydrogeological characteristics can be made.

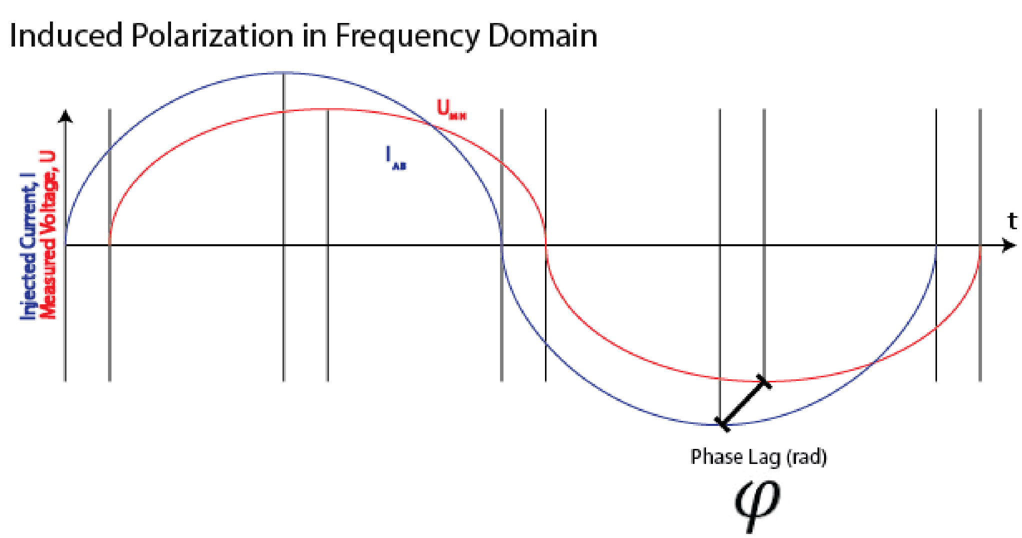

Figure 18. Induced Polarization in Frequency Domain

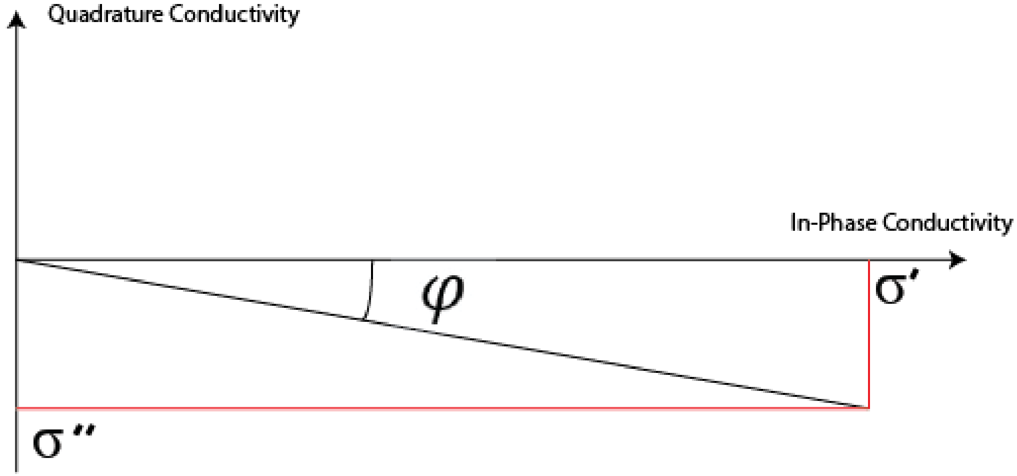

Figure 19. Phase Angle

$$\sigma = \frac{1}{\rho} = i\omega\varepsilon = |\sigma|e^{i\varphi} = \sigma' + i\sigma'' \tag{61}$$

$$\tan(\varphi) = \frac{\sigma''}{\sigma'} \tag{62}$$

Where $\sigma^\star$ represents complex conductivity, measured in millisiemens per meter (mS/m), which is comprised of components: σ', the in-phase conductivity (S/m) and σ", the quadrature-phase conductivity (S/m). ϕ is the phase lag, measured in milliradian (mrad). $\rho^\star$ represents complex resistivity (Ohm-m) and $\varepsilon^\star$ represents complex permittivity (F/m), both of which contain a real and imaginary component. ω is the angular frequency, measured in radian per second (rad/s).

8.3. Practical Implementation. The ABEM Terrameter SAS 4000 is the key instrument in the measurement of IP data. The ABEM connects to a switch box which then connects to reels of 32-channel wires with 20 meter take-out spacing. Electrodes are connected to each take-out and to the ground. The same set-up and equipment can be used for DC resistivity surveys. IP data requires DC resistivity data in order to be inverted for an image.

9. Deep Seismic

9.0.1. *Survey Design.* Deep seismic method provides incomparable resolution of the subsurface, and therefore is widely used especially by the oil and gas exploration industry. Each geological layer has specific physical properties, such as density and porosity, which make seismic waves travel at different velocities in different layers. By shooting seismic waves into the ground using VibroSeis trucks, the subsurface structures can be detected by the geophones planted at desired locations. Processing of the seismic data requires a vast knowledge of seismic wave behavior and instrumentation. Hence, various properties and principles of basic seismology are defined below.

9.1. Background and Theory.

9.1.1. *Theory Behind Survey Design.* Seismic survey design takes into account numerous factors such as topography, geology, desired target, and availability of time and resources. These variables guide decisions regarding geophone spacing, shot spacing, magnitude of the survey, and source parameters. Ideally, a seismic survey covers a large area with dense geophone and source spacing, while adhering to time and resource limitations. In designing a survey, bounds and spacing parameters must be determined so the survey will cover the target area with adequate spatial resolution. Receiver placement may be limited by accessibility due to rough terrain, bodies of water, or other topographic features. In addition, the source/receiver relationship should be considered. Source locations can be at any point along the receiver line, but receivers must have a distinguished spacing throughout the entire line. We must then determine where the location of the source will be, whether at the beginning or somewhere in the middle.

Assuming the source is a vibroseis truck, sweep parameters are determined to optimize data quality. Sweep parameters include the type of sweep (upsweep or downsweep, and linear or nonlinear), frequency range of the sweep, sweep time, and the stack number at each shot location. Upsweep and downsweep refer to whether the vibration increases or decreases in frequency during a sweep. Choosing linear or nonlinear determines how the sweep

moves between the start and end frequencies. The frequency range of the sweep affects the spatial resolution and depth of the investigation. High frequencies provide greater spatial resolution at shallow depths, but because high frequency waves attenuate quickly they will not give information at greater depths. Low frequency waves reach lower depths but result in lower resolution than high frequency wave. So when determining frequencies, we must consider the depth of the target and desired resolution. Sweep time determines how long it takes to move from the beginning to end frequency. A longer sweep gives more data and improves the signal/noise ratio, but shorter sweeps decrease the overall time required to complete the survey. Stack number is the number of sweeps run at each source location. Multiple stacks at one location improve the signal/noise ratio, but also increase the time required for the survey. Resource availability must be considered when determining sweep time and stack number because seemingly small time changes have a significant effect on the total time needed to complete the survey.

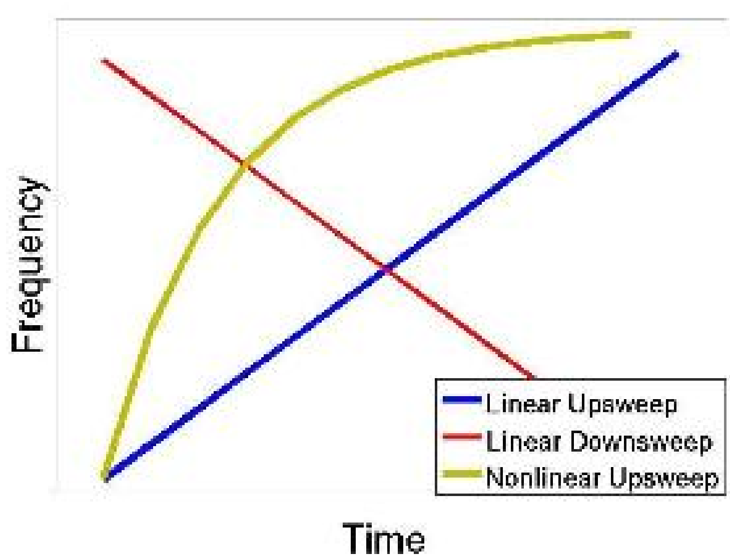

Figure 20. Types of sweeps

9.1.2. *Seismic Velocity.* The velocity at which any seismic wave propagates through the earth is dependent on factors such as the type of wave (P-wave or S-wave), the physical properties of the rock units in the medium, porosity, pore pressure, fluid content, and effective pressure. Generally, the velocity of a seismic wave will increase with increasing effective pressure. Seismic velocities can be described in function of the elastic parameters of the rock. For P-Waves:

$$\alpha = \sqrt{\frac{\lambda + 2\mu}{\rho}} \tag{63}$$

and for S-waves:

$$\beta = \sqrt{\frac{\mu}{\rho}} \tag{64}$$

where α is the velocity of P-wave (m/s), β is the velocity of a S-wave (m/s), λ is the first lam parameter (kg/ms^2), μ is the second lam parameter (or shear modulus) (kg/ms^2), and ρ is the mass density of the material (kg/m^3). The velocity of a P-wave is more sensitive to fluid content than the velocity of an S-wave. P-waves are always faster than S-waves. Below is a table describing the velocities of P- and S-waves through different types of rock formation:

Type of formation	P wave velocity (m/s)	S wave velocity (m/s)	Density (g/cm^3)	Density of constituent crystal (g/cm^3)
Scree, vegetal soil	300-700	100-300	1.7-2.4	-
Dry sands	400-1200	100-500	1.5-1.7	2.65 quartz
Wet sands	1500-2000	400-600	1.9-2.1	2.65 quartz
Saturated shales and clays	1100-2500	200-800	2.0-2.4	-
Marls	2000-3000	750-1500	2.1-2.6	-
Saturated shale and sand sections	1500-2200	500-750	2.1-2.4	-
Porous and saturated sandstones	2000-3500	800-1800	2.1-2.4	2.65 quartz
Limestones	3500-6000	2000-3300	2.4-2.7	2.71 calcite
Chalk	2300-2600	1100-1300	1.8-3.1	2.71 calcite
Salt	4500-5500	2500-3100	2.1-2.3	2.1 halite
Anhydrite	4000-5500	2200-3100	2.9-3.0	-
Dolomite	3500-6500	1900-3600	2.5-2.9	(Ca, Mg) CO_3 2.8-2.9
Granite	4500-6000	2500-3300	2.5-2.7	-
Basalt	5000-6000	2800-3400	2.7-3.1	-
Gneiss	4400-5200	2700-3200	2.5-2.7	-
Coal	2200-2700	1000-1400	1.3-1.8	-
Water	1450-1500	-	1.0	-
Ice	3400-3800	1700-1900	0.9	-
Oil	1200-1250	-	0.6-0.9	-

Figure 21. [64]

9.2. Instrumentation.

9.2.1. *Survey Connections.* In seismic surveys the primary device used to record wave propagations through the subsurface are geophones. Geophones operate by having a magnetic mass suspended on a spring wrapped in a coiled wire. As a wave travels through the ground, the magnetic mass moves relative to the shaking of the earth. This generates an electrical current in the coiled wire that is the recorded signal . The voltage is proportional to the velocity of the ground motion. Geophones are durable and are designed to install firmly without damage. For a geophone to operate as intended, it must be firmly planted in the ground as close to vertical as possible [**65**].

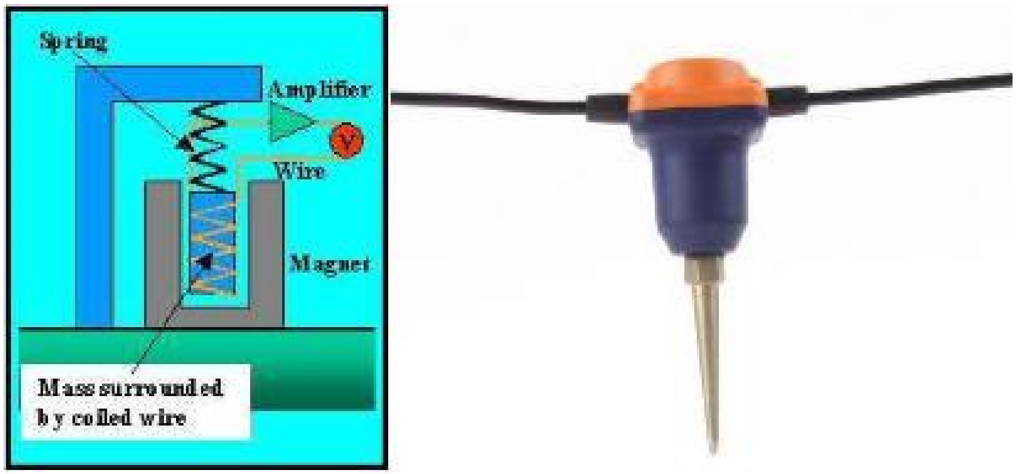

Figure 22. Internal System in a Geophone, Sercel SG-10 Geophone [**66**]

The field digitizing unit (FDU) is responsible for the connection between the doghouse and the geophones that were laid out along the main line. This unit is responsible for converting the analog signal taken from the geophones to a digital signal which can be sent to the doghouse. Each flag along the line had one FDU with a string of geophones attach to the center connector. Another important part of the cable connection is the line acquisition unit land (LAUL), which allows the complete seismic line to have a constant supply of power across the entire line. Lastly, each seismic survey needs a line acquisition unit cross (LAUX), which is the connection between the main line FDU's and the doghouse as shown in Figure 24.

Figure 23. Sercel 408-FDU [**66**]

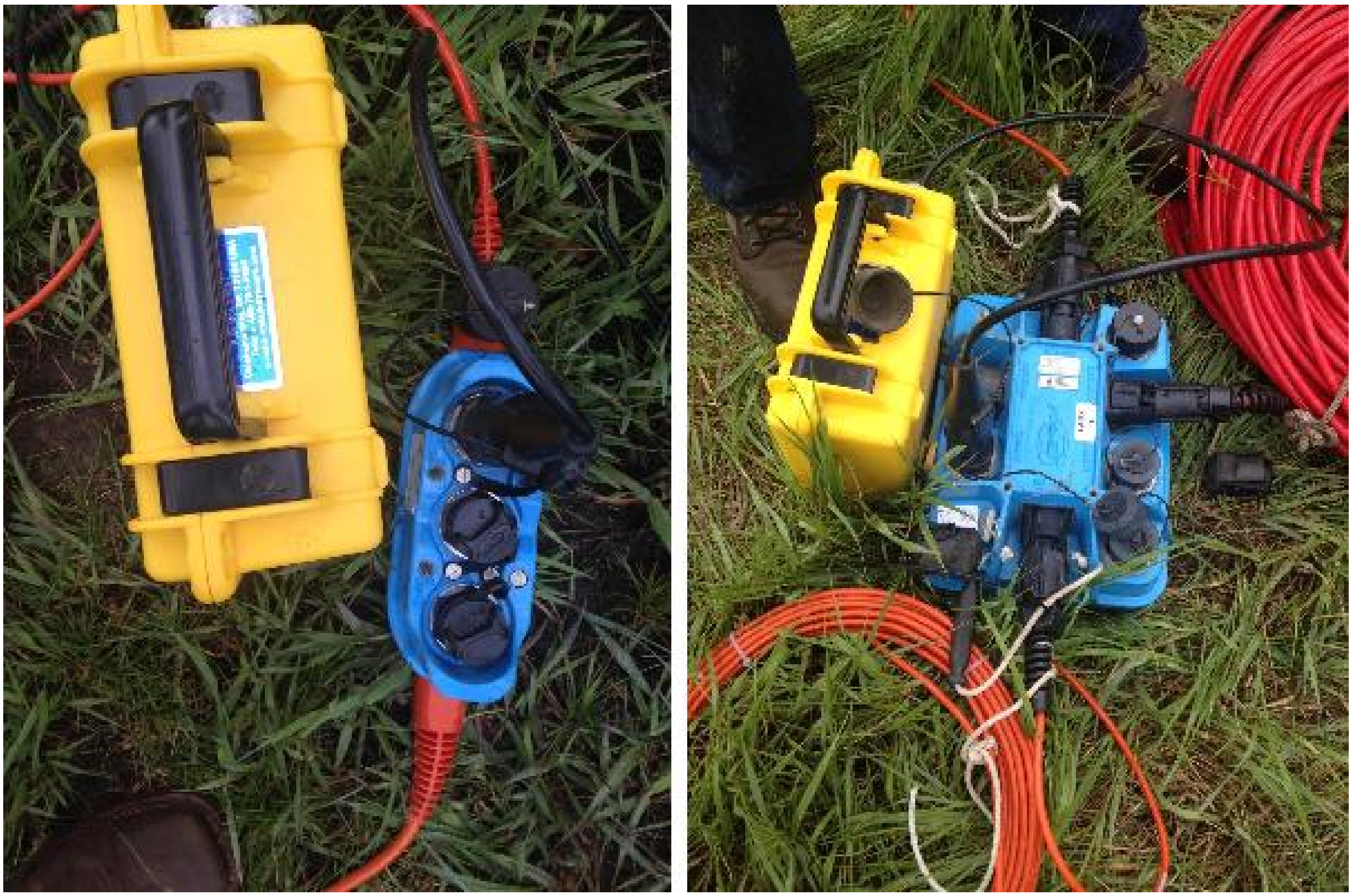

Figure 24. LAUX

9.2.2. *Vibroseis.* A variety of tools can be used as seismic sources. These include dynamite, shotgun blanks, compressed air guns, and sledge hammers. However, the most commonly used source is a vibroseis truck. We used two AHV-IV Commander INOVA vibroseis trucks provided by Dawson Geophysical to use as seismic sources. These vehicles transmit a controlled acoustic wave into the ground by lowering the baseplate at each vibroseis source point (VP) placing all the weight onto a smaller surface area and oscillating up and down at very fine rates. The trucks use INOVA's Vib Pro™ to perform a sweep specified by the doghouse along with a precise accelerometer to monitor the motion. A GPS receiver is located directly above the center of the baseplate and at each VP the precise location is recorded for use during data processing. Figure 25 shows the vibroseis trucks brought to the field [**67**].

Figure 25. One of the Dawson INOVA AHV-IV Commander used

9.3. Data Processing.

9.3.1. *CMP Gathers.* CMP gathers stands for common midpoint gathers, which means that the seismic data are sorted in a way that the traces share the same source-receiver midpoints. Figure X is an illustration of a CMP gather. In order to complete a CMP gather, there are several assumptions that need to be made:

- The boundaries of two layers of varying velocities are horizontal
- The layers are isotropic
- The layers are homogeneous

Satisfying these assumptions, CMP gathers have not only the same midpoint, but correspond to the same depth point in the subsurface, and therefore CMP gathers might also be called as CDP gathers.

The equation of a CMP gather is shown below as Equation (65). T_x is the two way travel time, T_0 is the zero offset travel time, x is the offset, and v_S is the stacking velocity.

$$T_x^2 = T_0^2 + (\frac{x}{v_s})^2 \quad (65)$$

CMP gathers are useful because the signal-to-noise ratio increases as the number of traces increases. The definition of ''fold" is also related to CMP gathers. ''Fold" is the number of traces in a CMP gather [**68**].

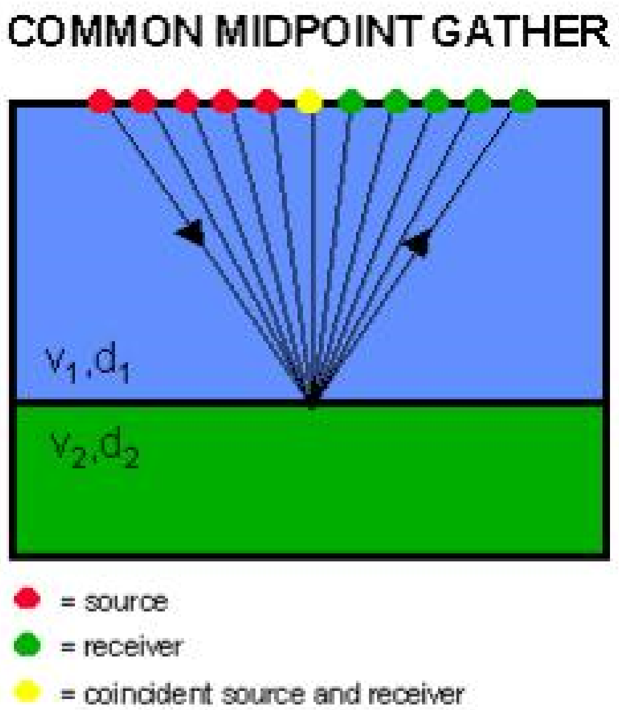

Figure 26. An illustration of a common midpoint gather.

9.3.2. *Fold.* Fold is used in seismic acquisition and interpretation to indicate how many times a common midpoint is surveyed along the seismic line. The fold value for a seismic line depends on the amount of source points, the number of sweeps at each source point, and the amount of receiver points. In multichannel seismic acquisition, the common midpoint is a location in the subsurface that is located halfway between the source and the receiver and is shared by multiple source-receiver pairs. This value of redundancy is used to obtain a measurement of signal to noise in the data set. A higher value of fold means we will have greater resolution of reflectors. Usually near the ends of a survey line, fold decreases due to a lack of common midpoints acquired at the end.

9.4. Mathematical Concepts.

9.4.1. *Impedance Contrast.* The impedance contrast is an essential factor in seismic because this physical parameter allows seismic to distinguish between different layers of rocks or lithologies in the subsurface. The impedance contrast is governed by the acoustic impedance of the subsurface layers. We are able to record the travel time for seismic waves to reflect off interfaces in subsurface and use this information to determine the acoustic impedance of the layers. With the recorded two-way travel time, the velocity of the propagation can be determined, and the acoustic impedance can be calculated as shown in the equation below:

$$Z = V\rho \tag{66}$$

where V is seismic wave velocity and ρ is density of rock/layer. This equation is then used to determine the impedance contrast by determining the impedance of one layer and subtracting it from the next.

$$Impedance\ Contrast\ (Amplitude\ Reflected) = Z_{n+1} - Z_n = V_{n+1}\rho_{n+1} - V_n\rho_n \tag{67}$$

We then use impedance contrast to find the reflection coefficient, R which tells us the reverse in polarity of the reflected wave, where positive R yields to unchanged wave polarity and negative R yields to reversed wave polarity.

$$R = \frac{Impedance\ Contrast\ (Amplitude\ Reflected)}{Sum\ of\ two\ Impedance\ (Amplitude\ Incident)} = \frac{Z_{n-1} - Z_n}{Z_{n+1} + Z_n} = \frac{V_{n+1}\rho_{n+1} - V_n\rho n}{V_{n+1}\rho_{n+1} + V_n\rho_n} \tag{68}$$

The polarity of wave provides information about compression and dilation. If polarity is unchanged (positive R) then compression remains compression and dilation remains dilation, whereas reversed polarity (negative R) shifts compression to dilation and vice versa. The equation holds the assumption that the wave hits a boundary at normal incidence. [**69**]

9.4.2. *Fermat and Huygens Principle/Fresnel Zone.* To develop an understanding why a wave bends when passing through different mediums, we refer to Huygens' principle, which is used in seismic theory and processing to analyze geometric patterns created by spherical wave propagation. The principle states that each wavefront can be approximated as many points that act as individual sources. As an external wave interacts with each of these individual points, secondary source waves begin to propagate, creating a threshold envelope which determines the wavefront at later times. The general complex amplitude of this propagation can be defined as:

$$U(p) = \frac{-i}{\lambda} U(r) * \iint_S \frac{e^{iks}}{s} K(x) dS \tag{69}$$

where $K(s)$ takes on different values for unique zones, defined as $K(x) = \frac{1}{2}(1 + cos(x))$.
From a more practical standpoint, Huygens' Principle can be used to solve for the reflection and refraction laws, which are also identified as Snell's Law.

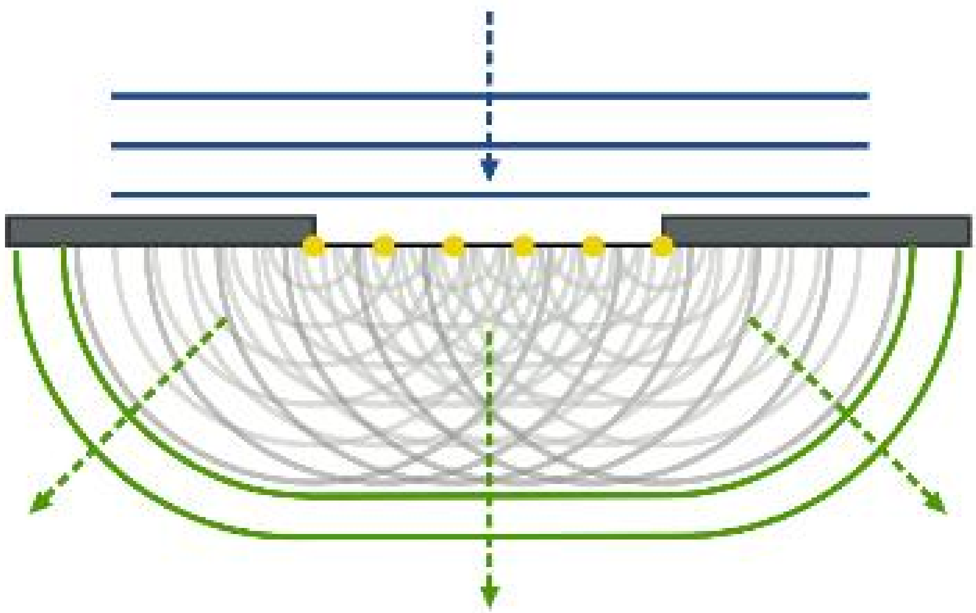

Figure 27. General visualization of Huygen's principle with the final wavefront envelope in green.

After Huygens' principle was introduced for wavefronts of light rays, a mathematician named Pierre de Fermat wanted to mathematically characterize the ray paths of light. The principle states that the path traveled by each ray between two points will always take the least amount of time. this time can be defined as the following:

$$T = \int_t^{t_1} \frac{c}{v} \frac{ds}{dt} dt \tag{70}$$

Fermat's principle can be used to mathematically prove Snell's Law of reflection and refraction [**70**] [**71**].

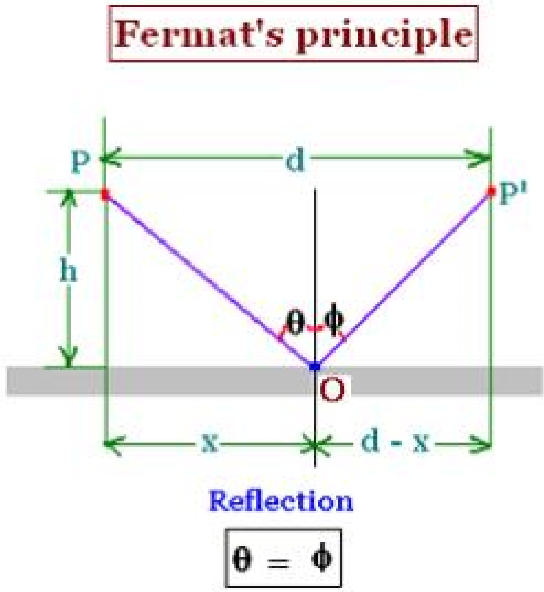

Figure 28. Fermat's principle of shortest ray path traveltime used to explain Snell's Law of Reflection.

9.4.3. *Snell's Law.* Seismic waves propagate in the subsurface until they reach a geologic interface between two media with different velocities. The contrasting physical properties of the materials cause the incoming wave to deflect, which results in the wave energy reflecting or refracting. The angle from vertical at which a primary wave reaches an interface is called the angle of incidence (Figure 29) and the reflected wave bounces off of the interface and travels back at the corresponding angle of reflection (Figure 29), which is equal to the angle of incidence. Each of these angles is measured from a line normal to the interface. Refracted waves travel through the interface and are transmitted at the angle of refraction, which is determined by the angle of incidence and the material velocities on either side of the interface (Figure 29). Snell's Law of Refraction demonstrates these relationships:

$$\frac{sin\Theta_1}{c_1} = \frac{sin\Theta_2}{c_2} \tag{71}$$

where c is the wave velocity in the interface and Θ is the angle of incidence, reflection, or refraction.

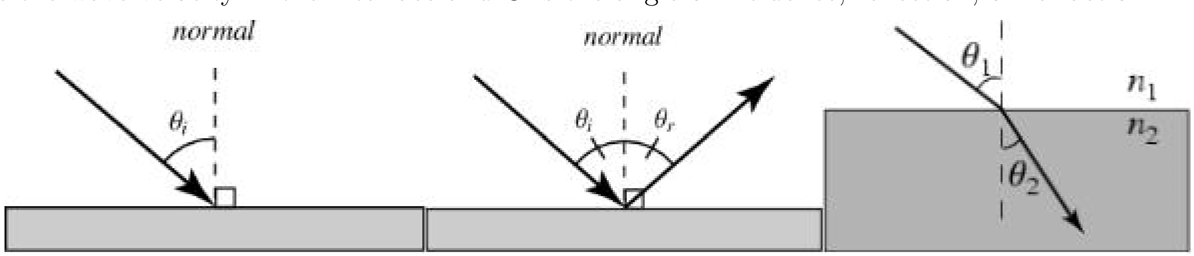

Figure 29. Angle of (a) Incidence, (b) Reflection, and (c) Refraction **[72]**

9.4.3.1. *Critical Angle.* The critical angle is the angle of incidence that results in total internal reflection. Total internal reflection describes how the propagating wave bounces completely back to the side of the source interface. The critical angle can be calculated with Snell's Law when the second angle, Θ_2, is set to 90 degrees.

$$\Theta_c = sin^{-1}\left(\frac{c_2}{c_1}\right) \tag{72}$$

If the angle of incidence is equal to the critical angle, then the refracted wave will travel directly tangent to the boundary between interface 1 and interface 2. When the incoming wave reaches the critical angle, a head wave develops. The head wave is the first wave to arrive to the receivers because it travels through the highest velocity rock, generally found closer to the surface. Overall, Snell's Law allows us to analyze the angles between two media in order to determine the angle of refraction as well as look at the critical angle and head waves **[73]** **[74]**.

10. Geologic Data

Formation	Depth to top (m)	Thickness (m)
Mancos	0	150.876
GreenHorn	150.876	7.62
Graneros	158.496	54.864
Dakota	213.36	n/a

Table 2. Bramwell Well. UTM: 13S 335536.67 E, 4100163.49 N [**31**]

Formation	Depth to top (m)	Thickness (m)
Carlile	590.4	125.6
Greenhorn	715.97	52.12
Dakota	768.1	58.5
Morrison	826.6	n/a

Table 3. James Greigo #1 Well. UTM: 13S 328900.30 E 4098511.42 N [**31**]

10.1. Well Logs.

11. Math and Physics Concepts

11.1. Waves. The two main categories of seismic waves are body waves and surface waves. Body waves travel through the interior of the earth and have lower frequencies, while surface waves have higher frequencies and are only able to propagate through the earth's crust.

11.1.1. *Surface Waves.* Surface waves are aptly named as they diminish the further they get from the surface. There are two types of surface waves, Rayleigh waves and Love waves. Rayleigh waves roll along the surface with longitudinal and transverse motion in the direction of wave propagation, much like waves in an ocean. The amplitude of the Rayleigh wave decreases exponentially as it propagates further away from the surface. They waves have a retrograde elliptical motion [**75**]. Love waves are faster than Rayleigh waves and move parallel to the surface and perpendicular to the direction of wave propagation[**75**]. Similarly to a Rayleigh wave, the amplitude also decreases exponentially with depth.

11.1.2. *Body Waves.* The types of waves more commonly considered in seismic investigations are body waves. Like surface waves, there are two different types: compressional (primary) waves and shear (secondary) waves. Compressional waves are the fastest seismic waves and are the result of alternating particle compression and extension in the same direction as wave propagation. The velocity of primary waves is written in (73).

$$V_p = \sqrt{\frac{K + \frac{4}{3}\mu}{\rho}} \tag{73}$$

In this equation K is the bulk modulus, μ is the shear modulus, and ρ is the mass density of the material through which the wave is propagating. The bulk modulus determines the compressibility of a medium with units of $\mathrm{N/m^2}$. Materials with higher a bulk modulus are harder to compress. The shear modulus is the ratio of shear stress to shear strain and it is used to determine the rigidity of a material with the dimensions for pressure. Shear waves are slower than compressional waves, and the particle motion within these waves is perpendicular to the direction of wave propagation.The velocity of S waves can be written as the following equation (74).

$$V_s = \sqrt{\frac{\mu}{\rho}} \tag{74}$$

In this equation μ is the shear modulus and ρ is the mass density of the material through which the wave is propagating[**76**].Compressional waves are able to propagate through solids and liquids, whereas shear waves only travel through solid rock because fluids and gasses do not support shear stresses.

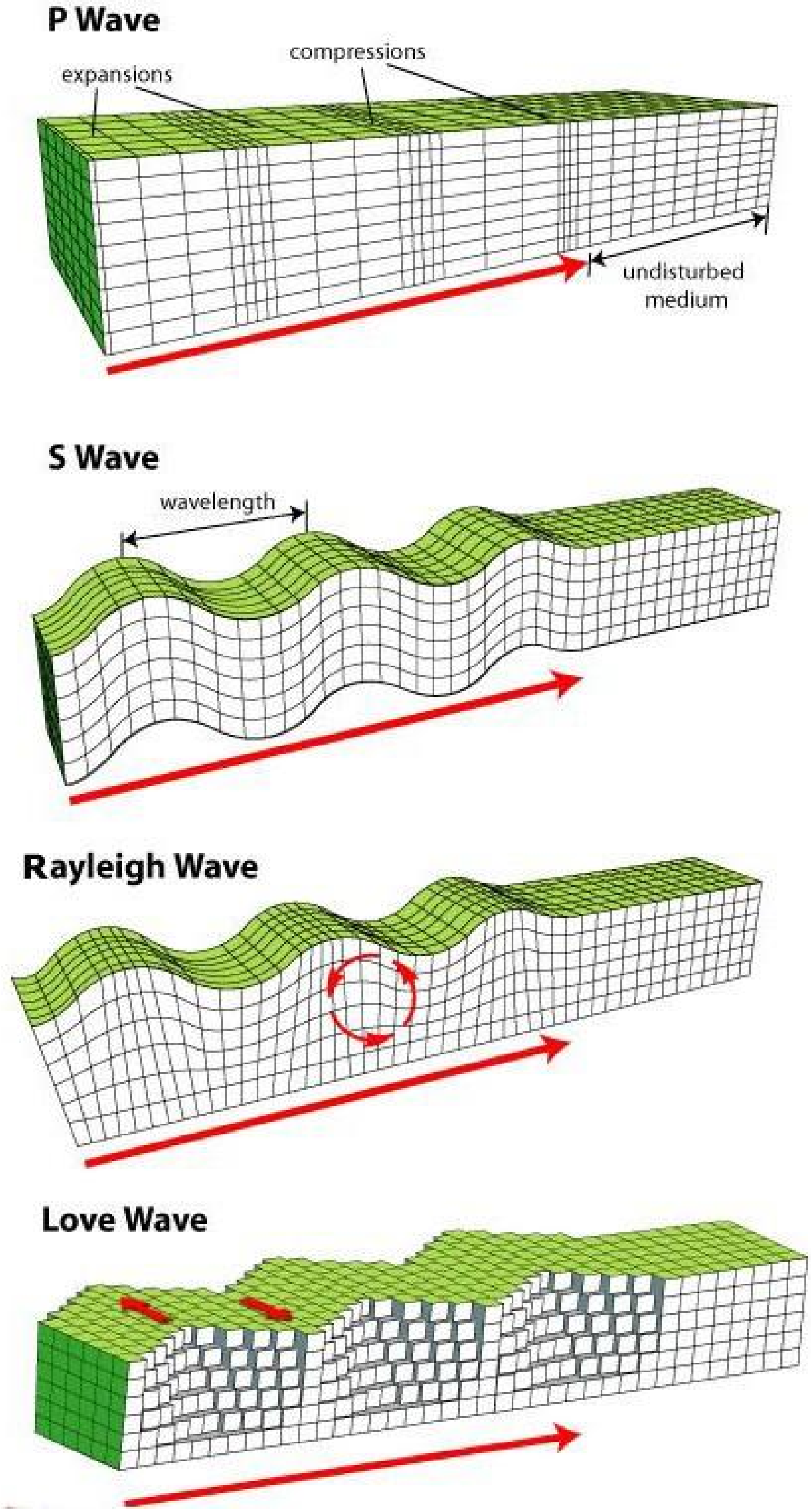

Figure 30. Visual description of P, S, Rayleigh, and Love waves.[**77**]

11.2. Maxwell's Equations. Maxwell's equations are the basis for the physics behind all electrical and electromagnetic geophysical methods. They were compiled from a number of previous equations from Gauss, Faraday and Ampere, which were expanded upon by Maxwell. By doing so Maxwell was able to connect all of the principles of electric and magnetic fields and flux.

11.2.1. *Gauss' Law for Electricity.* Gauss' law for electricity describes how an electrical field in a closed area is related to the total charge in that area. This law can also be used to describe the electrical flux Φ_E, or the flow of charge, out of a surface. This relationship is described in (75), where $\mathbf{E}$ is the electrical field, $\mathbf{A}$ is the area, q is the total charge, and ε_0 is the permittivity in a vacuum. The permittivity of a vacuum is a constant with a value of 8.854 x10^{-12} F/m.

$$\oint \mathbf{E} \cdot d\mathbf{A} = \frac{q}{\varepsilon_0} \tag{75}$$

This law can be used in any situation in which a Gaussian surface can be made. A Gaussian surface is an imaginary symmetric surface which encloses a distribution of charges. By using a Gaussian surface we can simplify the equation to $\mathbf{EA} = \frac{q}{\varepsilon_0}$, which makes solving for the electric field or total charge much simpler.

11.2.2. *Gauss' Law for Magnetism.* Gauss's law for magnetism is similar to his law for electricity, but it states that total magnetic flux Φ_B out of a closed surface is zero. This is described in (76), where $\mathbf{B}$ is the magnetic field, and $\mathbf{A}$ is again the area.

$$\oint \mathbf{B} \cdot d\mathbf{A} = 0 \tag{76}$$

The net flux is zero because in a magnetic dipole, a magnetic body with north and south poles, the magnetic field will flow out of the north pole and back into the south pole. Therefore any part of the magnetic field that leaves the surface will always re-enter the surface [**78**].

11.2.3. *Faraday's Law of Induction.* Faraday's law of induction states how an electrical field can be created. If a magnetic flux changing with respect to time is flowing through a body, then an electrical field is induced around that body [**78**]. This is described in (77), where $\mathbf{E}$ is the electrical field, $\mathbf{d}s$ is a small segment of the line over which the electrical field is flowing, Φ_B is the magnetic flux, and t is the time.

$$\oint \mathbf{E} \cdot \mathbf{d}s = -\frac{d\Phi_B}{dt} \tag{77}$$

This law is the principle for any kind of electrical generator. The generator has a coil of wire, usually made of copper, which has a magnetic flux flowing through the center of it. That produces the electrical field which then is used as a power source.

11.2.4. *Ampere's Law.* Ampere's law describes two different ways in which magnetic fields can be generated. The first method is to have an electrical current flowing through a body, while the second is to have a changing electrical field. Putting both of these methods gives us (78), where $\mathbf{B}$ is the magnetic field, $\mathbf{d}s$ is a differential segment of the line of which $\mathbf{B}$ flows, μ_0 is the magnetic permeability which has a value of $4\pi x10^{-7}$ N/A^2, i is the electrical current, c is the speed of light, and $\mathbf{E}$ and $\mathbf{A}$ are the same as in (75).

$$\oint \mathbf{B} \cdot \mathbf{d}s = \mu_0 i + \frac{1}{c^2}\frac{\partial}{\partial t}\int \mathbf{B} \cdot d\mathbf{A} \tag{78}$$

Having an electrical current flowing through a body generates a magnetic field that flows around the current. The portion of (78) that relates this is $\mu_0 i$. The portion relating changing electrical fields is $\frac{1}{c^2}\frac{\partial}{\partial t}\int \mathbf{B} \cdot d\mathbf{A}$. Notice that the later half of this expression contains a bit that looks very similar to (75). This is the electrical flux, which is changing in relation to time. This means that similarly to Faraday's law, if the electrical flux is changing a magnetic field will be generated [**78**].

12. Instrument Specifications

12.1. ABEM Terrameter SAS 1000/4000.

Figure 31. ABEM Terrameter SAS 1000/4000 [**79**]

12.1.1. *Receiver.*

- Isolation: Input channel is galvanically separated
- Input Voltage Range: +/- 400 V
- Input Impedance: 10 MOhm minimum
- Precision: Better than 0.1 % (in the range 4-200 ohm at 1s integration
- Accuracy: 1% typical
- Resolution: Theoretical 30 nV
- Dynamic range: Up to 140 dB plus 64 dB automatic gain (at 1s integration)
- Automatic ranging: +/- 2.5 V, +/- 10 V, +/- 400 V

12.1.2. *Measuring.*

- Resistivity: YES
- SP: YES
- IP: YES
- Current pulse length: from 0.1 s to 4 s - User selectable
- IP Windows: Up to ten time windows
- IP integration interval: Up to 8 s

12.1.3. *Transmitter.*

- Output power: 100 W
- Current transmission: True Current Transmitter
- Output Current Accuracy: Better than 0.5 % at 100 mA
- Output Current: 1, 2, 5, 10, 20, 50, 100, 200, 500, 1000 mA (operator set or auto ranging)
- Maximum Output Voltage: +/- 400 V (800 V peak-to-peak)
- Cycle type in resistivity mode: Plus-Minus-Minus-Plus
- Cycle type in IP mode: Plus-Zero-Minus-Zero

12.1.4. *General.*

- Casing: Rugged Aluminium case meets IEC IP 66
- Computer Display: PC compatible - LCD, 200 x 64 pixels, 8 lines of 40 characters
- I / O ports: Multifunction connector with current and potential including RS232 communication for external devices as PC, LOG and Imaging - Banana connectors for current and potential
- External devices: Lund Imaging System, SAS LOG
- Memory Capacity Power: More than 1 500 000 readings - Optional Clip-on rechargeable power pack or external 12V DC through SAS-EBA
- Dimensions (W x L x H): 105 x 325 x 270 mm with SAS-EBA
- Weight: 5.1 kg
- Ambient Temperature Range: -5°C to +50°C operating

12.2. AccuRef 20 Silver Chloride Permanent Reference Electrodes.

Figure 32. AccuRef 20 Silver Chloride Permanent Reference Electrodes

[80]

- Applications: Direct burial in soil, with or without chloride ion contamination
- Electrode Potential: In the range, 240 mV ±10mV, versus SHE @ 25°C
- Filling Solution: Saturated KCl plus additives
- Low Freezing Point: -20°C
- Design Life: 20 years
- Purity: High purity Ag, AgCl, Kcl and triple de-ionized H2O
- Tip: Moisture absorbent ceramic tip
- Evaporation: Will not dry out at low humidity and/or high heat
- Wire: 25ft of #12 AWG XLPE RHW-2 leadwire; cross-linked Polyethylene jacket, direct burial, low leakage, 600V, 90°C Rating. Longer lengths of wire are available
- Electrical Contact Surface Area: Approximately 16.4 square inches (a cylindrical surface, 1.5 inches in diameter and 3.5 inches in length)
- Contains: 3g of high purity Ag (99.99% pure) - 0.75g of high purity AgCl (99.99% pure) - 200ml of KCl solution
- Dimensions: Diameter: 2.77in, Length: 11in, Weight: 1.9lbs

12.3. AEMC MX 55III 50,000/100,000-Count Digital Multimeters.

Figure 33. AEMC MX 55III 50,000/100,000-Count Digital Multimeters

12.3.1. *AC Current.*

- Measurement Range: 500μA to 10A
- Resolution: 10nA to 1mA
- Basic Accuracy: $\pm$0.6 % of Reading $\pm$30cts

12.3.2. *AC Voltage.*

- Measurement Range: 0.5 to 750V
- Resolution: 10μV to 100mV
- Basic Accuracy: $\pm$0.3 % of Reading $\pm$30cts
- Input Impedance: 10MΩ

12.3.3. *DC Current.*

- Measurement Range: 500μA to 10A
- Resolution: 10nA to 1mA
- Basic Accuracy: $\pm$0.05 % of Reading $\pm$2cts

12.3.4. *DC Voltage.*

- Measurement Range: 0.5 to 1000V
- Resolution: 10μV to 100mV
- Basic Accuracy: $\pm$0.025 % of Reading $\pm$2cts
- Input Impedance: 10MΩ

12.3.5. *Resistance.*

- Measurement Range: 500Ω to 50MΩ
- Resolution: 10m Ω to 1000Ω

12.3.6. *Continuity.*

- Basic Accuracy: $\pm$0.07 % of Reading $\pm$2cts
- Measurement Range: 10Ω to 20Ω
- Response Time: 1ms

12.3.7. *Diode Test.*

- Resolution: 1mV
- Test Current: 1mA $\pm$20%

12.3.8. *Capacitance.*

- Measurement Range: 50nF to 50mF
- Resolution: 10pF to 10μF
- Basic Accuracy: ±1 % of Reading ±2cts

12.3.9. *Frequency.*

- Measurement Range: 0.62Hz to 500kHz
- Basic Accuracy: 0.03% of Reading

12.3.10. *dB Function.*

- Measurement Range: 100mV to 750V
- Resolution: 0.01dB

12.3.11. *General.*

- Digital Display: 50000-count
- Analog Bargraph: 34-segment
- Power Source: 9V Alkaline battery
- Dimensions: 7.4 x 3.2 x 1.5” (189 x 82 x 40mm)
- Weight: 0.8 lb (400g)

12.3.12. *Environmental.*

- Operation Temperature: 14°F to 140°F (-10°C to 60°C)
- Storage Temperature: -40°F to 158°F(-40°C to 70°C)

12.3.13. *Safety.*

- Safety Rating: EN 61010, 600V Cat. III and 1000V Cat. II
- Double Insulation: Yes
- CE Mark: Yes

12.4. Trimble 5800 GPS Receiver.

Figure 34. Trimble 5800 GPS Receiver

12.4.1. *Physical Specifications.*

- Size: 19cm (7.5”) wide x 10cm (3.9”) deep including connectors
- Weight: with internal battery and radio 1.21 kg (2.7 lbs)
- Battery life (at 20 °C) Approximately 5.5 hours for one 2.0 ah Lithium-ion battery
- External Power input: 11–28 VDC
- Operating temperature: –40 °C to +65 °C (–40 °F to +149 °F)
- Storage temperature: –40 °C to +70 °C (–40 °F to +158 °F)
- Humidity: 100% condensing, unit fully sealed
- Casing: Dust-proof, shock- and vibration-resistant

12.4.2. *Technical Specifications.*

- Tracking: 24 channels L1 C/A code, L1/L2 full cycle carrier - Fully operational during P-code encryption - WAAS satellite tracking
- Signal processing: Maxwell architecture - Very low-noise C/A code processing - Multipath suppression
- Start-up: Cold start: <60 seconds from power on - Warm start: <30 seconds with recent ephemeris
- Initialization: Automatic while moving or static
- Minimum initialization time: 10 sec + 0.5 x baseline length (km)
- Communications: Two RS-232 serial ports (Port 1, Port 2,) - Port 1: Baud Rates up to 115,200 bps - Port 2: Baud Rates up to 115,200 bps - RTS/CTS flow control negotiation supported on Port 2 only -Bluetooth communications with Trimble ACU or TSCe controller with BlueCap module

Positioning	Mode	Horizontal Accuracy (RMS)
RTK (OTF)	Synchronized	1cm + 1ppm (x baseline length)
	Low Latency	2cm + 2ppm (x baseline length)
L1 C/A Code Phase	Synchronized/Low Latency	.25m + 1ppm RMS
Static/FastStatic	N/A	5 mm + 0.5 ppm (x baseline length)
WAAS	N/A	Less than 5m

Table 4. Technical specifications

Positioning	Mode	Vertical Accuracy (RMS)
RTK (OTF)	Synchronized	2cm + 1ppm (x baseline length)
	Low Latency	3cm + 2ppm (x baseline length)
L1 C/A Code Phase	Synchronized/Low Latency	.50m + 1ppm (x baseline length)
Static/FastStatic	N/A	5mm + 1 ppm (x baseline length)
WAAS	N/A	Less than 5m

Table 5. Technical specifications

- Configuration: Via user-definable application files or GPS Configurator
- Output formats: NMEA-0183: AVR; GGA; GSA; GST; GSV; PTNL,GGK; PTNL,GGK_SYNC; HDT; PTNL,PJK; PTNL,PJT; ROT; PTNL,VGK; VHD; VTG; ZDA; GSOF (Trimble Binary Streamed Output) RT17

12.4.3. *Positioning Specifications.*

12.5. Trimble TSC2 Data Controller.

Figure 35. Trimble TSC2 Data Controller

12.5.1. *Physical Characteristics.*

- Length: 28.2 cm (11.1”)
- Width: 10.5 cm (4.1”)
- Height: 4.4 cm (1.7”)
- Handgrip: 7.6 cm (3”)
- Weight: 1.1 kg including battery, radio, and radio whip antenna
- Memory: 512 MB flash disk; 128 MB SDRAM
- Processor: Intel® Bulverde PX-A27 at 516 MHz
- Power: Li-Ion rechargeable pack, 6600 mAh, battery life of 30 hours under normal operating conditions. Fast charge to 80% in 2 hours; full charge in 4.5 hours. Battery charge status LED indicator

- Certification:
  - Class B FCC certification, CE Mark approval, CSA, and C-tick approval
  - Bluetooth type approvals and regulations are country specific
- Controller type:
  - Handheld controller.
  - Can be connected to the Trimble SPS781, SPS881, SPS751, and SPS851 GPS Receivers, the Trimble SPS610 Total Station and Trimble SPS730 and SPS930 Universal Total Stations, and robotic remote control radios

12.5.2. *Interface Characteristics.*

- Display: 320 x 240 pixel QVGA reflective color TFT, LED back-lit illuminated display
- Touch Screen: Passive touch screen, works with stylus or finger
- Keyboard: 52-key tactile action with separate navigation, alpha and numeric keypads, 8-way spider key
- Audio: Integrated speaker and microphone for audio events, warnings and notifications, recording
- Operating system: Microsoft® Windows Pocket PC 5.0

12.5.3. *Input/Output Characteristics.*

- Serial Port: COM1, 9-pin D-Sub RS232 (115 kB/s) with 5 V (250 mA) on pin 9
- USB Port 1: USB client connector v2.0
- USB Port 2: USB host connector v2.0
- Compact Flash 1: Compact Flash Card slot v1.2 Type 1
- Compact Flash 2: Compact Flash Card slot v1.2 Type 2
- SD I/O: Secure Digital Card slot
- Integrated Bluetooth: Bluetooth v1.2

12.5.4. *Environmental characteristics.*

- Operating Temperature: –30 °C to 60 °C (–22 °F to 140 °F)
- Storage Temperature: –40 °C to 60 °C (–40 °F to 140 °F)
- Sand and dust: IEC 529 IP6X, MIL-STD-810F, Method 510.3
- Water: IEC 529 IPX7, MIL-STD-810F, Procedure I
- Drops: 48” onto 2-inch plywood over concrete, 26 drops room temperature (all faces, edges, corners, one drop each), 6 face drops at 60 °C, 6 face drops at -20 °C
- Vibration: MIL-STD-810F, Method 514.5, Procedure I; General Minimum Integrity Test
- Altitude: MIL-STD-810F, Method 500.4

12.6. EM31-MK2.

Figure 36. EM31-MK2

- Operates at 9.8 kHz, with a fixed coil spacing of 3.66 m

- Power supply: 8 disposable alkaline "c" cells
- Measurement ranges: conduct.:10,100,1k ms/m, in-phase: +/- 20 ppt
- Measurement: resolution: +/- 0.1% of full scale
- Measurement: accuracy: +/-5% at 20 ms/m
- Noise levels: conductivity: 0.1 ms/m in-phase: 0.03 ppt
- Data storage: 16,500 records (1 component); ext. memory available
- Dimensions: boom: 4m ext.; 1.4m stored case: 145x38x23 cm
- Weights : Instrument: 12.4 kg

12.7. EM34-3 | EM34-3XL.

Figure 37. EM34-3 | EM34-3XL

- Measured quantities: apparent conductivity in millisiemens per meter (ms/m)
- Primary field source: self-contained dipole transmitter
- Sensor: self-contained dipole receiver
- Reference cable: lightweight, 2 wire shielded cable
- Intercoil spacings and operating frequency: 10 m at 6.4 kHz; 20 m at 1.6 kHz; 40 m at 0.4 kHz
- Power supply: transmitter: 8 disposable or rechargeable "d" cells; receiver: 8 disposable or rechargeable "c" cells
- Conductivity ranges: conductivity: 10, 100, 1k ms/m
- Measurement resolution: +/- 0.1% of full scale
- Measurement accuracy: +/- 5% at 20 ms/m
- Noise levels: conductivity: 0.2 ms/m (can be greater in regions of high power line interference)
- Dimensions: rx console: 19x13.5x26 cm; tx console: 15.5x8x26 cm; rx and tx coil: 63 cm; diameter em34-3xl; tx coil: 100 cm ;case: 27.5x75x75 cm
- Weights: instrument: 20.5 kg; XL: 26.5 kg

12.8. TEM57-MK2 Transmitter.

Figure 38. Tem57-MK2 Transmitter

- Base frequency : 0.3, 0.75, 3, 7.5, or 30 Hz (60 Hz power line frequency) 0.25, 0.625, 2.5, 6.25, or 25 Hz (50 Hz power line frequency); rates below 1 Hz available through cable reference; through crystal reference with modification
- Turn-off time: 20 to 115 μs, depending on size, current and number of turns in transmitter loop
- Transmitter loop: single turn: any dimension; minimum resistance is 0.7 ohms, up to 300 x 600 m 8-turn: 5 x 5 or 10 x 10 m
- Output voltage: 18 to 60 V continuously adjustable; up to 160 V (4,500 w) with external power source
- Output current: 28 A maximum
- Synchronization: reference cable or, optionally, highly stable quartz crystal
- Power source: 1,800W, 110/220V, 50/60 Hz single-phase motor-generator or, optionally, multiple 12V batteries
- Operating temperature: -35°C to 50°C
- Transmitter size : 43 x 25 x 25 cm
- Transmitter weight: 15 kg

12.8.1. *Receiver.*

Figure 39. Receiver for TEM57

- Time gates: 20 or 30 geometrically spaced gates for each base frequency; range from 6 μs to 800 ms
- Dynamic range: 29 bits (175 dB) including all gains
- Synchronization: internal; terminals provided for cable reference with external transmitters
- Data output: rs-232 serial, usb ports

12.8.1.1. *Transmitter Section.*

- Base frequency: 30, 75, or 285 Hz (60 Hz power line frequency) 25, 62.5 or 237.5 Hz (50 Hz power line frequency
- Turn-off time: 2.5 μs at 2 A into 40 x 40 m loop; faster into smaller loop
- Output voltage: cm: 0 to 9V continuously adjustable (at 1 A load), or 24V cm hp: 12 to 36V with external batteries
- Output current: cm: 3.5 A maximum (7 A pp) with internal battery cm hp: 11 A maximum (22 A pp) with external batteries

12.8.1.2. *General.*

- Power source: internal 12/24 V rechargeable lithium-ion battery
- Battery life: 8 h continuous operation with 2 A transmitter current at 12V output voltage
- Operating temperature: -30°C to 50°C
- Dimensions: 40 x 35 x 24 cm
- Weight: cm: 10.5 kg; cm hp: 11.7 kg

12.9. CG-5 Gravity Meter.

Figure 40. CG-5 Gravity Meter

- Sensor Type: Fused Quartz using electrostatic nulling
- Reading Resolution: 1 microGal
- Standard Field Repeatability: <5 microGal
- Operating Range: 8,000 mGal without resetting
- Residual Long-Term Drift: Less than 0.02 mGal/day (static)
- Automatic Tilt Compensation: ±200 arc sec
- Tares: Typically less than 5 microGals for shocks up to 20 G
- Automated Corrections: Tide, Instrument Tilt, Temperature, Drift, Near Terrain, Noisy Sample, Seismic Noise Filter
- Operating Temperature: -40°C to +45°C (-40°F to 113°F)

- Ambient Temperature Coefficient: 0.2 microGal/°C (typical)
- Pressure Coefficient: 0.15 microGal/kPa (typical)
- Magnetic Field Coefficient: 1 microGal/Gauss (typical)
- Memory: Flash Technology (data security)
- Dimensions: 30 cm (H) x 22 cm x 21 cm (12" (H) x 8.5" x 8")
- Weight (including batteries): 8 kg (17.5 lbs)
- Battery Capacity: 2 x 6.6 Ah (11.1 V) rechargeable Lithium-Ion Smart Batteries. Full day operation in normal survey conditions with two fully charged batteries
- Power Consumption: 4.5 W at 25°C (77°F)
- Standard System: CG-5 Console, Tripod base, 2 rechargeable batteries, Battery Charger 110/240 V, External Power Supply 110/240 V, RS-232 and USB Cables, Carrying Bag, Data dump and utilities software, Operating Manual (CD), Transit Case

12.10. Nova AHV-IV Commander (PLS 364) Vibroseis Truck.

Figure 41. Nova AHV-IV Commander (PLS 364) Vibroseis Truck [**81**]

- Shaker Model: P-Wave Vibrator; PLS-364
- Peak Force: 275 kN (61,800 lb)
- Piston Area: 132.9 sq cm (20.6 sq in)
- Mass Weight: 4,998 kg (11,020 lb)
- Driven Weight: 2,027 kg (4,469 lb)
- Useable Stroke: 9.83 cm (3.87 in)
- Frequency Limit: 1 Hz to 250 Hz
- Mass Accumulators (2): 3.8 L (1.0 gal.) Servo Manifold
- Lift Stroke: 97 cm (38 in)
- Balance Method: Airbags
- Isolation Method: Airbags
- Hydraulic System: Closed-loop
- Hydraulic System Pumps: 2 x 119 cc (7.25 in3); Denison P-7
- Servo Valve: Atlas 240H (with DR modification)
- Pilot Valve: MOOG
- Filtration: 3-micron absolute servo filter; 3.5-micron absolute, high and low pressure, triple element
- Accumulators: 2 x 19 L (5 gal); bladder-type
- Heat Exchanger: Steel core; multi-wing fan; hydraulically-driven
- Reservoir: 170 L (45 gal)
- Baseplate Type: Reinforced rectangular

- Baseplate Area: 2.5 m2 (3,864 in2)
- Winch Capacity: 13,608 kg (30,000 lb)

12.11. Sercel SG-10 Geophones.

Figure 42. Sercel SG-10 Geophones

- Natural Frequency (± 2,5 %): 10 Hz
- Coil Resistance (± 3,5 %): 350 Ω
- Tilt: 0°to 15°
- Pk-Pk Coil Travel: 1,78 mm
- Harmonic Distortion: <0,075%
- Sensitivity (± 2,5 %): 22,8 V/m/s
- Open Circuit Damping (±5 %): 0,68
- Damping Constant (RTBc fn): 4925 Ω.Hz
- Moving: 8,4g
- Spurious Resonance: >240 Hz
- Diameter: 274mm
- Length: 3,015mm
- Weight: 78 g
- Operating Temperature: -40°to 90°C

12.12. ADU-07e 24-Bit Geophysical EM Measurement System.

Figure 43. ADU-07e 24-Bit Geophysical EM Measurement System [**82**]

- Frequency range: DC to 250 kHz
- Number of channels: 1 up to 10 per ADU 07e

- Bands: 3 Bands (LF DC-1 kHz; MF DC-16kHz; HF 1 Hz-250kHz); Sub-bands are created by digital filtering; Both bands can be recorded simultaneously
- A/D conversion: 24 Bit (max. data rate max. 4096 samples/sec) LF Board, 24 Bit (max. data rate max. 65536 samples/sec) MF Board; 24 Bit (max. data rate 524,288 samples/sec) HF Board
- Dynamic range: >130dB
- System controller: 32 bit embedded controller, Linux
- Storage media: Internal SD card up to 32GB or more, USB devices
- E-field connector: input resistance >10 Mohm, ODU G32KON-T06QP00-000 (ADU E socket) ODU S22KON-T06MPL0-4000 (E-Field cable plug)
- H-field connector: input resistance 20 kOhm, socket ODU G32KON-T10QJ00-000 (ADU socket) ODU S22KON-T10MJG0-7000 (H-Field cable plug)
- Multipurpose connector (E/H): input resistance >10 Mohm (E), 20 kOhm (H); ODU G33KON-T30QF00-000 (ADU socket) ODU S23KOC-T30MFG0-7000 (cable plug)
- Network connection: standard 100 Mbit Twisted Pair, WLAN
- Synchronization: GPS clock +/- 30ns rms to satellite reference.
- Station position is also determined and stored
- Interfaces: network, magnetometers, E-field lines 2 battery inputs, GPS antenna, USB, wireless, Bluetooth
- Weight: appr. 7.1 kg
- External dimensions: 400 x 330 x 170 mm
- Operating temperature range: -40°C to + 60°C (with flash disk)

12.13. Geometrics G 858 MagMapper.

Figure 44. Geometrics G 858 MagMapper

12.13.1. *Magnetometer / Electronics.*

- Operating Principle: Self-oscillating split-beam Cesium Vapor (nonradioactive Cs133) with automatic hemisphere switching.

- Operating Range: 20,000 nT to 100,000 nT
- Operating Zones: For highest signal-to-noise ratio, the sensor long axis should be oriented at 45°, ±30°to the earth's field but operation will continue through 45°, ±35°. Sensor is automatic hemisphere switching.
- Sensitivity Statistics: 90% of all reading will fall within the following Peak-to-Peak envelopes: 0.03 nT at 0.2 sec cycle rate - 0.02 nT at 0.5 sec cycle rate - 0.01 nT at 1.0 sec cycle rate
- Noise: <0.008 nT/Hz-RMS
- Heading Error: <1.5 nT including backpack and GPS
- Gradient Tolerance: >500 nT /inch (>20,000 nT/ meter)
- Temperature Drift: <0.05 nT per°C
- Cycle Rate: Variable from 0.1 sec to 1 hr in 0.1 sec steps or by external trigger.
- Data Storage: Non-volatile RAM with capacity for 8 to 12 hrs of magnetometer, time, event marks, field notes and XYZ or GPS locations.
- Audio Output:
  (1) Audio tone of field variation; pitch and volume adjustable. (Search mode)
  (2) Audio pulse each 1 second (Pace metronome).
  (3) Alarm for loss of signal, low battery or quality control setting exceeded [**83**].
- Data Output: Three wire RS-232 standard serial port, optional continuous real time transmittal of data via RS-232 to PC. Total memory output transfer time less than 5 min. at 115,200 baud.
- Visual Output: 320 x 200 graphic liquid-crystal display, daylight visible with selectable outputs for:
  (1) Data display: Up to 5 stacked profiles, real time or review mode. Survey grid showing boundaries and position.
  (2) All system set-up functions, e.g., memory status, data transfer, sample time.
  (3) All Survey set-up functions, e.g., survey profile number and direction, station number or GPS data transfer protocol, line number.
  (4) Survey monitoring functions, e.g. total field, noise level, profile number x or x-y coordinates.
- Internal Clock: Resolution of 0.1 sec, drift: <1 sec/day
- Battery Life:
  (1) 24 VDC rechargeable gel cell, 6 hrs for Mag w GPS. Magnetic effect less than 1.5 nT Γ at 4 ft
  (2) Internal backup battery for clock and non-volatile RAM.

12.13.2. *Mechanical.*

- Sensor: 2-3/8" dia., 6-3/4" long, 12 oz. (6cm x 15 cm, 340 grams)
- Backpack: Backpack for Magnetometer, 9.5 lb (4.3 kg). Includes Nylon chest harness with all cables attached (1 kg to 1.3 kg)
- Battery: 3" H, 5" W, 8" L, 3.5 lbs (8 cm x 13 cm x 20 cm, 1.6 kg) belt mounted, attaches to harness.
- Console: 6" W, 3" H, 11"L, 3.5 lbs. (15 cm x 8 cm x 28cm, 1.6 kg), attaches to battery belt and harness. Magnetic effect less than 1 nT at 4 ft

12.13.3. *Environmental.*

- Operating Temperature: -25°C to 50°C (-13°F to + 122°F)
- Storage Temperature: -35°C to 60°C (-30°F to + 140°F)
- Watertight: Weatherproof in driving rain
- Shock: Survive a 3ft drop onto a hard surface

Warranty: 1 year on G-858 and sensor, one year on accessories

12.14. Metronix MFS-07e Broadband Induction Coil Magnetometer.

Figure 45. Metronix MFS-07e Broadband Induction Coil Magnetometer [**84**]

- Frequency range: 0.001 Hz 50 kHz
- Frequency bands: 0.001 Hz 500 Hz (chopper on) - 10 Hz 50 kHz (chopper off)
- Sensor noise: 3 x 10-2 nT/Hz @ 0.01 Hz
- 3 x 10-4 nT/Hz @ 1 Hz $\surd$ Hz (chopper off)
- Output sensitivity: 0.02 V/(nT x Hz) f «32 Hz - 0.64 V/nT f »32 Hz - for exact values refer to individual calibration file
- Output voltage range: +/- 10 V
- Function: Induction coil with magnetic field feedback
- Connector: ODU G32KON-T10QJ00-000 (coil socket)
- ODU S22KON-T10MJG0-7000 (cable plug)
- Calibration input sensitivity: 1.6 nT / V
- Feedback cut-off frequency: 32 Hz
- Supply voltage: +/- 12 V to +/- 15 V stabilized and filtered
- Supply current: +/- 25 mA
- Case: ruggedized, waterproof case
- Weight: approximately 5.5 kg
- External dimensions: length 700 mm, diameter 75 mm
- Operating temperature range: -25°C to 70°C

Bibliography

[1] P. S. V. Center, "Welcome to pagosa springs, colorado!." Online.
[2] G. F. C. 2012, "Geophysical characterization of the geothermal system in pagosa springs area," tech. rep., Colorado School of Mines, 2012.
[3] G. F. C. 2013, "Geophysical investigation of the pagosa springs geothermal system," tech. rep., Colorado School of Mines, 2013.
[4] G. F. C. 2014, "Geophysical investigation of the chromo geothermal system," tech. rep., Colorado School of Mines, 2014.
[5] V. C. Kelley, "Pre-cambrian rocks of the san juan basin," *New Mexico Geological Society*, pp. 53–55, 1950.
[6] J. E. Fassett, "Geology and coal resources of the upper cretaceous fruitland formation, san juan basin, new mexico and colorado," *U.S. Geological Survey*.
[7] I. Dalziel, L. Lawver, and J. Murphy, "Plumes, orogenesis, and supercontinental fragmentation," *Earth and Planetary Science Letters*, vol. 178, no. 1–2, pp. 1–11, 2000.
[8] S. Conner and C. Harrison, "The origins of the laramide orogeny," *The Traprock*, vol. 2, pp. 10–14, 2003.
[9] S. M. C. James L. Coleman, "Preliminary catalog of the sedimentary basins of the united states," tech. rep., 2012.
[10] C. E. C. Brian S. Brister, "Sedimentation and tectonics of the laramide san juan sag, southwestern colorado," tech. rep., The Rocky Mountain Association of Geologists, 2005.
[11] M. K. J. Z. B. R. A. Revil, S. Cuttler and M. Batzle, "The plumbing system of the pagosa thermal springs, colorado: Application of geologically constrained geophysical inversion and data fusion," *journal of Volcanology and Geothermal Research*, vol. 299, pp. 1–18, 2015.
[12] tech. rep.
[13] C. D. Conley, *Geology of the Chromo Anticline Archuleta County, Colorado and Rio Arriba County, New Mexico*. PhD thesis, Colorado School of Mines, 1958.
[14] J. E. Fassett, "Stratigraphy and oil and gas production of northwest new mexico," *U.S. Geological Survey*.
[15] R. Y. Anderson and D. W. Kirkland, "Origins, varves, and cycles of jurassic todilto formation, new mexico," *Bulletin of the American Association of Petroleum Geologists*, vol. 44, no. 1, pp. 37–52, 1960.
[16] B. Raynolds, "Colorado stratigraphy," 2015.
[17] R. B. O'Sullivan, "The base of the upper jurassic morrison formation in east-central utah," *U.S. Geological Survey Bulletin 1561*, 1984.
[18] J. Ridgley, "Sequence stratigraphic analysis and facies architecture of the cretaceous mancos shale on and near the jicarilla apache indian reservation, new mexico- their relation to sites of oil accumulation," tech. rep., U.S. Geological Survey, 2000.
[19] C. H. Dane, "The dakota sandstone and mancos shale of the eastern side of san juan basin, new mexico," *New Mexico Geological Society*, pp. 63–74, 1960.
[20] R. P. J.K. Barrett, "Hydrogeological data of thermal springs and wells in colorado," tech. rep., Colorado Geological Survey, 1976.
[21] W. Warren, *A geothermal exploration project in Pagosa Springs, Colorado*. PhD thesis, Colorado School of Mines, 1986.
[22] H. H. J.A. Cappa, "Low-temperature geothermal assessment program, colorado," tech. rep., Colorado Geological Survey, 1995.
[23] M. Galloway, "Hydrogeologic and geothermal investigation of pagosa springs, colorado," tech. rep., Colorado Geological Survey, 1980.
[24] L. P. D. Plouff, "Gravity study of the san juan mountains," tech. rep., United States Geological Survey, 2013.
[25] B. D. et al., "Geophysical study of the san juan mountains batholith complex, southwestern colorado," *Geosphere*, vol. 8, no. 3, pp. 669–684, 2012.
[26] R. Ryder, "Oil and gas potential of the chama-southern san juan mountains wilderness study area, mineral, rio grande, archuleta, and conejos counties, colorado," tech. rep., United States Geological Survey, 1977.
[27] N. National Coordination Office for Space-Based Positioning and Timing, "Official u.s. government information about the global positioning system (gps) and related topics," 2015.
[28] J. J. Milsom and A. Eriksen, *Field geophysics*, vol. 36. John Wiley & Sons, 2011.
[29] A. International, "Standard guide for using the seismic refraction method for subsurface investigation," 2011.
[30] Trimble, "Trimble gps tutorial - error correction," 2015.
[31]
[32] M. Loke.
[33] J. E. Nyquist and C. E. Corry, "Self-potential: The ugly duckling of environmental geophysics," *Leading Edge*, vol. 21, pp. 446–451, 2002.
[34] P. A. Bedrosian, M. J. Unsworth, and M. J. S. Johnston, "Hydrothermal circulation at mount st. helens determined by self-potential measurements," *Journal of Volcanology and Geothermal Research*, vol. 160, pp. 137–146, 2007.
[35]
[36] M. Senkaya and H. Karslı., "A semi-automatic approach to identify first arrival time: The cross-correlation technique.," *Earth Sciences Research Journal*, vol. 18.2, pp. 107–13, 2014.
[37] M. Cox, *Static Corrections for Seismic Reflection Surveys*. Society of Exploration Geophysicists, 1999.

[38] G. Schuster, "Deconvolution in practice," 1998.
[39] XSGeo, "Deconvolution in practice," 1999.
[40] M. Harrison, "F-x linear prediction filtering of seismic images," 1990.
[41] XSGeo, "Finite difference (implicit) migration," 1999.
[42] B. Han, "A comparison of four depth-migration methods," 1998.
[43] T. R. Dietrich Ristow, "Fourier finite-difference migration," *Geophysics*, vol. 59, no. 12, pp. 1882–93, 1994.
[44] S. Fomel, P. Sava, I. Vlad, Y. Liu, and V. Bashkardin, "Madagascar: open-source software project for multidimensional data analysis and reproducible computational experiments," *Journal of Open Research Software*, vol. 1, no. 1, p. e8, 2013.
[45] M. Cameron, S. Fomel, and J. Sethian, "Time-to-depth conversion and seismic velocity estimation using time-migration velocity," *Geophysics*, vol. 73, no. 5, pp. VE205–VE210, 2008.
[46] G. G. N. M. L. C. H. W. D. W. A. B. M. D. W. Stoeser, Douglas B. and B. S. V. Gosen, "Preliminary integrated geologic map databases for the united states central states: The state of colorado: U.s. geological survey open-file report 2005-1351," 2005.
[47] M. Nabighian, "The analytic signal of two-dimensional magnetic bodies with polygonal cross-section: Its properties and use for automated anomaly interpretation," *Geophysics*, vol. 37, no. 3, pp. 307–317, 1972.
[48] J. F. D. Siler and N. Hinz, "Regional and local geothermal potential evaluation: Examples from the great basin, usa, iceland and east africa," 2015.
[49] K. S. Ariffin, "Survei graviti (gravity survey)." online, nd.
[50] S. Farroq, 2015.
[51] Scintrex, "Cg-5 autograv gravity meter." Online, 222 Snidercroft Road, ND.
[52]
[53] U. EPA, "Frequency domain electromagnetic methods | environmental geophysics," 2015.
[54] A. Kaufman, "Frequency and transient responses of electromagnetic fields created by currents in confined conductors," *Geophysics*, vol. 43, no. 5, pp. 1002–1010, 1978.
[55] J. McNeill, "Applications of transient em techniques: Technical note tn-7," *Geonics Ltd*, 1980.
[56] M. Unsworth, "Electromagnetic and potential field methods," *Geophysics*, vol. 424, 2003.
[57] "Resistivity characteristics of geologic targets author=G.J. Palacky, journal= Electromagnetic Methods in Applied Geophysics , volume=1, pages=13–51, year=1987,"
[58] G. D. Naidu, *Deep Crustal Structure of the Son–Narmada–Tapti Lineament, Central India*. Springer-Verlag, 2012.
[59] U. of California at Berkeley, "Dc electric methods," 2015.
[60] A. Revil and M. Darot
[61] V. Naudet, A. Revil, E. Rizzo, J.-Y. Bottero, and P. Begassat, "Relationship between self-potential (sp) signals and redox conditions in contaminated groundwater," *Geophysical Research Letters*, vol. 30, p. 2091, 2003.
[62] R. F. Corwin and D. B. Hoover, "The self-potential method in geothermal exploration," *Geophysics*, vol. 44, pp. 226–245, 1979.
[63] R. Besancon. 1985.
[64] G. Mavko, "Conceptual overview of rock and fluid factors that impact seismic velocity and impedance," 2005.
[65] T. Boyd, "Geophones.."
[66] Sercel, "Sercel products land seismic acquisition," 2015.
[67] InovaGeo, "Ahv-iv series: Univib, commander, renegade, xvib - land seismic acquisition equipment, inova geophysical.," 2010.
[68] XSGeo, "Seismic acquisition," 1999.
[69] D. J. L. Ahern, "Seismic reflection method," 2007.
[70] "Huygens–fresnel principle," 2015.
[71] S. Sentence, "Geometrical optics.," 2009.
[72] E. Weisstein, "Snell's law.," 2015.
[73] Britannica, "Snell's law | physics," 2015.
[74] W. Whitman, "Seismic methods," 2001.
[75] K. Endsley, "What is seismology and what are seismic waves?," 2007.
[76] O. Novotny, "Some results of investigating the crustal and upper mantle structure in central europe by means of seismic surface waves," *International Congress of the Brazilian Geophysical Society*, vol. 2.
[77] U. of Waikato, "Types of seismic waves." Image Online.
[78] G. S. U. D. of Physics and Astronomy, "Maxwell's equations." Online.
[79] ABEM, "Terrameter sps 1000," 2014.
[80] MCM, "Accuref 20 permanent reference electrode," 201.
[81] Inova, "Ahv-iv commander (pls-364," 2012.
[82] M. Geophysics, "Adu-07e-technical-data," 2015.
[83] Geometrics, "A professional magnetics mapping system," 2014.
[84] M. Geophysics, "Mfs-07e-technical-data," 2015.